Surface Wave Interferometry

David Fraser Halliday
BSc. Hons. Geophysics, 2005
University of Edinburgh

Thesis submitted in fulfilment of
the requirements for the degree of
Doctor of Philosophy

School of GeoSciences
University of Edinburgh
2009

For Mum and Granny

"Je suis prest"

"I am ready"

Motto of the Clan Fraser

Acknowledgements

On a fateful day in the spring of 2005 I walked into the office of Andrew Curtis, introduced myself, and explained that I had applied for a PhD project in Cambridge and was looking for some advice. Within fifteen minutes I had been convinced to take on a PhD project in Edinburgh and little did I know that those fifteen minutes were to be the start of a fruitful four years. Those four years have gone beyond all of my expectations and without Andrew none of this could have been possible. His management of the project has ensured that everything has gone as smoothly as possible, his infectious enthusiasm, positive outlook, and ability to spot problems and new applications has fuelled the project, and his excellent relationship with both Schlumberger and WesternGeco allowed us to do work that would not have been possible with only the support of the University. I cannot begin to thank Andrew enough for allowing me this opportunity and hope that we keep in touch and continue to work together in the future.

My first real experience of being a researcher came in the summer of 2005 when I travelled to Oslo to work on a 3 month internship with Johan Robertsson and Dirk-Jan van Manen. Both made me feel most welcome in Oslo, taught me to be patient, and have continued to provide support and guidance throughout the course of my Ph.D. I can't thank them enough for their time.

In Cambridge, Ed Kragh gave his valuable time to help us acquire our own data with further assistance from David Leslie. In Cairo, Peter Vermeer helped to give us the capability to test our methods using industrial data. Peter was patient and allowed us to do our own thing and has hosted me three times as a visiting scientist in Egypt. Anna and Claudio's expertise in seismic data analysis really helped us to do some really 'magic' things with the data. I must also thank Larry, Hans, and Andreas who helped to make me feel most welcome in Cairo.

In Edinburgh, after almost 8 years there are too many people to mention. At the very least I must thank my Edinburgh Seismic Research colleagues and friends Tom,

Heather, Mohammad, Adam, and Simon who were always good company and willing to listen, I'm sure we'll keep in touch for years to come.

Much of the work in this thesis has been peer reviewed after submission for publication. I would like to thank Deyan Dragnanov, Xander Campman, Kasper van Wijk, Roel Snieder, Ivan Vasconcelos, Andrey Bakulin, and several anonymous reviewers for valuable comments on the work in this thesis.

Kristy has supported me all the way through, and despite threatening to, she didn’t steal any of my ideas! I promise that next time I go to Paris I'll take her instead of the gravity meter. Finally I must thank my family, they have supported me through my higher education, and tolerated infrequent visits. I must give special mention to my Mum and my late 'Granny' Agnes Fraser, this thesis is for them!

Declaration

I declare that this thesis has been composed solely by myself and that it has not been submitted, either in whole or in part, in any previous application for a degree. Except where otherwise acknowledged the work presented is entirely my own.

David Fraser Halliday

Abstract

This thesis concerns the application of seismic interferometry to surface waves. Seismic interferometry is the process by which the wavefield between two recording locations is estimated, resulting in new recordings at one location as if a source had been placed at the other. Thus, in surface-wave interferometry, surface waves propagating between two receiver locations are estimated as if one receiver had recorded the response due to a source of surface-wave energy at the other receiver. In global and engineering seismology new surface-wave responses can allow for imaging of the subsurface, and in exploration seismology it has been proposed that these new surface-wave responses can allow for the prediction and removal of so-called ground-roll (surface waves that are treated as noise). This thesis presents a detailed analysis of surface-wave interferometry: using a combination of modelling studies, real-data studies, and theoretical analyses the processes involved in the application of interferometry to complex (both multi-mode and scattered) surface waves are revealed. These analyses identify why surface waves are often dominant in the application of interferometry, where errors may be introduced in the application of surface-wave interferometry, and how interferometry may be processed in such a way as to minimise those (and other) errors. This allows for the proposal of new data-processing strategies in the application of seismic interferometry to surface waves, potentially resulting in improved surface-wave estimates. Much of the work in this thesis focuses on the use of seismic interferometry to predict and subtract surface waves in land-seismic exploration surveys. Using insights from the presented analyses it is shown that seismic surface waves can be successfully predicted and removed from land-seismic data using an interferometric approach. However, the work in this thesis is not only limited to applications in exploration seismology. In addition to the ground-roll removal method, improved estimates of higher-mode and scattered surfaces waves may allow for more advanced imaging algorithms to be used in conjunction with seismic interferometry. Also, as a consequence of the

analysis presented a Generalized Optical Theorem for Surface Waves is derived. This highlights a link between seismic interferometry and the optical theorem and may allow for further application of optical theorems in seismology.

Contents

1. Introduction

1.1 Green's function construction by cross-correlation

> *"by cross-correlating noise traces recorded at two locations on the surface, we can construct the wave field that would be recorded at one of the locations if there was a source at the other."*
>
> Claerbout's conjecture, from Rickett, J., and J. Claerbout, 1998, Acoustic daylight imaging via spectral factorization: Helioseismology and reservoir monitoring, *The Leading Edge*, Vol. 18, 957-960.

In 1968 Jon F. Claerbout showed that the reflection response of a layered medium could be synthesized from the transmission response of that medium. In other words by recording (at the surface) the response due to wave sources at depth, one can synthesize the recordings as if a source had also been placed at the surface recording location. The response (i.e., recording of the wavefield) at one point, due to an impulse at any point in space is often referred to as the impulse response, or Green's function. Claerbout proposed that Green's functions could be constructed by cross-correlation of noise (where the noise sources are at depth). This is often referred to as "Claerbout's conjecture", finally proved by Wapenaar in 2003, and the method of synthesizing Green's functions from noise (or background) wavefields in this way is now commonly known as seismic interferometry.

An example geometry for interferometry is shown in Figure 1.1a. Responses from each source point on an arbitrarily shaped surrounding boundary (S) are recorded at a pair of receivers ($\mathbf{r}_A$ and $\mathbf{r}_B$) and cross-correlated. By summing this whole set of cross-correlated recordings the inter-receiver Green's function (as in Figure 1.1b) is formed by a process of constructive and destructive interference. The

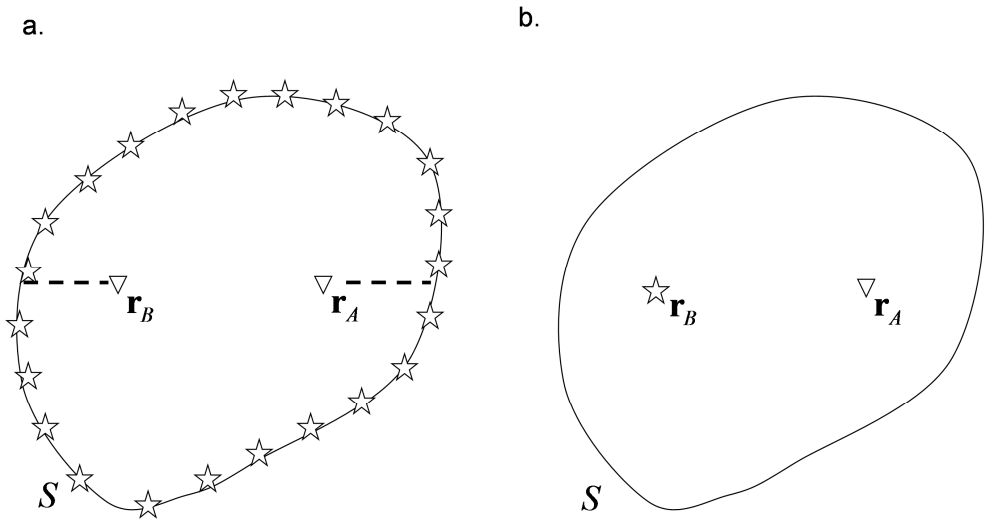

Figure 1.1: (a) Typical configuration for wavefield interferometry. Sources (stars) are located on the arbitrarily shaped surrounding boundary, *S* and responses are recorded at two receiver positions, $\mathbf{r}_A$ and $\mathbf{r}_B$ (triangles). (b) Interferometry synthesizes the response as if one of the receivers had been a source. Dashed lines in (a) illustrate the paths between the receivers and the stationary points on the boundary corresponding to the direct wave.

waves which propagate along paths between $\mathbf{r}_A$ and $\mathbf{r}_B$ sum constructively and the waves which do not propagate along those paths sum destructively.

The original application proposed by Claerbout in 1968 received little attention until around the turn of the century. Further advances in theory and application of interferometry can be traced back to the mid-nineties when the method of time-reversed acoustics was popularized by Mathias Fink and co-workers (for a thorough review see Fink *et al.*, 2000). The general principal of this work is that if waves from a point source are recorded at a perfect time-reversal device (a fully enclosing array of transducers surrounding the source point), the recorded waves can then be emitted back into the medium in time-reversed order (i.e. the last wave recorded is the first wave emitted). What one observes is the wavefield converging to a focus of energy at the original source location (Derode *et al.*, 1995). In Figure 1.2 a sketch from Fink *et al.* (2000) is shown illustrating an application of the time-reversal process. In a first step waves are emitted from a transducer (A) and propagate through a reverberating medium before being recorded at the transducer array (B). In the second step the recorded waves are emitted in time reverse from the array, propagate

back through the reverberating medium and focus on the original source position (A). In this example the transducer array (B) is equivalent to the boundary surface, *S* in Figure 1.1.

However, the energy at the focus is not removed if there is no time-reversal of the original source (an acoustic sink). In that case one then observes divergent wave propagation again, as though the original source had been reconstructed. However, since the experiment is now running in 'reverse-time' this results in a time-reversed Green's function. Derode *et al.* (2003a; 2003b) used this time-reversal argument to present an elegant derivation of interferometry. They found that it is possible to use the diverging wavefield from the focus to reconstruct the signal from an actual source at that position: imagine placing a receiver at the position of the focus and another somewhere else in that medium, the time-reversal process then constructs the inter-receiver Green's function. Thus Claerbout's conjecture was verified using time-reversal and reciprocity. This approach is discussed in more detail by Curtis *et al.* (2006).

Around the same time as these observations were made in the acoustics community, theoretical and experimental advances were being made in other fields. Experimental advances were made by Lobkis and Weaver (2001) and Weaver and Lobkis (2001) who showed that it was possible to extract inter-receiver Green's functions using diffuse ultrasonic wavefields. In seismology, Campillo and Paul (2003) and Shapiro and Campillo (2004) made similar observations using passive-seismic wavefields: they were able to extract estimates of inter-receiver surface-wave fields from noise recordings, the first successful application to seismic data. While the majority of this early work involved the use of diffuse (or passive) wavefields, applications in exploration seismology were also being proposed. For example the virtual-source method introduced by Bakulin and Calvert (2004; 2006) employs a time-reversal argument to explain how receivers in wells within the Earth's subsurface can be used to synthesize so-called 'virtual sources' in the subsurface using seismic interferometry.

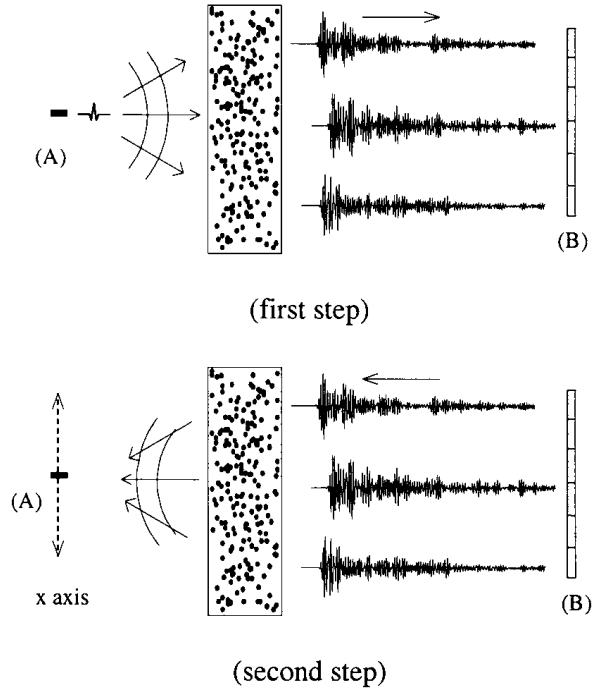

Figure 1.2: Illustration of a time-reversal experiment from Fink *et al.* (2000). (Top) A source pulse emitted from transducer A propagates through a reverberating medium (the dotted region) and is recorded at the transducer array B. (Bottom), the waves recorded at the array B are emitted in time-reversed order from the array; they propagate back through the reverberating medium before converging on the original source position A.

Firm theoretical foundations were provided by Wapenaar (2003) who gave a proof of Claerbout's conjecture using a method based on representation theorems and Wapenaar (2004) used a similar approach to derive a proof for point sources and distributed passive-noise sources. Later, Wapenaar and Fokkema (2006) considered noise fields, point sources and transient sources in acoustic and elastic media. A similar approach to that of Wapenaar and Fokkema (2006) was taken by van Manen *et al.* (2005; 2006) who again highlighted the link between interferometry and time-reversal as their interferometric full-wavefield modelling technique was based on the use of time-reversal and reciprocity.

To illustrate interferometry theoretically for the acoustic case, we follow van Manen *et al.* (2005). To time reverse a wavefield in a volume *V*, bounded by surface *S*, the wavefield $p(\mathbf{r})$ and its gradient $\partial_i p(\mathbf{r})$ due to a source inside *V* and measured around surface *S* have to be time reversed on the surface. The time-reversed pressure

field $p_{tr}(\mathbf{r}_A)$ radiated from the boundary and observed at a point $\mathbf{r}_A$ can then be written:

$$p_{tr}(\mathbf{r}_A) = \oint_{\mathbf{r}\in S} \frac{1}{\rho(\mathbf{r})}\left[\partial_i G(\mathbf{r}_A,\mathbf{r}) p^*(\mathbf{r}) - G(\mathbf{r}_A,\mathbf{r})\partial_i p^*(\mathbf{r})\right] n_i \, dS \, . \qquad (1.1)$$

Here $\rho(\mathbf{r})$ is the density at the surface *S*, n_i is the *i*th component of the normal vector to the surface *S*, and $G(\mathbf{r}_A,\mathbf{r})$ is the Green's function representing the pressure response at $\mathbf{r}_A$ due to a monopolar point source at $\mathbf{r}$ (a monopole source is a source that radiates energy equally in all directions; we refer to the spatial derivative of a monopole source in some direction *i*, $\partial_i G(\mathbf{r}_A,\mathbf{r})$, as a dipole source). Einstein's summation convention applies for repeated indices. In the example shown in the bottom part of Figure 1.2, $p_{tr}(\mathbf{r}_A)$ is the time-reversed wavefield at the transducer (A), $p(\mathbf{r})$ is the pressure recorded at the transducer array (B) in the top part, and $G(\mathbf{r}_A,\mathbf{r})$ are the Green's functions describing wave propagation between the transducer array (B) and the single transducer (A).

The wavefield $p(\mathbf{r})$ is assumed to be due to a point source at location $\mathbf{r}_B$ and the pressure response can be replaced by the Green's function describing the pressure response due to a monopole source $G(\mathbf{r},\mathbf{r}_B)$. van Manen *et al.* (2005) substitute these terms for the pressure field and use source-receiver reciprocity to show that the Green's function, $G(\mathbf{r}_B,\mathbf{r}_A)$ between points $\mathbf{r}_A$ and $\mathbf{r}_B$ can be determined by cross-correlation of Green's functions representing the responses at $\mathbf{r}_A$ and $\mathbf{r}_B$ due to impulsive sources at $\mathbf{r}$ on an enclosing surface *S*:

$$G^*(\mathbf{r}_B,\mathbf{r}_A) - G(\mathbf{r}_B,\mathbf{r}_A) = \oint_{\mathbf{r}\in S} \frac{1}{\rho(\mathbf{r})}\left[G^*(\mathbf{r}_A,\mathbf{r})\,\partial_i G(\mathbf{r}_B,\mathbf{r}) - \partial_i G^*(\mathbf{r}_A,\mathbf{r}) G(\mathbf{r}_B,\mathbf{r})\right] n_i \, dS \, . \qquad (1.2)$$

The right hand side of Equation (1.2) corresponds to the configuration shown in Figure 1.1a, and the left hand side corresponds to the configuration shown in Figure

1.1b. To illustrate the application of Equation (1.2) we use a simple 2D acoustic example using the layout shown in Figure 1.1a. We use a wave propagation velocity of 750 m/s, the boundary *S* is circular with radius 100 m and the two receivers are located 100 m apart, with the mid-point between the two receivers coinciding with the centre of the circle. We use 315 sources on the boundary surface separated at 2 m intervals. The source function is a Ricker wavelet with a central frequency of 20 Hz. In Figure 1.3a and b we show the pressure recordings due to monopole sources at each of the 315 boundary positions for receiver $\mathbf{r}_A$ and $\mathbf{r}_B$ respectively (expressions $G(\mathbf{r}_A,\mathbf{r})$ and $G(\mathbf{r}_B,\mathbf{r})$ in Equation (1.1)). In Figure 1.3c and d we show the equivalent spatial derivatives (expressions $\partial_i G(\mathbf{r}_A,\mathbf{r})n_i$ and $\partial_i G(\mathbf{r}_B,\mathbf{r})n_i$). In Figure 1.3e we show the evaluation of the integrand in Equation (1.2) as a function of source number, and in Figure 1.3f we show the summation (over boundary sources) of this term which corresponds to evaluating the integral in Equation (1.2). For reference we show the directly evaluated Green's function using a dashed line (the term on the left hand side of Equation (1.2)), while the result of Equation (1.2) is shown by the solid line which is deliberately shifted by 1 sample to better illustrate the match. Note that the result of interferometry is the difference of the forward time (causal) Green's function, and the reverse time (acausal) Green's function (see the left hand side of Equation (1.2)), emphasizing the connection with time-reversal.

After being dormant for over 30 years, the method has been developed greatly in a short space of time, creating a theoretical and practical basis for future work. The body of literature on interferometry continues to expand at pace: for example derivations of interferometry have been extended to include different operations such as convolution (Slob *et al.*, 2007; Slob and Wapenaar, 2007; Wapenaar, 2007) and deconvolution (Vasconcelos and Snieder, 2008a, 2008b; Wapenaar *et al.*, 2008b, 2008b), and also to different wave propagation regimes including electromagnetics (Slob *et al.*, 2007; Slob and Wapenaar, 2007), seismo-electrics, diffusion phenomena and quantum physics (Wapenaar *et al.*, 2006; Snieder *et al.*, 2007).

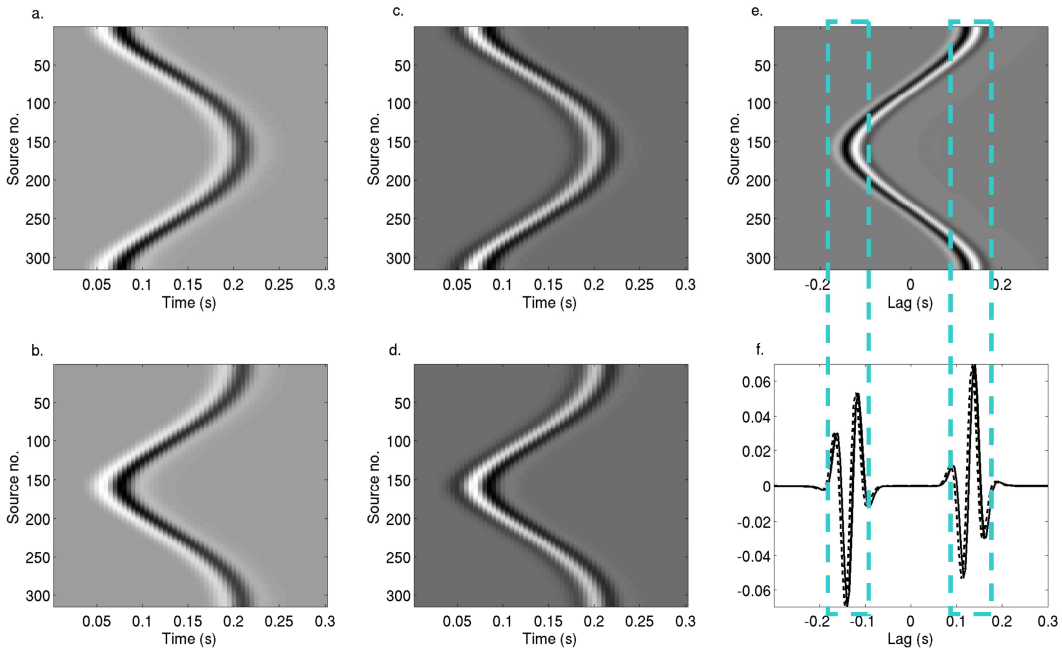

Figure 1.3: (a), (b) Pressure responses at $\mathbf{r}_A$ and $\mathbf{r}_B$ due to monopolar sources on the surface *S* in Figure 1.1a. (c), (d) Equivalent pressure responses at $\mathbf{r}_A$ and $\mathbf{r}_B$ due to dipolar sources. (e) Cross-correlation of (a) and (d) minus the cross-correlation of (b) and (c). (f) Solid line shows the sum of all source points in (e), with the directly modelled result shown for comparison deliberately offset by one time sample (dashed line).

1.2 Interferometric theory in seismology

Theory dictates that we require a boundary of sources that completely encloses the receiver locations of interest (i.e., the configuration shown in Figure 1.1), or when a free surface is present this surface can form part of the boundary which can be source free (Figure 1.4a). However, seismic interferometry is now applied across a range of settings in which such conditions are not met. In Earthquake seismology interferometric surface-wave estimates are made from recordings of noise, where noise sources such as oceanic microseisms are predominantly located in the near surface (e.g., Shapiro *et al.*, 2005). In exploration seismology estimates are predominantly made using active sources which are also typically located at the surface of the Earth (e.g., Bakulin and Calvert, 2004, 2006; Mehta *et al.*, 2007). In engineering seismology estimates can be made using both active and passive sources

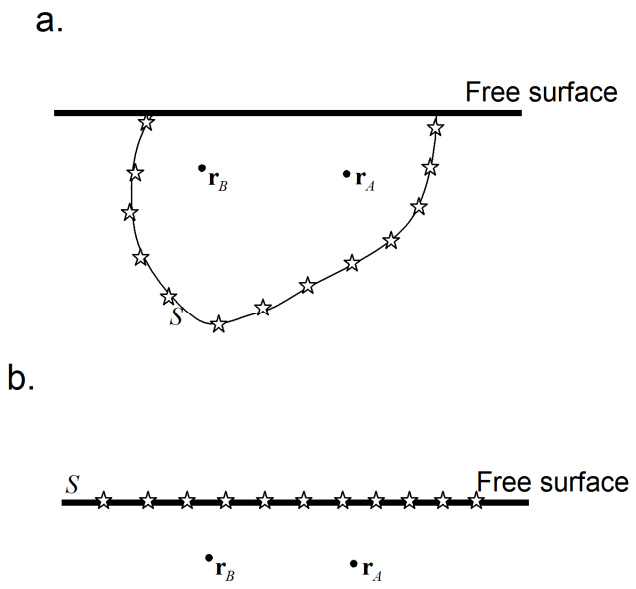

Figure 1.4: (a) Configuration with a free surface, where the boundary does not span the free surface, (b) configuration for typical applications of seismic interferometry, where sources are only available at the free surface and the surface *S* is forced to be located at the free surface.

(Chávez-García and Luzón, 2005; Draganov and Ghose, 2006; Picozzi *et al.*, 2009), which again are predominantly located at the surface of the Earth (e.g., traffic and other anthropogenic noise). Thus, we are forced to use a truncated boundary of sources *S*, located on the free surface, the one place where theory dictates that we do not require boundary sources (Figure 1.4b). We also require different source types, which are not likely to be available, and conventional correlation-type interferometry requires that there are no losses in the medium of interest whereas the Earth is often strongly attenuating.

Studies have been undertaken to determine the effect of relaxing some of these constraints. For example, Wapenaar and Fokkema (2006) use approximations to derive interferometric formulae which only use a single type of source. The approximations they use (including that the enclosing boundary is a circle with extremely large radius, and that the medium at and around the boundary is homogeneous) and the scale factors that are thus introduced illustrate the difficulty in recovering exact interferometric estimates in practical situations. Further, Wapenaar (2006) considers the effect of one-sided illumination (i.e., sources only at the surface,

with none at depth) and finds that body-wave components of Green's function estimates can be made provided that (1) the medium is strongly heterogeneous and (2) long recording times are used such that highly-reverberate coda waves are included in the application of interferometry.

One method to analyse the application of interferometry is the method of stationary phase. In Figure 1.3e and f we have highlighted the stationary-phase region using a dashed grey box: it is clear that the dominant contribution to the interferometric estimate in panel (f) comes from the apexes of the curves in panel (e). These apexes are the points of stationary phase; points where the phase does not change with respect to boundary source position. As a consequence, the so-called stationary-phase method can be used to solve interferometric surface integrals using analytical Green's functions. This is done by assuming that major contributions to the integral are derived from the points on the surface S at which the integrand has stationary phase (stationary paths for the direct wave between the two receiver locations are shown in Figure 1.1a using dashed lines). This method has been used to analyse direct body and surface waves (Snieder, 2004a), reflected body waves (Snieder *et al.*, 2006) and scattered acoustic waves (Snieder *et al.*, 2008). The analysis for reflected and scattered body waves reveals a significant source of error in practical seismic interferometry: non-physical waves are synthesized when source distributions are limited (e.g., when sources are only available at the surface of the Earth). The insights provided by stationary-phase analysis often allow steps to be taken to mitigate such errors. For example, Mehta *et al.* (2007) use wavefield separation to suppress the non-physical waves identified by Snieder *et al.* (2006) that appear in reflection-seismic settings.

The requirement that seismic interferometry be applied in lossless media is not realistic and the problem of attenuation has been discussed by several authors. For example, Snieder (2007) shows that an additional volume integral is required in Equation (1.2) in the presence of attenuation, and Slob and Wapenaar (2007) and Slob *et al.* (2007) show that convolution-type interferometry is a valid alternative to conventional correlation-type interferometry in attenuating media. These studies concentrate on electromagnetic applications; the convolution approach has not been utilised in seismology. Further Draganov *et al.* (2008) show that damping factors

(chosen to account for energy losses due to attenuation) can be applied to suppress artefacts related to the presence of attenuation in correlation-type interferometry. Deconvolution has also been proposed as a valid alternative to cross-correlation that would mitigate the effect of attenuation on the application of seismic interferometry (Wapenaar *et al.*, 2008b).

Despite the rapid growth of the field there are still a number of interesting areas that have not been fully addressed. For surface-wave interferometry, only the fundamental surface-wave mode has been used to invert for group-velocity tomography maps (Shapiro and Campillo, 2004; Gertstoft *et al.*, 2006). Many inversion schemes exist which utilise the information in fundamental, higher, and scattered surface-wave modes to better constrain both geological structure and elastic properties of the Earth (Snieder, 1986; Marquering and Snieder, 1995; Trampert and Woodhouse, 1995; Meier *et al.*, 1997; Ritzwoller *et al.*, 2002); if such wave types could be recovered using interferometry then these more sophisticated inversion schemes could also be applied to interferometric surface-wave estimates, providing more reliable and spatially more extensive subsurface images. Further, a better understanding of the application of interferometry to more complex surface waves may improve the use of the method in near-surface or exploration settings where higher-frequency surface waves often exhibit strong higher-mode energy and strong lateral scattering (see below). While errors introduced due to limited source coverage have been identified in simple situations, the errors introduced by limited source coverage in the presence of more complex wavefields have not been considered (e.g., where the complexity of non-physical waves is manifest in the presence of higher-mode surface waves and strong multiple scattering). Further errors may also be introduced due to non-uniform source distribution and while several authors have proposed methods to account for these errors (e.g., Stork, 2007; Wapenaar *et al.*, 2008a; van der Neut and Bakulin, 2009), at the time of writing no application to a general class of problem exists. This thesis focuses on these areas, considering the application of seismic interferometry to surface waves exhibiting both higher modes and strong lateral scattering. We consider sources of error, typical source geometries, and methods by which interferometric estimates can be improved, before using insights and observations from our various analytic approaches to apply

interferometry to decompose real surface waves recorded during a land seismic exploration survey with a view to enhancing subsurface images obtained in an industrial setting.

1.3 Applied interferometric ground-roll removal

One particular application forms the focus for many of the theoretical and practical developments in this thesis. In exploration seismology scattered surface waves are of great interest. Surface-wave (or ground-roll) signals generally provide little useful information in exploration seismology, and often mask other, more useful body-wave arrivals. Hence, surface waves are regarded as noise. Lateral scattering in the near-surface of the Earth results in a form of surface-wave noise that is particularly difficult to remove, since its time-varying directions of arrival are unknown a priori. Several algorithms have been proposed to remove the scattered surface waves (Blonk *et al.*, 1995; Blonk and Herman, 1996; Ernst *et al.*, 2002a; Ernst *et al.*, 2002b; Campman *et al.*, 2005; Campman *et al.*, 2006; Herman and Perkins, 2006). Such algorithms rely on single-scattering approximations, inverse-scattering schemes, and forward modelling (with the exception of Herman and Perkins (2006) who use a data-driven inversion approach). Acquisition-based suppression schemes also exist in which arrays are used to suppress near-surface scattering (Morse and Hildebrandt, 1989; Regone, 1998; Özbek, 2000a, 2000b). However, the spatial resolution of data may be compromised by using spatially-extensive arrays, and as the exploration-seismics industry moves towards so-called point-receiver (i.e., single-sensor, rather than stacked-array) recordings, new algorithms may be required in order to suppress such noise.

The application of interferometry to ground-roll removal is of particular interest because interferometry is naturally applied directly to point-receiver recordings. It provides the potential to synthesize complex scattered surface-wave fields without approximations, is entirely data driven, and no forward modelling or inversion is required. The potential downside is that the use of many cross-correlation operations and least-squares filtering for ground-roll removal (e.g., Dong *et al.*, 2006) may make the method more costly computationally than more conventional (and in some

cases ineffective) methods of ground-roll removal such as *f-k* (frequency-wavenumber) or *f-x* (frequency-offset) domain methods. Nevertheless, given the success of surface-wave interferometry in earthquake seismology it is not unreasonable to expect an application to surface waves in an exploration setting to be successful. Vasconcelos *et al.* (2008) have shown results for a synthetic modelling study where they consider scattered surface waves that lie on the same line as the source and receiver locations. However, such in-line scattered arrivals are easily suppressed using conventional noise removal methods as they exhibit the same apparent velocities and frequencies as the direct surface waves. At the time of writing while it has been shown, both theoretically and in data examples, that direct surface waves can be estimated interferometrically and removed from active source data, no successful application has been published for the estimation and removal of *real*, 3-dimensionally scattered surface waves. This thesis presents such an application.

1.4 Thesis plan

Chapter 2 shows that it is possible to isolate the direct surface wave propagating between two receiver locations when the sources used in interferometry are located at the surface of a 2-D Earth model. The adaptive removal of these surface waves is illustrated, showing that body waves that arrive at the same time as the surface waves can be preserved while the surface waves are removed.

In *Chapter 3* a 2-D seismic data set is used to illustrate the recovery of surface waves in a high-frequency, near-surface setting. It is shown that when using active sources the interferometric estimates are indeed dominated by surface waves as illustrated by the synthetic data in Chapter 2. Further it is shown that the phase of higher-mode surface waves can be successfully recovered using a 2-D seismic acquisition geometry. Additional passive-noise surface-wave estimates are illustrated using noise recordings in a sub-urban setting. These estimates are compared with both real active-source data and with active-source interferometric estimates, showing that a combined approach may lead to improved data bandwidth.

Chapter 4 presents a detailed stationary-phase analysis of the interferometric construction of multi-mode surface waves. By solving the interferometric integral for surface waves exactly we reveal several key processes in the recovery of surface waves using interferometry. Most significantly, this work reveals the role of sources at depth which were previously thought not to play a role in the recovery of surface waves: without sources at depth, significant amplitude errors may be introduced to the estimates, and non-physical waves are introduced in the presence of multiple surface-wave modes. We illustrate how these non-physical waves appear when interferometry is applied to surface waves using various realistic surface source geometries, and analyse the effect of such source distributions on the geometrical spreading and phase of the physical surface-wave arrivals.

In *Chapter 5* the stationary phase analysis presented in Chapter 4 is extended to the case of scattered surface waves. This chapter shows how the stationary-phase approach can be used to derive a Generalized Optical Theorem for surface waves. This theorem is new, and correctly describes the relationship between incident and scattered surface-wave modes. It should find application not only in seismology, but other fields of physics such as ocean acoustics, material science, quantum mechanics and ultrasonics. The stationary-phase analysis used here is the basis for the analysis of interferometry applied to scattered surface waves that appears in Chapter 6.

In *Chapter 6* insights provided by the stationary-phase analysis in Chapter 5 are discussed regarding the application of seismic interferometry to singly- and multiply-scattered surface-wave data. We consider the breakdown of stationary-phase analysis in the presence of attenuation, and the role of source geometry and attenuation in introducing non-physical arrivals. Convolution-type interferometry is introduced for scattered surface waves, showing improved results in attenuative media. We illustrate our results using semi-analytical scattered surface-wave Green's functions. The non-physical arrivals analysed here are the subject of the second part of Chapter 7 where we consider the estimation and removal of such non-physical events.

Chapter 7 presents an alternative approach to the processing of interferometric data that makes use of arrays of receivers and corrects for directionally-biased source distributions. By synthesizing virtual sources across an array of receivers (creating an array of virtual sources) it is possible to divide the interferometric estimates into their

directional components. In the presence of directional bias (where each virtual source has non-uniform directionality) this allows each of the directional components to be balanced, such that the resulting single virtual source has a more uniform radiation pattern. It is found that non-physical arrivals (such as those illustrated in Chapter 6) can be dominant after this balancing, and it is further shown that it is possible to estimate and adaptively subtract such non-physical arrivals from the interferometric estimates.

Chapter 8 presents the results of the interferometric processing of surface waves recorded in an industrial seismic survey, and also shows the application of the ground-roll removal method. In this chapter we use intuition gained from previous chapters to develop a processing scheme allowing for the estimation of scattered surface waves using both cross-correlation and cross-convolution. By combining both the correlation and convolution approach, and by using adaptive filtering we are able to remove the dominant scattered energy from source-receiver seismic data.

In *Chapter 9* it is shown that it is likely that much of this theory might be applied in the reciprocal situation where a real source of energy (recorded at a surrounding boundary of receivers) can be turned into a virtual *receiver*. Interferometric theory is derived for this case, and the method is illustrated using analytical surface-wave Green's functions and Earthquake data recorded at the USArray (a densely distributed network of seismograph stations).

Finally, *Chapter 10* presents areas for future work arising from the work presented in this thesis. This includes enhancements to the ground-roll removal method in Chapter 8, further uses of the non-physical arrivals identified in Chapters 4, 5 and 6, and the thesis is concluded by considering the link between interferometry and the generalized optical theorem exposed in Chapter 5.

1.5 Publications

Chapter 2 is published as**:**

- Halliday, D.F., A. Curtis, D.-J. van-Manen & J. Robertsson, 2007. Interferometric surface wave isolation and removal, *Geophysics*, 72, A69-A73.

Chapter 3 is published as:

- Halliday, D.F., A. Curtis & E. Kragh, 2008. Seismic surface waves in a suburban environment – active and passive interferometric methods, *The Leading Edge*, 27, 210-218.

Chapter 4 is published as:

- Halliday, D.F. & A. Curtis, 2008. Seismic interferometry, surface waves, and source distribution, *Geophys. J. Int.*, 175, 1067-1087.

Chapter 5 is published as:

- Halliday, D.F. & A. Curtis, 2009. A generalised optical theorem for surface waves and layered media, *Phys. Rev. E.*, 79, 056603.

Chapter 6 is published as:

- Halliday, D.F. & A. Curtis, 2009. Seismic interferometry of scattered surface waves in attenuative media, *Geophys. J. Int.*, 178, 419-446.

Chapter 7 is in press as:

- Curtis, A. & D.F. Halliday, 2009. Directional Balancing for Seismic Interferometry, *Geophysics* [Note: In this chapter I was more focused on testing the directionality correction method and the development and testing of the proposed method of predicting and subtracting non-physical arrivals.]

Chapter 8 is *sub judice* as:

- Halliday, D.F., A. Curtis, P. Vermeer, C. Strobbia, A. Gluschenko, D-J. van Manen and J.O.A. Robertsson, 2009. Interferometric Ground Roll Removal: Attenuation of near-surface scattered noise from single-sensor data, *Geophysics*. [Note: Figures showing Digital Group Forming were generated by Anna Glushchenko and Claudio Strobbia.]

Chapter 9 is in press as:

Curtis, A., H. Nicolson, D.F. Halliday, J. Trampert & B. Baptie, 2009. Virtual Seismometers in the Subsurface of the Earth from Seismic Interferometry, *Nature Geoscience*. [Note: In this chapter I focused on developing theory to include strain sensors and to demonstrate the strain sensors using theoretical surface-wave Green's functions.]

2. Interferometric surface wave isolation and removal

The removal of surface waves (ground roll) from land-seismic data is critical in seismic processing, since these waves tend to mask informative body-wave arrivals. When surface waves are scattered their removal becomes difficult, and data quality is often impaired. We apply a method similar to the “virtual source” form of seismic interferometry, using both sources and receivers at the surface of the Earth to estimate the surface-wave component of the Green's function between any two points. These estimates are adaptively subtracted from seismic-survey data, providing a new method of ground-roll removal that is not limited to non-scattering regions. We demonstrate the efficacy of this method using 2D synthetic data in acoustic and anelastic media.

2.1 ***Introduction***

In reflection seismology, surface waves constitute a strong source of noise that is difficult to remove and often obscures the reflected waves in which we are interested. In heterogeneous media, removal of these surface waves by conventional methods, such as frequency wavenumber (*f*-*k*) filtering, is often difficult as their energy is distributed over a wide portion of the *f*-*k* spectrum. We present a new method of surface-wave removal that can be applied in the time or frequency domain and has the potential to be effective in areas with both homogeneous and heterogeneous near-surface conditions.

It can be shown that the Green's function that accounts for wave propagation between two points, in lossless media, can be synthesised by cross-correlations of recordings of wavefields made at each point. These wavefields are excited by distributed active or passive (noise) sources, and details of the method differ depending on the source type (Wapenaar, 2004; van Manen *et al.*, 2005; van Manen *et al.*, 2006; Wapenaar and Fokkema, 2006). Such methods have found several

applications in seismology where they are collectively referred to as seismic interferometry.

When using active sources, theory indicates that sources are required to form a surface that bounds the portion of the earth in which we are interested. However, in practice this requirement can be relaxed: for example, in the virtual source method sources are located only at (or near) the Earth's surface and receivers are placed in a borehole. Recordings from these sources are used to create virtual sources at the down hole receivers (Bakulin and Calvert, 2004, 2006).

In the related field of passive-seismic interferometry cross-correlations of ambient noise at periods of 5 s to 20 s have been shown to produce estimates of the (direct) Rayleigh wave between surface receivers (Shapiro and Campillo, 2004; Shapiro *et al.*, 2005). The authors argue that the Rayleigh-wave component is isolated in these cross-correlations because (a) Rayleigh waves dominate the Green's function between surface locations, and (b) near-surface noise sources in this relatively low-frequency band preferentially excite Rayleigh waves.

We use a method similar to the virtual-source method but with a very different geometry, where both sources and receivers are located at the surface. Using the same reasoning as Shapiro *et al.* (2005) we expect, and observe, that our active-source method produces inter-receiver signals that are dominated by surface waves. In a conventional land-seismic survey, the response to surface sources can be recorded explicitly at any planned source and receiver locations. This allows the interferometric inter-receiver surface waves to be removed from source-receiver survey data, providing a new method of ground-roll removal (Curtis *et al.*, 2006; Dong *et al.*, 2006). Since interferometry works in any degree of heterogeneity, and indeed has been shown to work better in more strongly scattering media (Larose *et al.*, 2005), so should this method.

2.2 ***Guided wave construction in a 2-layer acoustic model***

By a simple process of cross-correlation and integration, Equation (1.2) determines the Green's function between two receivers. Similar expressions exist for differing

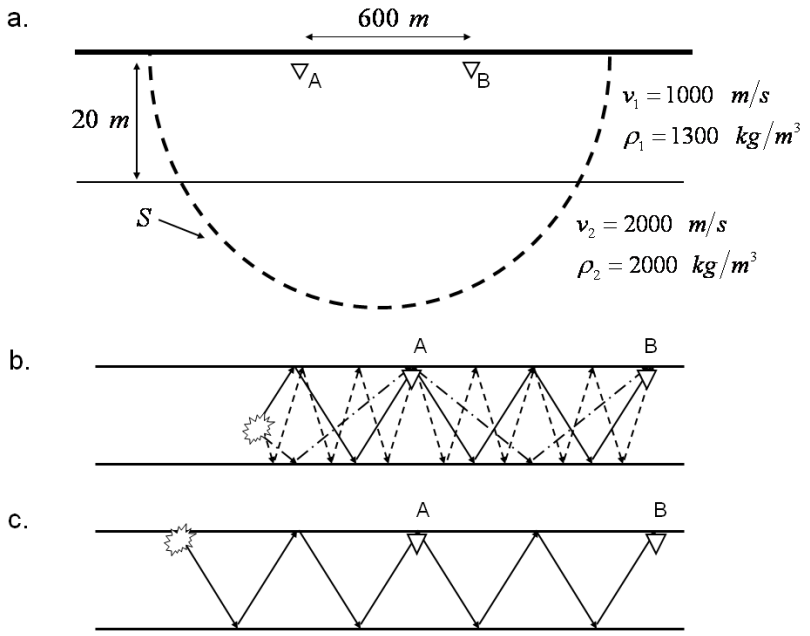

Figure 2.1: (a) Simple acoustic model used in initial testing. Receivers are labelled A and B and surface *S* is shown (dashed). (b) Top: an illustration of various multiple ray-paths from a source on the boundary *S* illustrated in (a). Bottom: Equivalent multiple ray-path to solid ray in top plot, but from a source at the surface. The source locations are stationary points for the multiples shown between the receiver pair A and B.

source and receiver types, and for elastic media (van Manen *et al.*, 2005; 2006; Wapenaar and Fokkema, 2006).

Equation (1.2) requires both monopole and dipole sources, and hence is difficult to apply in practice. To simplify this expression, Wapenaar and Fokkema (2006) assume that the region outside the surface *S* is homogeneous (with propagation velocity *c* and mass density ρ) and that the boundary is a sphere with large radius. These assumptions lead to the expression,

$$G^*(\mathbf{r}_B, \mathbf{r}_A) - G(\mathbf{r}_B, \mathbf{r}_A) = \frac{2i\omega}{\rho c} \int_{\mathbf{r} \in S} G^*(\mathbf{r}_A, \mathbf{r}) G(\mathbf{r}_B, \mathbf{r}) \; dS \,, \tag{2.1}$$

where $i = (-1)^{0.5}$ and only monopole sources are required. Where these assumptions are not met true amplitudes may not be correctly estimated, but the phase can still be correctly recovered (Korneev and Bakulin, 2006; Wapenaar and Fokkema, 2006). This expression still requires sources that surround the medium of interest which is

impractical, so we further approximate Equation (2.1). Consider the 2-layer model of Figure 2.1a, of which the integration boundary *S* encloses a part. We assume that the deepest sources provide a relatively small contribution to the inter-receiver surface waves (contributing predominantly up-going waves), and can be neglected. Furthermore, using simple geometrical arguments and applying the stationary-phase method of Snieder *et al.* (2006) it can be shown that for a stationary point on *S* (a position providing a dominant contribution to the interferometric integral) an equivalent stationary point exists at the surface (Figure 2.1b). This allows us to replace the integration over *S* in Equation (2.1) by a summation over *N* surface source positions, $\mathbf{r}_n$

$$G^*(\mathbf{r}_B,\mathbf{r}_A) - G(\mathbf{r}_B,\mathbf{r}_A) = C\sum_{n=1}^{N} G^*(\mathbf{r}_A,\mathbf{r}_n)G(\mathbf{r}_B,\mathbf{r}_n)\,, \tag{2.2}$$

where C is a scaling factor. Note that despite being at the free surface, this is non-zero as there are no derivatives present (cf. Equation 1.2). Equation (2.2) is similar to Equation (1) in Bakulin and Calvert (2004), but with a very different geometry using both surface sources and surface receivers. The results of Bakulin and Calvert (2004; 2006) show that despite the assumptions involved, expressions like Equation (2.2) are effective when using real data, where the boundary of sources is neither spherical nor located within a homogeneous region. Consider a group of high-order multiples that interfere to form a guided wave within the upper layer of Figure 2.1a. The acoustic guided wave is formed in a process similar to that of elastic surface waves (Shearer, 1999). From Figure 2.1b we can see that stationary points exist at the surface for any order of reflection, similar to the findings of Sabra *et al.* (2005), contributing multiples (and therefore guided waves) to Equation (2.2). An array of sources located in the region where we expect these guided-wave stationary points to occur can therefore be used to stimulate the guided-wave component of the Green's function. Mehta *et al.* (2007) show that upgoing reflections provide a weak contribution when compared to the contribution of the direct wave (or guided wave in this case). However, to ensure that any reflected wave contribution is further

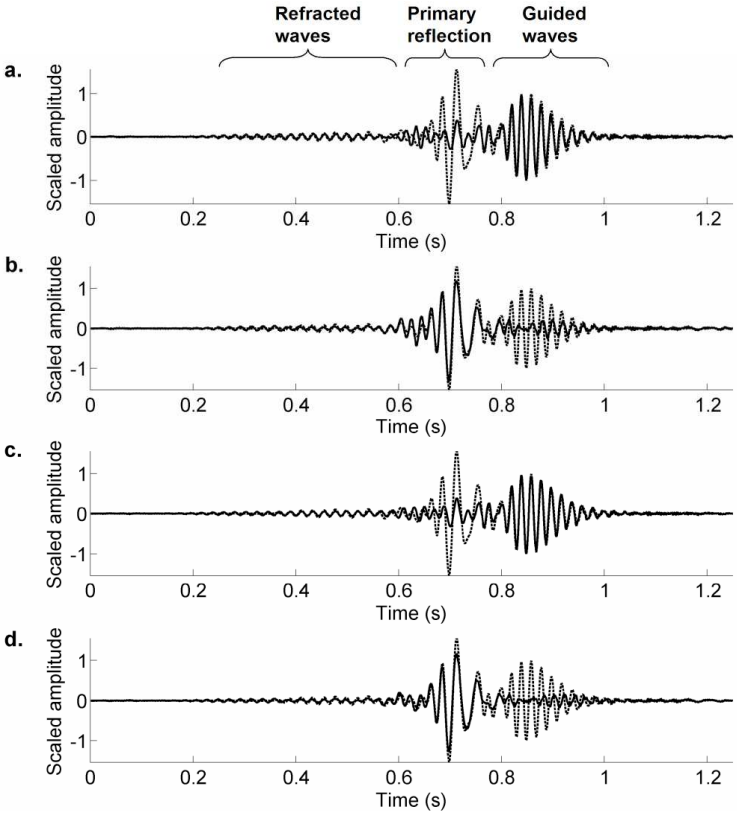

Figure 2.2: (a) The directly computed Green's function (dashed line), with the interferometrically estimated guided wave from one source pair superimposed (solid line). (b) The difference after scaling between the time series in (a), superimposed on the directly-modelled Green's function. (c) and (d) are similar to (a) and (b) except four source pairs are used in the estimate of the guided wave. Refracted waves, primary reflection and guided waves are labelled appropriately.

minimised we avoid placing sources near the locations where we expect primary-reflection stationary points.

To demonstrate our method we implement Equation (2.2) in the simple 2D model shown in Figure 2.1a. Synthetic data are computed using a viscoelastic finite-difference code (Robertsson *et al.*, 1994), with both attenuation and S-wave motion disabled. We first compute the Green's function between points A and B (located just below the free surface), band-limiting the result with a 25 Hz Ricker wavelet. This is shown as the dashed line throughout Figure 2.2. Three groups of waves can be seen: first the refracted wave arrives from around 0.35 seconds, then higher-amplitude body waves (a combination of direct and reflected waves) arrive at around

0.6 seconds, and the guided-wave train arrives from around 0.8 seconds. This full Green's function is treated as representing our measured seismic-survey data (obtained using a true source at either of the pair of receiver locations), from which we wish to remove the guided-wave component.

Two sources (located 40 m to the left of receiver A and to the right of receiver B, on the line where we expect guided-wave stationary points) are used to estimate the guided wave between the two receivers using Equation (2.2), resulting in both an acausal estimate and a causal estimate (band-limiting as above, but after cross-correlation). We consider only positive times in our analysis. Figure 2.2a shows the estimated trace (solid line), with the full Green's function plotted for reference (dotted line). The guided wave clearly dominates the estimate. After scaling the data to the guided-wave component, the difference of these two signals is plotted in Figure 2.2b. The scale factor is related to (amongst other effects) the source amplitude and wavelet, and the number of sources present. Note that in the difference trace the majority of the guided-wave energy has been removed, while the majority of the reflected wave remains.

If we had a full boundary of sources along S (i.e., if we apply Equations (1.2) or (2.1) exactly) the guided wave residual in Figure 2.2b would be zero, but the body waves would also have been annulled, as when the boundary of sources encloses the medium of interest the full, correct Green's function would be obtained for both curves in Figure 2.2a. However, if we use a line of several sources at the surface, then at least several of these sources will lie at stationary points providing contributions to Equation (2.2) that contain the correct inter-receiver surface wave. When these cross-correlations are stacked, the correct surface wave will sum constructively, and unwanted artefacts will interfere destructively. We may then apply a spatial taper in order that artefacts from the last few sources on the line do not remain un-cancelled. Also, in heterogeneous media secondary sources generated by lateral and vertical scattering of waves may supplement the source distribution, improving the results of Equation (2.2) (Larose *et al.*, 2005).

We therefore repeat the above experiment using 8 sources (with offsets of 20 m, 40 m, 60 m and 80 m either side of the receiver pair) summing and subtracting the

a.

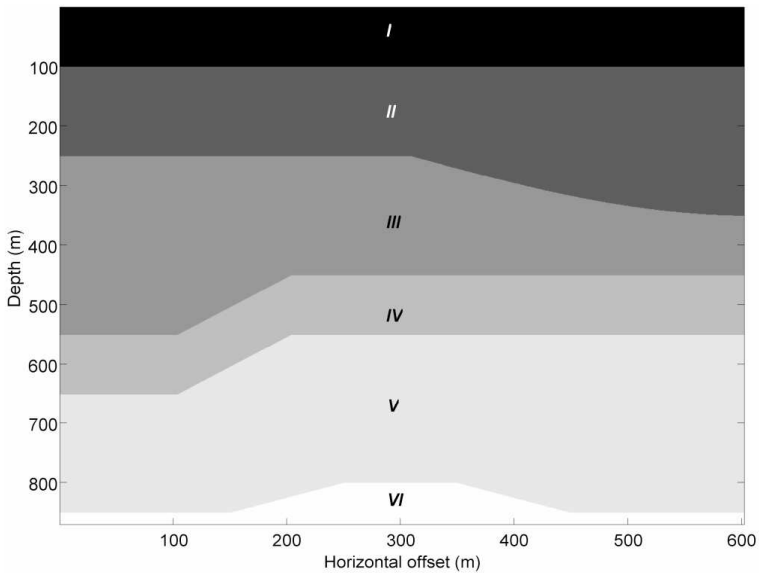

b.

Layer no.	v_p(m/s)	v_s(m/s)	ρ(kg/m^3)	Q_p	Q_s
I	1500	400	1700	150	100
II	1700	450	1800	10000	10000
III	2400	500	2000	10000	10000
IV	2750	600	2100	10000	10000
V	3000	700	2200	10000	10000
VI	4000	800	2500	10000	10000

Figure 2.3: (a) Model used for further testing. (b) Layer parameters.

estimated guided waves (Figure 2.2c and d). As expected the fit of the guided wave is improved in this case, resulting in a smaller residual in the difference trace.

In both examples artefacts have affected the earlier part of the data; if necessary the subtraction can be made in a certain *t-x* (time-offset) or *f-k* window, preserving these early arrivals and allowing the advantages of the *f-k* method to be combined with our new method.

2.3 ***Anelastic example***

The model in Figure 2.1a was sufficiently simple to analyse quantitatively and intuitively the effect of varying the position and number of sources. However, to analyse the method's application to anelastic media using physical energy sources in the real Earth the test model should exhibit elastic surface waves, rather than acoustic guided waves, shear motion and hence mode conversions and Rayleigh-type waves,

medium changes at depth producing deeper reflections (i.e., those of interest in reflection seismology), and energy losses by attenuation.

Wapenaar and Fokkema (2006) show that it is possible to find an expression similar to Equation (2.1) for elastic media requiring both P- and S-wave sources. These can be written as a sum of point forces, and by assuming that the vertical component dominates when using vertical point forces (Herman and Perkins (2006) have made and tested this assumption with field data), we implement Equation (2.2) in the elastic case using vertical particle velocity due to a vertical force source only. Because of this approximation we use a more sophisticated method of ground-roll subtraction (see below).

We introduce a more realistic 2D layered anelastic model (Figure 2.3) with near-surface attenuation, and property contrasts at depth producing more complex body-wave arrivals. Note that this also allows us to test the (elastic) interferometry theory in an Earth-like, anelastic setting; our tests show that it is applicable in practice despite this relaxation of the underlying assumptions (Curtis *et al.*, 2006).

Receivers are located on the free surface at horizontal locations from 50 m to 550 m with a separation of 5 m, and a full common-source gather is generating by implementing a source at 50 m. A delta-function is used as the source signature and data is band-limited by convolving with a 30 Hz Ricker wavelet. The common source gather is shown in Figure 2.4a, simulating recorded data from which ground roll is to be removed. These are scaled such that the reflections can be seen, while the lack of trace clipping emphasises the fairly typical strength of the ground roll in this example.

Using similar reasoning to the acoustic case above, we implement sources on either side of the receiver array at horizontal locations from 5 m to 40 m and from 560 m to 595 m with a separation of 5 m (results do not depend critically on this chosen separation). The traces recorded from these sources are used in (an elastic equivalent of) Equation (2.2) to estimate the ground roll, between all source and receiver pairs, shown in Figure 2.4a (band-limiting after cross-correlation). Tapers are applied to the source arrays as discussed in Section 2, and the estimated groundroll is shown in Figure 2.4b. To increase the fold, the acausal part of the

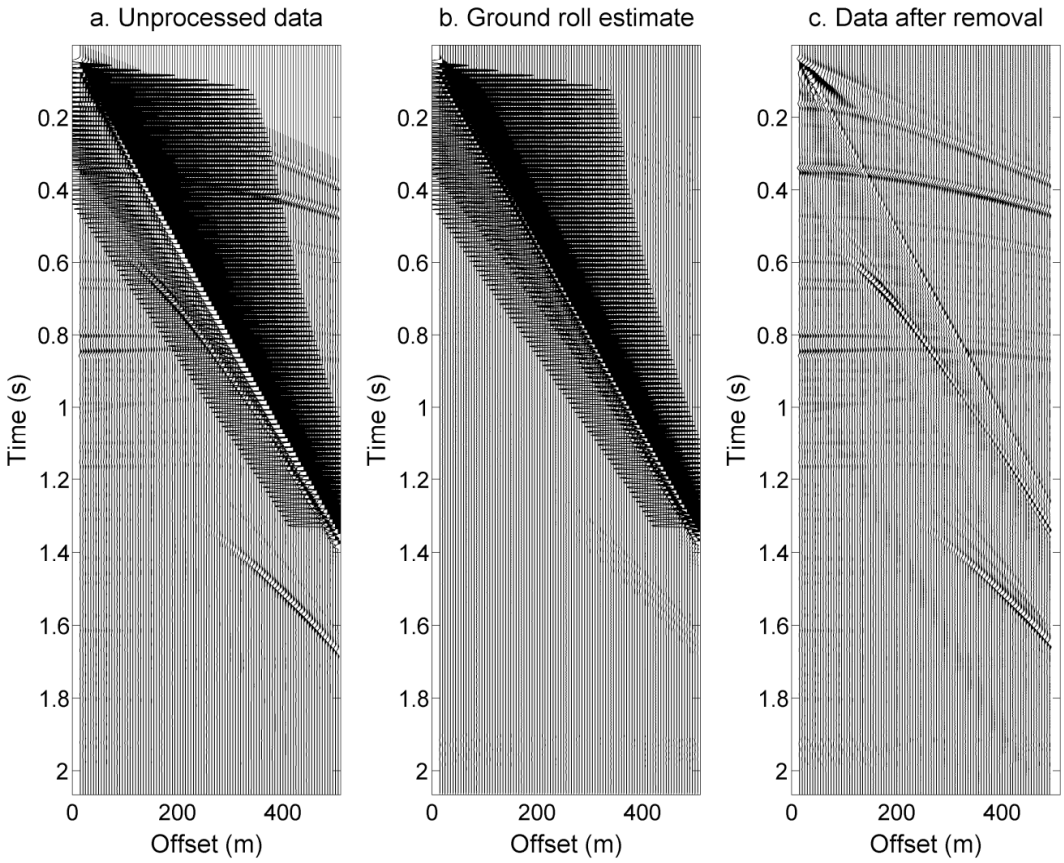

Figure 2.4: (a) Common-source gather from the model in Figure 2.3. (b) Interferometrically estimated ground roll. (c) Records in (a) after filtering and subtraction of records in (b). The offset is measured from the source location to each receiver.

constructed Green's function is added to the causal part, since these should be approximately equal in this case.

Because of further interferometric approximations in this case (i.e., lossy media, lack of horizontal source components), a least-squares filtering approach is used to optimise the subtraction of the estimated ground roll from the common-source gather (Claerbout, 1976; Dong *et al.*, 2006). For real data, Equation (2.2) must be modified to include source signatures (squared during cross-correlation), but this change in source signature can also be accounted for by filtering. In this example, we concatenate five neighbouring channels of 'recorded' data into a single trace, $d_c(t) = [d_1(t) \;\; d_2(t) \;\; d_3(t) \;\; d_4(t) \;\; d_5(t)]$ and the five equivalent channels of interferometric data are also concatenated into a single trace, $g_c(t) = [g_1(t) \;\; g_2(t) \;\; g_3(t) \;\; g_4(t) \;\; g_5(t)]$, where $d_n(t)$ and $g_n(t)$ are the *n*th

selected traces of recorded and interferometric data respectively. The window of five channels is centred in turn on each receiver of interest, and the difference between the two is minimised using a standard least-squares filtering procedure. The concatenated traces have 11824 samples and a filter of length 300 is chosen. After filtering, the central trace is extracted, i.e., we filter the central trace using a filter designed from that and four neighbouring traces.

The filtered interferometric data are subtracted from the common-offset gather. Figure 2.4c shows the resulting data. The ground roll has been suppressed effectively, while the body waves crossing the ground roll have mostly been preserved during the filtering process, as desired.

2.4 ***Conclusions***

We have shown synthetically that acoustic and anelastic surface waves propagating between two surface locations can be predicted and removed using seismic interferometry. We isolate the surface waves by locating surface sources on the line where we expect surface-wave stationary points to occur, and artefacts can be reduced by using an array of several such sources.

With a simple acoustic case we explained intuitively why surface waves can be estimated using surface sources. A more realistic, anelastic model was used to illustrate the promise of the method in land seismics; the majority of the surface waves in the synthetic survey data are removed using our method, while deeper body-wave reflections are preserved.

The examples presented are in 2D. In 3D media, although the geometric spreading factors change, relative amplitudes of (reflected) body waves and surface waves do not change significantly from the 2D case. Therefore we would expect similar results for direct surface waves in 3D media. When scattered surface waves are present, surface sources may also be required at off-line locations, since we expect cross-line scattered surface-wave stationary points.

In practice the sources used for interferometry could simply constitute other sources used to create shot gathers in the survey, and point receiver data would be used (prior to group forming). Consequently, requirements of interferometric

surface-wave removal may have to be considered during design of the survey in order that sufficient sources and receivers at appropriate locations are included as discussed above.

We expect that this method might be particularly advantageous in the presence of cross-line scattered ground roll. Suppression of such ground roll is problematic using conventional methods such as *f-k* filtering: ground roll is often spread over a large range of wavevectors, making filter design difficult. However, since interferometry is applicable in any degree of heterogeneity and has been shown to actually improve in the presence of scatterers, the method may be able to isolate and suppress both the direct and scattered ground roll. In Chapter 3 of this thesis we apply the surface-wave isolation method to direct surface waves recorded in a near-surface/engineering setting, and in Chapter 8 we test the prediction and removal of real scattered surface waves recorded in an exploration-seismic survey.

3. Seismic surface waves in a suburban environment – active and passive interferometric methods

Seismic interferometry refers to a new range of methods where inter-receiver wavefields (those that would have been recorded if one of each pair of receivers had been a source) can be estimated by cross-correlation of wavefields recorded at each of the receivers. These methods have found many applications in different fields of seismology, including creating "virtual" sources in wells under complex overburdens, computational full-wavefield modelling, and passive construction of surface-wave waveforms from background noise in the Earth.

3.1 Introduction

One particularly interesting aspect of seismic interferometry is the ability to estimate inter-receiver signals using background noise. This has become popular for crustal-scale imaging where crustal and uppermost mantle structure can be constrained using surface-wave velocity analysis. However, successful applications of similar methods to higher-frequency data are scarce. One application is presented by Draganov *et al*. (2007), who use long recordings of noise (around 10 hours) to recover both surface waves and reflected body waves in a hydrocarbon-exploration desert setting. This chapter will focus on surface-wave construction and isolation and is not restricted to passive noise sources; active sources have also been used to successfully isolate higher-frequency, inter-receiver surface waves. For example, direct surface waves determined in this way have been used as part of a predictive ground-roll removal algorithm in an exploration setting (Curtis *et al.*, 2006; Dong *et al.*, 2006; Chapter 2). In the civil engineering community, there are existing methods that extract near-surface information from background noise, known as "micro-tremor analysis." For example, the spatial-autocorrelation method (SPAC) of Aki (1957) extracts phase velocities from recordings of background noise, while Louie (2001) uses the

refraction micro-tremor technique to resolve velocity structure to depths of 100 m using slowness-frequency analysis of background noise. The advantages of such methods are the low cost and manpower in the data acquisition compared with active-source surveys, and the fact that noisy (sub-)urban settings in which the data are often acquired are ideal for the application of methods of noise analysis. Since the same types of data are used for passive interferometry, the same advantages apply. For example, Chávez-García and Luzón (2005) compare and contrast the analysis of micro-tremor measurements using both the SPAC method and the passive-interferometric method and found that the two methods provide complementary results.

In this study, we show results of several different approaches to the interferometric estimation of surface waves in a suburban environment, using both active and passive sources. For the active source case, we illustrate that multimode surface waves can be estimated robustly using specific source geometries that suppress body-wave arrivals. We also show that surface-wave gathers from a line of shots can be estimated at a fraction of the cost using interferometry. Further, we find that in this specific application, the interferometric estimates have a wider range of dominant frequencies due to differences in the receiver types used. These estimates have applications in deep seismic surveys, where surface waves are treated as noise and the estimates can be used as part of the aforementioned groundroll-removal methods. There are also potential applications in near-surface geophysics as the interferometric estimates may provide a cheap alternative for the acquisition of densely sampled surface-wave data, from which near-surface velocity profiles can be extracted (e.g., Roth and Holliger, 1999; Park *et al.*, 2007). For the passive case, we illustrate that surface-wave estimates can be produced using interferometry and that the quality of these estimates can be enhanced with some simple filtering steps. These steps account for the adverse effects of directional bias in the noise and the short recording periods used. To take full advantage of the noise in this setting, we conclude that it may be beneficial to account for known sources of noise during survey planning. The passive estimates occupy a lower-frequency range than both the directly-recorded data and the active-source interferometric estimates. A

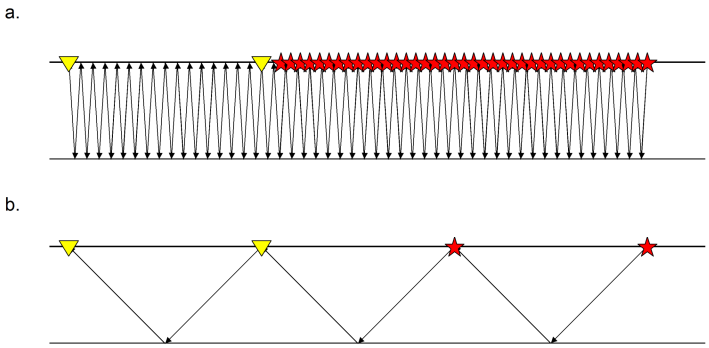

Figure 3.1:(a) For the guided wave between two receivers in this two-layer model, stationary points exist at all offsets on an extension of the inter-receiver line. (b) For a singly reflected wave, stationary points exist only at offsets equal to the receiver separation.

combination of these different approaches may therefore allow a wider frequency range to be covered, allowing a greater range of depths to be studied with the data.

3.2 Surface wave estimation

In theory, seismic interferometry between a pair of receivers requires that either noise or active-wavefield sources (both point-force and deformation-rate tensor sources – henceforth referred to as *background* sources) span a boundary which totally encloses a volume of the Earth that includes both of the receiver locations of interest. In this configuration the full inter-receiver wavefield is determined by calculating a so-called interferometric integral that includes cross-correlations and summations of the recordings at each receiver (Wapenaar and Fokkema, 2006). In practice, active background sources cannot be located so as to span an enclosing boundary completely and this affects our ability to estimate the inter-receiver signals accurately. Snieder *et al.* (2006) illustrate the resulting errors incurred for direct and reflected waves by analysing stationary-phase locations for the inter-receiver wavefield (a location where a background source provides a dominant contribution to a certain part of the constructed wavefield). Sabra *et al.* (2005) use a similar approach to that of Snieder *et al.* (2006) and consider the case of a simple acoustic guided wave (similar to the elastic surface waves considered here, which are formed by the interference of many high-order, free-surface multiples). This approach shows

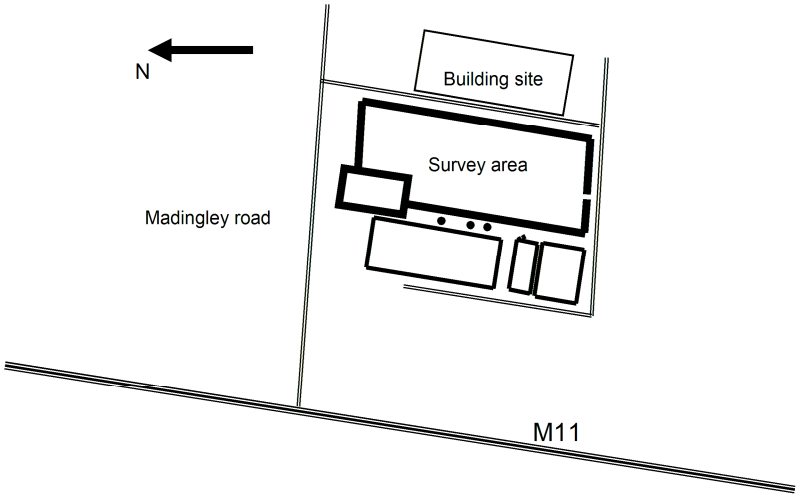

Figure 3.2: Sketch map of the survey area. Major sources of background noise are the M11 (a busy motorway), Madingley road (a main route into Cambridge) and a Building site to the east of the survey area.

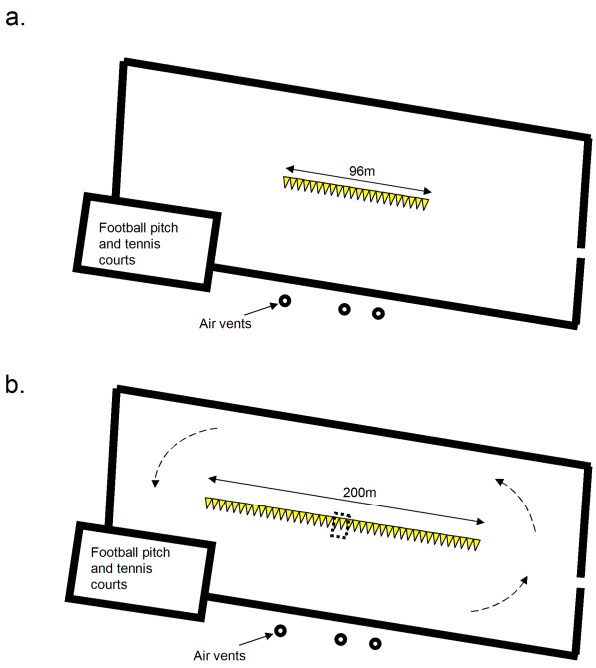

Figure 3.3: (a) Sketch of the location of the 96 m line of co-incident source and receivers within the survey area. Locations are numbered 1 to 96 from north to south. (b) Sketch of the location of the 200 m line of co-incident sources and receivers. Dashed box illustrates the 7-by-8 geophone grid. Dashed arrows indicate direction of motion of the family saloon car.

that for a guided (surface) wave, stationary points are those at which a source would produce a packet of energy that would pass (and be recorded by) one receiver of the

pair, and then the *same* packet of energy would pass through the other. In a horizontally-layered Earth these would exist at locations all along an extension of the inter-receiver line (Figure 3.1a), while primary reflected wave stationary points only exist at offsets equal to the receiver separation (Figure 3.1b). We define two regions of stationary points: one at short offset (offsets less than the receiver separation) where there are predominantly stationary points for the surface waves, and one at longer offsets (those offsets equal to and greater than the receiver separation) where we may expect stationary points for all types of arrivals.

By restricting background active sources to the extension of the inter-receiver line we expect that the inter-receiver estimate is dominated by (direct) surface waves since these are stimulated by many more stationary points than are the body waves (see Figure 3.1 and the discussion on stationary-points in Chapter 2). A similar argument can be used for the passive case, i.e. when passive-noise sources are predominantly located at or near the surface of the earth they are more likely to contribute inter-receiver surface waves than body waves.

Equation 2.2 describes the interferometric integral for active sources as a sum over cross-correlations for *n* source positions. On the other hand, for passive sources we write the interferometric construction as a sum over cross-correlations for *n* time windows, i.e.

$$G_{ik}^{est}(\mathbf{r}_A,\mathbf{r}_B,t)+G_{ik}^{est}(\mathbf{r}_A,\mathbf{r}_B,-t)=\frac{1}{\left|S(\omega)\right|^2}\sum_n v_i^{\ obs}(\mathbf{r}_A,t_n)*v_k^{\ obs}(\mathbf{r}_B,-t_n)\,. \qquad (3.1)$$

Here $v_i^{\ obs}(\mathbf{r}_A,t_n)$ is the *i*th component of particle velocity at $\mathbf{r}_A$ due a distribution of random noise sources, recorded for a time window t_n, $G_{ik}^{est}(\mathbf{r}_A,\mathbf{r}_B,t)$ is the time-domain Green's function representing the *i*th component of particle velocity at $\mathbf{r}_A$ due to a point force in the *k*-direction at $\mathbf{r}_B$, the superscript *est* indicates that this is an estimate of the Green's function, and $*$ denotes convolution. $\left|S(\omega)\right|^2$ is the power spectrum of the excitation. Wapenaar and Fokkema (2006) discuss in detail the assumptions required in expression such as (3.1).

3.3 Data acquisition

In this study we use three different but complimentary data sets acquired in a field adjacent to the Schlumberger Cambridge Research centre (Cambridge, England). A sketch map of this area, including known sources of background noise is shown in Figure 3.2.

The first data set is an active-source data set consisting of 96 receiver locations with 1 m separation along a straight line, with sources beside each receiver location in turn (Figure 3.3a). The data were acquired using a wacker vibrator as source (Barbier *et al.*, 1976), with a 'sweep' length of around 30 seconds. Two geophone types were used: 95 standard 10 Hz vertical-component geophones to record the seismic data, and a single damped geophone placed beside each source location to record the source sweep of the vibrator. The latter record can be cross-correlated with all other records to create shot gathers with a pseudo-impulsive source signature, a typical example of which is shown in Figure 3.4. Note (a) the shallower body-wave arrivals (guided P-waves, 0 to 0.1 s), (b) the more horizontal shallow reflection events (0.1 to 0.2 s), (c) the higher-frequency surface waves, and (d) the less clear lower-frequency surface waves. The equivalent frequency-wavenumber (*f*-*k*) plot is shown in Figure 3.5, note that in addition to (a) the fundamental mode, there is (b) one strong higher mode, and (c) at least one other higher-mode surface wave. The dominant body waves (d) are clearly separated from the surface waves in this plot.

The second and third data sets were acquired using a second geophone layout: a 200 m line of receivers with 5 m geophone separation, and an additional 7 by 8 geophone grid located in the centre of this line with a grid spacing of 1 m (Figure 3.3b). Using this geometry we first recorded around 30 minutes of controlled noise (a Skoda Octavia estate family-saloon car circling the geophone spread in an inwards spiral motion, Figure 3.3b) followed by approximately ninety minutes of background, suburban noise (Figure 3.2 shows known sources of background noise).

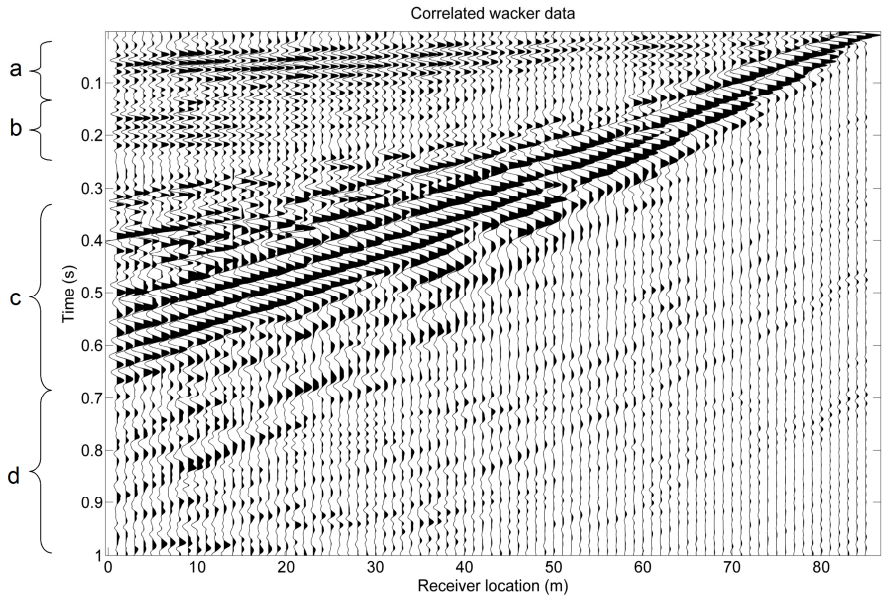

Figure 3.4: Example correlated vibrator gather from a source at location 86. Labels correspond to (a) guided P-waves, (b) shallow P-wave reflections, (c) higher-frequency surface waves, and (d) lower-frequency surface waves.

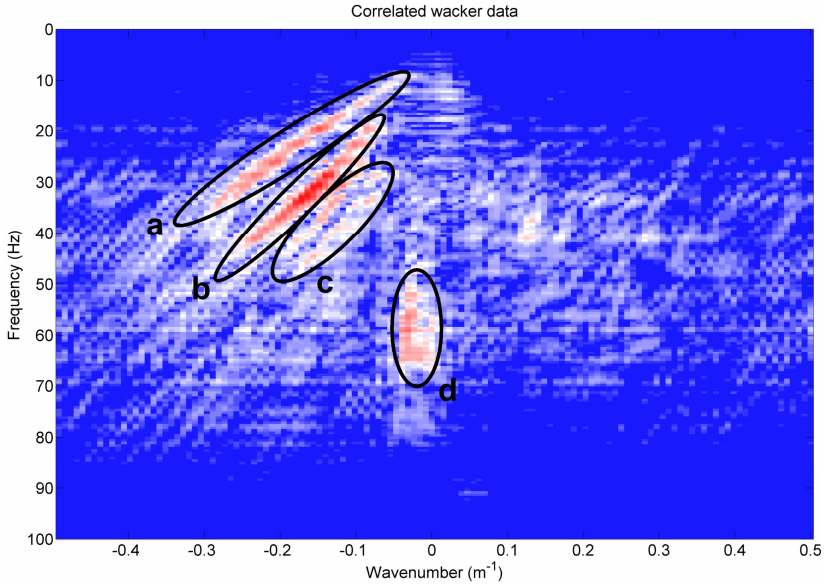

Figure 3.5: Data shown in Figure 3.4 plotted in the *f-k* domain. Labelled areas show the dominant areas of (a) the fundamental-mode surface wave, (b) a strong higher mode surface wave, (c) weaker higher-mode surface waves, and (d) the body waves (both guided P-waves and shallow reflected P-waves).

3.4 Active source interferometry

To estimate the Green's functions between a pair of receivers, the responses from a series of outer sources (sources on one or both sides of the receiver pair) recorded at both receivers are cross-correlated (that is, the outer sources are used as background sources). Consider the uncorrelated vibrator data, $d_{33}(\mathbf{r}_A,\mathbf{r}_B,t)$ from a source at location B and a receiver at location A

$$d_{33}(\mathbf{r}_A,\mathbf{r}_B,t)=[G_{33}(\mathbf{r}_A,\mathbf{r}_B,t)*s(t)*f^s(t)], \tag{3.2}$$

where $s(t)$ is the vibrator source signature, and $f^s(t)$ is the receiver-response function of the standard geophone. By cross-correlating and summing the uncorrelated data recorded at A and B from *n* in-line shots we gain an estimate of the inter-receiver Green's function

$$\begin{aligned}\hat{G}_{33}^{est}(\mathbf{r}_A,\mathbf{r}_B,t)&=\sum_n[G_{33}(\mathbf{r}_A,\mathbf{r}_n,t)*s(t)*f^s(t)]*[G_{33}(\mathbf{r}_B,\mathbf{r}_n,-t)*s(-t)*f^s(-t)]\\&=\sum_n[G_{33}(\mathbf{r}_A,\mathbf{r}_n,t)*G_{33}(\mathbf{r}_B,\mathbf{r}_n,-t)]*[s(-t)*s(t)]*[f^s(-t)*f^s(t)].\end{aligned} \tag{3.3}$$

Where $\hat{G}_{33}^{est}(\mathbf{r}_A,\mathbf{r}_B,t)$ is the estimated Green's function modified by source signatures and receiver-response functions. We replace the Green's function cross-correlation and summation (the first term in square brackets) with the estimated Green's function (Equation 3.1) and write our modified estimate as

$$\hat{G}_{33}^{est}(\mathbf{r}_A,\mathbf{r}_B,t)=G_{33}^{est}(\mathbf{r}_A,\mathbf{r}_B,t)*[s(t)*s(-t)]*[f^s(t)*f^s(-t)], \tag{3.4}$$

i.e., the estimated signal is equal to the Green's function between receiver A and B modulated by the auto-correlation of the source signature (approximately an impulse at t = 0) and the auto-correlation of the receiver response function.

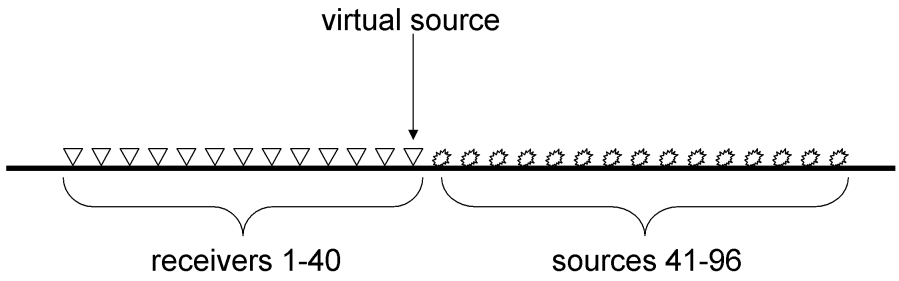

Figure 3.6: Source and receiver positions used in Figure 3.7 and Figure 3.8. Receivers are show as triangles, sources as flashes.

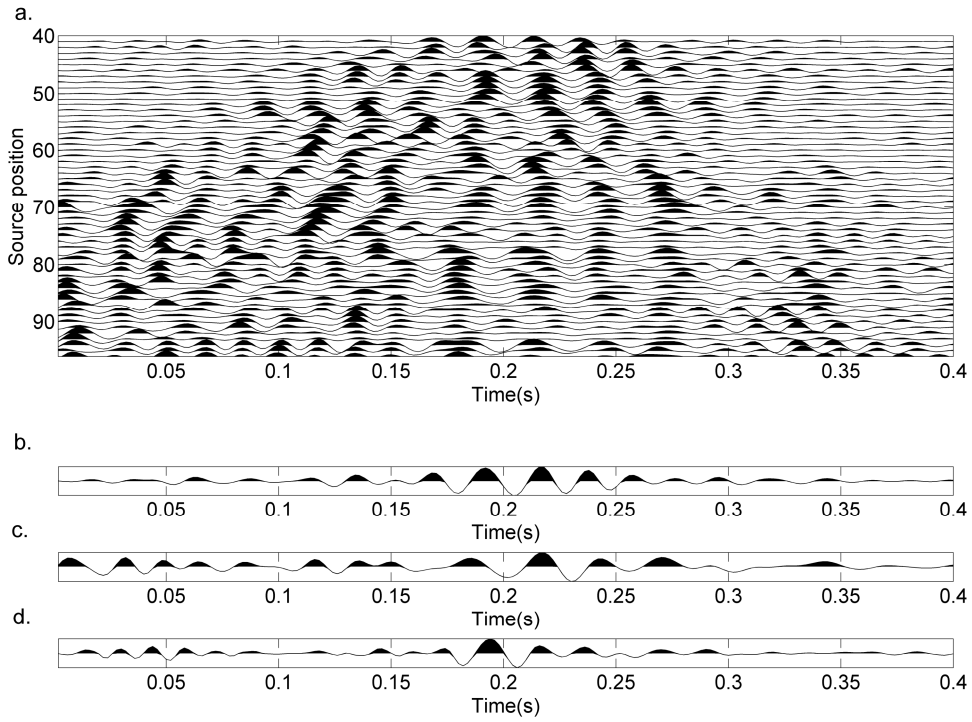

Figure 3.7: (a) Cross-correlations between receivers 10 and 40 using sources at different locations (see Figure 3.6); (b) the sum of cross-correlations 44 to 53; (c) the sum of all cross-correlations; (d) true source-receiver data.

We can then compare this result with that obtained in an actual source-receiver record after correlation with the vibrator source signature:

$$d_{33}(\mathbf{r}_A,\mathbf{r}_B,t) = g_{33}(\mathbf{r}_A,\mathbf{r}_B,t) * [s(t) * s(-t)] * [f^s(t) * f^d(-t)], \tag{3.5}$$

where $f^d(t)$ is the receiver response function of the special damped geophone.

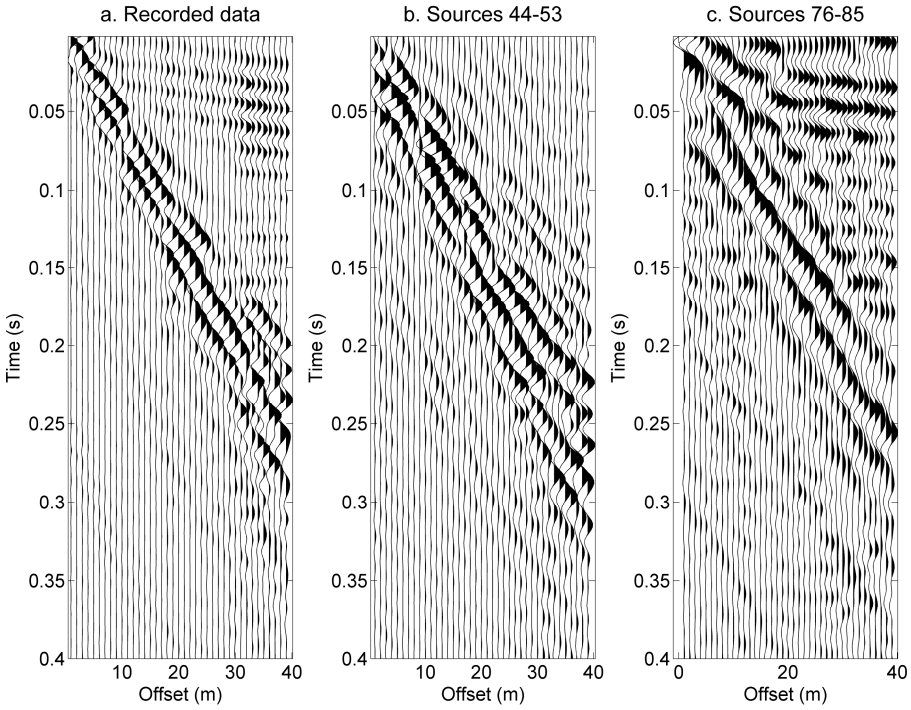

Figure 3.8: (a) Shot-gather showing surface and body waves, (b) interferometric estimates produced by summing background source locations 44-53, and (c) by summing background source locations 76-85.

Note the similarities between the shot record in Equation (3.5) and the interferometric estimate in Equation (3.4). Differences arise due to the difference in the damped geophone-response function and the standard geophone-response function. Further differences arise depending on the source and receiver configuration: i.e., when we have background sources distributed as described above then the estimate is dominated by the inter-receiver surface waves. Differences also occur due to attenuation: the energy arriving at the first receiver (the virtual source) in the interferometric construction in Equation (3.4) has already propagated a certain distance, hence energy will have been lost due to anelastic attenuation. This energy loss does not occur when an active source is placed at that point as in Equation (3.5).

Figure 3.7d shows the recorded data at receiver 10 (in Figure 3.6) from a source-receiver record where the source was placed beside the virtual-source location at receiver 40. The ground roll can be seen between 0.13 s and 0.28 s. Figure 3.7a illustrates the cross-correlations of signals recorded at two receivers (numbers 10 and 40) from individual sources at various offsets from (and to the right of) the virtual

source at position 40 (for visualization, all traces are normalized to a peak amplitude of 1). The set of non-normalized records would be summed (Equation 2.2) to construct an interferometric waveform from a virtual source located at receiver 40, as shown in Figure 3.7c. We now analyse contributions to the summed waveform in Figure 3.7c in more detail.

In the region of the ground roll in Figure 3.7d there are contributions to the sum from sources at short, and long, offsets (i.e., these contributions sum positively). Whereas, for other arrivals such as those identified as guided waves and shallow reflections (0 s to 0.13 s), contributions exist for background sources at long offsets but do not occur for short offsets.

In Figure 3.7b, we limit the source array to shorter offsets (up to 20 m): after summation (Equation 2.2), the surface-wave component dominates the result (compare Figure 3.7b, c, and d). This agrees with the stationary-phase argument presented earlier: contributions to the interferometric construction of a surface wave come from both short offsets (i.e., those less than the receiver separation) and long offsets (up to and beyond the receiver separation), while contributions to reflected waves and low-order multiples come from offsets close to and beyond the receiver separation as discussed in Chapter 2.

Figure 3.8a shows the complete shot gather of sweep-correlated vibrator data from a source placed at receiver location 40 recorded at receivers 1 to 39. Figure 3.8b shows the sum of the interferometric cross-correlations for background sources 44 to 53 (short offsets), and Figure 3.8c the sum of cross-correlations for background sources 76 to 85 (offsets around the maximum virtual source/receiver separation). As we expect, the result using sources at near offsets is dominated by surface waves, while the result using the far offsets includes both the surface waves and body waves as predicted above. The appearance of the surface-wave train changes across the three parts of Figure 3.8. These changes are likely to be due to the variation in the source signatures and receiver response functions identified above. Also, as expected note that the long-offset sources in Figure 3.8c produce results that are lower frequency than those from near-offset sources due to attenuation.

Figure 3.9 shows the estimate of the surface waves corresponding to the data shown in Figure 3.4. Here we have used background sources at locations 89–96 and

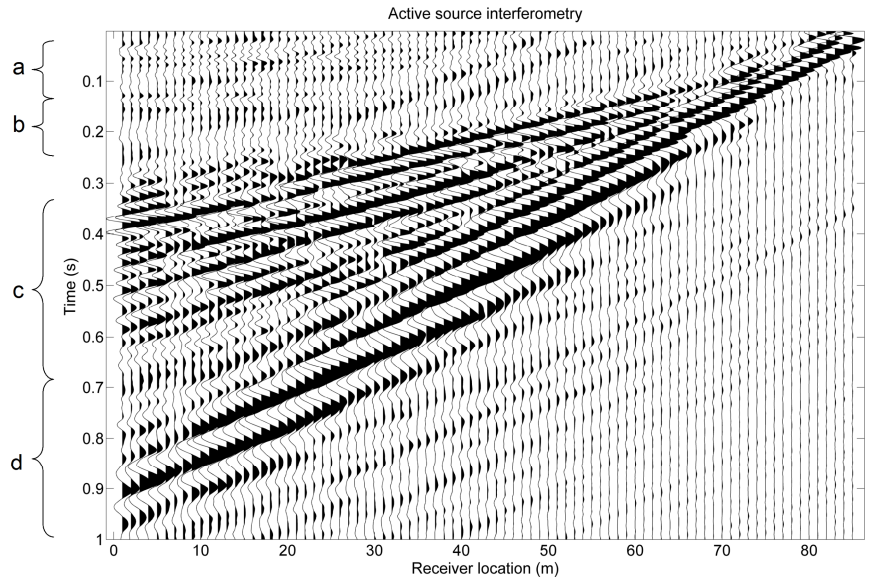

Figure 3.9: Interferometric estimate for a virtual source at location 86. Background sources used in the estimate are at locations 89 to 96. Labels correspond to (a) guided P-waves, (b) shallow P-wave reflections, (c) higher frequency surface waves, and (d) lower frequency surface waves.

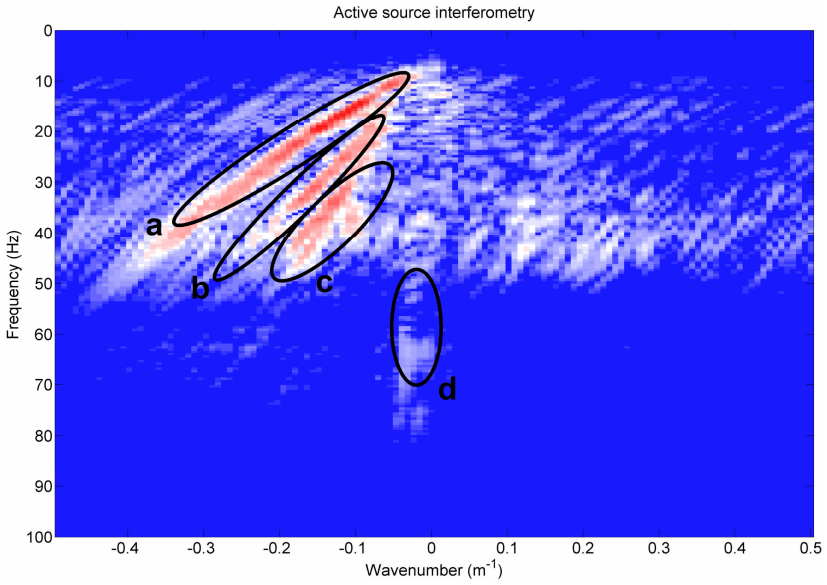

Figure 3.10: Data shown in Figure 3.9 plotted in the *f-k* domain. Labelled areas are the same as those in Figure 3.5.

therefore expect our estimate to be dominated by inter-receiver surface waves (similar to Figure 3.8b). Compared with Figure 3.4, we see the estimate is dominated by both (c) the higher-frequency surface waves and (d) the lower-frequency surface

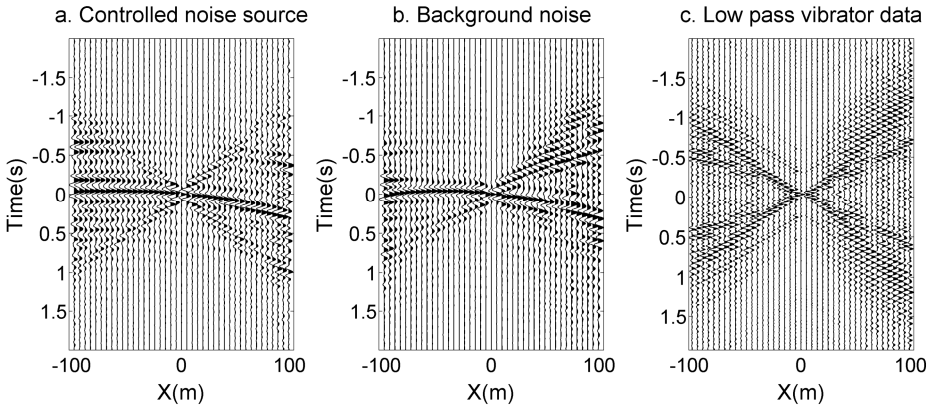

Figure 3.11: (a) Cross-correlation of controlled noise, (b) cross-correlation of random background noise, (c) and the vibrator data. Both causal and acausal results are shown. X(m) is the source/receiver offset - negative offsets are to the south, with positive offsets to the north.

waves. Where we expect body waves (a, b), there are no strong arrivals. The corresponding *f-k* plot is shown in Figure 3.10. The same areas indicated in Figure 3.5 are indicated here, and we can identify (a) the fundamental-mode surface wave, (b) the stronger higher mode, and (c) the other higher-mode surface waves. As in Figure 3.9, any body-wave arrivals (d) are weak. Note that the different modes occupy larger areas than those in Figure 3.5 and that there is a broader dominant frequency band. The difference in strength of the surface waves in the interferometric estimate, relative to those in Figure 3.4 and Figure 3.5, is likely to be related to the difference between the two types of receiver used, i.e., the differences between Equations (3.4) and (3.5) above. Our results illustrate that by using active-source interferometry, we can create high quality estimates of both fundamental and higher-mode surface waves. In Figure 3.9, we have used seven sources to estimate a single shot gather, and the same seven sources can be used to create "virtual" sources at each of the 86 receivers. In other words, we can turn each receiver into a virtual source, but at a fraction of the effort and cost required.

3.5 Passive interferometry

Both of the passive datasets are processed in a similar fashion to above: first the data are split into many time windows and one-bit normalized (this stops high-amplitude noise bursts dominating interferometric cross-correlations); for each receiver pair the

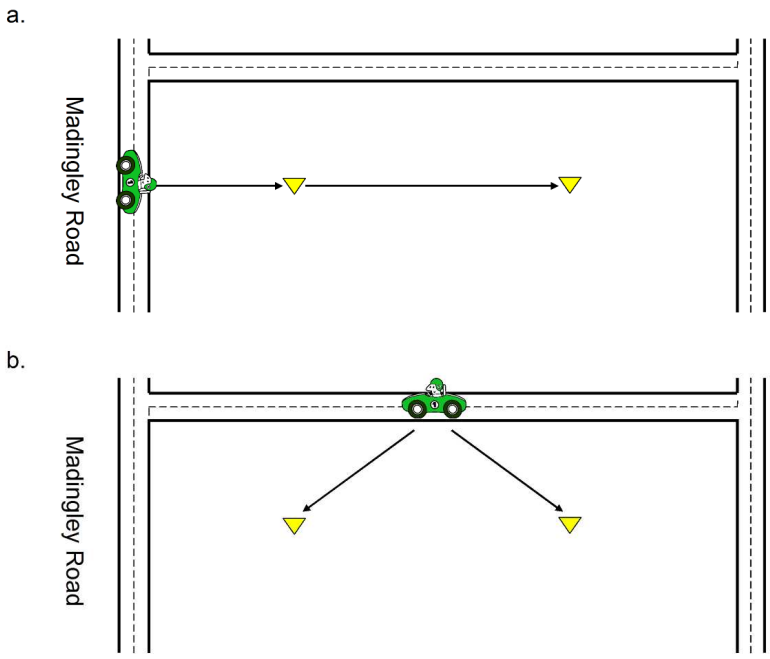

Figure 3.12: Cartoon illustrating the role of different passive-source locations (indicated by a car) relative to receiver locations (triangle). (a) A car (travelling along the busy Madingley Road) passes the extension of the receiver line and emits a packet of seismic noise that travels to the first receiver, is recorded at this receiver and then travels along the inter-receiver path to the second receiver. This packet of noise contributes to the inter-receiver surface wave in the interferometric estimate. (b) A car travels along a road that lies off the receiver line. A packet of noise travels to both the first and second receivers but does not travel along the inter-receiver path. Hence this does not contribute to the interferometric estimate.

corresponding time windows are cross-correlated and the results are integrated over time. We use overlapping time windows of 3 seconds, as this provides sufficient time for the slowest surface wave to be observed by all receivers within the same time window.

Figure 3.11a and b show the results of cross-correlating windows of noise recorded from the controlled Skoda noise (around 30 minutes in total) and uncontrolled noise (around 90 minutes in total). Both of these examples are for a "virtual source" in the centre of the line. Figure 3.11c shows the recorded data for a real source at the same location for comparison. Again, traces are normalised to peak amplitude of 1 prior to plotting. The cross-correlations have lower-frequency content (5 to 15 Hz) than the vibrator data (approximately 10 to 100 Hz); therefore we plot the lower-frequency part of the vibrator data (10 to 20 Hz).

Both of the noise results are dominated by a strong spurious event that curves around the zero-time axes. We have confirmed that this strong event is due to a stationary source of noise that operated throughout the recording period (a piece of heavy machinery periodically hammering piles into the ground on the building site shown in Figure 3.2). Nevertheless, the trend of the dispersive surface-wave pattern can be seen in some parts of the interferometric estimates. For example, the Skoda data show the same X-pattern of the surface waves. Part of the pattern can also be seen in the background-noise data. At positive times, these events can be seen moving out from zero offset to -100 m offset, and for negative times, a similar event can be seen moving out from zero offset to 100 m offset. Note that because we have controlled the location of the Skoda, which circled the receiver array spiralling inwards, we expect to have noise from all directions; therefore, in (a) we see these arrivals both upline (from 0 to 100 m), downline (from 0 to -100 m), and at both positive and negative times, i.e., we have estimated both causal and acausal Green's functions (Equation 3.2). Traffic on Madingley Road dominated the recordings of background noise used in (b), and due to this bias in noise directionality we do not necessarily expect to have the same coverage of source locations, hence the less complete surface wave pattern (in Chapter 7 we introduce a method which can account for such bias-noise directionality).

Since the estimates are dominated by the strong spurious event we take action to reduce its effect, in order to extract better surface-wave estimates. A simple process to extract the inter-receiver surface waves is to use a beam-forming method on the small array in the middle of the 200 m line (Figure 3.3). Using this approach we can detect and isolate noise coming from certain directions, e.g., from the direction of either end of the line where we expect the majority of stationary points contributing to the direct inter-receiver surface waves to be located (Snieder, 2004 and Figure 3.12). We refer to this process as target-orientated passive interferometry, where in this case our 'target' is the direct surface wave (borrowing the terminology of Vasconcelos *et al.* (2007) who apply a similar technique to active-source data).

We repeat the estimation process using the isolated noise, resulting in the surface-wave estimates shown in Figure 3.13. The surface waves are clearer, but the spurious

event can still be seen in the controlled-noise source plot and faintly in the background noise plot.

Since the unwanted noise is coming from the broadside of the receiver array, it will plot close to the zero-wavenumber axis in *f-k* space, and hence can be suppressed using an *f-k* filter as the (direct) surface waves will not occur in the same region. Figure 3.14a and c show the data in Figure 3.11a and b in *f-k* space, and Figure 3.14b and d show the *f-k* plots after filter application (note that this type of filtering is not desirable when we are interested in near-surface scattering, since it also suppresses any cross-line scattered surface waves). The equivalent time/distance plots are shown in Figure 3.15; the unwanted arrival is not visible in either the controlled-noise data or the background-noise data, while the estimate of the direct Rayleigh wave remains. Note that for the background noise there is also an event propagating in the opposite direction. This is not recovered in the beam-forming approach. Since this arrival (and hence the source of noise) is weak, the noise from the building site was dominant and the desired noise was not detected during directional analysis.

We combine both of these filtering processes with results shown in Figure 3.16 and Figure 3.17. Note that the weak event identified in Figure 3.15b is not seen in Figure 3.17b (or the equivalent *f-k* plot in Figure 3.16b), confirming that the directional filtering does not preserve this arrival. However, the estimates produced using both this directional approach and *f-k* filtering are affected less by artefacts (compare the regions at longer offsets around the zero time axes in Figure 3.15 and Figure 3.17). These artefacts are likely to be introduced by other off-line sources of noise that are not cancelled in the interferometric summation but which can be eliminated using the target-orientated approach.

The results illustrate that by applying passive-seismic interferometry, we can extract inter-receiver surface wave signals, even when recording times are short and there is poor azimuthal coverage of background-noise sources (typical of a suburban area). This results in estimates that are dominated by un-cancelled non-stationary phase sources. By applying some simple processing steps to both the passive-noise records, and the interferometric estimates themselves, we can nevertheless extract reasonable estimates of the surface waves.

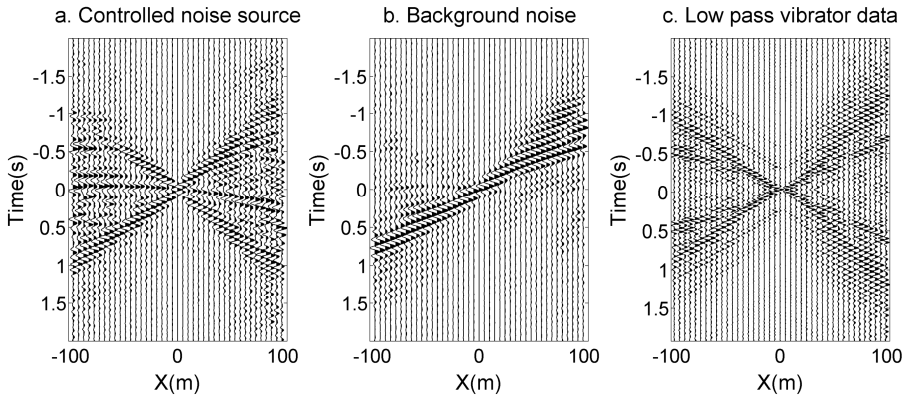

Figure 3.13: As for Figure 3.11. Here data have been selected using directional analysis across the 2D array.

3.6 Discussion and Conclusions

We have shown that it is possible to use seismic interferometry to extract estimates of inter-receiver surface waves in a suburban setting. Active sources allow multimode surface-wave data to be estimated with a bandwidth similar to that acquired in active surveys. Lower-frequency surface wave estimates are extracted from recordings of background noise (excited by a controlled, continuous-noise source and random background sources), but these estimates are of lower quality than those from active sources (at least for the short recording periods used here).

In the passive case, the use of relatively short recording intervals and non-uniform directionality of the noise sources results in problems due to cross-correlation contributions that do not correspond to real inter-receiver signals. To overcome these problems we use target-orientated passive interferometry and *f-k* filtering to enhance the estimates of the inter-receiver surface waves. Since our ability to estimate surface waves passively is controlled by the availability of noise sources it may be desirable to plan such surveys around prior knowledge of the noise. Receivers can be aligned such that noise sources lie in stationary regions for the inter-receiver surface waves. For example, in the above it may have been beneficial to have a second line of receivers perpendicular to the current array, since this line would have a stationary-phase region coinciding with the busy motorway and the building site.

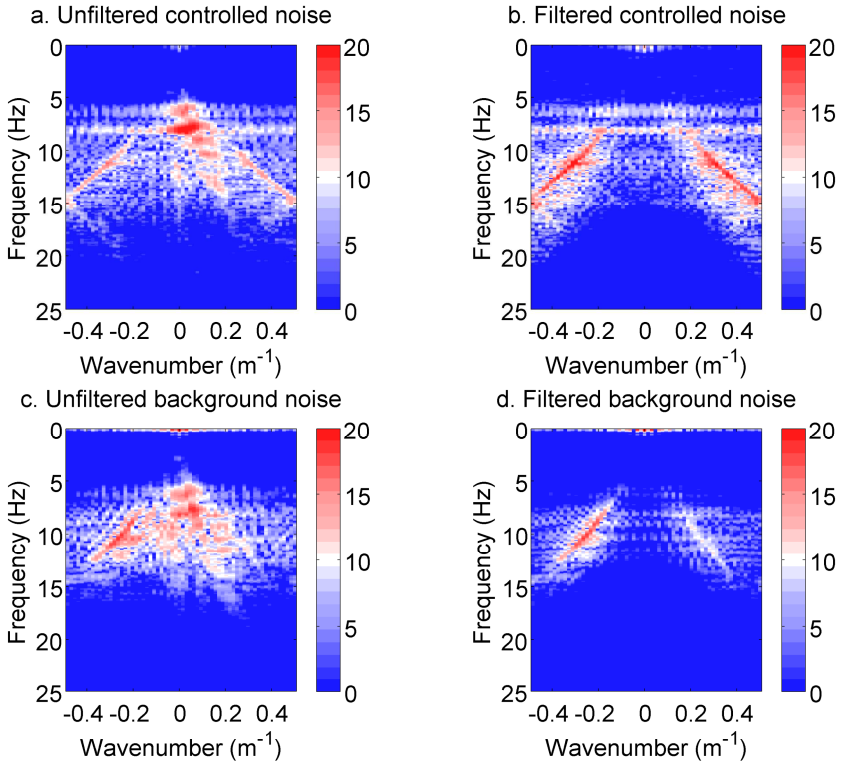

Figure 3.14: *f-k* plots for (a) controlled-noise interferometric data, (b) *f-k* filtered controlled-noise interferometric data, (c) unfiltered background-noise interferometric data, and (d) *f-k* filtered background-noise interferometric data.

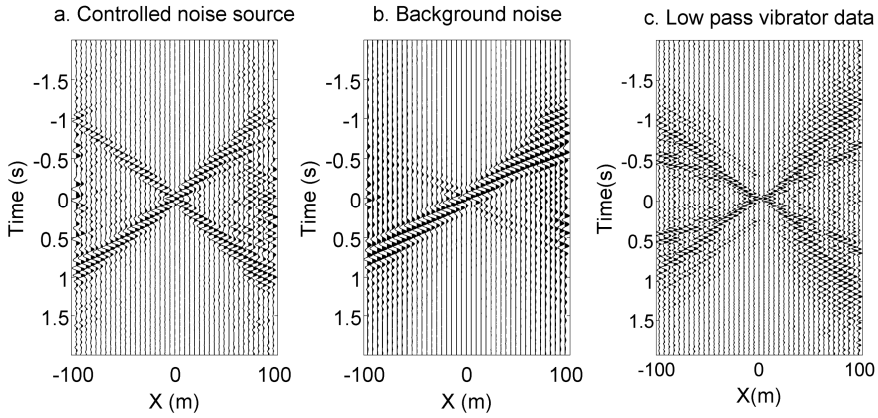

Figure 3.15: Time-offset equivalents of Figure 3.14b and d.

One of the benefits of seismic interferometry is that source-receiver data can be estimated without active sources, or with only a few carefully located active sources. Thus, interferometry can be used to acquire surface-wave data sets equivalent to those recorded in more costly active-source near-surface surveys.

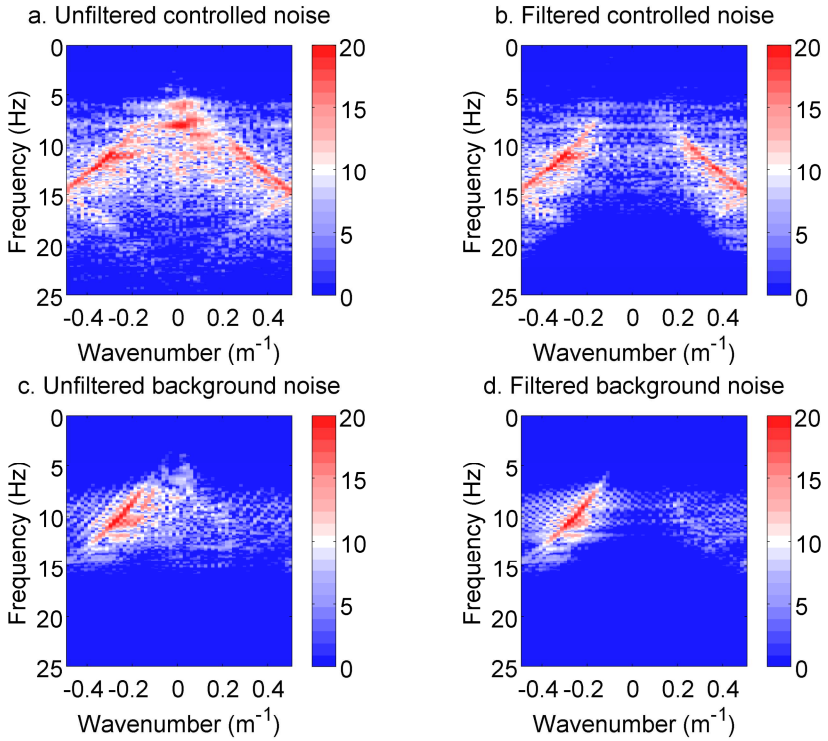

Figure 3.16: *f-k* plots (after directional analysis) for (a) controlled-noise interferometric data, (b) *f-k* filtered controlled-noise interferometric data, (c) unfiltered background-noise interferometric data, and (d) *f-k* filtered background-noise interferometric data.

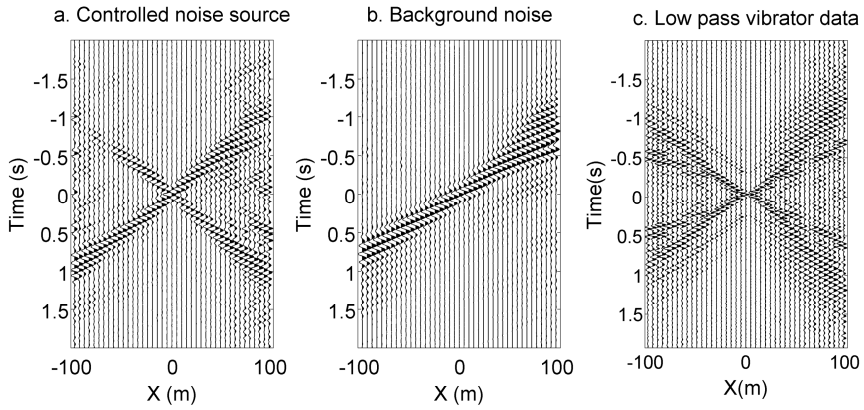

Figure 3.17: Time-offset equivalent of Figure 3.16b and d.

Comparing the different surface-wave measurements we can observe that the surface waves estimated using active-source interferometry have a broader-frequency band than those in the real active data. This frequency difference is likely to be due to the differing receiver-response functions of the two geophone types used (for the active vibrator sources a highly damped geophone must be used to record the source

wavelet, which is not necessary in the active-source interferometric case). This is therefore a side effect of the acquisition equipment, and by using interferometry we can recover surface waves for a broader range of frequencies. A wider range of frequencies allows a greater range of depths to be studied with the data. Secondly, the passively-estimated surface waves have lower-frequency content than both the active-source interferometry and the real active data (e.g., Figure 3.9 and Figure 3.17). This presents the possibility of combining the active and passive methods to allow an even wider frequency range to be used when determining subsurface velocity from surface-wave data. Park *et al.* (2007) propose a similar combination of active and passive recordings using the multi-channel analysis of surface waves (MASW) technique. However, they apply their method directly to the recorded noise as opposed to using an interferometric approach as presented here.

The application of the passive method is common in earthquake seismology but applications on the small-scale presented here are rare. However, successful application can provide valuable information about the near surface without the use of dense source distributions. This approach may find applications in near-surface characterisation in exploration environments, or in engineering geophysics.

In the next chapter it is shown theoretically and with synthetic examples that the use of certain geometries introduces spurious events in interferometric estimates of surface waves. A modal separation method is proposed as a solution to this problem. The results show that for in-line geometries, such as those presented above, the recovery of surface waves propagating approximately in the in-line direction is not strongly affected by these spurious events.

In areas with strong near-surface heterogeneity, a similar approach to that considered in this chapter may allow for the estimation of inter-receiver scattered surface waves, and therefore the analysis of near-surface scattering properties. In Chapter 6 we investigate the effects of source distribution in two dimension at the surface of the Earth and we further investigate the potential of this method to recover scattered surface waves. In Chapter 8 we apply similar methods to a 3D data set from a real setting displaying strong scattering of surface waves.

4. Seismic interferometry, surface waves, and source distribution

Seismic interferometry can be used to estimate inter-receiver surface-wave signals by cross-correlation of signals recorded at each receiver. The quality of the estimated surface waves is controlled by the distribution of sources exciting the cross-correlated wavefields, and it is commonly thought that only sources at or near the surface are required to generate accurate estimates. We study the role of source distribution in surface-wave interferometry for both surface and subsurface sources using surface-wave Green's functions for laterally homogeneous media. We solve the interferometric integral using a Rayleigh-wave orthogonality relationship combined with a stationary-phase approach. Contrary to popular opinion we find that sources at depth do indeed play a role in the recovery of surface waves by interferometry. We find that interferometry performs well when surface sources are distributed homogeneously at the surface of the Earth. However, when this homogeneous distribution is not available amplitude errors are introduced, and when multiple modes are present strong spurious events appear and higher-mode surface waves may not be correctly estimated. In order to recover higher-mode surface waves we propose an additional step in the processing of surface-wave data for seismic interferometry: by separating modes and applying interferometry to each mode individually it is possible to recover the inter-receiver surface-wave modes, without the artefacts introduced by limited source coverage.

4.1 Introduction

A popular application of seismic interferometry is the isolation of inter-receiver surface-wave signals. When the sources used in interferometry are located at or near the surface of the earth they predominantly excite surface waves that travel between the two receivers. For example, in exploration seismology, direct and scattered inter-

receiver surface waves can be estimated using active sources at the surface. The estimated surface waves can then be used as part of a source-receiver surface-wave removal algorithm in order to expose the desired and much weaker, body-wave energy (Curtis *et al.*, 2006; Dong *et al.*, 2006; Chapter 2; Chapter 3). In earthquake seismology interferometry is applied to so-called passive wavefields emanating from unknown sources in or on the Earth (Shapiro and Campillo, 2004; Shapiro *et al.*, 2005), or from secondary scattering sources (as illustrated using the seismic coda by Campillo and Paul, 2003). The resulting inter-receiver seismograms are dominated by fundamental-mode Rayleigh waves and these are used to invert for group-velocity maps (e.g., Gertstoft *et al.*, 2006). In engineering/near-surface seismology near-surface shear-wave velocity profiles can be extracted from recordings of ambient noise (a process referred to as micro-tremor analysis e.g., Aki, 1957; Louie, 2001) and from active-source surface wave recordings (Xia *et al.*, 2000; Beaty *et al.*, 2002). Chávez-García and Luzón (2005) investigate the relationship between micro-tremor analysis and passive-seismic interferometry and in Chapter 3 of this thesis it was illustrated that in a suburban environment interferometric surface-wave estimates can be produced using both background-noise sources (i.e., motorway traffic, building sites, main roads, etc.) and active sources (similar to the estimates used for ground-roll removal).

Theory dictates that a closed surface of sources is required for seismic interferometry (e.g., Wapenaar and Fokkema, 2006). It may be possible, in practice, to relax this requirement. However, limited source coverage does introduce errors and it is important to understand these. For example, Snieder *et al.* (2006) use a stationary-phase approach to show how spurious multiples are introduced when attempting to recover reflected body waves using only surface sources. As a consequence Mehta *et al.* (2007) use wavefield separation to suppress the contribution of such spurious events in an application of the virtual-source method of Bakulin and Calvert (2004; 2006).

In this chapter we study the effect of missing subsurface sources and different source distributions on the interferometric construction of surface waves. We use a stationary-phase approach similar to Snieder (2004a), who uses a 2-dimensional source distribution to show that inter-receiver surface waves can be correctly

recovered from recordings of passive-noise fields when the sources of noise are distributed homogeneously at the surface of the Earth. We present a comprehensive 3-dimensional analysis of the interferometric integral using surface wave Green's functions, considering the effects of source type, sources at depth, and in particular the effect on higher-mode surface waves.

We conclude that: (1) contrary to commonly cited opinion, sources at depth play an important role in seismic interferometry for surface waves, particularly when we are interested in the construction of higher-mode surface waves – without sources at depth we cannot expect to estimate higher-mode surface waves correctly; (2) both point forces and deformation-rate-tensor sources are required to recover the correct relative amplitudes of different surface-wave modes; (3) when the homogeneous surface-source distribution assumed by Snieder (2004a) is not present we can still recover good estimates of the correct inter-receiver surface waves but only when individual modes can be isolated; and (4) it is more difficult to recover correct multi-mode inter-receiver surface waves due to the introduction of spurious events in the interferometric synthesis.

The above conclusions do not prohibit interferometric higher-mode surface wave estimation. While amplitude errors are introduced it is still possible to recover the correct phase of the surface waves. The spurious events introduced in the presence of higher modes are created by the cross-correlations between different modes and may be avoided by separating the individual surface-wave modes prior to interferometry. We therefore propose modal separation (where possible) prior to the application of seismic interferometry. Surface-wave modes can be separated using band-pass filters (Crampin and Bath, 1965), phase matched filtering (Hwang and Mitchell, 1986), or mode-branch stripping (van Heijst and Woodhouse, 1997), but modes are more efficiently separated using frequency-wavenumber analysis, common in exploration geophysics where receiver arrays are well sampled spatially (e.g., Vermeer, 2002). In earthquake seismology, densely sampled seismograph arrays are rare, however array methods still exist to identify and separate higher modes (e.g., Nolet, 1975; Nolet and Panza, 1976; Cara, 1978; Mitchel, 1980).

In exploration seismology our findings have implications for the prediction and removal of ground roll with interferometry. Ground roll often consists of complex

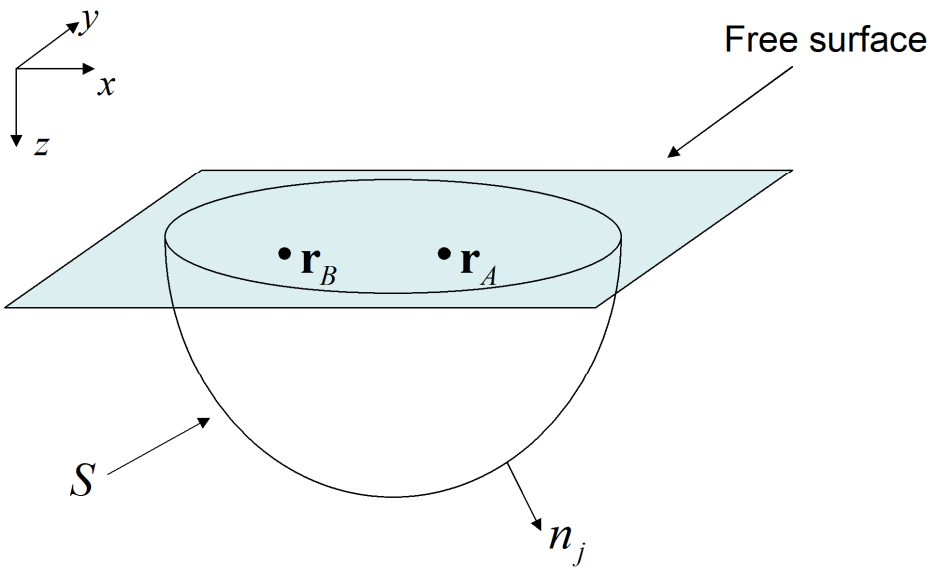

Figure 4.1: Geometry for Equation (4.1). Note that $\mathbf{r}_A$ and $\mathbf{r}_B$ lie beneath the free surface in this case.

surface waves, exhibiting higher modes and multiple scattering (e.g.,Al-Husseini *et al.*, 1981; Herman and Perkins, 2006; Chapter 3). Hence, when only surface source geometries are available (as is the usual case in exploration seismology) modal separation may be a key process in the application of seismic interferometry to such settings, as in order to remove higher modes correctly we must be able to estimate these with the smallest possible error.

In earthquake seismology, our results explain why higher-mode surface waves may not be recovered correctly, since the Earth's passive-noise fields are predominantly excited by heterogeneous near-surface source distributions. To date, applications of interferometry at crustal and lithospheric scale only consider the recovery of fundamental-mode surface waves (Gertstoft *et al.*, 2006; Moschetti *et al.*, 2007; Yang *et al.*, 2007; Lin *et al.*, 2008; Yao *et al.*, 2008). While these surface waves produce velocity maps in agreement with regional geology, higher modes can be used to provide information in depth ranges unsampled by the fundamental mode (e.g., MacBeth and Burton, 1985; Dost, 1990; Yoshizawa and Kennet, 2004). Thus the recovery of higher-mode surface waves using modal separation may allow for improved velocity maps from seismic interferometry. This argument also applies to

applications of interferometry to near-surface engineering surveys, where higher-mode surface waves are commonly used to enhance the depth resolution of near-surface velocity models (e.g., Xia *et al.*, 2000; Beaty *et al.*, 2002).

Finally, the methods used here may also be extended to body waves. Under certain circumstances the full elastic response of a system can be written as a sum of normal modes (Aki and Richards, 2002, ch.7; Snieder, 2002b). Therefore an extension of this approach may allow for detailed analysis of errors introduced by restricted source coverage in the body wave case, or for the analysis of the effect of body waves on surface-wave interferometry.

In this chapter we first introduce the appropriate interferometric equations and surface-wave Green's functions and use a 2-dimensional synthetic example to illustrate the effect of using only surface sources in seismic interferometry. We then use the surface-wave Green's functions to analyse the interferometric integral for surface waves. This analysis allows us to investigate the role of missing subsurface sources in more detail and the effect of different surface source distributions. Finally, we discuss possible implications of our results and observations, providing possible solutions to allow for the recovery of higher-mode surface waves in different applications of seismic interferometry.

4.2 Full interferometric construction of surface waves

We begin with the frequency domain version of the elastic interferometric formula of van Manen *et al.* (2006),

$$G^{*}_{im}(\mathbf{r}_B,\mathbf{r}_A) - G_{im}(\mathbf{r}_B,\mathbf{r}_A)$$
$$= \int_S \Big\{ G_{in}(\mathbf{r}_B,\mathbf{r})\ n_j c_{njkl} \partial_k G^{*}_{ml}(\mathbf{r}_A,\mathbf{r}) - n_j c_{njkl} \partial_k G_{il}(\mathbf{r}_B,\mathbf{r})\ G^{*}_{mn}(\mathbf{r}_A,\mathbf{r}) \Big\}\, dS\,, \qquad (4.1)$$

where $G_{im}(\mathbf{r}_B,\mathbf{r}_A)$ denotes the Green's function representing the *i*th component of particle displacement at location $\mathbf{r}_B$ due to a uni-directional, impulsive, point force in the *m* direction at $\mathbf{r}_A$, $\partial_k G_{ml}(\mathbf{r}_B,\mathbf{r})$ is the partial derivative in the *k* direction of the Green's function $G_{ml}(\mathbf{r}_B,\mathbf{r})$, c_{njkl} is the elasticity tensor, * denotes complex

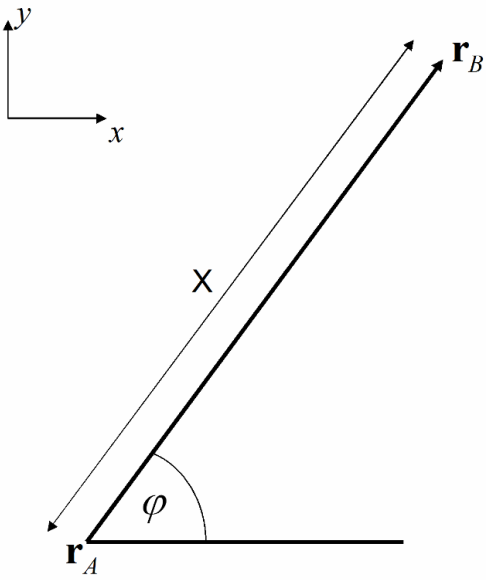

Figure 4.2: A plan view showing geometric variables used to describe the surface wave Green's function (Equation 4.2).

conjugation, n_j is the outward normal to the arbitrarily shaped surface S, where S encloses the locations $\mathbf{r}_A$ and $\mathbf{r}_B$ (Figure 4.1) and the term $n_j c_{njkl} \partial_k G_{ml}(\mathbf{r}_B, \mathbf{r})$ represents the particle displacement at $\mathbf{r}_B$ due to a deformation-rate-tensor source at $\mathbf{r}$. Again, Einstein's summation convention applies for repeated indices.

We assume that the portion of the earth in which we are interested is a lossless, horizontally-layered medium, and that in this medium the wavefield is dominated by (or can be represented by) surface waves. The Green's functions for such a medium are given by Snieder (2002b, eq. 14) as,

$$G_{im}(\mathbf{r}_B, \mathbf{r}_A) = \sum_{\nu} p_i^{\nu}(z_B, \varphi)\, p_m^{\nu *}(z_A, \varphi) \frac{e^{i\left(k_\nu X + \frac{\pi}{4}\right)}}{\sqrt{\frac{\pi}{2} k_\nu X}}, \tag{4.2}$$

and (from Appendix 4A),

$$n_j c_{njkl} \partial_k G_{ml}(\mathbf{r}_B, \mathbf{r}_A) = \sum_{\nu} p_m^{\nu}(z_B, \varphi)\ T_n^{\nu *}(z_A, \varphi) \frac{e^{i\left(k_\nu X + \frac{\pi}{4}\right)}}{\sqrt{\frac{\pi}{2} k_\nu X}}, \tag{4.3}$$

where z_A and z_B are the depths of the locations $\mathbf{r}_A$ and $\mathbf{r}_B$ respectively. Here p_i^{ν} is the *i*th component of the polarisation vector,

$$\mathbf{p}^{\nu}(z_A, \varphi) = \begin{pmatrix} r_1(z_A)\cos\varphi \\ r_1(z_A)\sin\varphi \\ i r_2(z_A) \end{pmatrix}, \tag{4.4}$$

T_n^{ν} is the *n*th component of the traction vector,

$$\mathbf{T}^{\nu}(z, \varphi) = e_{kl}^{\nu} n_j c_{njkl}, \tag{4.5}$$

or

$$\mathbf{T}^{\nu}(z, \varphi) = \begin{pmatrix} i k_\nu r_1^{\nu}(z)\cos^2\varphi & i k_\nu r_1^{\nu}(z)\cos\varphi\sin\varphi & -k_\nu r_2^{\nu}(z)\cos\varphi \\ i k_\nu r_1^{\nu}(z)\cos\varphi\sin\varphi & i k_\nu r_1^{\nu}(z)\sin^2\varphi & -k_\nu r_2^{\nu}(z)\sin\varphi \\ \frac{\partial}{\partial z} r_1^{\nu}(z)\cos\varphi & \frac{\partial}{\partial z} r_1^{\nu}(z)\sin\varphi & \frac{\partial}{\partial z} i r_2^{\nu}(z) \end{pmatrix} n_j c_{njkl}, \tag{4.6}$$

where $e_{kl}^{\nu} = p_l{}^{\nu}(z_A, \varphi) E_k^{\nu}(\varphi)$, k_ν is the wavenumber associated with the *ν*th surface wave mode, $E_k^{\nu}(\varphi)$ is the strain operator (Appendix 4A), X is the horizontal offset between the locations $\mathbf{r}_A$ and $\mathbf{r}_B$, φ is the azimuth of the horizontal path between $\mathbf{r}_A$ and $\mathbf{r}_B$ (Figure 4.2), and $r_1^{\nu}(z)$ and $r_2^{\nu}(z)$ are the horizontal and vertical Rayleigh-wave eigenfunctions, respectively. To simplify the expression the modal normalization $8 c^{\nu} U^{\nu} I_1{}^{\nu} = 1$ is assumed (Snieder, 2002b), where c^{ν}, U^{ν}, and I_1^{ν} are the phase velocity, group velocity and kinetic energy for the current mode

a.

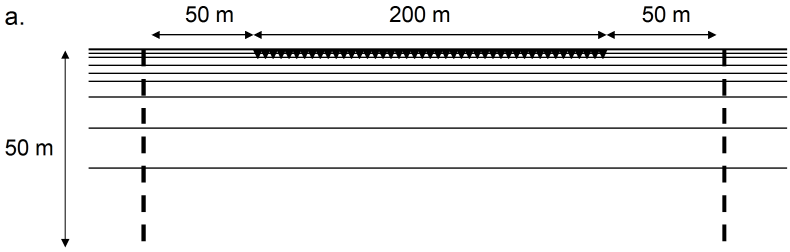

b.

Depth (m)	V_p (m/s)	V_s (m/s)	Density (kg/m^3)
0-1	404	101	1400
1-2	504	126	1460
2-4	508	127	1470
4-6	584	146	1520
6-8	688	172	1590
8-12	736	184	1610
12-20	800	200	1650
20-30	928	232	1710
30-	1228	307	1840

Figure 4.3: (a) Geometry used in Figure 4.4, Figure 4.5, and Figure 4.6. Thick dashed lines indicate the location of the integration surface, black triangles indicate the location of the receiver line, and horizontal lines indicate the free surface (top) and each successive interface below that. (b) Layer parameters.

respectively. This Green's function is for a single frequency, and in the following we assume summation over the relevant frequency range.

Wapenaar and Fokkema (2006) show that when the integration surface S is a sphere with extremely large radius, and if the area around S is homogeneous it is possible to approximate integrals such as Equation (4.1) to include a sum only over P- and S-wave source types. Since P- and S-wave sources can be written as a sum of point-force sources we can consider that it is reasonable to approximate Equation (4.1) using the cross-correlation and summation of only point-force source responses, i.e.,

$$G^{*}_{im}(\mathbf{r}_B,\mathbf{r}_A) - G_{im}(\mathbf{r}_B,\mathbf{r}_A) \approx \int_S G_{mn}(\mathbf{r}_A,\mathbf{r})\; G^{*}_{in}(\mathbf{r}_B,\mathbf{r})\; dS\,. \tag{4.7}$$

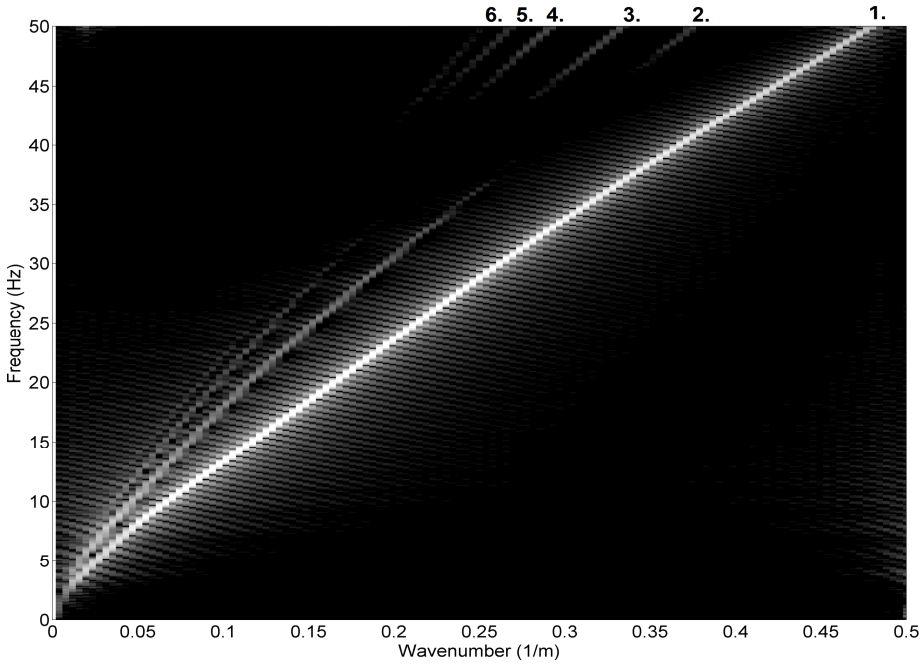

Figure 4.4: Frequency-wavenumber plot representing a directly computed source gather for the model in Figure 4.3. The fundamental mode is labelled 1 and the higher modes are labelled 2 to 6.

This allows interferometry to be applied to real situations where only point-force sources may be available. This approximation is discussed in more detail at the end of this section.

The effect of missing subsurface sources

We now use a layered 2-dimensional example to illustrate the application of exact seismic interferometry (Equation 4.1) before illustrating the effect of removing the subsurface part of the boundary of sources *S*. Figure 4.3 illustrates a layered 2D model that generates significant higher-mode surface waves (adapted from the shear wave velocity profile of Gabriels *et al.*, 1987). We solve the eigenvalue problem for Rayleigh waves in a horizontally-layered medium to calculate displacement eigenvectors ($r_1^{\nu}(z)$ and $r_2^{\nu}(z)$) and their derivates for each of the first 6 modes (Lai and Rix, 1998; Aki and Richards, 2002). While both the length-scale of this model and the frequencies considered are more relevant to exploration seismology, the same theory can be applied to larger scale, earthquake seismology problems. One

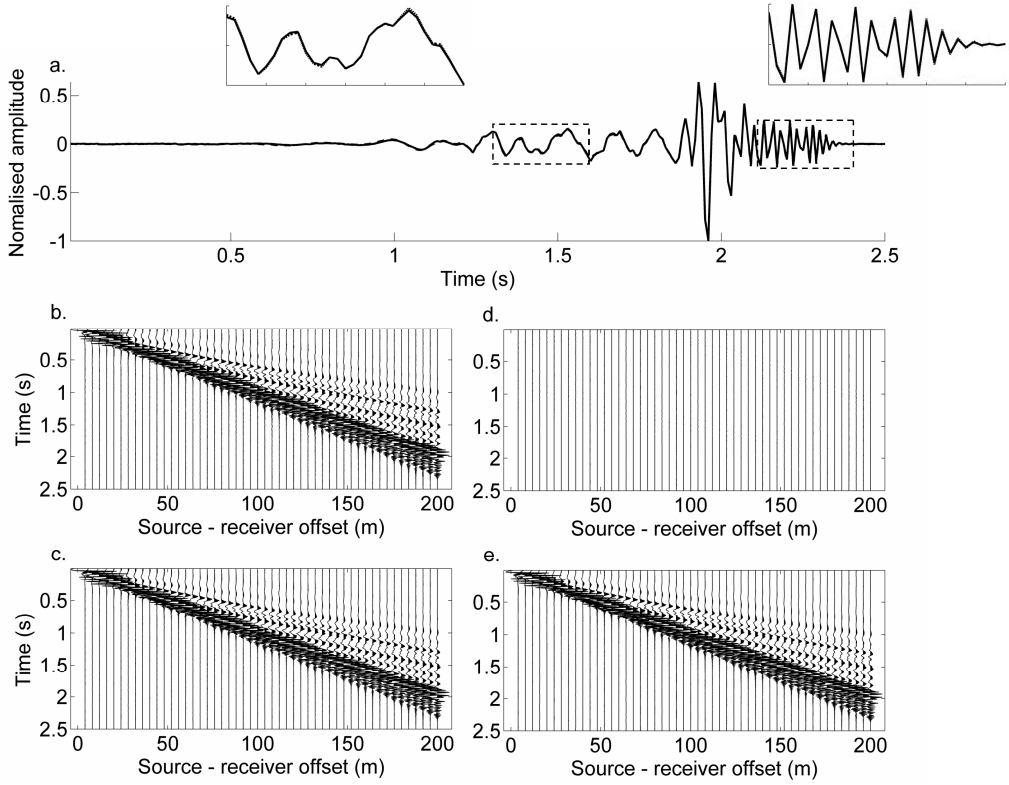

Figure 4.5: (a) Single Green's function computed using exact seismic interferometry (solid line), directly computed Green's function (dashed line); (b) Source gather computed using the same method as (a); (c) Source gather computed by applying interferometry to each mode in turn, then carrying out the modal summation; (d) Difference of (b) and (c); (e) The directly computed Green's function. Left and right inserts show zooms of left and right boxed areas respectively.

benefit of using an example like this to illustrate our results is that it is easier to identify different arrivals (such as higher-mode surface waves) when using densely sampled arrays typical of exploration seismology.

Using (the 2-dimensional equivalent of) Equation (4.2) we calculate vertical particle velocity for a single vertical point-force source at a range of offsets from 2 to 200 m and plot these data in the *f-k* domain (Figure 4.4). The surface-wave modes are labelled 1 to 6. The equivalent time-offset plots appear in both Figure 4.5e and Figure 4.6e.

We now estimate this set of surface-wave seismograms using seismic interferometry. First we implement Equation (4.1), i.e., we determine the exact inter-receiver responses using seismic interferometry. Rather than using a totally enclosing boundary, we extend two vertical lines of sources to a depth of 50 m with a sampling

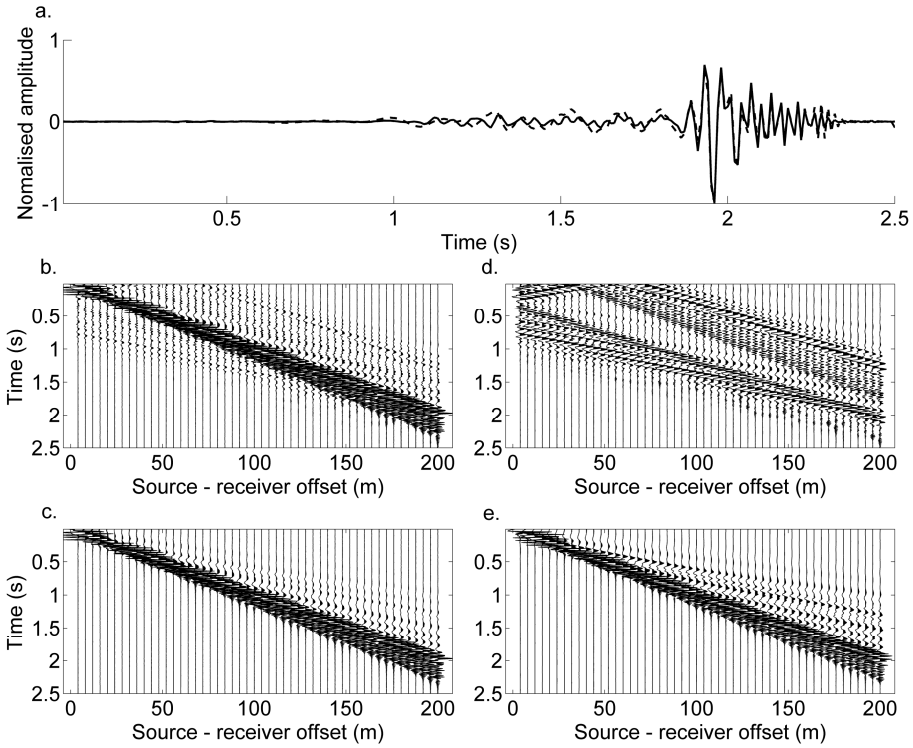

Figure 4.6: As for Figure 4.5, but computed only with point-force sources, using two sources at a depth of 0.5 m (one on either side of the receiver line). Note that the time derivative of the interferometric estimates has been plotted here. Panel (d) is shown at 3 times zoom of other panels.

interval of 0.5 m resulting in two hundred boundary sources (Figure 4.3a). This is equivalent to using an enclosing boundary since the values of dispersion curves $r_1^{\nu}(z)$ and $r_2^{\nu}(z)$ approach zero at this depth. Figure 4.5a illustrates a single example of this implementation using a receiver separation of 200 m (i.e., the maximum receiver offset). The solid line shows the interferometrically determined surface-wave Green's function, while the dashed line shows the directly computed inter-receiver surface wave. We use zoom panels to emphasize the similarity between these two plots (the small errors are due only to numerical noise). This result is repeated for each pair of receivers (fixing the first receiver as the 'virtual' source location) and is shown in Figure 4.5b. The directly computed result is shown in Figure 4.5e for comparison. In Figure 4.5c we show the result of computing the cross-correlation for each individual mode and carrying out the modal summation after interferometry - we refer to this process as "same-mode correlation". The

difference of Figure 4.5b and Figure 4.5c is shown in Figure 4.5d illustrating that these plots are identical.

The same steps are then repeated, except only two point-force sources are used at source locations with a depth of 0.5 m, one on either side of the receiver line, typical of an application of seismic interferometry to real data (i.e., applying Equation (4.7) using only the boundary sources just beneath the surface). Figure 4.6a is equivalent to Figure 4.5a, except only these two point-force sources have been used, rather than the two hundred sources used to generate Figure 4.5a. To be able to compare the interferometric estimates we plot the time-derivative of the directly computed Green's function (the need for a time-derivative in this case was predicted by Snieder (2004a) and Wapenaar and Fokkema (2006)). Note that the higher frequency, higher amplitude part of the fundamental mode has been constructed accurately; but the higher mode part of the surface wave is poorly estimated. This can be seen more clearly in Figure 4.6b where the entire source-gather estimate is shown. By applying interferometry to the individual modes, then carrying out the modal summation we get a much better estimate of the Green's functions (Figure 4.6c). Discrepancies still arise in this case due to scale factors introduced in the approximation of Equation (4.7), and by only using surface sources (cf. Figure 4.6e, where the earlier lower frequency arrivals appear to be slightly stronger). The difference between Figure 4.6b and Figure 4.6c shown in Figure 4.6d (scaled up by a factor of 3) illustrates the error introduced by the cross-correlation of different surface-wave modes - we refer to this type of error as "cross-mode correlation". These results show that in certain circumstances errors are incurred when estimating higher-mode surface waves using only surface sources, and hence subsurface sources may be required for accurate estimates of multi-mode surface waves. We later show that this is not strictly true for certain surface-source geometries.

Analysis of the interferometric integral for surface waves

We now investigate how the interferometric integral synthesizes surface waves. Here we solve the integral using a Rayleigh-wave orthogonality relationship and the method of stationary-phase integration. This method assumes that dominant contributions to the integral come from locations around the integration boundary S

where the phase of the integrand becomes stationary and that the amplitude of the term being integrated varies slowly around this location (Snieder, 2004b). The integral is then solved by evaluating the contribution from each of these stationary-phase locations. This approach reveals the processes that account for both the elimination of cross-mode terms of different surface-wave modes and the recovery of correct amplitudes, both of which are shown to require integration in depth as well as in the horizontal plane.

We begin by illustrating the steps necessary to show the consistency of Equations (4.2) to (4.6) with Equation (4.1). While the mathematics may seem a little involved, it is useful later in the chapter when we show how various parts of the derivation break down for different source geometries and modal combinations.

Substituting Equation (4.2) and Equation (4.3) into Equation (4.1) gives

$$G^{*}_{im}(\mathbf{r}_B,\mathbf{r}_A)-G_{im}(\mathbf{r}_B,\mathbf{r}_A)=\sum_{\nu,\nu'}\int_S \frac{e^{i\left(k_\nu X_B-k_{\nu'}X_A\right)}}{\frac{\pi}{2}\sqrt{k_\nu k_{\nu'}X_A X_B}}\; p_i^{\nu}(z_B,\varphi_B)\;\; p_m^{\nu'*}(z_A,\varphi_A)$$

$$\times\Big(\;\; p_n^{\nu*}(z,\varphi_B)T_n^{\nu'}(z,\varphi_A)-T_n^{\nu*}(z,\varphi_B)\,p_n^{\nu'}(z,\varphi_A)\;\;\Big)\,dS\,, \qquad (4.8)$$

where z, z_A, and z_B are the depths of the boundary source, and receivers $\mathbf{r}_A$, and $\mathbf{r}_B$ respectively, and φ_A and φ_B are the azimuths of the horizontal projection of the paths between the boundary source and receivers $\mathbf{r}_A$ and $\mathbf{r}_B$. Snieder (2004a) solves a similar integral to Equation (4.8) but considers integration only in the horizontal plane and does not include the effect of the terms representing the boundary source types (equivalent to setting the bracketed term on the right hand side of Equation (4.8) equal to one). This analysis results in the correct surface-wave Green's functions scaled by a factor π/ik_ν. We now investigate the importance of the source terms, and the need for integration in both the horizontal direction and in depth, resulting in the exact inter-receiver multi-mode surface wave Green's function. The part of our analysis that coincides with that of Snieder (2004a) is included in Appendix 4B.

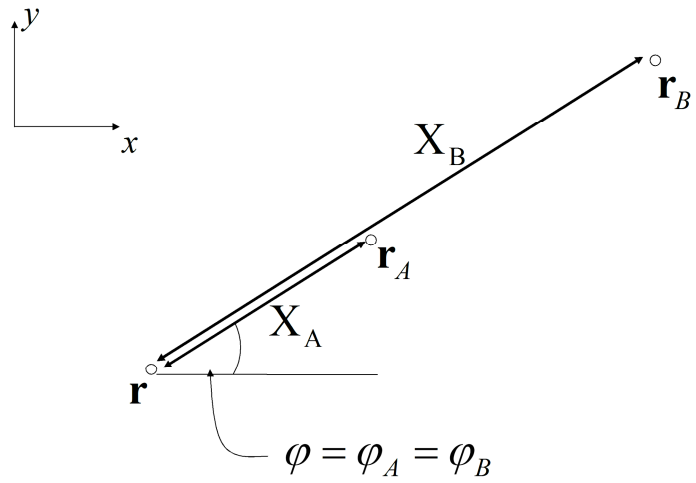

Figure 4.7: Geometric configuration for a stationary point for the direct surface wave.

Notice that a double summation over surface wave modes (ν, ν') is carried out in Equation (4.8), yet only a single summation over modes is present in the desired Green's function representation in Equation (4.2). Aki and Richards (2002, ch.7, eq. 7.100) present a 2-dimensional Rayleigh wave orthogonality relationship, derived from a representation theorem of the convolution type (de Hoop, 1995, eq. 15.2-7; Wapenaar and Fokkema, 2006, eq. 5), and Bostock (1990) extends this relationship to 3-dimensional Rayleigh waves. A similar expression can be derived using the reciprocity theorem of the correlation type (Appendix 4D), giving

$$0 = \int_S \left(p_i^{\nu^*}(z,\varphi_B) T_i^{\nu'}(z,\varphi_A) - T_i^{\nu^*}(z,\varphi_B) p_i^{\nu'}(z,\varphi_A) \right) dS \,. \tag{4.9}$$

This relationship holds for any pair of modes $\nu \neq \nu'$. Equation (4.8) is then non-zero only when $\nu = \nu'$, reducing it to a single sum over modes:

$$G_{im}^*(\mathbf{r}_B,\mathbf{r}_A) - G_{im}(\mathbf{r}_B,\mathbf{r}_A) = \sum_\nu \int_S \frac{e^{ik_\nu(X_B - X_A)}}{\frac{\pi}{2} k_\nu \sqrt{X_A X_B}} \; p_i^\nu(z_B,\varphi_B) \; p_m^{\nu^*}(z_A,\varphi_A)$$

$$\times \left(p_n^{\nu^*}(z,\varphi_B) T_n^\nu(z,\varphi_A) - T_n^{\nu^*}(z,\varphi_B) p_n^\nu(z,\varphi_A) \right) dS \,. \tag{4.10}$$

i.e., the orthogonality relationship removes the undesired cross-terms of different modes from Equation (4.8), provided we integrate around a fully enclosing boundary.

Snieder (2004a) finds that integrals like Equation (4.10) have stationary phase when $\varphi = \varphi_A = \varphi_B$ (where φ is the azimuth of the desired inter-receiver Green's function, Appendix 4B; see Figure 4.7). We write the normal to the boundary at the stationary point, n_j^{sp} as the vector $(n_x^{sp}, n_y^{sp}, n_z^{sp})$ and evaluate the source terms using this stationary-phase condition, the forms of the polarization vector, $\mathbf{p}^\nu$, and the traction vector, $\mathbf{T}^\nu$, in Equations (4.4) and (4.6) respectively, and the isotropic form of the stress-tensor:

$$p_n^{\nu\,*}(z,\varphi)T_n^\nu(z,\varphi) - T_n^{\nu\,*}(z,\varphi)p_n^\nu(z,\varphi) = 2ik_\nu(\cos\varphi n_x^{sp} + \sin\varphi n_y^{sp}) \times\left[(\lambda+2\mu)\left\{r_1^\nu(z)\right\}^2 + \mu\left\{r_2^\nu(z)\right\}^2 + \frac{\lambda}{k_\nu}r_1^\nu(z)\frac{\partial}{\partial z}r_2^\nu(z) - \frac{\mu}{k_\nu}r_2^\nu(z)\frac{\partial}{\partial z}r_1^\nu(z)\right]. \tag{4.11}$$

Here λ and μ are the Lamé parameters. Using the energy integrals (Aki and Richards, 2002, ch.7, eq. 7.74)

$$I_2^\nu = \frac{1}{2}\int_0^\infty \left[(\lambda+2\mu)\left\{r_1^\nu(z)\right\}^2 + \mu\left\{r_2^\nu(z)\right\}^2\right] dz, \tag{4.12}$$

and

$$I_3^\nu = \int_0^\infty \left[\lambda r_1^\nu(z)\frac{\partial r_2^\nu(z)}{\partial z} - \mu r_2^\nu(z)\frac{\partial r_1^\nu(z)}{\partial z}\right] dz, \tag{4.13}$$

allows the integration of Equation (4.11) over the entire surface *S* to be written as

$$\int_0^\infty \left[\; p_n^{\nu *}(z,\varphi) T_n^{\nu}(z,\varphi) - T_n^{\nu *}(z,\varphi) p_n^{\nu}(z,\varphi) \; \right] dz =$$

$$2ik_\nu (\cos\varphi n_x^{sp} + \sin\varphi n_y^{sp}) \left[2I_2^\nu + \frac{I_3^\nu}{k_\nu} \right]. \qquad (4.14)$$

Thus we have solved the part of the integral dependent on depth. Using Equation (7.76) from Aki and Richards (2002), $I_2^\nu + I_3^\nu / 2k_\nu = c^\nu U^\nu I_1^\nu$, and recalling from the definition after Equation (4.6) that $8c^\nu U^\nu I_1^{\;\nu} = 1$, then

$$G_{im}^*(\mathbf{r}_B,\mathbf{r}_A) - G_{im}(\mathbf{r}_B,\mathbf{r}_A) \approx \sum_\nu \frac{ik_\nu}{\pi} \int_S \frac{e^{ik_\nu (X_B - X_A)}}{k_\nu \sqrt{X_A X_B}} \; p_i^\nu(z_B,\varphi) \; p_m^{\nu *}(z_A,\varphi) dS$$

$$\times \; (\cos\varphi n_x^{sp} + \sin\varphi n_y^{sp}) \; . \qquad (4.15)$$

In Appendix 4B we show that this integral can be solved following the stationary phase argument of Snieder (2004a), resulting in

$$G_{im}^*(\mathbf{r}_B,\mathbf{r}_A) - G_{im}(\mathbf{r}_B,\mathbf{r}_A) \approx -\eta \sum_\nu p_i^\nu(z_B,\varphi) \; p_m^{\nu *}(z_A,\varphi) \frac{e^{i\eta\left(k_\nu X + \frac{\pi}{4}\right)}}{\sqrt{\frac{\pi}{2} k_\nu X}}, \qquad (4.16)$$

where X is the horizontal offset between $\mathbf{r}_A$ and $\mathbf{r}_B$. There are two types of stationary-phase locations, one where $X_A > X_B$ and one where $X_A < X_B$, these two cases are denoted by $\eta = -1$ and $\eta = 1$ respectively. This result is virtually identical to Equation (4.2), the only difference being that in Equation (4.16) both causal (forward-time) and acausal (reverse-time) Green's functions exist. Note that by considering source terms and integration in depth we have not only correctly accounted for the higher-mode surface waves, but we have also accounted for the factor π / ik_ν introduced in the analysis of Snieder (2004a). This result is illustrated in Figure 4.5, where we have plotted the causal part of the interferometrically determined Green's functions.

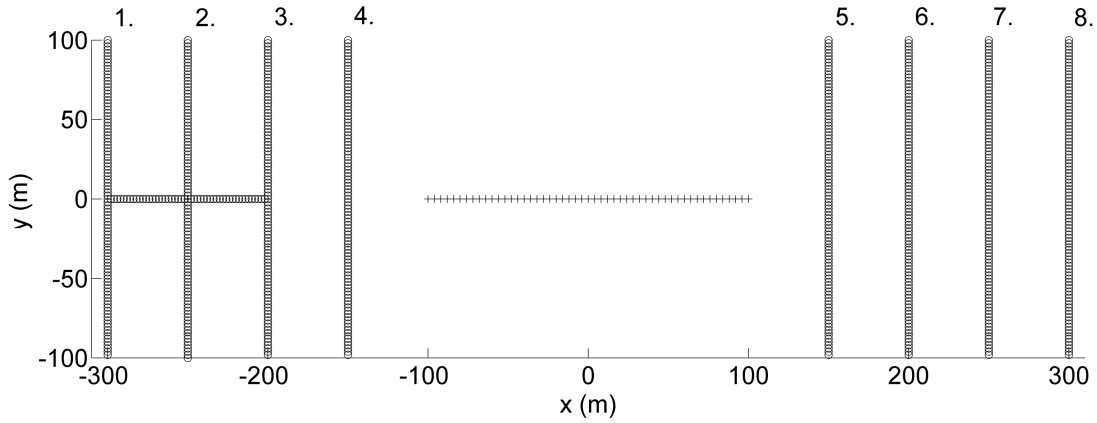

Figure 4.8: Geometry of sources (circles) and receivers (crosses) used to illustrate the effects of surface source distribution. Orthogonal source lines are labelled 1 to 8.

In Equation (4.7) we approximated the interferometric integral to be a sum over only point-force sources. In Appendix 4C we investigate the effect of this approximation and using the far-field condition we derive a scale factor allowing us to quantify the effect of using only point-force sources, as is common in applications of interferometry to real data. We find that Equation (4.7) can be re-written as

$$G^{*}_{im}(\mathbf{r}_B,\mathbf{r}_A) - G_{im}(\mathbf{r}_B,\mathbf{r}_A) \approx ik^{\nu} \int_S M^{\nu}(\omega)\; G_{mn}(\mathbf{r}_A,\mathbf{r})\; G^{*}_{in}(\mathbf{r}_B,\mathbf{r})\; dS\,, \tag{4.17}$$

where $M^{\nu}(\omega)$ is a scale factor accounting for the changes introduced by using only uni-directional point-forces, given by

$$M^{\nu}(\omega) = 2n_j c^{\nu} U^{\nu} \rho\,. \tag{4.18}$$

We can expect results using only point-force sources to vary with frequency (ω), surface wave mode (ν), and the near-surface density, ρ. The term $ik_{\nu}(=i\omega/c^{\nu})$ can partly be accounted for with a time derivative (in the frequency domain a time derivative is equivalent to multiplication by $i\omega$). This is the only term that affects the phase of the Green's function (for a single frequency); hence, without accounting for the rest of the scale factor we can still expect the estimated surface wave to have

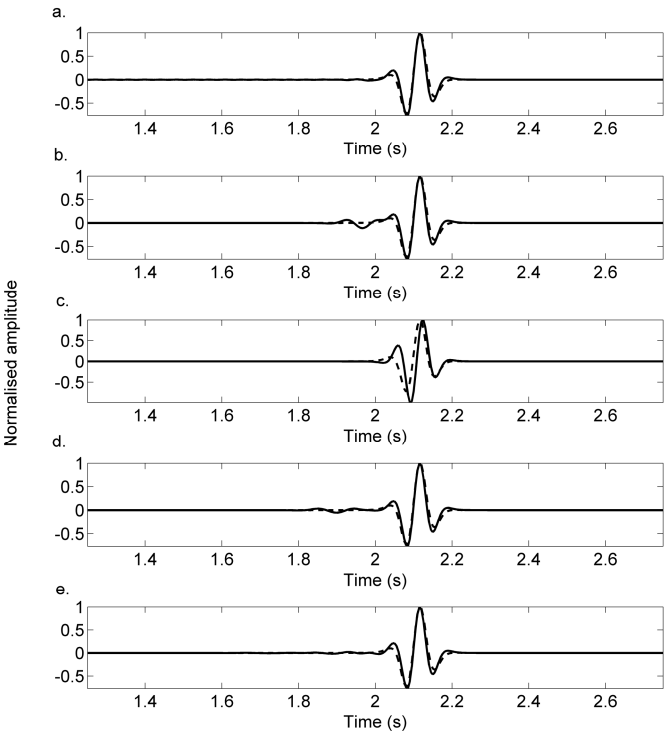

Figure 4.9: Time derivative of the interferometric estimates of the fundamental mode surface wave between the first and last receivers shown in Figure 4.8: (a) using a homogeneous distribution of sources (solid line), with the directly computed surface wave (dashed line); (b) as for (a) but using orthogonal source line 3; (c) using the in-line source line; (d) using 6 lines of sources around source line 3, separated at 2 m; (e) using orthogonal source lines 1 to 8.

the correct phase. Note that the presence of higher modes complicates the application of the term $i\omega/c^{\nu}$, as it varies for each mode. Of course, methods exist to estimate local material properties (e.g., Aki, 1957; Curtis and Robertsson, 2002; van Vossen *et al.*, 2005), and it is possible to identify and separate different surface-wave modes using array-based frequency-wavenumber methods, or single-station methods (e.g., van Heijst and Woodhouse, 1997). Hence, if required, these scale factors could be estimated and used explicitly.

In Appendix 4C we note that a similar approach to the above can be used to solve the single source-type interferometric integral (Equation 4.17). In this case, due to complications with scale factors we have neglected the effect of higher-mode surface waves. However, in Appendix 4D we also derive a Rayleigh-wave orthogonality relationship for the single source case. Hence, apart from varying scale factors, we expect sources at depth to play a similar role in this case.

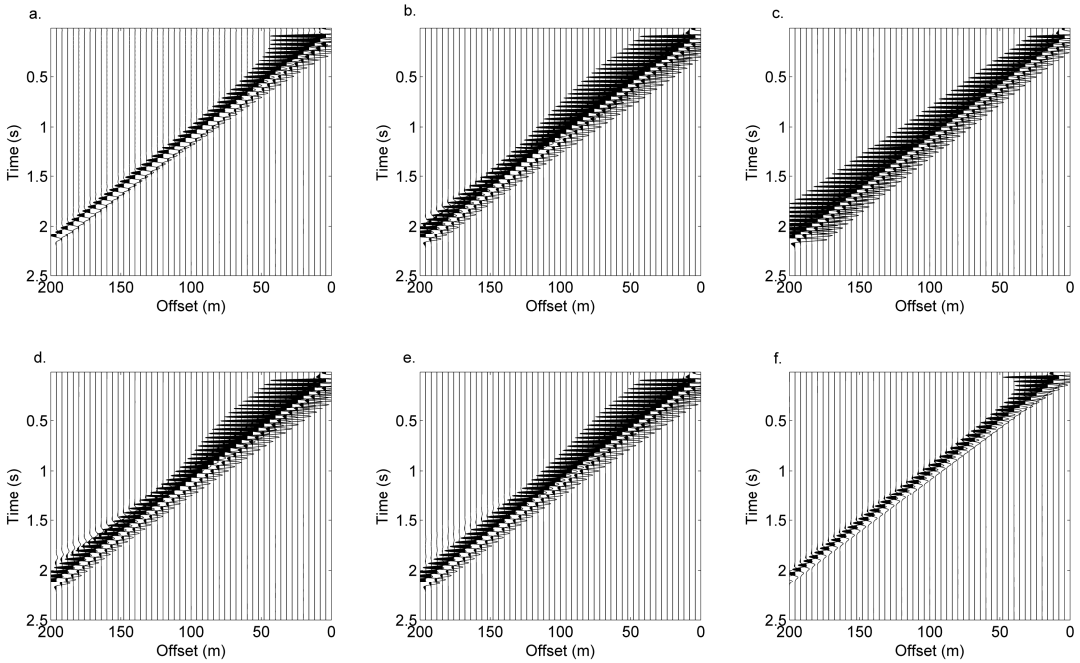

Figure 4.10: Equivalent results to Figure 4.9, but surface waves are estimated for all receivers paired with the farthest right receiver: (a) using a homogeneous distribution of sources; (b) using orthogonal source line 3; (c) using the in-line source line; (d) using a thick boundary of sources; (e) using source lines 1 to 8; (f) directly computed surface wave. x (m) indicates the x-coordinate of the receivers.

4.3 Interferometry with only surface sources

In practice the most likely case is that sources will only be available at (or near) the surface of the earth as this is the usual case in active-source seismology, and also in passive interferometry where passive wavefields are believed to be excited by predominantly near-surface sources (Shapiro and Campillo, 2004; Shapiro *et al.*, 2005). Here we illustrate the effect of different surface source distributions on the estimation of inter-receiver surface waves, for both single and multi-mode cases.

Surface source distribution – single mode surface waves

Snieder (2004a) considers a homogeneous distribution of sources at the surface of the Earth and shows that the correct inter-receiver surface wave can be recovered, and we begin by illustrating this case. The scale factor in Equation (4.17) applies when a fully enclosing boundary of sources is present. Since we now only use

sources at the surface, and terms such as Equations (4.12) to (4.14) which require integration in depth do not hold, this scale factor no longer applies. Here we use a single mode, hence there are no complications due to varying scale factors for different modes. To account for the lack of sources at depth we introduce a modal- and frequency-dependent scale factor, $A^{\nu}(\omega)$, that may differ from $M^{\nu}(\omega)$ depending on source configurations. For this homogeneous distribution we replace the integration surface *S* by integration over the *x*- and *y*-coordinates,

$$G_{im}^{est}(\mathbf{r}_B,\mathbf{r}_A) \approx ik_{\nu}A^{\nu}(\omega)\int_{y_1}^{y_2}\int_{x_1}^{x_2} G_{mn}(\mathbf{r}_A,\mathbf{r})\; G_{in}^{*}(\mathbf{r}_B,\mathbf{r})\; dxdy\,. \qquad (4.19)$$

Here we define the estimated Green's function resulting from the chosen source geometry as $G_{im}^{est}(\mathbf{r}_B,\mathbf{r}_A)$. Using the simple case of a homogeneous half space (with a P-wave velocity of 1000 m/s, an S-wave velocity of 250 m/s and a density of 1700 kg/ms^3) we first illustrate this case using the receiver layout shown in Figure 4.8. We compute 3D Rayleigh-wave Green's functions with Equation (4.2), using a grid of sources located across the whole area of this figure, separated at 2 m. The parameters used here result in a fundamental-mode Rayleigh wave with a velocity of 95 m/s. For the source sampling interval of 2 m this allows the wavefield to be well sampled (within the Nyquist sampling criteria) up to a frequency of approximately 25 Hz - we use a Ricker wavelet with centre frequency 10 Hz to band-limit the data. Note that in passive-seismic interferometry, signals from different sources can overlap in time and sufficient time averaging is required in order to reduce the impact of cross-terms that this can introduce (Snieder, 2004a). We implement sources one at a time and hence, when considering our examples in respect of the application of passive seismic interferometry there are no overlapping signals from different sources.

The result of the application of Equation (4.19) using a homogeneous surface-source distribution (applying the time derivative, but not the scale factor) for a single receiver pair is shown in Figure 4.9a (solid line) with the directly computed Green's function for comparison (dotted line). For visualization, both of these plots (and subsequent plots in Figure 4.9b to Figure 4.9e) are normalized to a maximum amplitude of one. Note that in this case the interferometric estimate is a good match

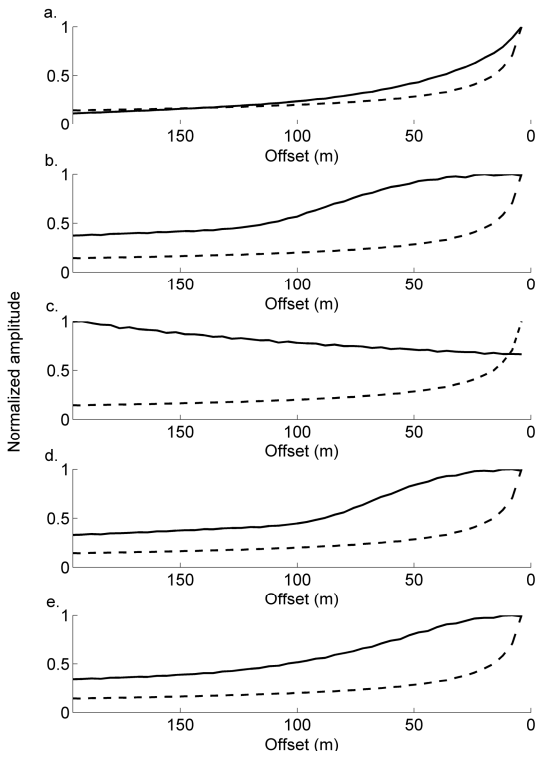

Figure 4.11: Maximum amplitude of each trace versus offset for Figure 4.10a to Figure 4.10e. Directly computed result is shown for reference (dotted line).

for the directly-computed surface wave. A similar estimate is made for each receiver pair of interest (fixing the farthest right receiver) producing an estimate of a common-source gather (Figure 4.10a). Comparing with Figure 4.10f (directly computed data) we can see that both the arrival times, and the relative amplitudes of the surface-wave arrivals are well predicted. This is illustrated in Figure 4.11a, where we plot the maximum amplitude of each trace versus offset (solid line), with the directly computed result shown for reference (dotted line, all plots are normalized to a maximum of 1).

In reality, such a homogeneous distribution of surface sources is not often available. To illustrate the effect of source distributions we now investigate some limited source geometries typically found in applications of surface-wave interferometry in both exploration and earthquake seismology.

In Equation (4.15) the denominator includes a term dependent on the product of two path lengths (X_A and X_B). After the stationary phase evaluation (Equation 4.16)

this reduces to a single offset X ($X = X_A - X_B$), and the correct geometrical spreading term is recovered. If we align the *x*-axis with the inter-receiver line then at the stationary point we have $n_x^{sp} = 1$ and $n_y^{sp} = 0$, i.e., an orthogonal source line allows for the recovery of the correct geometrical spreading term (a result observed by Snieder, 2004a). Orthogonal source lines are commonly used in industrial seismic surveys, or they may represent a noise-generating coastline and we now consider this configuration. Note that amplitude errors may exist in this application due to the scale factor appearing in Equation (4.19).

We estimate the surface waves between the first and last receiver using orthogonal source line 3 of Figure 4.8 (solid line, Figure 4.9b), and compare this with the time-derivative of the directly computed Green's function (dashed line). We have applied cosine tapers across the end of the source line to reduce truncation artefacts, which can be seen prior to the arrival of the surface wave (1.9 to 2 s). As predicted the phase of the main peaks are well matched and this result is similar to the result for the homogeneous source distribution. We estimate the source gather using this source distribution (Figure 4.10b): note that here, while the geometrical spreading factor is not recovered exactly, the amplitude still decreases with increasing offset (the maximum amplitude of each trace versus offset is shown in Figure 4.11b).

In Chapter 2 a line of sources on an extension of the inter-receiver line were used to estimate inter-receiver surface waves (i.e., integration in the *x*-direction). Since these synthetic examples are in 2D this is adequate to recover the correct inter-receiver surface waves. However, in 3D, integration in only the *x*-direction does not recover the correct spreading term. The *x*-integral is always stationary (as $|X_B - X_A| = |X|$ for any source position), i.e.,

$$G_{im}^{est}(\mathbf{r}_B, \mathbf{r}_A) = A^{\nu}(\omega) \frac{e^{ik_{\nu}\left(X + \frac{\pi}{2}\right)}}{ik_{\nu}} p_i^{\nu}(z_B, \varphi)\ p_m^{\nu *}(z_A, \varphi) \int_{x_1}^{x_2} \frac{1}{\sqrt{X_A X_B}} dx . \qquad (4.20)$$

Comparing with Equation (4.2) we see that a phase shift of $\pi/4$ is required to retrieve the Green's functions correct phase. Note that after a time derivative has

been applied (as in Equation 4.19) a factor of $1/\sqrt{k_\nu}$ is missing (cf. the denominator in Equation 4.2); hence higher frequencies will have artificially high amplitudes in this case (both the phase shift and the factor $1/\sqrt{k_\nu}$ were observed by Snieder et al. (2006) for 3D body wave acquisition along a line). Results using the in-line source line in Figure 4.8 are shown in Figure 4.9c and Figure 4.10c. Since we have fixed the farthest right receiver the term $X_A X_B$ is actually greater for the shorter inter-receiver offsets explaining why the amplitudes increase (incorrectly) as the receiver moves away from the 'virtual' source (Figure 4.11c). The errors are exemplified by the phase discrepancy in Figure 4.9c and the errors in relative amplitudes between Figure 4.10c and f.

In passive interferometry, surface-wave signals appear most clearly between receivers whose inter-receiver azimuths are perpendicular to the (noise-generating) coast lines. For example in the results of Gertstoft *et al.* (2006), inter-receiver azimuths perpendicular to the Californian coast give clearer surface-wave signals than those sub-parallel to the coast. Such source geometry may be represented approximately by a single orthogonal source line corresponding to results in Figure 4.9b and Figure 4.10b. However, we may also consider the coastline as a 'thick' boundary of sources, since wave energy may be dissipated over a significant range of distances from the shore. Therefore we use a series of eight closely spaced orthogonal source lines (separated at 2 m, located around source line 3) to produce inter-receiver estimates shown in Figure 4.9d (note the truncation artefacts around 1.8 to 1.95 s) and Figure 4.10d and these estimates are very similar to the single orthogonal source line (also compare Figure 4.11b and Figure 4.11d).

In exploration seismology, source and receiver lines are often distributed with orthogonal geometries. The 8 orthogonal source lines and the receiver line in Figure 4.8 illustrate such geometry. We repeat the processing used for the single orthogonal source line for each of these lines and sum the result, shown in Figure 4.9e and Figure 4.10e (with maximum amplitudes for each trace shown in Figure 4.11e). This result is again very similar to the result for a single source line but with a reduction of truncation artefacts (these vary for each source line and interfere destructively).

Hence, when there is only a single surface-wave mode present, as is the case for a homogeneous-half-space, a source distribution restricted to the surface does not have a strong influence on the recovered inter-receiver surface waves, provided that sources are distributed in the cross-line direction.

Surface source distributions – multi-mode surface waves

Above we have shown that various different surface source geometries allow for the recovery of estimates of the inter-receiver fundamental-mode surface waves. Errors are introduced in both the phase and amplitudes of the surface waves due to the use of only point-force sources, and the omission of sources at depth. We now investigate the effect of these source geometries on the estimation of multi-mode surface waves.

When there are only surface sources and hence there is no integration over depth we cannot apply the Rayleigh-wave orthogonality relationship in Equations (4.8), (4.9), and (4.10), and hence the cross-mode terms do not cancel. Above we only considered single-mode surface waves. We now consider both a same-mode integral where $\nu = \nu'$ and a cross-mode integral where $\nu \neq \nu'$. Substituting the appropriate Green's functions

$$G_{im}^{est}(\mathbf{r}_B, \mathbf{r}_A) = \sum_{\nu=\nu'} ik_\nu A^\nu(\omega) \int_{y_1}^{y_2} \int_{x_1}^{x_2} \frac{e^{i(k_\nu X_B - k_\nu X_A)}}{\frac{\pi}{2}\sqrt{k_\nu k_\nu X_A X_B}}$$

$$\times p_i^\nu(z_B, \varphi_B) p_m^{\nu *}(z_A, \varphi_A) p_n^\nu(z, \varphi_B) p_n^{\nu *}(z, \varphi_A)\ dxdy$$

$$+ \sum_{\nu \neq \nu'} iA^{\nu\nu'}(\omega) \int_{y_1}^{y_2} \int_{x_1}^{x_2} \frac{e^{i(k_\nu X_B - k_{\nu'} X_A)}}{\frac{\pi}{2}\sqrt{k_\nu k_{\nu'} X_A X_B}}$$

$$\times p_i^\nu(z_B, \varphi_B) p_m^{\nu' *}(z_A, \varphi_A) p_n^\nu(z, \varphi_B) p_n^{\nu' *}(z, \varphi_A)\ dxdy, \qquad (4.21)$$

where $A^{\nu\nu'}(\omega)$ is a scale factor dependent on both modes and frequency. The first integral term can be evaluated in a similar manner as in Appendix 4B, resulting in an

estimate of the inter-receiver, multi-mode surface wave. We now consider the behaviour of the second integral term when various source distributions are used.

Following the procedure in Appendix 4B, we find that the phase of the second part of Equation (4.21) can only be stationary when

$$0 = k_{\nu} \frac{\partial X_B}{\partial y} - k_{\nu'} \frac{\partial X_A}{\partial y}, \tag{4.22}$$

and

$$0 = k_{\nu} \frac{\partial X_B}{\partial x} - k_{\nu'} \frac{\partial X_A}{\partial x}. \tag{4.23}$$

From the first order derivatives in Equations (A4.15) to (A4.18) in Appendix 4B

$$0 = k_{\nu} \cos\varphi_B - k_{\nu'} \cos\varphi_A, \tag{4.24}$$

$$0 = k_{\nu} \sin\varphi_B - k_{\nu'} \sin\varphi_A. \tag{4.25}$$

Therefore the stationary condition can be written as

$$\frac{k_{\nu}}{k_{\nu'}} = \frac{\cos\varphi_A}{\cos\varphi_B}, \tag{4.26}$$

for integration in the *x*-direction, and

$$\frac{k_{\nu}}{k_{\nu'}} = \frac{\sin\varphi_A}{\sin\varphi_B}, \tag{4.27}$$

for integration in the *y*-direction. Figure 4.12a and b show examples of the pattern of these two stationary points for the cross-mode correlation of the first and second modes between the two shown locations (circles). Similar patterns are found for

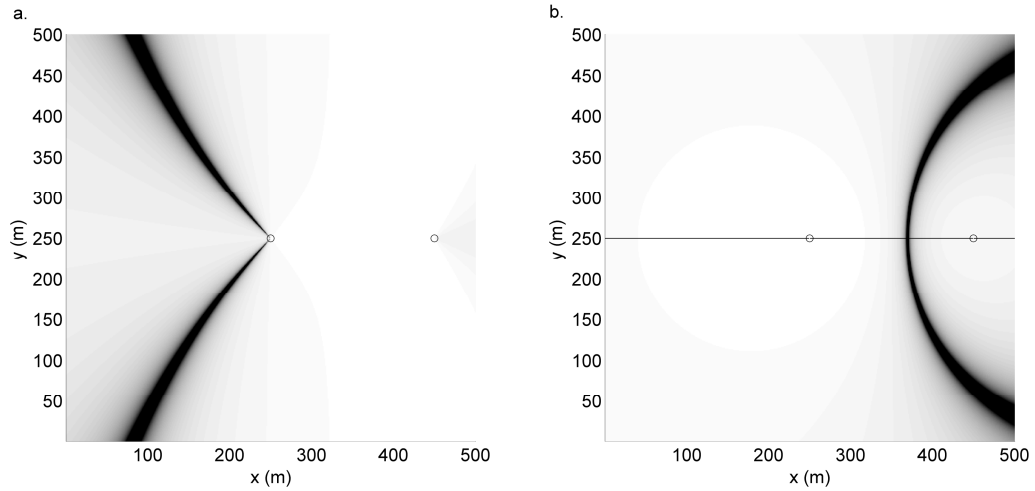

Figure 4.12: Black areas indicate the region of stationary phase for a pair of different surface-wave modes observed at the two receivers shown (circles). (a) For integration in the x-direction; (b) for integration in the y-direction.

differing source pairs. We have plotted the absolute values of Equation (4.24) and (4.25) respectively; black areas (zero) indicate stationary phase regions and all other values are non-zero (i.e. they are non-stationary). Figure 4.12a shows the pattern for integration in the *x*-direction, i.e. this stationary region applies if sources are distributed in *only* the *x*-direction. Likewise, for Figure 4.12b which shows the pattern for integration in the *y*-direction, i.e. this stationary region applies if sources are distributed in *only* the *y*-direction. Note that the two different stationary regions never coincide. Hence, if integration is across the surface (extending in *both* the *x*- and *y*-directions) then there is no stationary region; the second part of Equation (4.21) is then never stationary and therefore cancels.

We illustrate the homogeneous source distribution (i.e., integration in both the *x*- and *y*- directions) using the same source and receiver geometries as used in Figure 4.10a but now we use the model illustrated in Figure 4.3. The fundamental mode has a minimum velocity of 105 m/s and therefore the 2 m sampling allows the wavefield to be well sampled up to a frequency of approximately 25 Hz (we again use a 10 Hz Ricker wavelet to band-limit the data). Each trace is normalized to peak amplitude of 1 (as are the subsequent plots in Figure 4.13b to Figure 4.13e) as we concentrate on the effect of multiple modes as opposed to the phase and amplitude errors illustrated in Figure 4.9 and Figure 4.10. The interferometric estimate using this homogeneous

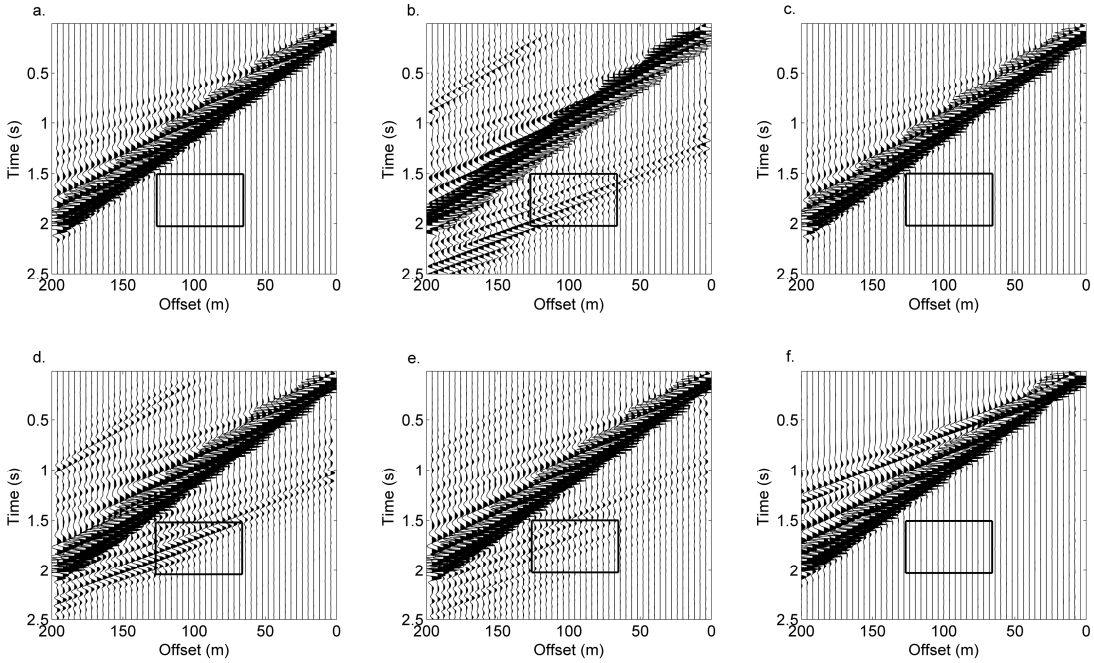

Figure 4.13: As for Figure 4.10 but computed with the model in Figure 4.3.

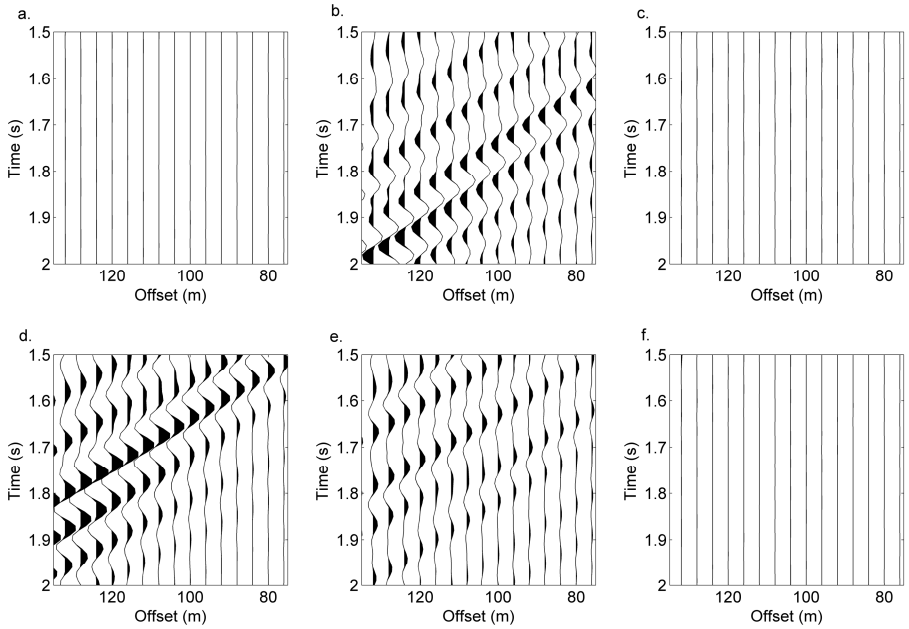

Figure 4.14: Zoom of boxed areas in Figure 4.13.

source distribution is shown in Figure 4.13a. Comparisons with the directly computed Green's function in Figure 4.13f are favourable, although we expect amplitude anomalies between modes due to the scale factor in Equation (4.21).

Above we introduced a series of source distributions that represent different situations in which seismic interferometry is often applied. When only orthogonal source lines are present (either a single orthogonal source line, a thick orthogonal source line, or several well spaced orthogonal source lines), integration is only being carried out along a line (in this case a line in the *y*-direction) and a distribution of cross-mode stationary points such as those shown in Figure 4.12b will exist. Note that for any orthogonal source line there is at least one stationary point for any offset in the in-line direction. When these source distributions are used we cannot be positive that the cross-mode integral cancels to zero. We accommodate for this non-cancellation by writing the solution of Equation (4.21) as

$$G_{im}^{est}(\mathbf{r}_B,\mathbf{r}_A) = -\eta\sum_{\nu} ik_\nu A^\nu(\omega)\ \frac{e^{i\eta(k_\nu X+\frac{\pi}{4})}}{\sqrt{\frac{\pi}{2}k_\nu X}}\ p_i^\nu(z_B,\varphi)\ \ p_m^{\nu\,*}(z_A,\varphi) + E\,, \tag{4.28}$$

where E represents the errors introduced by the cross-mode correlation.

The distribution of cross-mode stationary points in Figure 4.12b is typical of those that exist when integration is carried out in the *x*-direction. Note, that no stationary points exist on the extension of the inter-receiver line, hence by using an in-line source line we can avoid such cross-mode stationary points, i.e., this geometry should not be affected by the cross-mode spurious events.

We now reproduce the results of Figure 4.10b to Figure 4.10e using the multi-mode model as shown in Figure 4.13. Figure 4.13b illustrates the surface waves resulting from the use of orthogonal source line 3, showing spurious events that are introduced similar to those in Figure 4.6. In Figure 4.14b we show a zoom of an area affected by these spurious events, where we expect the answer to be zero (cf. Figure 4.14a and Figure 4.14f). The in-line source line (Figure 4.13c) does not show these spurious events and the results are dominated by the higher-frequency surface waves as predicted in the previous section (Figure 4.14c shows the equivalent to Figure 4.14a). In this case the higher-mode surface waves are still recovered, but due to the dominance of the fundamental mode at higher frequencies these higher modes have low relative amplitudes. In Chapter 3 a similar distribution of sources and receivers

were used and it was shown that, despite the introduction of amplitude anomalies, it is possible for the phase of both fundamental and higher-mode surface waves to be estimated using such a geometry.

Both the 'thick' source line and the well spaced orthogonal source lines (Figure 4.13d and Figure 4.13e) also show spurious events, for the thick line these are shorter in duration, and for the well spaced lines these are weaker than those in Figure 4.13b. This is clear from the associated zoom plots in Figure 4.14d and e. These source geometries reduce the impact of the spurious events as the phase of these events changes with the location of the boundary. This is similar to the observation of Draganov *et al.* (2004) who discover that the use of an irregular boundary of sources reduces the effect of ghost events introduced by heterogeneities external to the boundary of sources. The phase of the ghost event varies with source location, hence they begin to cancel due to a similar effect observed in our examples.

Our analysis suggests that the recovery of surface waves using only surface sources is not straight forward when higher modes are present. As expected the surface wave recovery is good when both a homogeneous distribution of sources is used and also when an in-line source distribution is used, despite the varying scale factors. When only limited orthogonal source distributions are available the estimates are far from ideal – orthogonal source lines introduce spurious events due to the cross-mode correlation.

Note that the above relations require that the sources are distributed within the spatial Nyquist criteria. Spatial aliasing will result in uncancelled terms and further spurious events will be introduced into the Green's functions estimates. van Manen *et al.* (2005) show that it is still possible to retrieve the correct phase of dominant parts of the Green's function when the surface S is spatially aliased.

4.4 Discussion

The analysis and results presented here illustrate the adverse effects of only using surface sources in seismic interferometry for surface-wave analysis. In our analysis we illustrate how integration around a full boundary of sources cancels the contribution of cross-mode terms in the interferometric integral and allows for the

recovery of the correct amplitudes of the different surface-wave modes, i.e., to estimate higher-mode surface waves correctly we require sources at depth. Hence, when sources are only available at the surface of the Earth estimates are affected by amplitude errors and the introduction of spurious arrivals relating to the higher modes.

We have investigated the role of different surface-source distributions in seismic interferometry for surface waves. When integration is carried out in both the in-line and cross-line direction (i.e., when a homogeneous distribution of surface sources is used) a good estimate of the correct inter-receiver surface wave is recovered (both higher modes, and the correct geometrical spreading factors are recovered). This result was derived by Snieder (2004a, eq. 24), but here we also show that relative amplitudes of different surface-wave modes may not be correctly recovered due to the presence of modal- and frequency-dependent scale factors, related to the boundary source types used. When integration is only carried out in the in-line direction the geometrical spreading factor is not recovered, and the higher frequency part of the surface wave may be more dominant. Despite this the higher-mode surface waves can still be recovered, for example in Chapter 3 the recovery of both fundamental- and higher-mode surface waves was illustrated using a real data example. When only orthogonal source geometries are available spurious events are introduced due to the cross-correlation of different higher-mode surface waves. These errors are reduced when several orthogonal source lines are used due to the non-stationary phase of the error across different source boundary locations.

In passive surface-wave interferometry, the best surface wave estimates occur for receiver pairs whose inter-receiver azimuths are orthogonal to noise generating coast lines (Gertstoft *et al.*, 2006). Further research is required in such settings to determine the effect of the spurious events and whether or not the higher-modes can be recovered. The fundamental mode is often the dominant arrival, and in applications of interferometry this mode is efficiently extracted (e.g., Shapiro *et al.*, 2005; Gertstoft *et al.*, 2006). Nevertheless if multiple modes can be successfully recovered then it may be possible to use these to improve the estimates of shear-wave velocity structure (e.g., MacBeth and Burton, 1985; Dost, 1990; Trampert and Woodhouse, 1995; Yoshizawa and Kennet, 2004).

In exploration seismology orthogonal source and receiver lines are often used (Vermeer, 2002). High-frequency surface waves (on the order of tens of Hz) sample the very near-surface of the Earth (tens to hundreds of metres), often exhibiting higher-mode surface waves (e.g., Al-Husseini *et al.*, 1981; Chapter 3). Hence the errors illustrated above may have a more significant impact in exploration than in earthquake seismology. This also applies to engineering settings where high-frequency, higher-mode surface waves are used to invert for shear-wave velocity profiles, providing extra information that cannot be extracted from the fundamental mode alone (e.g., Xia *et al.*, 2000; Beaty *et al.*, 2002).

Due to these cross-mode errors pre-processing may be required to recover higher-mode surface waves successfully with only surface sources. Such pre-processing may be easier to apply in exploration or engineering seismology with well sampled receiver arrays allowing for separation of modes, for example in the frequency-wavenumber domain (e.g., Vermeer, 2002). In earthquake seismology, mode separation can be attempted using band-pass filters (e.g., Crampin and Bath, 1965), phase-matched filtering (e.g., Hwang and Mitchell, 1986) but detailed analysis and isolation of higher-mode Rayleigh waves typically requires array measurements (e.g., Nolet, 1975; Nolet and Panza, 1976; Cara, 1978; Mitchel, 1980), although single-station methods do exist (e.g., van Heijst and Woodhouse, 1997). Densely sampled arrays are seldom available, and hence it may be more difficult to identify and separate all higher-mode surface waves.

4.5 Conclusions

We have investigated seismic interferometry for surface waves using Green's functions terms for surface waves in laterally homogeneous media. This analysis has revealed that there are two key components to the application of full and exact interferometry:

1. Integration over a fully enclosing boundary allows for the cancellation of cross-mode terms by the Rayleigh-wave orthogonality relationship.

2. Integration in the cross-line direction allows for the retrieval of the correct spreading terms in the surface-wave Green's functions (a result previously derived by Snieder (2004a, eq. 24)).

Both of these components play an important role in recovering the correct relative amplitudes for different surface-wave modes. Using only a single source type provides similar results, with the introduction of a frequency- and modal-dependent scaling term that varies depending on source geometries. When sources are not present in the subsurface further scaling terms may emerge, cross-mode terms may not cancel, and spurious events can be introduced when attempting to recover higher-mode surface waves.

The insight provided by this analysis allows the effect of surface-source distribution to be considered when designing surveys and experiments and interpreting results of interferometry in future:

1. By integrating across the surface of the Earth (i.e., integration in both the *x*- and *y*-direction) the correct geometrical spreading term is recovered and the effect of cross-mode correlation is cancelled.
2. Integration along a line perpendicular to the inter-receiver line allows for the recovery of approximate geometrical spreading terms. However, unless only a single surface-wave mode is present (or a single mode is dominant) spurious events are introduced due to un-cancelled cross-mode correlations.
3. Integration along an extension of the receiver line gives incorrect spreading terms, and introduces a phase shift of $\pi/4$. While this phase error does not matter when we wish to measure group velocities, if unaccounted for it can introduce errors when measuring phase velocities. Our examples illustrate a dominance of higher frequencies, suggesting that the variation of scale factors in this case may be more extreme. One benefit of this source distribution is that it is not affected by the strong spurious events observed when using orthogonal source distributions.

We have illustrated our findings using synthetic Rayleigh-wave Green's functions, showing the problems surrounding the recovery of higher-mode surface waves for various source geometries. We propose that by using a modal-separation pre-processing step, the results of surface-wave interferometry can be improved to allow for the recovery of multi-mode surface waves.

These observations have implications in exploration seismology, where inter-receiver surface waves can be estimated by interferometry and removed from source-receiver data. There are also implications for earthquake seismology where inter-station surface waves are estimated using passive-seismic interferometry, and in engineering geophysics where both the active and passive method may be applied - successful recovery of higher-mode surface waves can allow for the extraction of more detailed subsurface velocity structure.

Finally, since it is possible to represent the full elastic response of a layered medium using a modal summation, these results could be extended to study the role of surface-source distribution in interferometry for body waves, or to study the effect of body waves in interferometry for surface waves. However, both of these topics require further research.

5. A generalized optical theorem for surface waves and layered media

In this chapter we present a generalized optical theorem for surface waves. The theorem also applies to body waves since under many circumstances body waves can be written in terms of surface-wave modal summations. This new theorem therefore extends the domain of applicability of the optical theorem from homogeneous background media to a general class of body and surface-wave propagation regimes within layered, elastic media.

5.1 Introduction

The optical theorem uses the conservation of energy to relate the energy radiated from a scattering body to the amplitude decay of the wave that was incident upon the scatterer (e.g., due to backscattering). For homogeneous background media it is possible to formulate a generalized optical theorem that correctly describes the conservation of energy in a general class of scattering problems (for both acoustic and elastic waves). A similar generalized optical theorem that accounts for the scattering of multi-mode surface waves would extend the applicability of the optical theorem to account for vertical heterogeneity in the background medium. In this chapter we derive such an optical theorem.

By a generalized optical theorem we refer to an optical theorem which gives an integral condition on the scattering amplitude for any specific angle of incidence and any scattering angle. From this generalized optical theorem, other relationships can then be derived which describe scattering relationships for more specific forms of scattering. The generalized optical theorem for acoustic waves has been derived in different ways by many authors. For example, Newton (1976) gives an account of Heisenberg's use of the unitarity properties of the scattering matrix in order to derive the generalized optical theorem. Glauber and Schomaker (1953) use reciprocity relations to show the reversibility of scattering between any pair of directions and

further to derive the generalized optical theorem. They then derive more specific optical theorems for forward scattering (when the angle of incidence equals the scattering angle) and for scattering with inversion symmetry. Marston (2001) uses a similar approach using symmetry, reciprocity and energy conservation to derive the same result for acoustic scattering with inversion symmetry. Representation theorems (or reciprocity relations) have also been used extensively to study energy relations in scattering problems (Tan, 1977; de Hoop, 1985, 1995), and Snieder *et al.* (2008) present an alternative derivation of the generalized optical theorem using an approach based on the use of interferometric Green's function representations, specific forms of representation theorems (Wapenaar and Fokkema, 2006; Wapenaar, 2007). Further, Budreck and Rose (1992) have derived a generalized optical theorem for elastodynamics using elastodynamic scattering theory and a Newton-Marchenko equation.

Optical theorems find a wide range of applications in physics including testing of algorithms for the computation of scattered wavefields (Chinnery *et al.*, 1997; Burnett and Holford, 1998), the estimation of backscattering from measurements of the scattered wavefield taken at other angles (Marston, 2001), determining phase shifts from the measurement of scattering data (e.g., in quantum mechanics (Newton, 1968; Chadan and Sabatier, 1989)), the investigation of the attenuation effect of scatterers (e.g., in acoustics (Groenenboom and Snieder, 1995), and in seismology (Snieder, 1988; Brandenburg and Snieder, 1989)), the determination of the energy both scattered and absorbed by a scatterer (in acoustics (de Hoop, 1985)), and by using a statistical approach it may be possible to infer the structure of the scattering media (Carney and Wolf, 1997).

In this chapter we derive a generalized optical theorem for surface waves. The benefit of such a theorem over and above body-wave optical theorems is that surface wave theory allows us to consider vector wavefields and multiple surface-wave modes (Snieder, 1986, 2002b). In seismology a surface wave mode refers to a wave that propagates laterally across the surface of the Earth and exists due to the presence of the free surface. In a homogeneous half space only one mode exists (the fundamental Rayleigh mode). However, if the medium of interest is vertically heterogeneous then so-called higher-mode Rayleigh waves (and fundamental and

higher-mode Love waves) exist, all propagating with different, frequency-dependent phase velocities (Aki and Richards, 2002). Therefore the generalized optical theorem for surface waves derived here enables the range of applications of the generalized optical theorem to be extended to cases where surface waves are produced, or where media may be represented as layered. This includes seismology (Snieder, 2002b), quantum physics (Stenflo and Yu, 2002), acousto-electrics (Wixforth *et al.*, 1986) and materials science (Steg and Klemens, 1974). Since body waves can also be represented by a sum over many surface-wave modes (Haddon, 1986; Nolet *et al.*, 1989), the optical theorem for surface waves extends to a general class of body and surface wave propagation regimes within layered, elastic media.

We derive the new optical theorem by considering interferometric Green's function representations for elastic media, and using appropriate scattered surface wave Green's functions. In places our approach mirrors that of Snieder *et al.* (2008). However, while those authors consider scalar acoustic wavefields propagating in homogeneous media, our approach uses surface-wave Green's functions for wave propagation in elastic media. Hence, we derive the first such theorem for vector wavefields in layered elastic media.

We first define an appropriate interferometric Green's function representation: such representations relate the Green's functions between two-points within a bounding surface to the Green's functions between the bounding surface and each of the two points (van Manen *et al.*, 2005; van Manen *et al.*, 2006; Wapenaar and Fokkema, 2006). Second, we define appropriate Green's functions to describe a single-scattered surface-wave field, and insert those into the interferometric representation. This results in four different contributing terms that can be analysed using a stationary phase approach (where we assume that the dominant contribution of each integral term comes from the point on the integration surface at which the phase of the integrand is stationary). We find that in order for the interferometric representation to hold, two sets of non-physical terms must cancel; this condition results in a generalized optical theorem for surface waves. While we consider only Rayleigh surface waves, an identical analysis exists for Love waves.

5.2 Green's functions for surface wave propagation

Interferometric Green's function representations can be derived from representation theorems by using appropriate mathematical representations of Green's functions between two locations ($\mathbf{r}_A$ and $\mathbf{r}_B$), and between each of those locations and all points on a bounding surface S (Figure 4.1). S may be arbitrarily shaped, but in the following we consider the specific case of a cylinder extending to great depth. In this chapter we use semi-analytical representations of particle-displacement surface-wave Green's functions; hence we consider the application of Equation (4.1).

In order to solve Equation (4.1) for scattered surface waves we require an appropriate coordinate system and appropriate forms for the Green's functions. To solve the interferometric integral we use a cylindrical co-ordinate system with the scatterer placed at radius equal to zero, and define the locations $\mathbf{r}_A$, $\mathbf{r}_B$, $\mathbf{r}_S$ and $\mathbf{r}_0$ as (Figure 5.1):

$$\mathbf{r}_A = \begin{pmatrix} X_{A0}\cos(\varphi_{A0}+\pi) \\ X_{A0}\sin(\varphi_{A0}+\pi) \\ z_A \end{pmatrix},\ \mathbf{r}_B = \begin{pmatrix} X_{0B}\cos\varphi_{0B} \\ X_{0B}\sin\varphi_{0B} \\ z_B \end{pmatrix},\ \mathbf{r}_S = \begin{pmatrix} X_{S0}\cos(\varphi_{S0}+\pi) \\ X_{S0}\sin(\varphi_{S0}+\pi) \\ z_S \end{pmatrix},\ \mathbf{r}_0 = \begin{pmatrix} 0 \\ 0 \\ z_0 \end{pmatrix}. \quad (5.1)$$

In the Green's functions that we introduce in Appendix 5A, the terms such as X_{A0} and φ_{A0} describe the propagation path of the surface wave. The order of the subscripts identifies the direction of propagation, for example $A0$ denotes that these parameters describe the wave propagating from $\mathbf{r}_A$ to $\mathbf{r}_0$. For consistency we have defined the vectors (5.1) using the same notation as Appendix 5A. The cylindrical co-ordinate system is centred on the scatterer and this requires that for the angles describing propagation *towards* the scatterer we must add a factor π since all vectors are defined pointing *away* from the scatterer.

In our analysis we assume a single incident surface wave mode (ν) and a single scattered surface wave mode (σ); to simplify the notation we define a partial Green's function (herein referred to as *the* Green's function) representing the combination of these two modes. To represent a *full* Green's function we would

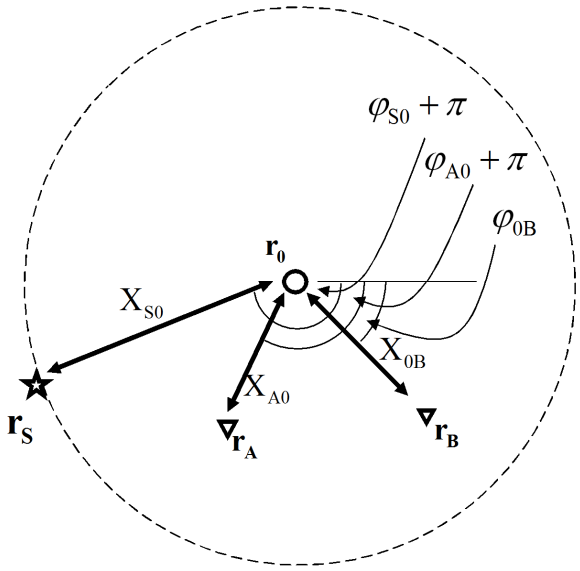

Figure 5.1: Sketch illustrating the geometry in the horizontal plane that is used in the stationary phase analysis. The scatterer $\mathbf{r}_0$ is placed at the centre of the co-ordinate system (r = 0).

require a sum over all partial Green's functions, hence over all incoming and outgoing modes.

The Green's function representing the particle displacement due to a point force is the sum of the incident and scattered wavefields. For notational convenience we drop superscripts $\sigma\nu$ as follows:

$$G_{im}^{\sigma\nu}(\mathbf{r}_B,\mathbf{r}_A) = G_{im}^{0}(\mathbf{r}_B,\mathbf{r}_A) + G_{im}^{sc}(\mathbf{r}_B,\mathbf{r}_A), \tag{5.2}$$

and the equivalent particle-displacement deformation-rate Green's function is

$$n_j c_{njkm} \partial_k G_{im}^{\sigma\nu}(\mathbf{r}_B,\mathbf{r}_A) = \partial G_{im}^{0}(\mathbf{r}_B,\mathbf{r}_A) + \partial G_{im}^{sc}(\mathbf{r}_B,\mathbf{r}_A), \tag{5.3}$$

where $G_{im}^{0}(\mathbf{r}_B,\mathbf{r}_A)$ and $\partial G_{im}^{0}(\mathbf{r}_B,\mathbf{r}_A)$ represent the direct waves observed at $\mathbf{r}_B$ due to a uni-directional point force at $\mathbf{r}_A$ and a deformation rate tensor source at $\mathbf{r}_A$, respectively, and $G_{im}^{sc}(\mathbf{r}_B,\mathbf{r}_A)$ and $\partial G_{im}^{sc}(\mathbf{r}_B,\mathbf{r}_A)$ are the corresponding terms for the

scattered wavefield. These terms are defined in detail in Appendix 5A, with appropriate geometrical variables illustrated in Figure 4.2 and Figure 5.2.

5.4 Solution of the interferometric representation

For Equations (5.2) and (5.3) to solve the interferometric representation successfully we require that when the right hand side of Equation (4.1) is evaluated using the Green's functions (5.2) and (5.3) we obtain Green's function of the same form (as defined by the left hand side of Equation (4.1)).

To evaluate the right hand side we must solve the integral over the surface *S* (Figure 4.1). To do so we use the method of stationary phase. This method has been shown to be a valuable tool to analyse and understand the application of seismic interferometry in various settings (Snieder, 2004a; Snieder *et al.*, 2006; Chapter 4). With a stationary-phase analysis we make a high-frequency approximation and assume that the dominant contributions to the interferometric integral come from those points at which the phase of the integrand is stationary (Snieder, 2004b). We further assume that the amplitude of the integrand varies slowly around these stationary points.

To solve the interferometric integral we substitute Green's functions (5.2) and (5.3) into Equation (4.1) resulting in four terms: the cross-correlation of the direct Rayleigh wave at one receiver with the direct Rayleigh wave at the other (*T1*), the cross-correlation of the direct Rayleigh wave at one receiver with the scattered surface wave at the other (and vice versa, *T2* and *T3*), and the cross-correlation of the scattered surface wave at one receiver with the scattered surface wave at the other (*T4*). We label our terms T1 to T4 to keep our notation consistent with previous work in seismology (Snieder *et al.*, 2006) and in acoustics (Snieder *et al.*, 2008). In Appendix 5A we analyse each of these terms (for isotropic elastic media) using a stationary- phase analysis and find that each term contributes as follows:

T1: The stationary-phase analysis of this term is identical to that presented in Chapter 4. This results in the part of the Green's function corresponding to the direct

surface wave (i.e., the wavefield in the layered background medium). We can therefore write term *T1* as:

$$T1 = G_{im}^{0\,*}(\mathbf{r}_B, \mathbf{r}_A) - G_{im}^{0}(\mathbf{r}_B, \mathbf{r}_A). \tag{5.4}$$

***T2* and *T3*:** In appendix 5A we show that the stationary phase analysis naturally divides these two terms into four separate sub-terms (the geometries for the stationary phase analysis are illustrated in Figure A5.1). Each of terms *T2* and *T3* contribute a first sub-term that corresponds to part of the Green's function in Equation (5.2). We refer to this contribution as the physical contribution (indicated by a subscript *p*, with geometries illustrated in Figure a and c):

$$T2_p + T3_p = G_{im}^{sc\,*}(\mathbf{r}_B, \mathbf{r}_A) - G_{im}^{sc}(\mathbf{r}_B, \mathbf{r}_A). \tag{5.5}$$

Hence, the correct (physical) scattered surface waves are recovered from terms *T2*, and *T3*. However, we find that the second sub-terms of each of *T2* and *T3* do not correspond to any part of the true Green's function (5.2) that we expect from the left hand side of Equation (4.1). We use subscript *np* to indicate that this is a non-physical term and geometries are illustrated in Figure b and d (note for the rest of this chapter, Einstein's summation convention for repeat indices *does not* apply):

$$T2_{np} + T3_{np} = -\frac{2}{\pi} \mathrm{A}^{\sigma\nu} \left[S_{im}^{\sigma\nu}(\hat{\mathbf{r}}_B, \hat{\mathbf{r}}_A) - S_{im}^{\sigma\nu\,*}(\hat{\mathbf{r}}_B, \hat{\mathbf{r}}_A) \right]. \tag{5.6}$$

In Equation (5.6), $\mathrm{A}^{\sigma\nu}$ represents the propagation characteristics of the incident and scattered waves (i.e., the phase, wavenumber, and geometrical spreading) between the excitation and observation point respectively. $S_{im}^{\sigma\nu}(\hat{\mathbf{r}}_B, \hat{\mathbf{r}}_A)$ is the 3-D surface wave scattering matrix for an incident surface wave mode ν, travelling in the direction of the unit vector $\hat{\mathbf{r}}_A$, that is scattered in the direction of the unit vector $\hat{\mathbf{r}}_B$ as surface wave mode σ, where it is understood that $\hat{\mathbf{r}}_A$ and $\hat{\mathbf{r}}_B$ are the horizontal

components of the unit vectors. We refer to $S_{im}^{\sigma\nu}(\hat{\mathbf{r}}_B, \hat{\mathbf{r}}_A)$ as the 3-D scattering matrix as it includes polarization terms for the excitation of the incident wavefield and for the observed scattered wavefield, i.e.,

$$S_{im}^{\sigma\nu}(\hat{\mathbf{r}}_B, \hat{\mathbf{r}}_A) = P_{im}^{\sigma\nu}(\hat{\mathbf{r}}_B, \hat{\mathbf{r}}_A) f^{\sigma\nu}(\hat{\mathbf{r}}_B, \hat{\mathbf{r}}_A), \tag{5.7}$$

where $P_{im}^{\sigma\nu}(\hat{\mathbf{r}}_B, \hat{\mathbf{r}}_A)$ is the product of the polarization terms of the excited wavefield (a point-force in the *m*-direction exciting mode ν) and the observed wavefield (the *i*-component of particle displacement of the scattered mode σ), and $f^{\sigma\nu}(\hat{\mathbf{r}}_B, \hat{\mathbf{r}}_A)$ is the surface wave scattering matrix for an incident surface wave mode ν travelling in the direction of unit vector $\hat{\mathbf{r}}_A$, scattered in the direction of unit vector $\hat{\mathbf{r}}_B$ as surface wave mode σ. Since the polarization terms are dependent on the depth of excitation and observation, the scattering term $S_{im}^{\sigma\nu}$ is dependent on the depths of the scatterer and the points of excitation and observation.

T4: Term *T4* is the cross-correlation of the scattered surface waves recorded at both receivers. In Appendix 5A we show that this can be written as,

$$T4 = -\frac{2i}{\pi^2} A^{\sigma\sigma} \int_0^{2\pi} \left[\frac{1}{P_{im}^{\nu\nu}(\hat{\mathbf{r}}_B, \hat{\mathbf{r}}_A)} S_{im}^{\sigma\nu}(\hat{\mathbf{r}}_B, -\hat{\mathbf{r}}_S) S_{im}^{\sigma\nu *}(\hat{\mathbf{r}}_A, -\hat{\mathbf{r}}_S) \right] d\Omega, \tag{5.8}$$

where $P_{im}^{\nu\nu}(\hat{\mathbf{r}}_B, \hat{\mathbf{r}}_A)$ is the product of the polarization terms of the surface wave mode ν travelling in the direction of the horizontal unit vectors $\hat{\mathbf{r}}_A$ and $\hat{\mathbf{r}}_B$, and $A^{\sigma\sigma}$ accounts for the propagation characteristics of the scattered waves observed at $\mathbf{r}_A$ and $\mathbf{r}_B$. The integration is over the azimuth of the incident wave upon the scatterer (i.e., over $-\hat{\mathbf{r}}_S$). The term $1/P_{im}^{\nu\nu}$ cancels the excitation terms for the incident wavefield that appear in the product $S_{im}^{\sigma\nu} S_{im}^{\sigma\nu *}$, hence the depths of the sources exciting the incident wavefields do not have an effect on Expression (5.8).

5.5 A generalized optical theorem for surface waves

We have already shown that the correct direct and scattered surface waves are recovered from terms *T1, T2*$_p$, and *T3*$_p$. Note that from Equations (5.4) and (5.5) we can write,

$$T1+T2_p+T3_p=\left[G_{im}^{0*}(\mathbf{r}_B,\mathbf{r}_A)+G_{im}^{sc*}(\mathbf{r}_B,\mathbf{r}_A)\right]-\left[G_{im}^{0}(\mathbf{r}_B,\mathbf{r}_A)+G_{im}^{sc}(\mathbf{r}_B,\mathbf{r}_A)\right], \qquad (5.9)$$

$$=G_{im}^{*}(\mathbf{r}_B,\mathbf{r}_A)-G_{im}(\mathbf{r}_B,\mathbf{r}_A)\,. \qquad (5.10)$$

Thus, the combination of these terms satisfies the left hand side of Equation (4.1). However, since Equation (4.1) is exact, the non-physical arrivals introduced by terms $T2_{np}$, $T3_{np}$, and *T4* must cancel. We therefore require that $T2_{np}+T3_{np}+T4=0$, which on expansion becomes,

$$\frac{2}{\pi}\mathrm{A}^{\sigma\nu}\left[S_{im}^{\sigma\nu}(\hat{\mathbf{r}}_B,\hat{\mathbf{r}}_A)-S_{im}^{\sigma\nu^*}(\hat{\mathbf{r}}_B,\hat{\mathbf{r}}_A)\right]=$$

$$\frac{2}{i\pi^2}A^{\sigma\sigma}\int_0^{2\pi}\left[\frac{1}{P_{im}^{\nu\nu}(\hat{\mathbf{r}}_B,\hat{\mathbf{r}}_A)}S_{im}^{\sigma\nu}(\hat{\mathbf{r}}_B,-\hat{\mathbf{r}}_S)S_{im}^{\sigma\nu^*}(\hat{\mathbf{r}}_A,-\hat{\mathbf{r}}_S)\right]d\Omega\,. \qquad (5.11)$$

Equation (5.11) can then be written in the form:

$$S_{im}^{\sigma\nu}(\hat{\mathbf{r}}_B,\hat{\mathbf{r}}_A)-S_{im}^{\sigma\nu^*}(\hat{\mathbf{r}}_B,\hat{\mathbf{r}}_A)=$$

$$\frac{\mathrm{D}^{\sigma\nu}}{i\pi}\int_0^{2\pi}\left[\frac{1}{P_{im}^{\nu\nu}(\hat{\mathbf{r}}_B,\hat{\mathbf{r}}_A)}S_{im}^{\sigma\nu}(\hat{\mathbf{r}}_B,-\hat{\mathbf{r}}_S)S_{im}^{\sigma\nu^*}(\hat{\mathbf{r}}_A,-\hat{\mathbf{r}}_S)\right]d\Omega\,. \qquad (5.12)$$

This is recognisable as a surface wave equivalent to the generalized optical theorem. This describes the relationship between any incident surface wave mode ν excited by any point-force component *m* and any scattered surface wave mode σ observed as any particle-displacement component *i*. It has a slightly more complicated form in layered media due to the presence of multiple modes: the term $\mathrm{D}^{\sigma\nu}$ contains ratios of the phase and wavenumber of each of the modes σ and ν (i.e., it accounts for the

fact that each mode has different propagation characteristics), and the term $P_{im}^{\nu\nu}(\hat{\mathbf{r}}_B, \hat{\mathbf{r}}_A)$ removes the polarization terms of the incident wavefields from the scattering terms $S_{im}^{\sigma\nu}(\hat{\mathbf{r}}_B, -\hat{\mathbf{r}}_S)$ and $S_{im}^{\sigma\nu^*}(\hat{\mathbf{r}}_A, -\hat{\mathbf{r}}_S)$.

Note that in the case of a homogeneous half-space $\mathrm{D}^{\sigma\nu} = 1$ (i.e., only one surface wave mode is present). If we assume that the outgoing mode is observed with the same component as that with which the incoming mode was excited (i.e., $i = m$) then the polarization terms of the excited and observed wavefields, implicit in $S_{im}^{\sigma\nu}$, cancel. This allows us to use only the scattering matrix f and the reversibility of the scattering matrix to find,

$$f^{\sigma\nu}(\hat{\mathbf{r}}_B, \hat{\mathbf{r}}_A) - f^{\sigma\nu^*}(\hat{\mathbf{r}}_A, \hat{\mathbf{r}}_B) = \frac{1}{i\pi} \int_0^{2\pi} f^{\sigma\nu}(\hat{\mathbf{r}}_B, -\hat{\mathbf{r}}_S)\, f^{\nu\sigma^*}(\hat{\mathbf{r}}_A, -\hat{\mathbf{r}}_S)\, d\Omega, \qquad (5.13)$$

which resembles the previously derived generalized optical theorem.

5.6 Conclusions

We have derived a generalized optical theorem for surface waves using an interferometric Green's function representation and semi-analytical Green's functions for scattered surface waves. This analysis accounts for the scattering of higher-mode surface waves, and while our analysis uses Rayleigh-wave Green's functions the results are equally applicable to Love-wave modes. Also note, that while we consider isotropic elastic media it may be possible to use adaptations of surface-wave theory to derive a similar relation for anisotropic media. See, for example the discussion on surface-wave propagation in anisotropic layered media presented by Aki and Richards (2002, Chapter 7).

The ability to account for higher-mode surface waves means that this theorem can be applied to surface waves propagating in layered media, as this layering is manifest in the presence of such higher-mode surface waves. It has also been shown in previous studies that it is possible to represent a body wavefield as a sum over surface-wave modes using Green's functions such as those used here. For example,

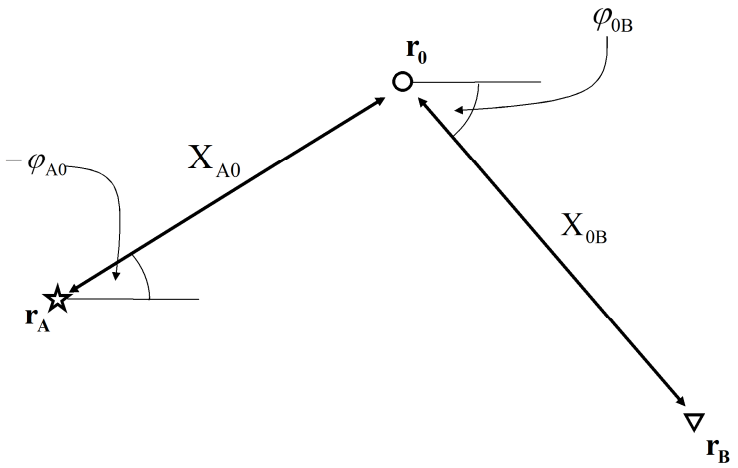

Figure 5.2: Geometric variables used to describe the scattered surface wave propagating between $\mathbf{r}_A$ and $\mathbf{r}_B$.

in a seismological study Nolet *et al.* (1989) use a locked-mode approximation (the introduction of a total-internal reflector at some depth) to model the full wavefield using surface-wave Green's functions for vertically heterogeneous media. This approximation essentially turns the problem into one of elastic wave-propagation in a closed, layered medium. Hence the optical theorem derived here not only applies to surface waves in layered elastic half-spaces, but also to surface *and* body waves in closed, layered elastic media. Note also that modal summations can be used to model the exact wavefield in an open, layered elastic half-space using so-called leaky modes (Haddon, 1986). Hence, the new theorem can be applied to a general class of body and surface wave propagation regimes within layered, elastic media.

This generalized optical theorem for surface waves complements previous derivations of the generalized optical theorem for homogeneous background media (Glauber and Schomaker, 1953; Newton, 1976; Marston, 2001; Snieder *et al.*, 2008), and previous work considering the role of (more specific versions of) the optical theorem on the attenuation of surface waves due to scattering (Snieder, 1988; Brandenburg and Snieder, 1989). The generalized optical theorem for surface waves that we derive here may allow the range of applications of the generalized optical theorem to be extended to those areas of physics where surface waves are observed, including quantum physics (Stenflo and Yu, 2002), material physics (Steg and

Klemens, 1974), seismology (Snieder, 2002b) and acousto-electrics (Wixforth *et al.*, 1986) .

Finally, using the above method of derivation it may be possible to obtain similar relationships for other modes of energy propagation or for different source and receiver quantities. For example, Wapenaar *et al.* (2006) and Snieder *et al.* (2007) derive generalized interferometric relations that include (amongst others) seismo-electric, electro-kinetic, electromagnetic and diffusion-phenomena Green's functions. With appropriate representations of these Green's functions an interferometric approach may allow for the derivation of similar optical theorem-type relationships for these other domains of energy propagation.

6. Seismic interferometry of scattered surface waves in attenuative media

In this chapter we study seismic interferometry for scattered surface waves using the stationary-phase analysis and surface-wave Green's functions for isotropic point scatterers embedded in laterally-homogeneous media used in Chapter 5. The analysis reveals key differences between the interferometric construction of reflected and point-scattered body or surface waves, since point scatterers radiate energy in all directions but a reflection from a finite flat reflector is specular. In the case of surface waves we find that additional cancelling terms are introduced in the stationary-phase analysis for scattered waves related to the constraint imposed by the optical theorem for surface waves. The additional terms are of second order even for single-scattered waves, and we show that these can be highly significant in multiple-scattering cases. In attenuative media errors are introduced due to amplitude errors in these additional terms. Further, we find that as the distribution of scatterers in a medium becomes more complex the errors in correlation-type interferometry caused by attenuation in the background medium become larger. Convolution-type interferometry has been shown to be effective when considering electromagnetic wavefields in lossy media and we show that this is also true for scattered surface waves in attenuating elastic media. By adapting our stationary-phase approach to this case we reveal why convolution-type interferometry performs well in such media: the second-order cancelling terms that appear in the correlation-type approach do not appear in convolution-type interferometry. Finally we find that when using both correlation- and convolution-type interferometry with realistic source geometries (illustrative of both industrial seismics and "passive noise" interferometry), we cannot necessarily expect to produce estimates with all dominant scattering events present. This is shown to be especially important if, as proposed previously for electromagnetic applications, the convolution

and correlation approaches are compared to help identify errors in the interferometric estimates.

6.1 Introduction

The ability to create estimates of inter-receiver surface waves by seismic interferometry is of great interest to seismologists: since passive-noise sources tend to occur near the Earth's surface, inter-receiver surface wave estimates can be constructed from noise recordings and can be used to create velocity maps or profiles in global or regional seismology (Shapiro and Campillo, 2004; Shapiro *et al.*, 2005; Gertstoft *et al.*, 2006; Moschetti *et al.*, 2007; Yang *et al.*, 2007). Such studies focus on group-velocity travel-time tomography and extract only fundamental-mode surface-wave information since this mode is synthesized relatively easily using background noise. However, in Chapter 4 by analysing the errors that occur specifically when attempting to extract higher-mode surface wave information from interferometry using only near-surface sources a method was proposed to measure inter-receiver, direct, higher-mode surface waves robustly.

Actively induced source signals can also be cross-correlated to synthesise inter-receiver surface wave estimates: for example, in Chapter 3 it was demonstrated that it is possible to recover higher-mode inter-receiver surface waves using specific geometries as predicted in Chapter 4. In Curtis *et al*. (2006), Dong *et al*. (2006) and Chapter 2 it was proposed that similar inter-receiver surface wave estimates can be used as part of a ground-roll (surface-wave) removal method in exploration seismology.

In addition to direct, inter-receiver surface waves, in many cases it may be desirable to recover scattered surface waves using interferometry, since these contain additional information about near-surface heterogeneities (Snieder, 1986; Snieder and Nolet, 1987; Levander, 1990). In Rayleigh-wave tomography it is important to consider scattering effects when significant heterogeneities exist on length scales comparable to the wavelength of seismic waves or to the width of Fresnel zones, as ray theory tends to break down in such circumstances (e.g., Spetzler and Snieder, 2001). This has prompted many different (non-interferometric) studies of surface

wave scattering. For example, Snieder (1986), and Snieder and Nolet (1987) developed a theoretical framework for analysing scattered surface waves, and employed the Born (single-scattering) approximation to construct an inversion scheme that identified strong crustal-scale surface wave scatterers such as mountain roots. Further single-scattering methods are proposed by Meier *et al.* (1997), Marquering *et al.* (1999), Spetzler *et al.* (2002) and Ritzwoller *et al.* (2002). When compared with ray-theoretical approaches, these methods often find significant differences in imaged features. For example, Ritzwoller *et al.* (2002) find that by using a single-scattering approach (so-called diffraction tomography) larger velocity anomalies and deeper mantle features can be identified. Thus, if scattered surface waves can be recovered by seismic interferometry, the power and applicability of the method to crustal seismology may be greatly increased.

Scattered surface waves are also observed in higher-frequency near-surface settings. For example, in engineering seismology higher-frequency scattered surface waves can be used to image the near-surface properties of the Earth (e.g. Herman *et al.*, 2000; Campman and Riyanti, 2007; Kaslilar, 2007). Further, in Chapter 1 we discussed the interest in high-frequency scattered surface waves in exploration seismology, and the potential for interferometry to predict and subtract those waves.

From this wide range of applications it is clear that the recovery of scattered surface waves using interferometry could be of great benefit to a range of methods in seismology. Scattered surface waves have been recovered in ultrasonic lab experiments, for example Malcolm *et al.* (2004) recover estimates of the Rayleigh-wave Green's function in a strongly scattering diffusive regime. However, a successful application for seismic scattered surface waves has yet to be published. There are several possible reasons for this, including poor source coverage, the weak strength of scattered waves relative to errors in the interferometric estimates, or it could simply be that these arrivals are not being sought – without arrays of seismometers it is difficult to identify fundamental, higher-mode and scattered surface waves unambiguously.

In order for correlation-type interferometry to produce exact, inter-receiver Green's functions, there are a number of conditions that must be met, including that the medium is non-attenuating, and that there exists a closed boundary of

'background' noise sources of both the uni-directional point force, and deformation-rate-tensor types (Wapenaar, 2004; van Manen *et al.*, 2005; van Manen *et al.*, 2006; Wapenaar and Fokkema, 2006). However, note first that in reality the near surface often exhibits very strong attenuation, and second that it is by relaxing the conditions on boundary sources that we observe a dominance of surface waves (Shapiro *et al.*, 2005; Chapter 2). Hence, in order to apply interferometry to scattered surface waves successfully, we must first understand characteristics of the method in non-ideal circumstances.

In exploration applications, similar relaxation of these conditions are forced upon us. For example, sources are often restricted to the surface of the earth and only vertical point-force sources may be available. Nevertheless in certain cases there are methods with which resulting errors in the interferometric results can be suppressed. For example, in the virtual-source method of Bakulin and Calvert (2004; 2006), the stationary-phase work of Snieder *et al.* (2006) illustrates a source of spurious arrivals (any non-physical arrival in the interferometric estimates that does not correspond to an actual inter-receiver event) in the simple case of a two half-space model, and Mehta *et al.* (2007) use wavefield separation to suppress the effect of spurious arrivals.

In Chapter 4 a similar stationary phase approach to Snieder (2004a; 2004b) and Snieder *et al.* (2006) was used to investigate the effects of relaxing conditions on the surrounding boundary for the case of direct, multi-mode surface waves, illustrating the effectiveness of various depleted background noise-source geometries, and the errors that occur in such cases in the presence of higher-mode direct surface waves. In Chapter 5 this approach was extended for scattered surface waves to derive a generalized optical theorem for surface waves.

In this chapter a stationary-phase evaluation reveals the steps involved in interferometric estimation of scattered surface waves. We find that there are key differences between the stationary-phase analysis of interferometry for reflected and scattered waves that are accounted for by considering second order terms in the interferometric integral, even for single-scattered waves. This suggests that a first order Born-approximation is not suitable to analyse the effect of interferometry on scattered waves (and since our approach can be applied to general scattering of

waves this observation applies not only to surface waves but to different wave types, e.g., see Snieder *et al*. (2008)).

We find that errors in the cross-correlation approach are sensitive to attenuation and limited aperture. Convolution-type interferometry is an adaptation of interferometric theory that allows for the presence of attenuation (Slob *et al.*, 2007; Slob and Wapenaar, 2007). By adapting our stationary-phase approach for the convolution case we identify why interferometry performs better in that case: mutually cancelling terms identified in the correlation approach do not exist in convolution-type interferometry. In addition to the expected improvements in the presence of attenuation, this also suggests that convolution-type interferometry is less sensitive to non-physical arrivals introduced by limited aperture (e.g., an incomplete boundary of sources, or boundary sources of significantly diminished magnitude over some set of locations). Slob *et al.* (2007) propose combining correlation- and convolution-type interferometry to identify non-physical errors in electromagnetic wavefield estimates, and likewise we may consider a similar approach in the scattered surface wave case. However by considering realistic geometries we find that certain geometries may not produce estimates containing all dominant scattered surface waves in either or both cases. Hence, if we wish to use a combined approach we must be careful as scattered surface waves could be incorrectly identified as spurious arrivals. Results and discussions are illustrated throughout using semi-analytical, scattered surface-wave examples.

We first discuss stationary points on a closed boundary of 'background' noise sources for the interferometric synthesis of scattered surface waves, explaining how interferometry works for scattered surface waves (leaving mathematical derivations to appendices). We then investigate the effect of attenuation on the recovery of scattered surface waves, showing how spurious arrivals are introduced in this case. By using an adaptation of the convolution approach of Slob *et al.* (2007) and Slob and Wapenaar (2007) for elastic surface waves, we adapt our stationary-phase analysis to identify why scattered surface waves are better estimated using this approach (note that Wapenaar (2007) also derives convolution-type interferometric relationships for the general case of diffusion, flow, and wave phenomena). Finally, we combine the effects of realistic source geometries with the use of only point-force

sources in an attenuating medium, illustrating the sensitivities of the two approaches to non-physical arrivals introduced by attenuation and limited aperture.

In Appendix 6A we extend the stationary-phase analysis for scattered surface waves presented in Chapter 5, discussing these findings with respect to the application of seismic interferometry to scattered surface waves. Our analysis reveals key differences between the reflected body-wave case and the scattered surface-wave case (and this analysis can be generalised to reveal differences between reflected and scattered waves for other wave types). These differences are only resolved by using an optical theorem for surface waves. In Chapter 5 a generalized optical theorem for surface waves was derived, and here we consider the special case of scattering due to a symmetric, isotropic, density perturbation. In Appendix 6A, where we derive the necessary constraints on the real and imaginary parts of the surface-wave scattering amplitude for an isotropic density perturbation.

In Appendix 6B we discuss aspects of changes that occur when we consider convolution-type interferometry in place of correlation-type interferometry, and illustrate where errors may be introduced in that case.

6.2 Stationary phase analysis for scattered surface waves

Seismic interferometry is applied by solving a so-called interferometric integral, of which there are many forms depending on factors such as quantities radiated and measured by sources and receivers respectively and the type of media considered, e.g., for acoustic wavefields (Wapenaar, 2004; van Manen *et al.*, 2005), for elastic wavefields (van Manen *et al.*, 2006; Wapenaar and Fokkema, 2006), and for electromagnetic wavefields (Slob and Wapenaar, 2007). Here we use the method of stationary-phase integration to evaluate the integral in Equation (4.1) using scattered surface-wave Green's functions (e.g., see Snieder (2002) and Chapter 5). This method assumes that the dominant contribution to the integral comes from locations on the integration boundary where the phase of the integrand becomes stationary with respect to locations on the boundary, and that the amplitude of the term being integrated varies slowly around this location (Snieder, 2004b). This is a useful tool for analysing the processes and approximations involved in seismic interferometry.

By using analytical Green's functions we can determine the conditions where the integral is stationary, and evaluate the contribution from such points, explicitly.

For example, Snieder (2004a) uses the stationary-phase approximation to demonstrate that a homogeneous distribution of scatterers, acting as secondary wavefield sources, could be used to estimate inter-receiver, direct, ballistic waves, and applies the same approach to the special case of inter-receiver surface waves. Snieder *et al.* (2006) use the stationary-phase approximation to evaluate the interferometric integral for reflected body-wave fields when using only Earth-surface sources (i.e., a truncated surface, S) and find a significant source of error that occurs in the form of 'spurious multiples'. Independently, Sabra *et al.* (2005) applied a similar approach but for acoustic guided waves, illustrating that guided-wave stationary points exist at a range of offsets throughout a waveguide.

In Chapter 4 the approach of Snieder (2004a) for direct surface waves was extended to illustrate the adverse effects of limited surface source geometry, especially in the presence of higher-mode surface waves. Here we take this approach one step further and consider scattered surface waves. In what follows we assume that steps have been taken to treat higher-mode surface waves correctly: using only surface sources, non-physical cross-mode correlation terms are introduced into the interferometric estimate in the presence of multiple surface-wave modes; by separating modes prior to interferometry these cross-mode terms are suppressed.

Single scattered surface waves

In Chapter 5 we have shown that there are four different stationary-phase contributions to the interferometric estimation. This is similar to the analysis of reflected body waves by Snieder *et al.* (2006). However, we find that in the scattering case there are additional contributions to interferometry that do not appear in the approach of Snieder *et al.* (2006). To account for these differences we consider the optical theorem for surface waves (Snieder, 1988; Brandenburg and Snieder, 1989; Chapter 5). We now discuss each of these stationary-phase contributions and illustrate them both graphically and synthetically.

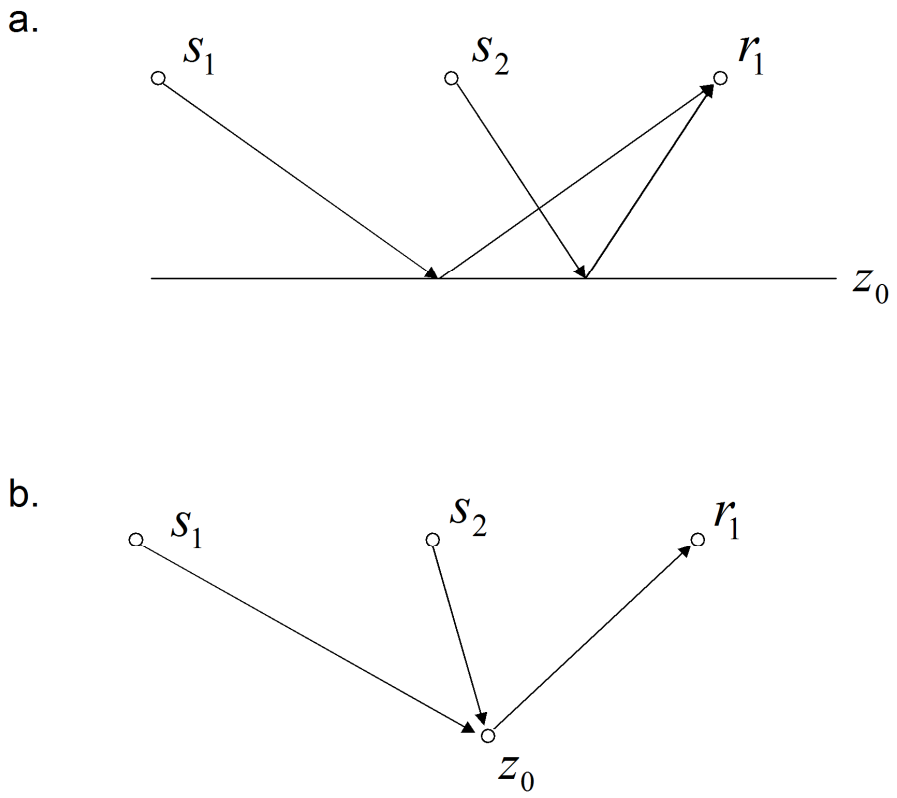

Figure 6.1: Sketch geometries illustrating the differences between reflected wavefields and scattered wavefields. Ray-paths between two source locations (s_1 and s_2) and a receiver location (r_1) that have (a) been reflected by a planar interface (z_0), and (b) been scattered by a point scatterer (z_0).

The four different contributions (*T1* to *T4*) to the interferometric integral are: the cross-correlation of the direct surface waves recorded at each receiver (*T1*); the cross-correlation of the direct surface wave at receiver one with the scattered surface waves at receiver two (*T2*); the cross-correlation of the scattered surface wave at receiver one with the direct surface wave at receiver two (*T3*); and the cross-correlation of the scattered surface waves at both receivers (*T4*). Provided that multiple surface-wave modes are properly dealt with (as discussed above), we can consider that this analysis holds for sources distributed only at (or just beneath) the surface of the Earth with the introduction of some frequency-dependent scale factors (see Chapter 4).

Snieder *et al.* (2006) find that the cross-correlation of two direct body waves results in the recovery of the direct inter-receiver body-wave. Likewise, the cross-

correlation of the direct surface waves (*T1*) results in the recovery of the direct inter-receiver surface waves. This part of the integral is similar to the case discussed by Snieder (2004a) and is the same as that discussed in Chapter 4.

T2 and *T3* are similar to the cross-correlation of the direct and reflected body-waves in Snieder *et al.* (2006). They find that one term provides the causal reflected body-wave and the other provides the acausal reflected body-wave. Similarly, we find that *T2* and *T3* provide the causal and acausal inter-receiver scattered surface wave.

However, the analysis presented in Chapter 5 reveals a difference between the previous approach of Snieder *et al.* (2006) for singly reflected body-waves and that for scattered surface waves: in addition to these physical terms, there are also non-physical terms associated with *T2* and *T3* that are introduced in the case of scattered waves. Such non-physical terms are often referred to as spurious arrivals and have previously been observed in applications of interferometry in the presence of multiple reflections where source distribution is insufficient, where the recording time is not long enough, and in the presence of losses (Snieder *et al.*, 2006; Draganov *et al.*, 2008; Ruigrok *et al.*, 2008). In the lossless case these arrivals are destructively cancelled by including the second order term *T4*. Thus we highlight general differences between the stationary-phase treatments of reflected and scattered wavefields in seismic interferometry. In an independent study, Snieder *et al.* (2008) derive similar results for acoustic-wave scattering, hence we expect analogous results to hold for other scattering regimes.

The differences between the stationary-phase analysis for reflected- and scattered-waves might seem counter-intuitive: since a plane reflector could be modelled as a line of scatterers separated within the Nyquist spatial-sampling criteria it could be argued that the two cases should be inter-related. However, the key difference is that for a plane reflector there is a single angle of reflection for any given angle of incidence. For an isolated point scatterer waves are scattered over 360 degrees for any angle of incidence. This affects the manner in which these waves are observed for different source-receiver configurations. We illustrate this difference in Figure 6.1. Part (a) illustrates ray paths of waves from two source locations (s_1 and s_2), reflected at a plane reflector (z_0) and recorded at a single receiver (r_1). The azimuths

of the incident and reflected waves, and the position of the specular-reflection point changes with source position. Part (b) illustrates the same case, but the reflector has been replaced by a single point scatterer (z_0). For the different source locations, the azimuths of the incident wave changes, but the azimuth of the scattered wave does not as the scatterer-receiver path is the same (i.e., is stationary) for all source locations. This is why we see differences between the cases for reflected- and scattered-waves.

We now discuss the contribution of *T2* and *T3* in more detail (geometric variables used to define these stationary points are illustrated in Figure 5.5). In Chapter 5 we found the stationary phase condition for scattered waves given by *T2* to be $\varphi_{S0} - \varphi_{A0} = 0$ and $\varphi_{S0} - \varphi_{A0} = \pi$ (or $\varphi_{S0} - \varphi_{B0} = 0$ and $\varphi_{S0} - \varphi_{B0} = \pi$ for *T3*). In Figure 5.6 we illustrate the geometries associated with these conditions. Figure5.6a and b illustrate what we will call the physical and non-physical parts of *T2*, respectively. For the physical part we see that, since both the direct and scattered waves have the same take-off angle ($\varphi = \varphi_{A0} = \varphi_{S0}$), the initial part of both waves have the same path (i.e., this corresponds to the stationary condition $\varphi_{S0} - \varphi_{A0} = 0$). Interferometric cross-correlation acts to remove the time delay between the boundary stationary point and the first receiver resulting in an estimate of the wavefield as if the source had been at $\mathbf{r}_A$. The latter is also why the second part of *T2* is non-physical: in Figure 5.6b we can see that both waves reach the scatterer before they reach $\mathbf{r}_A$ (corresponding to the stationary condition $\varphi_{S0} - \varphi_{A0} = \pi$). The time-delay between the stationary point and the scatterer is removed, resulting in a non-physical contribution corresponding to the cross-correlation of the direct waves between the scatterer and the two receiver locations. In Figure 5.6c and Figure 5.6d we examine *T3* by reversing the roles of $\mathbf{r}_A$ and $\mathbf{r}_B$, and again find one physical stationary point and one non-physical stationary point (where by physical and non-physical stationary points we refer to those stationary points providing a physical contribution and a non-physical contribution, respectively).

The contribution from the physical stationary point relating to *T3* has the negative phase of the physical part of *T2,* so thus we recover both causal and acausal scattered events. We find that the non-physical parts of *T2* and *T3* have equal phase. If the

scattering amplitude is real (as in a first-order Born analysis) these terms have opposite sign and cancel mutually. However, if the scattering amplitude has an imaginary part then the terms do not cancel (the imaginary parts have equal amplitude due to the complex conjugation in Equation (4.1)). We now discuss why it is necessary to consider complex-scattering amplitude in any analysis where we are interested in scattering beyond the Born approximation.

Term *T4* of Snieder *et al.* (2006) provides a stationary-phase contribution that corresponds to the acausal direct body-wave. *T4* in our scattering analysis is altogether different as it is always stationary: the scatterer does not move, hence the phase of the cross-correlation of the two scatterer-to-receiver waves remains constant (Equation (A5.22) in Chapter 5). The cross-correlation has the opposite phase to that of the non-physical parts of *T2* and *T3*, and the combination of these 3 terms must mutually cancel to zero. In Appendix 6A we show that in order for this cancellation to occur it is necessary to consider a complex scattering amplitude, and as a result of this analysis we derive the constraints that the optical theorem places on surface-wave scattering due to an isotropic density perturbation We must therefore require that scattering be computed in a manner consistent with the optical theorem. This indicates that linearised Born scattering (which is inconsistent with the optical theorem) does not produce the correct interferometric result, even in this simple single-scattering case. This is because the cross-correlation of two scattered waves can be considered a second-order term, and term *T4* would therefore not be considered in a Born analysis (that is, for real scattering amplitudes we would only consider terms *T2* and *T3*). Vasconcelos (2007) derives interferometric relations using representation theorems for perturbed media and finds similar results to our stationary phase approach. That approach is for general perturbations to the background medium in acoustic media and considers remote sensing applications of terms equivalent to *T2*, *T3* and *T4* of our analysis. However, it did not identify the critical role of the imaginary part of the scattering amplitude.

We now illustrate the above results using synthetic data generated in a simple model with a boundary *S* of radius 200 m from the origin on which the source separation is 4 m, a single scatterer at [50, 50], and receivers located internally at [-140, 0], and from [-16, 0] to [140, 0] in steps of 4 m (Figure 6.2a). For illustrative

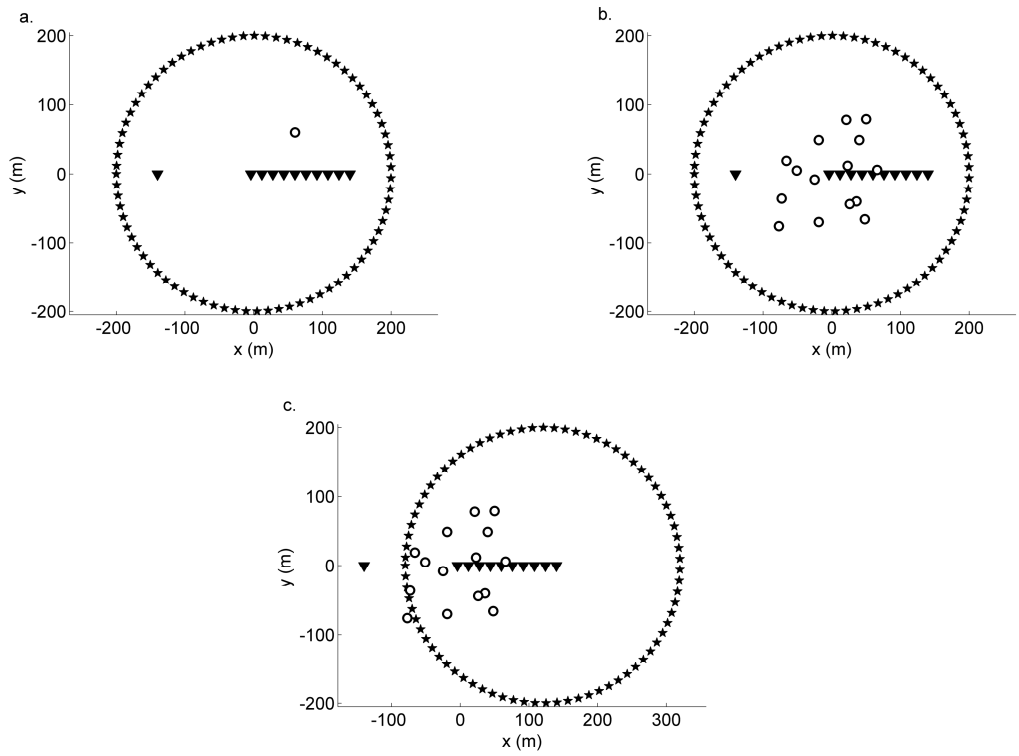

Figure 6.2: Geometries for testing interferometry for scattered surface waves: (a) single scatterer, (b) multiple scattering, and (c) convolution configuration for multiple scattering. Stars indicate source locations, triangles indicate receiver locations, circles indicate point scatterers. Only every fourth source and receiver are plotted for clarity – note that this only applies to the line-array as the leftmost receiver is isolated.

purposes we use both point-force sources and deformation-rate-tensor sources to be precisely consistent with the terms G_{in} and $n_j c_{njkl} \partial_k G_{il}$ in Equation (4.1), respectively (this also ensures that no amplitude errors are introduced due to far-field approximations such as those discussed by Wapenaar and Fokkema (2006)). We also consider only a single surface-wave mode (taken from the horizontally plane-layered Earth model used in Chapter 4) with a frequency-dependent velocity range of approximately 100 m/s to 160 m/s over the frequency band of interest (selected by using a Ricker wavelet with a centre frequency of 15 Hz). We therefore assume that we can consider a boundary of sources located only at (or just beneath) the surface of the Earth, and hence we expect frequency-dependent scaling terms due to the omission of sources at depth as predicted in Chapter 4. We compute the synthetic data using Equations (A5.3) to (A5.4). To produce strong scattering we use the upper

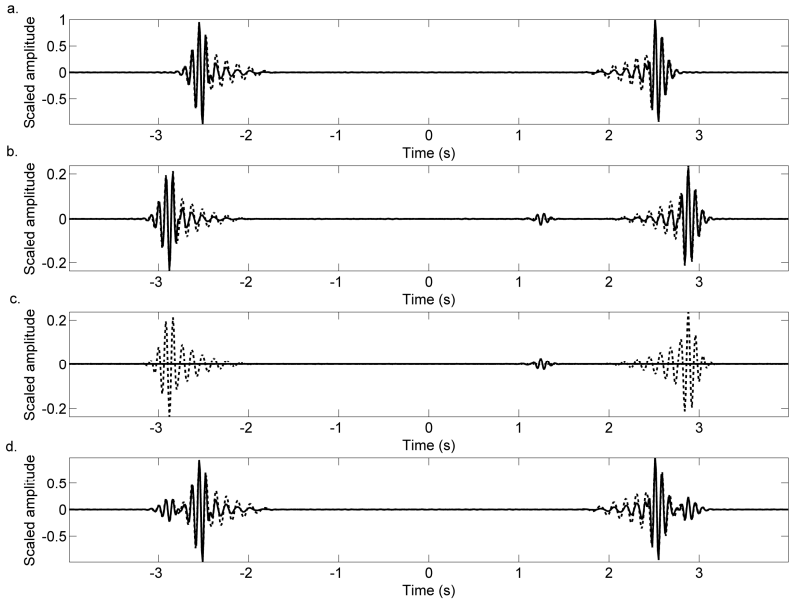

Figure 6.3: Waveforms for the scattering model in Figure 6.2a. (a) Interferometry using the direct wave only; (b) Interferometry using the direct waves at one receiver and the scattered waves at the other; (c) Interferometry using the scattered waves only); (d) Sum of the three contributions above. Directly modelled direct wave (a), scattered waves (b, c) and the sum of both (d) are shown for reference (dashed lines).

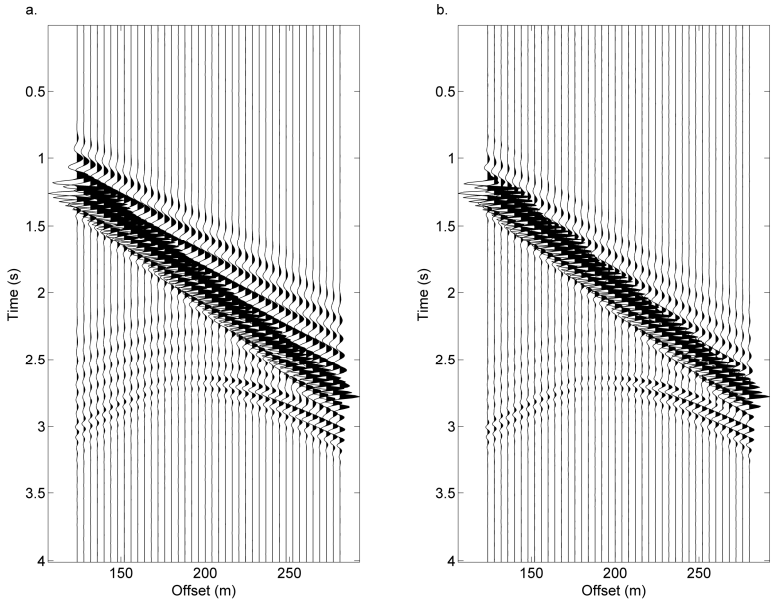

Figure 6.4: Waveforms for the scattering model in Figure 6.2a. (a) Directly modelled gather for a source at receiver [-140, 0]; (b) Interferometric estimate of the gather in (a). Both plots are for the scattering model in Figure 6.2a. Note that the *x*-axis represents offset, as opposed to the *x*-coordinate plotted in Figure 6.2.

limit of these constraints imposed by the optical theorem on the imaginary and real

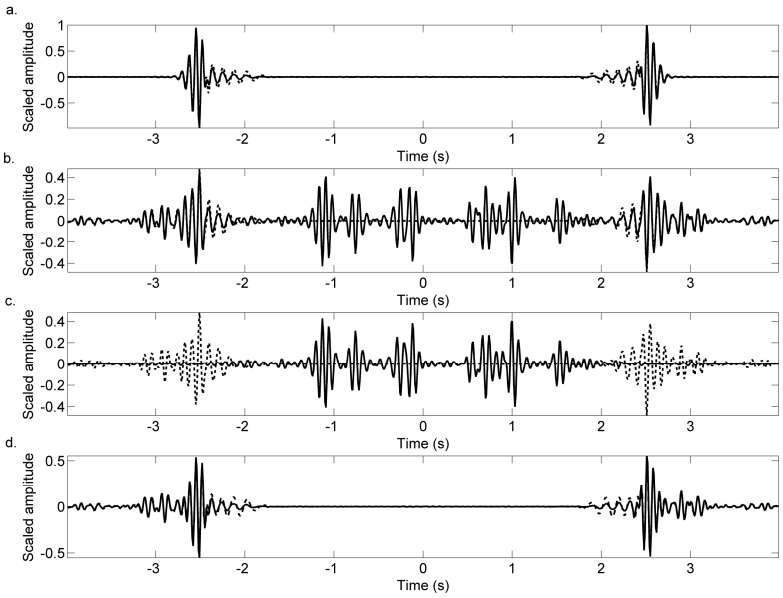

Figure 6.5: As for Figure 6.3 but waveforms are for the scattering model in Figure 6.2b.

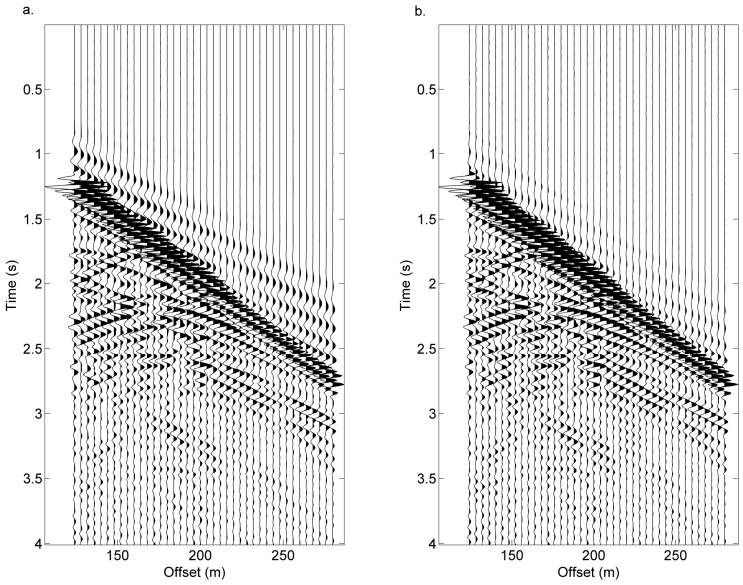

Figure 6.6: As for Figure 6.4 but waveforms are for the scattering model in Figure 6.2b.

parts of the scattering amplitude, as derived in Appendix 6A. The imaginary part of the non-azimuthally dependent scattering amplitude is set to -0.9, and the imaginary part of the azimuthally dependent scattering amplitude is set to -1.9.

In Figure 6.3 we consider the receivers [-140, 0] and [120, 0]. Panel (a) illustrates the cross-correlation and summation of the direct surface waves recorded at these two receivers from all boundary sources, and the exact direct surface wave is plotted

for reference (dashed line). All plots are scaled to the maximum amplitude of this estimated direct surface wave. Panel (b) illustrates the result of cross-correlating the direct surface waves with the scattered surface waves (and vice versa) and summing the results. The exact scattered surface waves are shown for reference (dashed line). The scattered surface waves have been well estimated, but the non-physical parts of terms *T2* and *T3* can be seen around 1.1 to 1.3 s lag. As expected the contribution provided by *T4* (panel c) provides an equal contribution of opposite sign to the non-physical parts of (b), so after summing all four terms the correct inter-receiver Green's function is recovered (panel d).

Note that in all of these plots the lower frequency, earlier arrivals have lower amplitudes in the estimates than in the exact result. While this error appears to be significant, it is explained in Chapter 4, where frequency-dependent scale factors are derived for the case when sources are only present at the surface of the Earth. We do not apply scaling here as these errors do not affect the phase of the estimates, neither do they introduce non-physical arrivals.

While in this example *T4* is small, we later show that it can be large in multiple-scattering cases, and hence provides a significant contribution to the interferometric integral. In the multiple scattering case there is more energy in the scattered wavefields between the two receivers, and hence there is more energy in the cross-correlation of the scattered waves (term *T4*). It is also interesting to note that the calculation of terms *T2* and *T3* are equivalent to applications of interferometry where wavefield separation is used. Thus the non-physical parts of terms T2 and T3 are indicative of the types of errors that may be introduced in such applications (e.g., Mehta *et al.*, 2007; 2008; Vasconcelos, 2007; Vasconcelos and Snieder, 2008a).

In Figure 6.4 we show the estimate of the full gather of receivers [-16, 0] to [140, 0], from a source at [-140, 0]. Figure 6.4a shows the directly modelled gather, and Figure 6.4b shows the interferometric estimate. The amplitude errors can be seen (lower frequencies are stronger in panel a), but apart from this both the direct and scattered waves are well recovered. Note that the variation around 180 m offset shows that we have also estimated the radiation pattern of the scatterer. If we had used only point-force sources this may not have been recovered correctly as

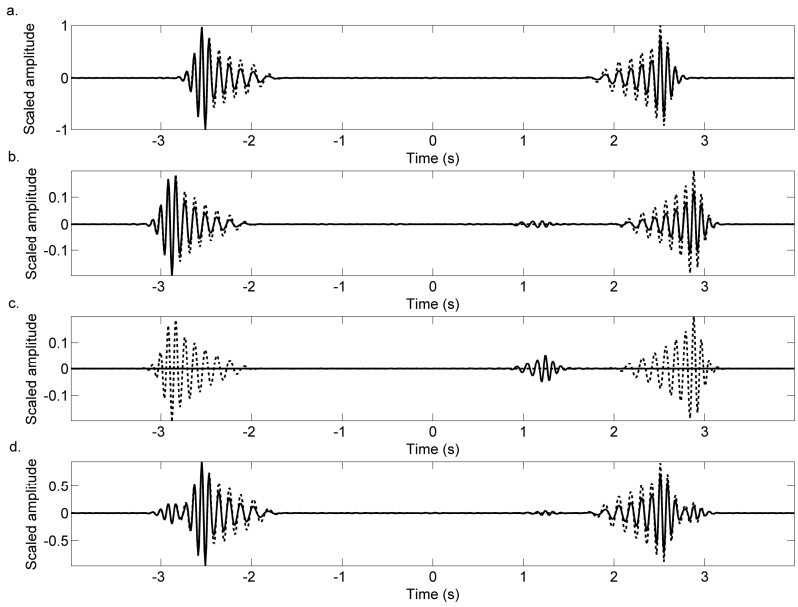

Figure 6.7: As for Figure 6.3, waveforms are for the scattering model in Figure 6.2a with the introduction of attenuation.

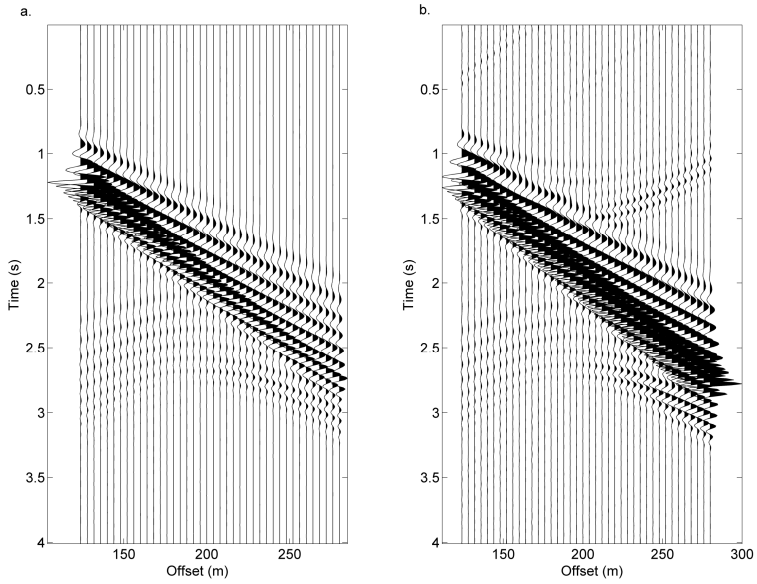

Figure 6.8: As for Figure 6.4, waveforms are for the scattering model in Figure 6.2a with the introduction of attenuation.

azimuthally-dependent scale errors are introduced in that case (e.g., Snieder *et al*., 2006).

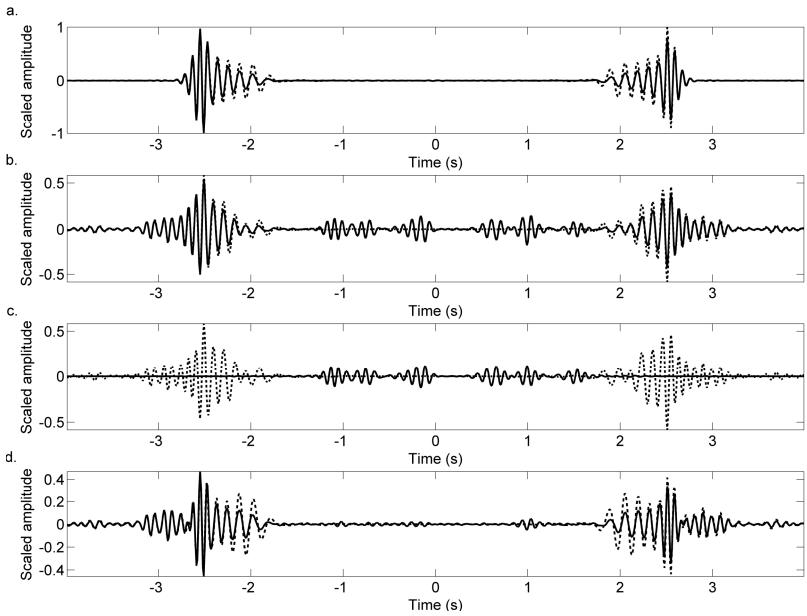

Figure 6.9: As for Figure 6.5, waveforms are for the scattering model in Figure 6.2b with the introduction of attenuation.

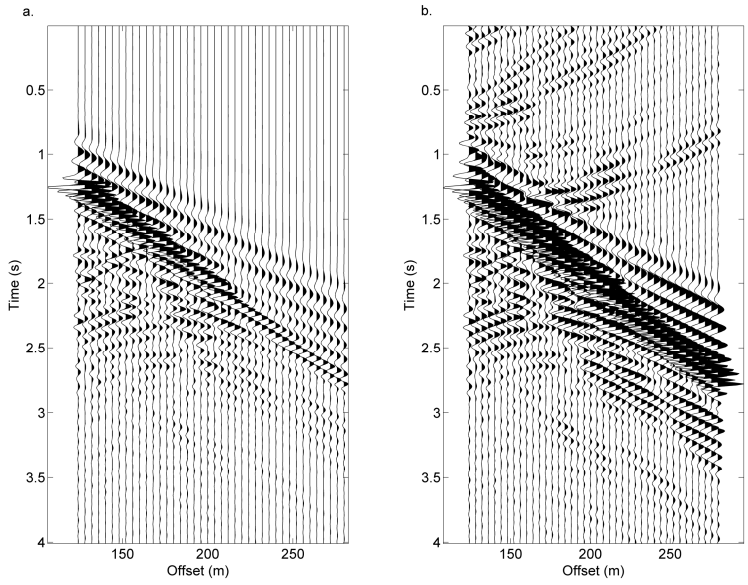

Figure 6.10: As for Figure 6.6, waveforms are for the scattering model in Figure 6.2b with the introduction of attenuation.

Multiply scattered surface waves

We now illustrate that similar principles apply to multiply-scattered surface waves. From the above analysis we expect the following to occur:

1. The direct inter-receiver surface wave will result from the cross-correlation and summation of the direct source-receiver surface waves recorded at each receiver.
2. The scattered inter-receiver surface waves will result from the cross-correlation of the direct source-receiver surface wave with the scattered source-receiver surface waves (and vice-versa).
3. The cross-correlation of the source-receiver scattered surface waves will account for non-physical arrivals introduced in point 2.

We reproduce the results of the previous section, but use a random distribution of 15 scatterers (geometry shown in Figure 6.2b). In order to compute the multiply-scattered surface waves we use a deterministic variant of Foldy's method (Foldy, 1945; Groenenboom and Snieder, 1995; van Manen *et al.*, 2006). This method assumes that there is no angular dependence of the scattering amplitude. While this assumption is not particularly realistic, it allows us to compute multiply-scattered wavefields efficiently within the optical theorem, and can still be used to demonstrate the effects discussed herein.

Figure 6.5a shows the direct waves and is the same as Figure 6.3a. The contribution of the cross-correlation of the direct wave with the scattered waves is shown in Figure 6.5b. This is more complex than that shown in Figure 6.3b, but we observe that the scattered waves are (in parts) well estimated by this step. However, there are many non-physical terms introduced which we expect to be cancelled by the contribution of term *T4* shown in Figure 6.5c. Figure 6.5d shows the sum of panels (a), (b), and (c) which results in an approximately correct estimate of the multiply-scattered surface waves. Again, the frequency-dependent amplitude errors are expected, but as described above these do not affect the phase of the estimate and neither do they introduce spurious arrivals. We show the estimate of the whole gather in Figure 6.6, and as expected both the direct and multiply-scattered surface waves are well recovered.

Note that term *T4* has relatively large amplitude (of the same order as the dominant scattered wave). Had we computed the scattered wavefields using a first-order Born analysis (i.e., without the optical theorem) this term would introduce

large errors in the interferometric estimates. Hence, when applying interferometry to forward modelled wavefields, the use of the Born approximation is not appropriate to analyse the effects of interferometry on scattered waves. Note that Wapenaar and Fokkema (2006) present a simple single-scattering example within the Born approximation and their interferometric results appear to be exact. This is because, in order to be consistent with the Born approximation, they include only the zeroth and first order terms of the cross-correlations, omitting those terms that would contribute to *T4*.

6.3 Attenuation

In the previous section we have investigated seismic interferometry for scattered surface waves in a near-ideal setting using an elastic medium and a well-sampled, closed, 1-dimensional boundary of sources on the ground surface. To achieve exact results would have required a 2-dimensional boundary of sources extending to depth, reducing the similarity between our example and geometrical constraints in practical applications (Wapenaar *et al.*, 2004; Snieder *et al.*, 2006; Mehta *et al.*, 2008). We found that the mutual cancellation of non-physical contributions to the interferometric integral is a key step in producing reliable estimates of the inter-receiver surface waves. However it is unlikely that these near-ideal settings will be achieved in real data applications of the method. Amplitude imbalances (for example, due to attenuation or non-uniform boundary source strength distribution) will result in non-cancellation of these non-physical contributions and the introduction of spurious arrivals. Similar effects will be observed in the case of limited source aperture where sources may not lie at all of the stationary points required for cancellation.

Cross-correlation based interferometric theory does not account for attenuation, yet the near surface through which surface waves travel is often strongly attenuating. We therefore introduce attenuation to illustrate the importance of these cancelling terms. We reproduce our examples using a realistically attenuating medium. To model attenuation we apply the following offset-dependent damping factor to the calculated surface waves (Aki and Richards, 2002, ch. 7.3.4),

$$\exp\left[\frac{(-\omega X)}{2c_v(\omega)Q}\right], \tag{6.1}$$

where Q is the quality factor (given a value of 50 here), c_v is the phase velocity, ω is the angular frequency and X is the horizontal offset.

Figure 6.7 and Figure 6.8 are similar to Figure 6.3 and Figure 6.4 showing singly-scattered surface waves but for an attenuating medium. Note that while the scattered surface waves are still recovered, there are changes in amplitude due to the energy lost during propagation between the boundary and each receiver (e.g., compare the causal and acausal parts of Figure 6.7a, which would be exactly anti-symmetric in the application of Equation (4.1) to non-attenuating media). Gosselet and Singh (2007) use this symmetry breaking to derive estimates of the quality factor of the medium. This symmetry breaking also has an effect on the parts of terms *T2* and *T3* which should cancel to give the exact inter-receiver surface wave. This un-cancelled term can be seen in the interferometric estimate in both Figure 6.7d (around 1.25 s) and Figure 6.8b (between 1 s and 1.5 s for receiver offsets 200 m to 280 m). Figure 6.8b exhibits time- and offset-dependent amplitude errors due to the presence of attenuation. The amplitude errors are not large here due to the specific geometries used, however, later we show that these errors can indeed be large when less ideal geometries are considered.

For the multiply-scattered surface-wave case (Figure 6.9 and Figure 6.10) the errors are far more abundant due to the complicated nature of the mutually-cancelling terms provided by *T2*, *T3* and *T4*. This illustrates that the more complex the scattered surface-wave field, the larger errors are introduced in the presence of attenuation. The relative amplitudes with respect to both time and offset have not been recovered correctly, but scattered surface waves can still be identified.

Data can be processed to compensate for the effects of attenuation. In exploration seismology this is often done by applying inverse-Q filters to amplify higher frequencies (e.g., Hargreaves and Calvert, 1991; Wang, 2002). Application of such methods prior to interferometric processing may allow for enhanced recovery of the higher-frequency surface waves, for example Draganov *et al.* (2008) identify non-

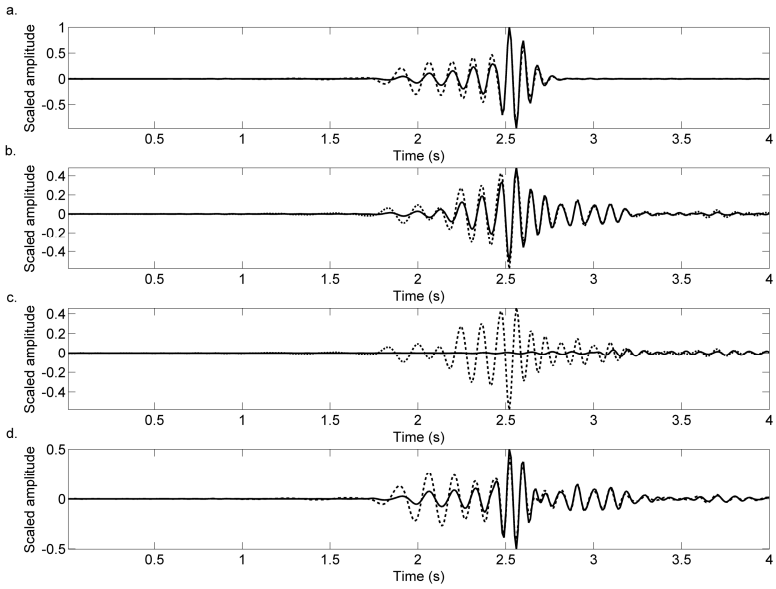

Figure 6.11: As for Figure 6.9, waveforms are for the scattering model in Figure 6.2c and here we have used convolution-type interferometry in an attenuating medium. Note that convolution-type interferometry does not produce an acausal Green's function, hence only forward times are shown.

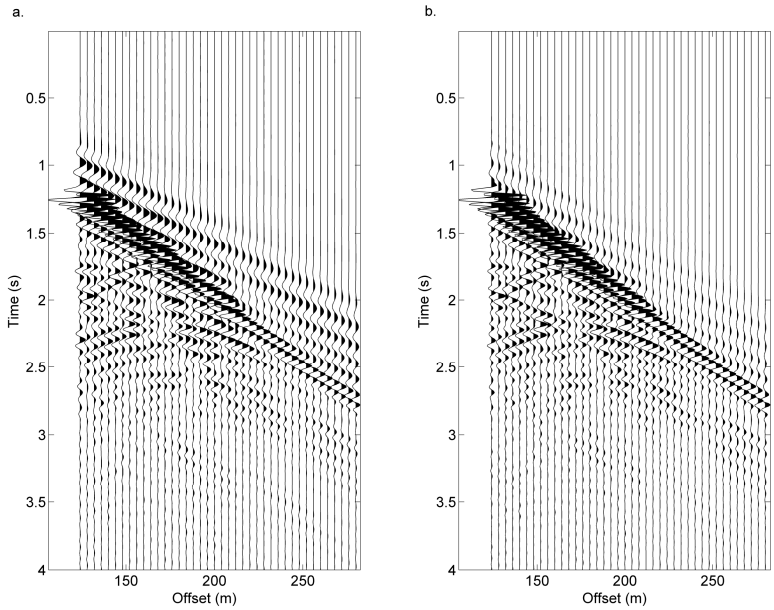

Figure 6.12: As for Figure 6.10, waveforms are for the scattering model in Figure 6.2c and here we have used convolution-type interferometry in an attenuating medium.

physical arrivals in seismic interferometry and estimate a damping factor, which when applied to the data prior to interferometry allows for the elimination of the non-

physical arrivals.

There are also adaptations to the interferometric theory that account for the presence of attenuation. For example Snieder (2007) demonstrates that acoustic wave interferometry can still be applied exactly in the presence of attenuation, provided that energy sources are distributed throughout the medium of propagation, and that the attenuation values are known throughout the medium. A similar formulation could be developed for surface waves, and it may be possible to recover the exact surface waves given a homogeneous distribution of sources at the surface. However, the disadvantage of such an approach is it requires a model of the medium attenuation.

Instead we concentrate on another approach adapted from the work of Slob *et al.* (2007), and Slob and Wapenaar (2007) in electromagnetic interferometry. Electromagnetic applications often involve very lossy media, and for interferometry to be successfully applied in such media a method to account for wave attenuation must be used. One particularly simple method is to replace cross-correlation with cross-convolution. This is done by deriving interferometric relationships from the reciprocity theorem of the convolution type, as opposed to the reciprocity theorem of the correlation type (e.g., Wapenaar, 2007). This new configuration requires that one of the receivers be inside the boundary of sources, while the other lies outside of that boundary.

The important difference between correlation-type interferometry and convolution-type interferometry is that the cross-correlation operator requires time-reversal (or complex conjugation) of one of the inputs, while the convolution operator does not. Since wavefields cannot be time-reversed in the presence of attenuation we require that the media be lossless for the application of exact correlation-type interferometry as expressed by Equation (4.1). In convolution-type interferometry we only consider causal Green's functions and no constraints are placed on the attenuation of the medium. In addition, we only recover a causal Green's function, as opposed to the causal and acausal Green's functions recovered using correlation-type interferometry. Hence, we can expect convolution-type interferometry to be useful in the presence of strong attenuation. [For a more detailed view on the differences between the correlation- and convolution-type reciprocity

theorems, including the presence of volume integrals as considered by Snieder (2007), see de Hoop (1995, e.g., Equations 15.4-7 and 15.5-7).]

Rather than simply adapting the findings of Slob *et al.* (2007) and Slob and Wapenaar (2007) for the elastic case, in Appendix 6B we briefly discuss changes in our stationary-phase analysis of scattered surface waves for the cross-convolution case, and find similar results as for the cross-correlation case, term *T1* provides the direct surface wave and terms *T2* and *T3* combine to provide the scattered surface waves. However, the stationary phase condition for the physical scattered waves changes from, $\varphi_{S0} - \varphi_{A0} = 0$ to $\varphi_{S0} - \varphi_{A0} = \pi$ and the stationary-phase condition for the non-physical waves changes from $\varphi_{S0} - \varphi_{A0} = \pi$ to $\varphi_{S0} - \varphi_{A0} = 0$. This change is important as combined with the absence of complex conjugates in convolution-type interferometry it results in the non-physical arrivals cancelling in the convolution case (see Appendix 6B). Therefore no non-physical arrivals are introduced and term *T4* provides a zero contribution. Thus we reveal why we expect convolution-type interferometry to perform well in the presence of attenuation, or even in cases where the source boundary has limited aperture: since the non-physical arrivals introduced by terms *T2*, *T3* and *T4* do not exist in the convolution case there are no mutually cancelling terms and there are no errors introduced due to amplitude imbalances or limited aperture as in the cross-correlation case. Hence, for convolution-type interferometry the second-order interactions vanish when considering a single-scattering model and Born-type analysis may be sufficient in this case. Note that this also means that wavefield separation can be applied using convolution-type interferometry without the introduction of non-physical arrivals – this may be significant if terms *T2* and *T3* are to be calculated using real data to estimate only the scattered wavefield.

To illustrate the convolution case we use the multiple-scattering model above, shifting the boundary such that receiver [-140, 0] is located externally, with the rest of the receivers located internally, the position of the scatterers relative to the receiver array does not change (Figure 6.2c). The corresponding set of results for convolution-type interferometry are shown in Figure 6.11 and Figure 6.12, again we expect and observe errors in the lower-frequency, earlier arrivals as only sources at the surface are used. Compared with Figure 6.9 and Figure 6.10 there are no strong

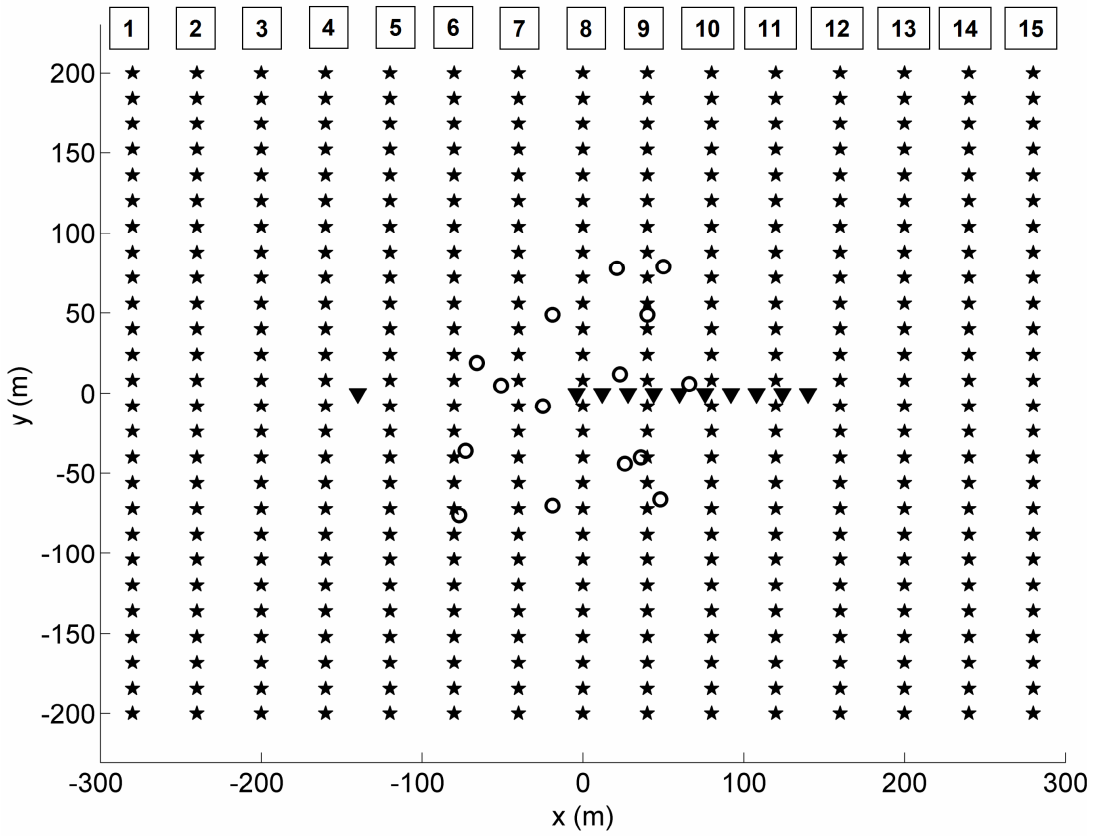

Figure 6.13: Orthogonal source and receiver geometries used in Figure 6.14, Figure 6.15, and Figure 6.16. Symbols are as in Figure 6.2. Boxed numbers label different source lines.

errors introduced into the estimates (except for the expected frequency-dependent amplitude errors), and the amplitudes are well recovered. Note term *T4* provides a small contribution to the estimate; in Appendix 6B we show that this is an error in the estimate as term *T4* should provide a zero contribution. This error occurs due to a pseudo-stationary source point on the surface: in Chapter 4 it was shown that sources at depth are required to correctly construct higher mode surface waves with interferometry, and the current case is similar in nature. The pseudo-stationary source point appears to be stationary when the boundary of sources is confined to the near-surface, but in reality it is not stationary in the depth direction, so integration in depth would remove this error. In our example these errors do not have a strong impact on the resulting surface-wave estimates (Figure 6.12b). If these errors are large enough to be problematic then a 'thick' boundary of sources may be used to reduce their effect as the pseudo-stationary point also varies with surface boundary location.

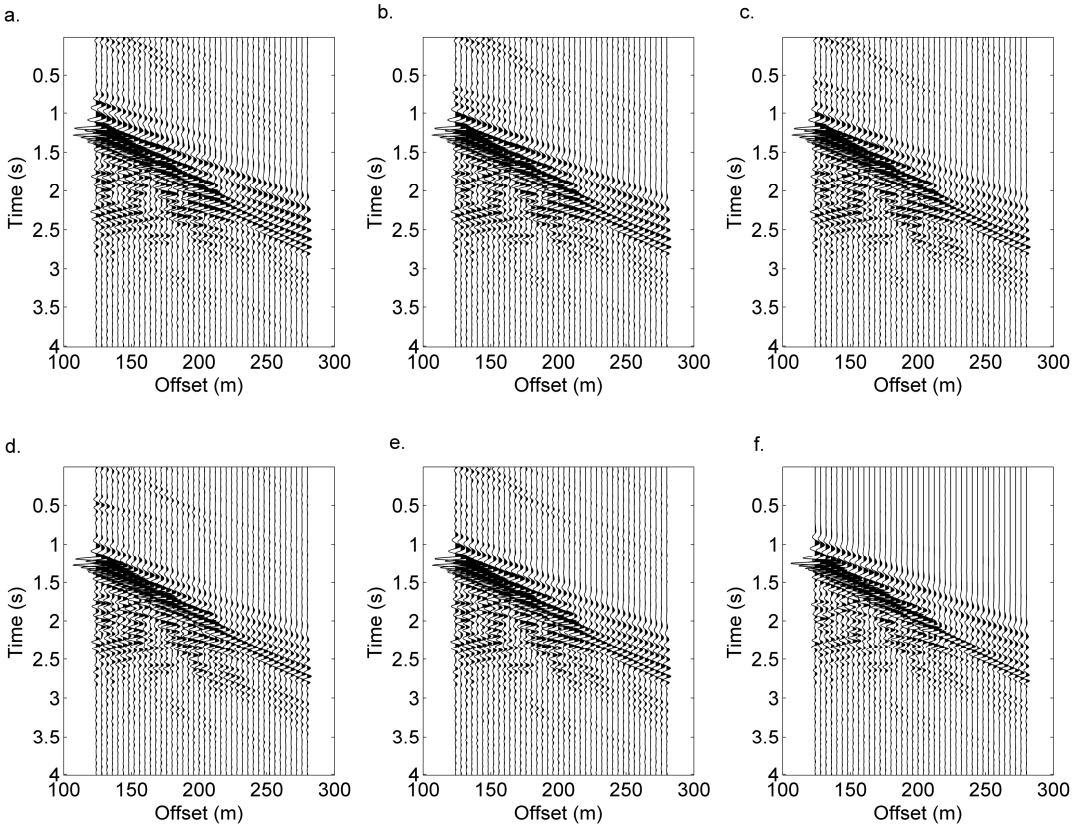

Figure 6.14: (a) – (d) Correlation-type interferometric estimates in the presence of attenuation of a gather at source location [0, -140] using source lines 1 to 4 individually; (e) Sum of panels (a) – (d) after normalization of each gather to maximum amplitude of one; (f) Directly modelled source gather.

6.4 Practical source geometries

Up to this point we have shown that under ideal circumstances, it is possible to make good estimates of inter-receiver scattered surface waves using correlation-type interferometry. In attenuating media, correlation-type interferometry introduces errors both in amplitude (in addition to those that we expect due to having only sources at the surface) and in the introduction of spurious arrivals. Convolution-type interferometry does not suffer from the same errors and the estimates are of higher quality. We now consider some more realistic source distributions in attenuating media (Q = 50), using orthogonal source and receiver geometries typical of exploration surveys on land (Figure 6.13). We also now consider the situation where

only point-force sources and particle-displacement measurements are available, as typically these are the only quantities acquired in industrial seismic surveys. Note that rather than use a larger spread of scatterers we use the same distribution as previously for ease of comparison to previous results, for computational efficiency of the Foldy modelling method used, and because the dominant scatterers are anyway expected to be those located close to the inter-receiver line (for example, due to geometrical spreading).

While these examples demonstrate exploration/engineering-type geometries, the scattering theory presented is not limited to such cases. Accounting for differences in length-scale, frequency and velocity, these geometries could also be considered to represent simplified versions of real life crustal-seismology settings. For example, a line of sources could be illustrative of a coastline where micro-seismic energy is released as the waves interact with the coastal shelf, or an active fault plane where numerous seismic events create a line of sources when considered over long time intervals. A regularly spaced distribution of surface sources might represent the case where background noise is generated in a spatially-diffuse manner at the surface by wind, anthropogenic activity or other near-surface noise sources.

One particular advantage of illustrating our findings using exploration style geometries is that it is easier to observe scattering using linear arrays as opposed to sparsely located receivers. Hence the quality of our interferometric results, and the nature of any errors imposed on them, are clearer to the naked eye.

In Figure 6.14 we consider the (acausal) contributions from source lines 1 to 4. Since these receiver lines lie outside of all receiver pairs we consider correlation-type interferometry. Panels (a) to (d) illustrate the contributions from each source line individually, with weighting tapers applied to sources at the end of each line to suppress truncation artefacts (this tapering is applied in all of the following results). Compared with the directly-modelled source gather (panel f) many of the scattering events are well recovered suggesting that these source lines coincide with stationary points for many of the scattering events. The relative amplitudes are well recovered and the strong errors that were observed prior to the first arrival of the direct surface waves in Figure 6.10 are not present here. The relative amplitudes are well estimated here for two reasons: first, the relatively narrow frequency band used (a Ricker

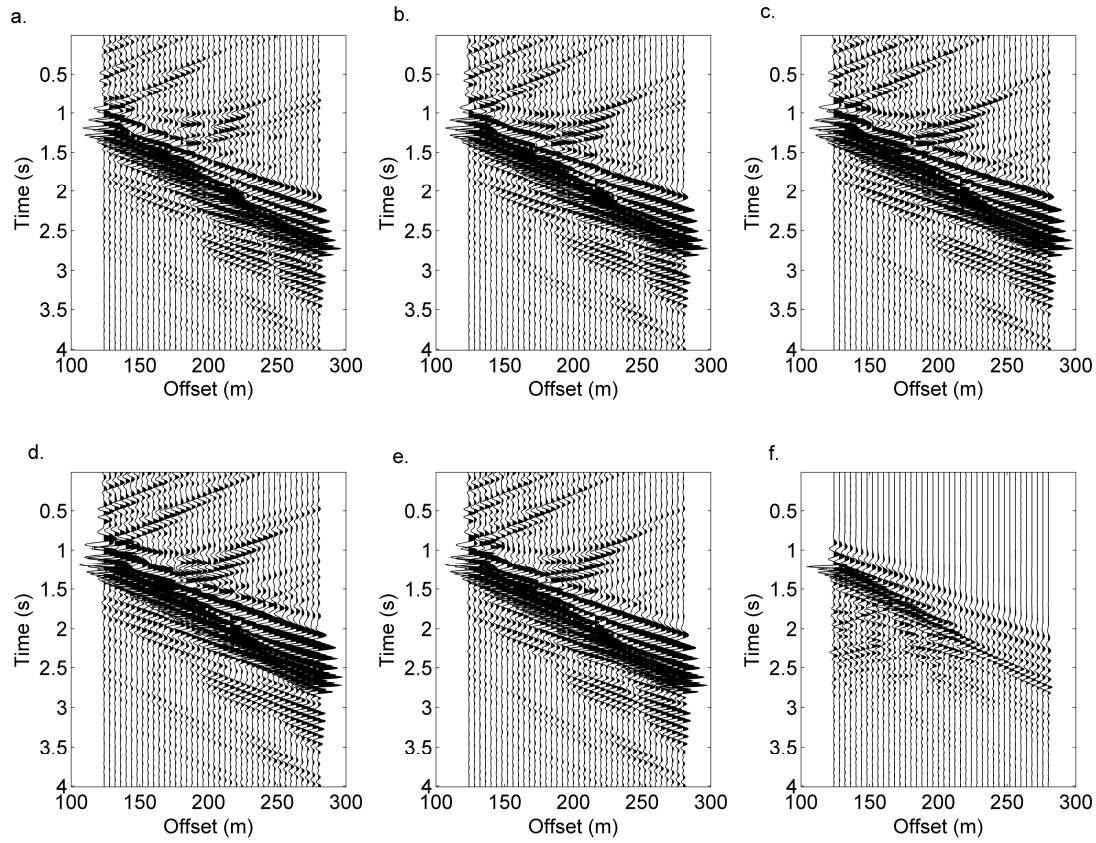

Figure 6.15: (a) – (d) Correlation-type interferometric estimates in the presence of attenuation of a gather at source location [0, -140] using the four right-most source lines; (e) Sum of panels (a) – (d) after normalization of each gather; (f) Directly-modelled source gather.

wavelet with a central frequency of 15 Hz) means that there are not large differences in attenuation between the lowest (~10 Hz) and highest (~20 Hz) peak frequencies. Second, the distance between one source line and the closest receiver for each pair in the gather is always constant i.e., the nearest receiver to the source line is always the same. Hence, at least for the direct surface wave, the energy lost due to attenuation before the first receiver is encountered is the same for each receiver pair. This is not true for the scattered waves and we expect energy loss to vary accordingly.

Panel (e) shows the sum of all four estimated gathers (after normalization of each gather to a maximum amplitude of one to account for varying amplitudes in the estimates from different source lines, ensuring that each provides an equal contribution to the sum). Some of the errors (e.g., the event observed to move out from zero seconds at 124 m offset) do not vary with source line position, and hence sum constructively. This is expected from our stationary-phase analysis of a

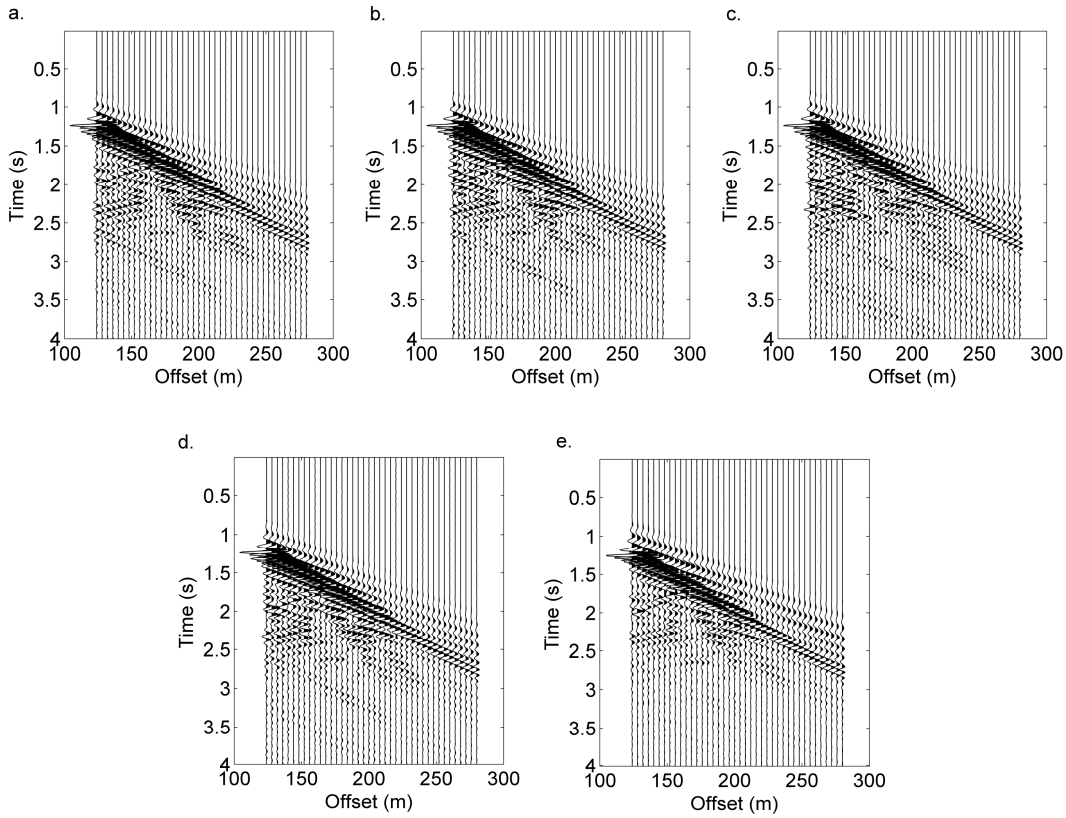

Figure 6.16: (a) – (c) Estimates using convolution-type interferometry in the presence of attenuation of a gather at source location [0, -140] using source lines 5, 6 and 7 in Figure 6.13; (d) Sum of panels (a) – (c) after normalization of each gather; (e) Directly-modelled source gather.

scattering medium, as the phase of these errors (introduced by non-cancellation of the non-physical parts of *T2* and *T3*, and the whole of *T4*) is stationary for any boundary source configuration. This is different to other errors in interferometry for cross-mode contributions identified previously in Chapter 4, or from the ghost events identified by Draganov *et al.* (2004), both of which diminish when neighbouring source boundaries are used and the results stacked.

In Figure 6.15 we take source lines 12 to 15 and repeat the estimation process used in Figure 6.14. Panels (a) to (d) again illustrate the (causal) estimates using each source line. These results differ greatly to those in Figure 6.14. Firstly, the relative amplitudes with respect to time and offset are incorrect compared to the directly-modelled results in panel (f). This is because for these geometries the distance from a source line to the nearest receiver is not constant for each pair in the receiver array,

i.e., the position of the nearest receiver relative to the source line varies for each pair. Hence there are different source-receiver energy losses for each receiver pair, producing erroneous relative amplitudes and due to these losses the energy travelling between the virtual source and each receiver is less than in the case illustrated in Figure 6.14. The weaker direct surface waves may amplify the appearance of the non-physical arrivals discussed below. Secondly, many of the scattered surface-wave arrivals are not constructed, most notably those around 124 to 200 m offset. This is because, for this particular geometry and distribution of scatterers, the source lines miss a lot of the stationary points for the scattered surface waves. However, as can be seen by the strong events prior to the arrival of the direct surface wave, these source lines include stationary points for the non-physical part of the integral (i.e., the non-physical parts of *T2* and *T3* identified above). Finally, here we can see that the strong spurious arrivals have the same phase across all four estimates, and again stack constructively in panel (e). These two sets of results (Figure 6.14 and Figure 6.15) illustrate the sensitivity of the cross-correlation approach to non-physical arrivals introduced by attenuation and limited aperture. These two cases represent extreme situations: in Figure 6.14 results seem favourable, but by considering the same scattering and receiver geometry with a different source distribution the results deteriorate greatly.

In Figure 6.16 we use source lines 5, 6 and 7 in Figure 6.13. Each of these source lines lies between the receiver at [-140, 0] and all other receivers. We therefore use convolution-type interferometry in this case. Panels (a) to (c) show the estimates from each source line. The scattered surface waves are well estimated from all gathers. Note that there are no strong spurious arrivals prior to the arrival of the direct surface wave but we do observe amplitude anomalies. For example there is a relatively strong event in the interferometric estimates moving out from 2.6 s at 124 m offset to 3.2 s at 200 m offset, which is present, but much weaker, in panel (e).

Slob *et al.* (2007) identified that spurious arrivals in convolution-type interferometry are different to those observed in correlation-type interferometry and propose the combination of the two methods to identify which arrivals are physical and which are non-physical. However, it remains unclear as to how this can be achieved, other than by comparison to find those events constructed by both

methods. We must be careful however, as this approach may not be suitable for scattered surface waves. For example, if we were to compare the results in Figure 6.16 with those in Figure 6.14 and Figure 6.15 individually, the comparisons would vary significantly. Figure 6.14 and Figure 6.16 compare favourably and both contain many of the same scattered events. However, comparing Figure 6.16 with Figure 6.15 many scattering events are not estimated in the latter, so it is difficult to identify which (if any) of the scattering events recovered in Figure 6.16 are spurious. Note that in the exploration case it is possible that estimates can be checked against the actual source-receiver data from which we may wish to remove the surface waves.

The results shown here indicate that it is possible to make estimates of scattered surface waves in attenuating media using realistic source geometries, and using only point-force sources. The cross-correlation results indicate that the quality of the estimate varies depending on the geometries of the chosen sources and receivers – in our examples certain source geometries are affected more by attenuation and certain source geometries also miss stationary points for scattered surface waves. By also producing results for convolution-type interferometry we obtain an additional set of estimates. By applying the convolution-type approach to our example we observe the relative insensitivity of the method to non-physical arrivals which may be introduced due to the effects of attenuation and limited aperture. This is explained by our stationary-phase analysis which indicates that there are only physical contributions to interferometry in the convolution-type approach whereas in the correlation-type approach there are non-physical events which may not cancel in non-ideal circumstances.

6.5 Discussion

In correlation-type seismic interferometry for scattered surface waves, the presence of attenuation introduces time- and offset-dependent amplitude errors and strong spurious arrivals. The latter relate to non-cancellation of contributions from stationary points that would cancel if there were no energy losses. Since these cancelling contributions are second order in the sense of being an interaction of two

scattered fields, first-order (Born) theory does not provide correct analysis of correlation-type interferometry, even for singly-scattered waves.

Vasconcelos (2007) derives an expression to account for these cancelling terms when interferometry is applied using wavefield separation. This requires a volume integral which accounts for energy losses due to back-scattering from heterogeneities along paths between boundary-source positions and receiver locations. Snieder (2007) derives a similar expression to account for energy losses along stationary paths due to anelastic attenuation. These expressions are,

$$i\omega\int_{r\in V}(\kappa_0-\kappa)G_0(\mathbf{r},\mathbf{r}_A)G^*(\mathbf{r},\mathbf{r}_B)dV \tag{6.2}$$

and

$$2\omega\int_{r\in V}\kappa_i G(\mathbf{r},\mathbf{r}_A)G^*(\mathbf{r},\mathbf{r}_B)dV \tag{6.3}$$

respectively, where G_0 is the Green's function in the background medium, G is the full Green's function, $(\kappa_0-\kappa)$ is the medium (compressibility) perturbation, and κ_i is the imaginary part of the compressibility. In the analysis of Vasconcelos (2007), $\kappa_i=0$ and integrals such as Snieder's would vanish. However, the similarity of these expressions suggests that the two effects are not unrelated, we can expect that volume integration over both the medium perturbations and the anelastic properties of the medium will be required to account for these non-cancelling terms in the presence of attenuation. Indeed, we noted in Section 6.3 that the errors due to un-cancelled non-physical events in the presence of attenuation are more abundant when the medium has greater complexity.

These spurious arrivals do not appear when we consider convolution-type interferometry; since there are no mutually-cancelling terms, spurious arrivals are not introduced due to attenuation. Therefore, where appropriate geometries are available we propose that the convolution-type approach be used in place of (or in addition to) correlation-type interferometry (convolution-type interferometry requires the

boundary of sources to intersect the inter-receiver path). What is more, for singly-scattered waves Born theory is correct for convolution-type interferometry.

Using more practical source geometries we have illustrated the difference in errors introduced between the convolution case and the cross-correlation case. A combined approach may therefore help identify spurious arrivals and select the best available estimates of the scattered surface waves as proposed previously for electromagnetic applications (Slob *et al.*, 2007; Slob and Wapenaar, 2007). While this may be appropriate in electromagnetic applications we have illustrated that it may not be suitable when considering scattered surface waves, as with restricted source geometries some scattering events may not appear in the interferometric estimate for one type of interferometry, but they may for the other. It then becomes difficult to discriminate between real scattered events and those that are spurious or non-physical. In exploration applications, in which surface waves are to be removed from source-receiver data, this is less of a problem due to the presence of the actual source-receiver data, which can act as an extra control against which to check the estimates.

In natural- or passive-source seismology we can only use sources that nature makes available. However, we know a lot about such sources. Extensive earthquake catalogues exist, and specific events can be selected to create a chosen boundary of sources (provided those earthquakes have been observed at all receivers of interest). The growing interest in seismic interferometry has created a better understanding of the sources of ambient noise that are used in passive interferometry (e.g., Stehly *et al.*, 2006; Pedersen *et al.*, 2007) and further to this, new methods, such as time-reversed focusing can be used to identify sources of ambient noise (Rhie and Romanowicz, 2004, 2006; Steiner *et al.*, 2008). With this in mind, it should be possible to identify locations (1) where we expect to observe inter-receiver scattered surface waves, and (2) where sources are available that may allow us to recover these using seismic interferometry (e.g., by forming orthogonal source lines, or closed boundaries of sources at the surface of the Earth that will cover stationary points for scattered surface waves). To date the vast majority of applications of seismic interferometry in such settings utilise the correlation-type integral. However, our findings suggest that better results may be obtained using the convolution-type

integral, and for surface waves it can be relatively straight-forward to find appropriate geometries of sources and receivers.

If scattered surface waves can be recovered successfully it may be possible to apply more complex inversion methods in passive-seismic tomography. Methods accounting for scattered surface waves such as those of Snieder (1986, 2002), Snieder and Nolet (1987), Meier *et al.* (1997), Marquering *et al.* (1999), Spetzler *et al.* (2002), and Ritzwoller *et al.* (2002) can take into account heterogeneities that lie off the great-circle path, and do not rely on the assumption that heterogeneities are of the same scale as the Fresnel zone or the dominant wavelength (as used in ray-geometrical tomography). This would allow the capabilities of seismic interferometry to be extended, allowing for more detailed imaging of the Earth's subsurface.

In exploration seismology, the successful recovery of scattered surface waves would allow for the adaptive removal of those surface waves from seismic surveys. Cross-line scattered surface waves are a particularly difficult form of noise to remove, and subsurface image quality is often compromised in areas with strong scattering. Interferometry provides an alternative method by which these arrivals can be estimated and then subtracted from source-receiver data, without the need for single scattering approximations and inverse-scattering schemes (e.g., such as in Blonk *et al.*, 1995; Blonk and Herman, 1996; Ernst *et al.*, 2002a; Ernst *et al.*, 2002b; Campman *et al.*, 2005; Campman *et al.*, 2006; Herman and Perkins, 2006), or the use of arrays required for acquisition-based methods (e.g., such as in Morse and Hildebrandt, 1989; Regone, 1998; Özbek, 2000a, 2000b).

While we have focussed on correlation- and convolution-type interferometry, recent advances have illustrated that deconvolution is a valuable tool in seismic interferometry, and may also be suitable for application in attenuative media (Vasconcelos and Snieder, 2008a, 2008b; Wapenaar *et al.*, 2008b).

6.6 Conclusions

The stationary-phase analysis in Chapter 5 has been used to illustrate the contributions involved in correctly recovering the inter-receiver scattered surface

wave, complementing the work in Chapter 4 on the recovery of inter-receiver direct multi-mode surface waves. This analysis reveals key differences between the stationary-phase analysis of seismic interferometry for reflected and scattered wavefields.

This analysis is illustrated using synthetic-scattered surface waves. We considered both single- and multiple- scattering models and confirmed the following observations from our theoretical analysis:

1. The direct surface wave is recovered from the cross-correlation of the direct surface waves only – previously shown by Snieder (2004a) and in Chapter 4.
2. The inter-receiver scattered surface wave is recovered from the cross-correlation of the direct surface waves with the scattered surface waves. This set of cross-correlations also introduces a spurious or non-physical arrival.
3. When scattering amplitudes are determined within the optical theorem, the spurious arrival introduced in step 2 is cancelled by the cross-correlation of the scattered surface waves observed at both receivers.

In order to solve for the correct scattered surface waves using the stationary-phase analysis, we observe that scattering amplitudes must have complex values, with the constraints on these values governed by the optical theorem for surface waves. Here we treat the particular case of isotropic density perturbations, and derive the constraints that the optical theorem places on the scattering amplitude. This emphasizes the importance of the optical theorem in such cases, and of stationary-phase analysis in furthering the understanding of physical phenomena.

The addition of attenuation into our examples causes further problems. Errors in amplitude due to energy losses result in steps 2 and 3 above not providing mutually cancelling terms. The direct and scattered surface waves can still be seen, but they exhibit amplitude errors. We have shown that by using convolution-type interferometry it is possible to avoid these errors, as this variation of the method accounts for attenuating media and is less sensitive to the non-physical arrivals introduced by limited aperture and attenuation.

We also find that a first-order Born analysis is not suitable for analysing the effects of correlation-type interferometry on scattered wavefields, while due to the absence of the non-physical parts of terms T2 and T3, such a Born analysis suffices when considering convolution-type interferometry.

We then consider more realistic geometries, representative of a 3-dimensional seismic survey but also perhaps of other passive situations such as a coastline emitting microseisms, an active fault plane or distributed anthropogenic-noise sources. These illustrate that different geometries are affected differently by attenuation, and certain geometries also result in the omission of stationary points for scattered surface waves. The use of convolution-type interferometry provides estimates that exhibit different types of errors than those seen in correlation-type interferometry. It may be possible to combine the two methods to identify those events which are errors and those which are real events (as proposed for the electromagnetic case). One might then select the source geometries which result in the best estimates.

Given that in some cases the geometry is such that correlation-type interferometry must be used in place of convolution-type interferometry, in Chapter 7 it is shown that move-out can be used to identify non-physical arrivals from correlation-type interferometry. Chapter 7 also shows how these arrivals can be removed, and also how directional balancing can be used to improve interferometric estimates.

Seismic interferometry has great potential. Successful recovery of more detailed seismograms, including features such as scattered surface waves may go some way to seeing this potential realised. In exploration geophysics this can allow for removal of scattered surface waves, allowing for more reliable subsurface imaging. In near-surface geophysics scattered surface waves can be used to invert for near-surface properties, and in regional and global seismology this can allow for the application of more complex tomography and imaging schemes, allowing the additional information contained in scattered waves to be put to use to create more informative images of the Earth’s crust and upper mantle.

7. Directional Balancing for Seismic and General Wavefield Interferometry

In passive-seismic interferometry using naturally occurring, heterogeneous noise sources, and in active-source seismic interferometry where sources can usually only be distributed densely on the exterior of solid bodies, bias can be introduced in Green's function estimates when amplitudes of energy have directional variations. In this chapter an algorithm is presented that removes bias in Green's function estimates constructed using seismic interferometry when amplitudes of energy used have uncontrollable directional variations. The new algorithm consists of two parts: (1) a method to measure and adjust the amplitudes of physical, incoming energy using an array of receivers, and (2) a method to predict and remove non-physical energy that remains (and can be accentuated) in interferometrically-derived Green's functions after application of the method in step (1). To accomplish step (2) we present two data-driven methods to predict the non-physical energy using either direct computation or move-out based methods, and a way to suppress them using (in this case) helical least-squares filters. We illustrate the algorithm's effectiveness using 2D acoustic-scattering examples.

7.1 Introduction

Seismic interferometry has recently become an important and popular approach to synthesise and analyse wavefields. Energy recorded at two receivers from an array of transient or noise sources spanning a boundary surface surrounding the receiver pair can be converted by simple crosscorrelation operations into approximations to the inter-receiver Green's function. This Green's function is the signal that would have been recorded at one receiver if the other receiver had been an impulsive source.

While Claerbout (1968) proved this in a 1-dimensional medium for the case of both receivers being at the same location (i.e., using only a single receiver),

Wapenaar (2003; 2004), van Manen *et al.* (2005; 2006) and Wapenaar and Fokkema (2006) proved this mathematically for 3-dimensional acoustic and elastic media, showing that in principle both monopolar (e.g., pressure) and dipolar (e.g., particle velocity/displacement) sources are required on the bounding surface.

van Manen *et al.* (2005; 2006; 2007) showed how either the impulsive- or noise-source versions of the above theory created a new computational schema with which synthetic wavefields between receivers could be modelled flexibly. In an industrial seismic setting, Bakulin and Calvert (2004; 2006) showed that in the case of receivers located in a subsurface horizontal borehole and sources located on the surface above the borehole, seismic interferometry can be used to re-datum sources into the borehole, removing many undesirable near-surface related effects from the seismic data. Draganov *et al.* (2007) showed that major body-wave components of Green's functions could be estimated using background (passive) noise records in a particularly quiet area. In Curtis *et al.* (2006), Dong *et al*. (2006) and Chapters 2 to 6 it is shown that in a seismic setting surface waves are particularly well recovered and can be used as part of a general surface-wave removal algorithm for use in cases where surface waves arrive simultaneously with important body-wave information.

In all of the above applications, Green's functions are constructed between a pair of receivers within the medium. In the acoustic case one of the receivers is effectively converted into a 'virtual' (imagined) source using Equation (1.2).

Note that in the application of Equation (1.2) the sources are implemented separately, as is the case in exploration geophysics where active sources are used. In the case where passive (i.e., uncontrolled) sources are used it can be considered that those sources act simultaneously. In this case time-averaging is required in order to cancel cross-terms appearing due to the crosscorrelation of different sources (see Snieder (2004a) and van Manen *et al.* (2006)). In the following we consider the exact application of Equation (1.2) for acoustic waves; however, given the relationships between Equation (1.2) and other forms of the interferometric integral our results can be interpreted in terms of both active- and passive-source interferometry (Wapenaar and Fokkema, 2006). van Manen *et al.* (2006) and Wapenaar and Fokkema (2006) give equivalents of these formulae for elastic-wave propagation, and Slob and Wapenaar (2007) and Slob *et al.* (2007) give equivalents for electromagnetic-wave

propagation. Under a unified formulation of the theory it has been shown that other types of Green's functions can be retrieved, such as electrokinetic Green's functions in poroelastic or piezoelectric media (Wapenaar *et al.*, 2006), and Wapenaar and Fokkema (2006) also show by using the Sommerfield radiation condition (Born and Wolf, 1999) that the source requirements for integrals such as Equation (1.2) can be relaxed such that only monopole sources are required. Hence, while the examples in this chapter concern acoustic wave propagation and the use of both monopole and dipole sources, the method proposed here can be applied using equivalent formulae for other wave propagation regimes and the use of single source types.

In order to obtain the Green's functions using Equation (1.2) it is necessary that Green's functions from the boundary are known, and hence that the medium within S has been illuminated evenly from all directions. In practical situations with impulsive sources this implies that energy from all boundary sources should be normalizable to unit impulses, while for random-noise sources it implies that the total power radiated by each source is equal.

While normalisation might be possible for actual sources fired given source signature recordings, nobody has described how to do this correctly where the source recording is inaccurate or incomplete, or for missing boundary sources such as is the norm in industrial-exploration seismology where sources are generally confined to the near-surface of the Earth (and hence do not surround the receiver pair at depth). Nor has there been any method presented to correct the case of seismic interferometry using passive- or background-noise sources where these could each have quite different magnitudes such as is commonly the case in passive-noise seismology (Stehly *et al.*, 2006). Hence, from numerical experiments we know that in such cases strong biases will be introduced in the interferometric Green's functions (van Manen *et al.*, 2005; van Manen *et al.*, 2006; Wapenaar, 2006; Vasconcelos and Snieder, 2008a, 2008b).

While one method of correction has been proposed by Douma and Snieder (2006), it relies on a statistical model of the noise which is generally unknown in exploration-geophysical applications. In another method by Mehta *et al.* (2007) it was shown that wavefield separation into up- and down-going components prior to interferometry, and crosscorrelation of down-going and up-going wavefields could

help to suppress spurious overburden-related effects in the horizontal well-based method of Bakulin and Calvert (2004; 2006). They also apply the method to seabed data to remove the effects of sea level changes. However, neither of these methods creates uniform noise directionality, and they do not generalise in an obviously robust way to 3D heterogeneous media with a less linear source or receiver array. van der Neut and Bakulin (2009) propose a method by which the amplitude radiation pattern of a virtual source can be estimated and corrected using wavefield separation prior to directional balancing. Their approach is for a linear array of sensors in the subsurface, where the array lies inside a homogeneous layer and spans both virtual-source and receiver locations. The method simultaneously adjusts directionality and removes the effect of any overburden on the estimated wavefields in a similar fashion to the method of Mehta *et al.* (2007). Another method is introduced by Wapenaar *et al.* (2008a) who propose the use of multi-dimensional deconvolution (MDD) of separated passive wavefields. They show that theoretically MDD will solve the problem of irregular source strength *and* irregular amplitude; however this requires that data can be processed to separate the wavefield into the components required for MDD.

In this chapter we present a method that corrects for directional bias in interferometric estimates where the sources on the boundary surface S have variable source strength. This method requires no knowledge of the background source distribution, hence it is ideal for application to cases where passive-seismic interferometry is applied, but is equally applicable to situations using active sources. Here we show that if the wavefield at either of the pair of receivers can be decomposed directionally at one of the receiver locations (e.g., by using a local receiver array), a virtual source with near-uniform directionality can be constructed using an algorithm that we call directional balancing. This algorithm is applicable to full wavefields (i.e., no other wavefield separation is required prior to its use), and works implicitly with multi-dimensional arrays and (since it requires only *local* directional decomposition) in heterogeneous media. However, the method we use to correct directionality does not remove non-physical arrivals that are introduced during directionally-biased interferometry in heterogeneous media. We therefore propose a second method that predicts and removes such non-physical arrivals post

directional balancing. The resulting corrected Green's function estimates show much reduced effects of non-uniform source-strength distribution in the presence of directional bias. These estimates are therefore more appropriate for use in a conventional seismic processing flow, especially those where both travel-time and amplitude information are required. This is especially important where passive-seismic interferometry is used to supplement active-source data, in which case it is desirable that the passive estimates closely resemble the character of the active-source data.

We begin by detailing the directional-balancing algorithm, and apply it to examples of increasing complexity, illustrating the emergence of non-physical arrivals as the medium complexity increases. We explain from where these arrivals originate, and propose two new methods to identify them from physically-propagating waves. Finally we use least-squares filters to remove the non-physical arrivals from the directionally-balanced data.

7.2 Directional Balancing

We wish to estimate a directionally unbiased (isotropic) Green's function between a virtual source at $\mathbf{r}_1$ and a receiver at $\mathbf{r}_2$ at both of which there are physical receivers, where $\mathbf{r}_1$ is also surrounded by a local array of receivers $\mathbf{r}_{x_i}$.

In order to estimate correction factors to account for directional bias in the interferometric estimate we first consider *only* the virtual source location ($\mathbf{r}_1$) and the surrounding local array of receivers ($\mathbf{r}_{x_i}$). Using interferometry we calculate all biased Green's functions $G'(\mathbf{r}_1, \mathbf{r}_{x_i})$, we apply Equation (1.2), but in practice one may consider any interferometric integral. $G'(\mathbf{r}_1, \mathbf{r}_{x_i})$ contains information about the local radiation pattern of the virtual source. Later we show that if the medium is heterogeneous the estimates contain non-physical arrivals, hence we assume that physical arrivals dominate the estimates in the immediate near field at early times (the following results show that this assumption is valid). We determine a local model at and around the receiver array and model wave propagation *locally around the virtual source* (i.e., we model only the initial radiation pattern within the array,

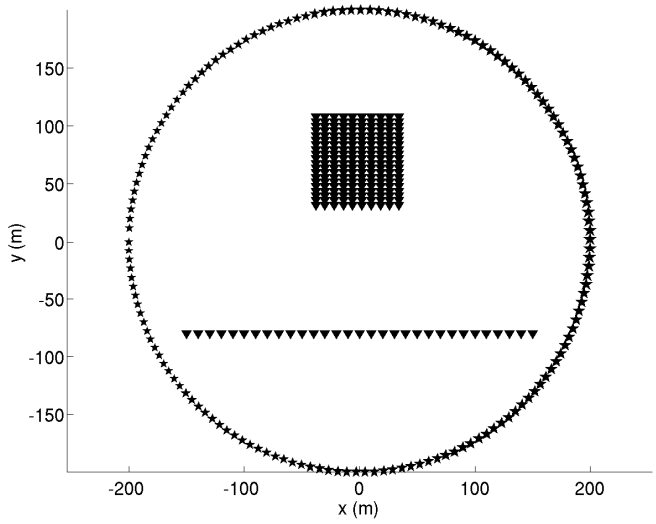

Figure 7.1: Source (stars) and receiver (triangles) geometry for the homogeneous example. Every second boundary source and array receiver is plotted for clarity. Note that the size of the source symbol varies with source strength (i.e., strongest source at [200, 0] m and weakest at [-200, 0] m).

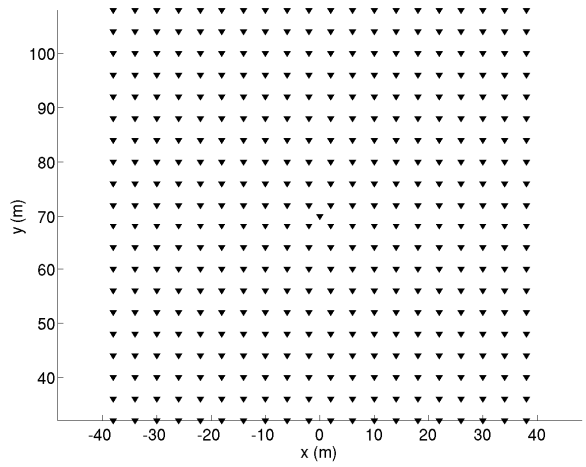

Figure 7.2: Geometry of the receiver array.

hence a simple model may be sufficient), and calculate synthetic Green's functions $G(\mathbf{r}_1, \mathbf{r}_{x_i})$, which are isotropic and diffraction limited (see below). We wish to find a scaling factor in some domain *D* that adjusts the source directionality of the biased interferometric estimates to have the same source directionality as the modelled data.

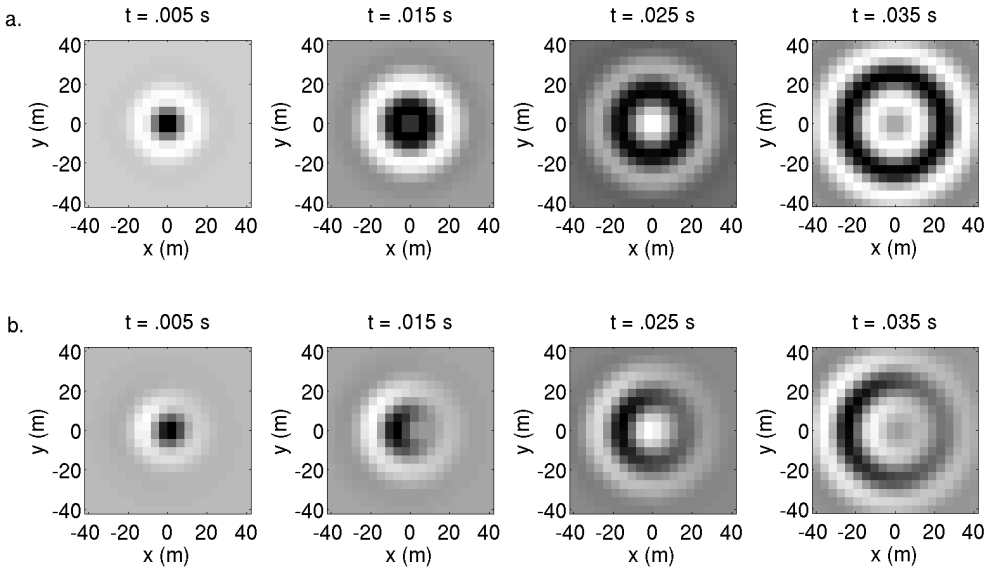

Figure 7.3: (a) Snapshots of the uniform radiation pattern across the virtual source array. (b) Equivalent snapshots for the non-uniform radiation pattern across the virtual source array in the homogeneous medium (see Figure 7.1). In this figure the centre of the array is at the origin of the co-ordinate system.

As such, the method relies on having a good estimate of the Earth properties (for the model) immediately at and around the virtual-source array.

As an example of the method, we consider the case where the domain D is the frequency-wavenumber (*f-k*) domain and we cast the problem of finding the optimal directional balancing scaling factor $C^{OPT}(\mathbf{r}_1, \mathbf{k}_{x_i})$ as a least-squares problem:

$$C^{OPT}(\mathbf{r}_1, \mathbf{k}_{x_i}) = \underset{\arg\ C}{\min} \left(\left\| G(\mathbf{r}_1, \mathbf{k}_{x_i}) - C(\mathbf{r}_1, \mathbf{k}_{x_i}) G'(\mathbf{r}_1, \mathbf{k}_{x_i}) \right\| \right). \tag{7.1}$$

Note that the *f-k* transform is taken across the array, hence the change of co-ordinate from $\mathbf{r}_{x_i}$ to $\mathbf{k}_{x_i}$ but not from $\mathbf{r}_1$ to $\mathbf{k}_1$, and since the array is in 2D this is a 3D Fourier transform. The scaling factor $C^{OPT}(\mathbf{r}_1, \mathbf{k}_{x_i})$ corrects for directional bias in interferometrically estimated Green's functions $G'(\mathbf{r}_1, \mathbf{r}_{x_i})$, but since this involves correcting for energy directionality it can also be used to correct $G'(\mathbf{r}_{x_i}, \mathbf{r}_2)$ (i.e., between the virtual source array ($\mathbf{r}_{x_i}$) and any other receiver ($\mathbf{r}_2$)). Transforming

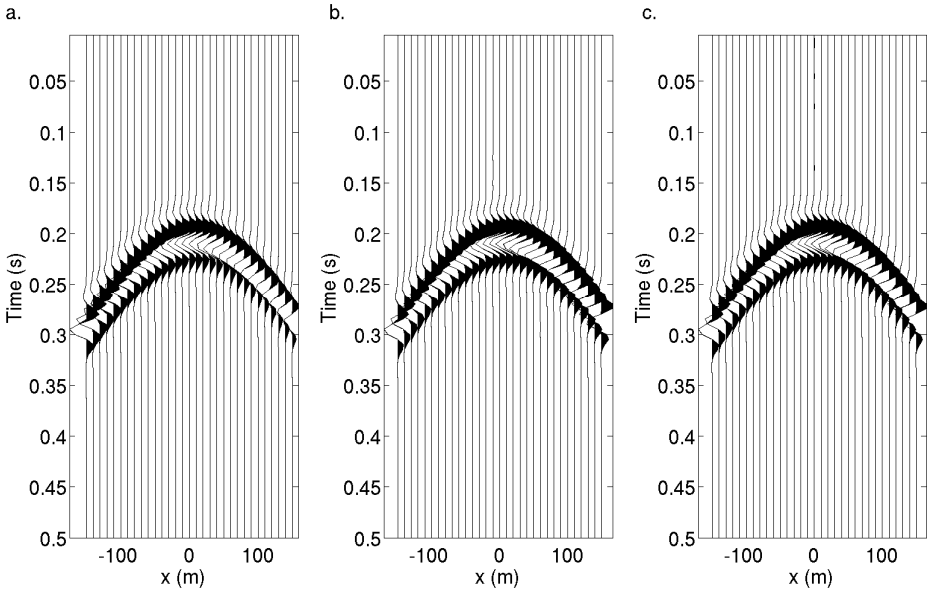

Figure 7.4: Results for the homogeneous medium. (a) Biased interferometric estimate, (b) corrected interferometric estimate, (c) exact Green's functions. The virtual source is in the centre of the receiver array shown in Figure 7.2 and the response is recorded at the line array at the bottom of Figure 7.2.

$G'(\mathbf{r}_{x_i}, \mathbf{r}_2)$ to $G'(\mathbf{k}_{x_i}, \mathbf{r}_2)$ (or any other chosen domain *D*), allows the correction factor to be applied as,

$$G''(\mathbf{k}_{x_i}, \mathbf{r}_2, \omega) = C^{OPT}(\mathbf{r}_1, \mathbf{k}_{x_i}, \omega)\ G'(\mathbf{k}_{x_i}, \mathbf{r}_2, \omega), \tag{7.2}$$

where $G''(\mathbf{k}_{x_i}, \mathbf{r}_2, \omega)$ are the corrected Green's function in the *f-k* domain. Transforming back to the original domain and interpolating to the location $\mathbf{r}_1$ gives $G''(\mathbf{r}_1, \mathbf{r}_2)$: this is a less biased estimate of the Green's function $G(\mathbf{r}_1, \mathbf{r}_2)$.

We have to interpolate to the location $\mathbf{r}_1$ because the modelling method used cannot model a coinciding source and receiver (there is a singularity at zero offset); other modelling approaches may not require this additional interpolation step. Note that we have chosen to implement the algorithm in a frequency-dependent manner because different frequencies of wave propagation are sensitive to different Fresnel zones in the medium.

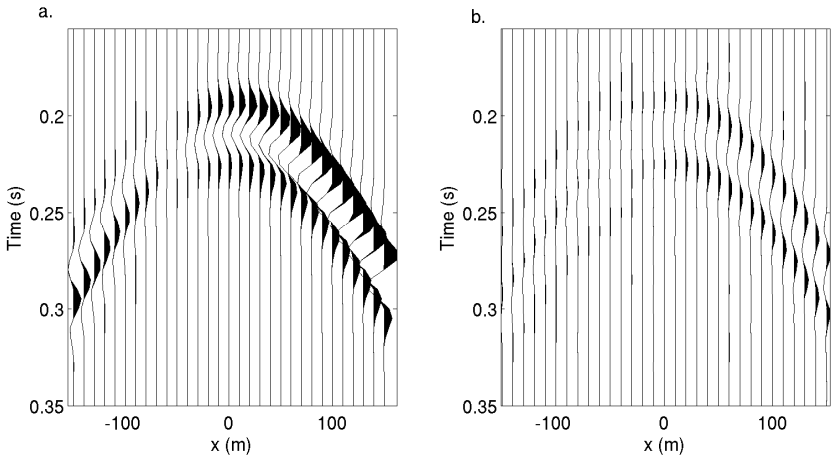

Figure 7.5: (a) Zoomed plot of the mismatch between gathers in Figure 7.4a and c after normalization of each gather to peak amplitude of 1. (b) Zoomed plot of the mismatch between gathers in Figure 7.4b and c (no normalization is used).

To construct the ideal radiation pattern, $G(\mathbf{r}_1, \mathbf{r}_{x_i})$ we deliberately use the diffraction-limited modelling method of van Manen *et al.* (2005; 2006; 2007). Those authors show that in the application of seismic interferometry, in the very near field of the virtual-source point the Green's function cannot be constructed correctly. This is attributed to the diffraction-limited nature of seismic interferometry and time-reversal. This is related to the work of de Rosny and Fink (2002) who discuss the role of the diffraction limit in time-reverse imaging. Consequently, experiments show that using a non-diffraction limited modelling method gives incorrect results in the above algorithm. However, by using this interferometric modelling method our modelled radiation pattern is consistent with the limitations of the interferometric estimates in the very near field.

In the above algorithm we have assumed that the ideal source radiation is isotropic, but of course any other desired source radiation pattern could be modelled in $G(\mathbf{r}_1, \mathbf{r}_{x_i})$, and hence approximated by the algorithm in Equations (7.1) and (7.2).

Application of Directional Balancing

To illustrate the directional balancing algorithm we use a series of synthetic acoustic models. We first use a homogenous acoustic example to step through the application

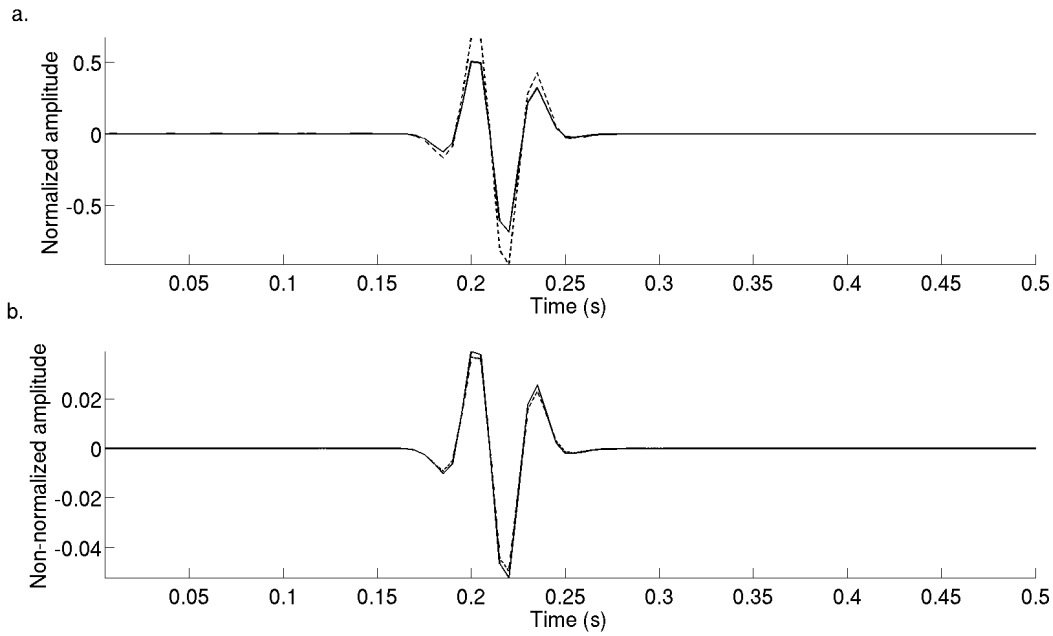

Figure 7.6: (a) Single trace from Figure 7.4a (solid line), with single trace from Figure 7.4c (dashed line) for receiver at x = 50 m. Gather normalization has been applied. (b) Same as for (a) but using traces from Figure 7.4b and c.

of the algorithm and to illustrate that it can correct for non-uniform boundary-source amplitude distribution. We then consider more complex examples.

We use a 2-D geometry (Figure 7.1), consisting of a circular boundary of sources (radius 200 m, sources separated at 4 m) with a 20 by 20 array of receivers (4 m separation) around the virtual source location, the boundary is centred on [0, 0] m and the array is centred on [0, 70] m. At the centre of the array we place an additional receiver at the virtual source location, i.e., this is the location at which we wish to apply our corrections (Figure 7.2). The size of the virtual source array was chosen as it was found that a 20 by 20 square array of receivers gives good results – the array geometry has not been optimised in any way. We choose a line of 31 receivers, ranging from [-150, -80] m to [150, -80] m with a separation of 10 m at which we want to record energy from the virtual source. The wave propagation velocity of the medium is 750 m/s and a Ricker wavelet with centre frequency of 30 Hz allows the source separation of 4 m to be well sampled.

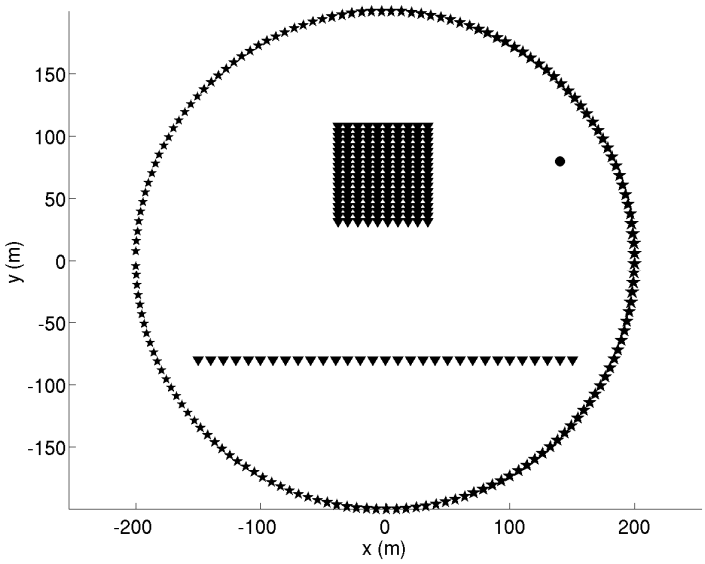

Figure 7.7: Single scatterer geometry. Symbols are as for Figure 7.1, dot indicates the scatterer location.

We define a non-uniform source strength by the function T_j where T is the strength of the source and j denotes the boundary location. We use a cosine function with a minimum value of 1 and a maximum value of 2 to define this variation in source strength (Figure 7.1).

Seismic interferometry estimates superpose a causal and an acausal Green's function. In all examples below we consider (and time-reverse for plotting purposes) the acausal part of the interferometric estimate. We do not show both acausal and causal parts since these would require the derivation and application of different scaling factors.

For this first example we use a simple homogeneous medium. Following step 2 we model the desired source radiation pattern, $G(\mathbf{r}_1, \mathbf{r}_{x_i})$ using interferometric modelling (van Manen *et al.*, 2005; 2006; 2007). This allows us to model a diffraction-limited Green's function, which as discussed above is what we expect in an interferometric estimate. Snapshots of this radiation pattern are shown in Figure 7.3a. We then determine the non-uniform radiation pattern of the interferometric Green's function $G'(\mathbf{r}_1, \mathbf{r}_{x_i})$ as detailed in step 1. Snapshots of this radiation pattern are shown in Figure 7.3b.

To determine the scaling factor ($C^{OPT}(\mathbf{r}_1, \mathbf{k}_{x_i})$) the radiation patterns are first tapered in space. We use a relatively harsh spatial taper (spatial cosine tapers are applied to 90% of the array) as we find that this provides good results in this case. A 3-dimensional (3-D) Fourier transform is applied to the tapered source-radiation patterns, i.e., we transform the data to the f-k_x-k_y domain, so $G(\mathbf{r}_1, \mathbf{r}_{x_i})$ and $G'(\mathbf{r}_1, \mathbf{r}_{x_i})$ become $G(\mathbf{r}_1, \mathbf{k}_{x_i})$ and $G'(\mathbf{r}_1, \mathbf{k}_{x_i})$ respectively. To determine a scaling factor we divide the absolute values of $G(\mathbf{r}_1, \mathbf{k}_{x_i})$ by the absolute values of $G'(\mathbf{r}_1, \mathbf{k}_{x_i})$. Using the absolute values ensures that the scaling factor is real valued. However, if in another application both phase and amplitude are to be corrected then a complex valued scaling factor may be used. A small factor is added to the denominator to stabilise the division; we use a water level method and set the minimum level to 5% of the maximum value of the denominator (Clayton and Wiggins, 1976). In the following we apply the scale factor by tapering the biased interferometric estimates in space (using the same taper as for the radiation patterns), transforming the biased estimates into the f-k_x-k_y domain, multiplying by the scale factor, and applying the 3-D inverse Fourier transform. This gives the corrected estimates in the t-x-y domain. Since we have corrected Green's functions across an array while our desired virtual source location is at the centre of the array, we interpolate between the four central array receivers to obtain our final, unbiased estimate of $G(\mathbf{r}_1, \mathbf{r}_2)$.

In Figure 7.4a we show the set of biased interferometric Green's function estimates between the central-array receiver (the virtual-source position) and all receivers on the receiver line in the geometry plot in Figure 7.2 i.e., we determine $G'(\mathbf{r}_1, \mathbf{r}_2)$ as in step 4 above. The corrected Green's functions $G''(\mathbf{r}_1, \mathbf{r}_2)$ are shown for comparison in Figure 7.4b, with the desired (directly-modelled, unbiased) result plotted in Figure 7.4c. It is difficult to see any variation between these plots. Since only a small portion of the boundary around the top and bottom of the boundary-source array contributes to these estimates (Snieder, 2004a) the amplitude variation in Figure 7.4a is not particularly large. To highlight the differences we normalize both the entire, biased, estimated gather in Figure 7.4a and the exact gather in Figure 7.4c to a maximum of 1, and plot the difference between these normalized gathers (zoomed plots shown in Figure 7.5a). We also take the difference between the

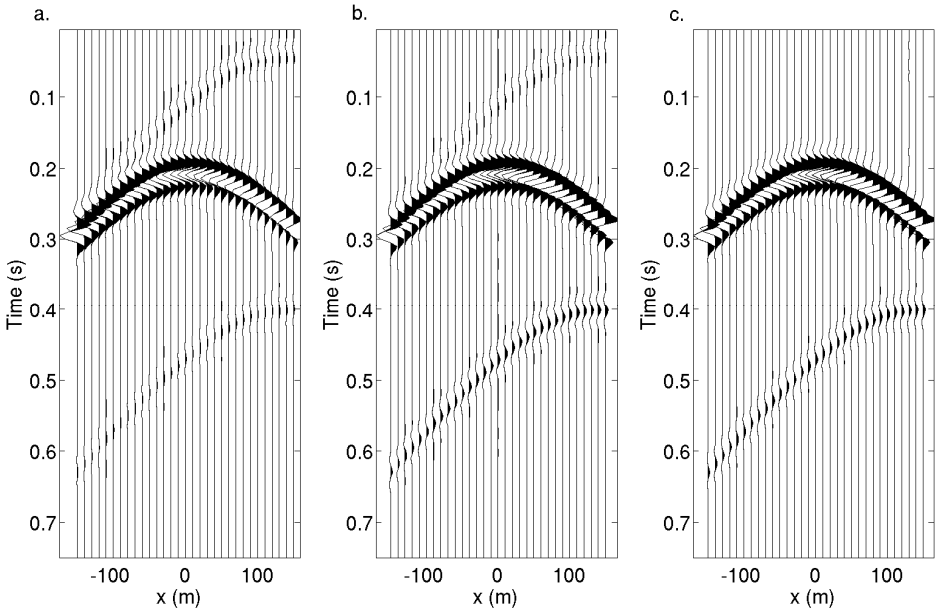

Figure 7.8: As for Figure 7.4 but using the single scatterer example.

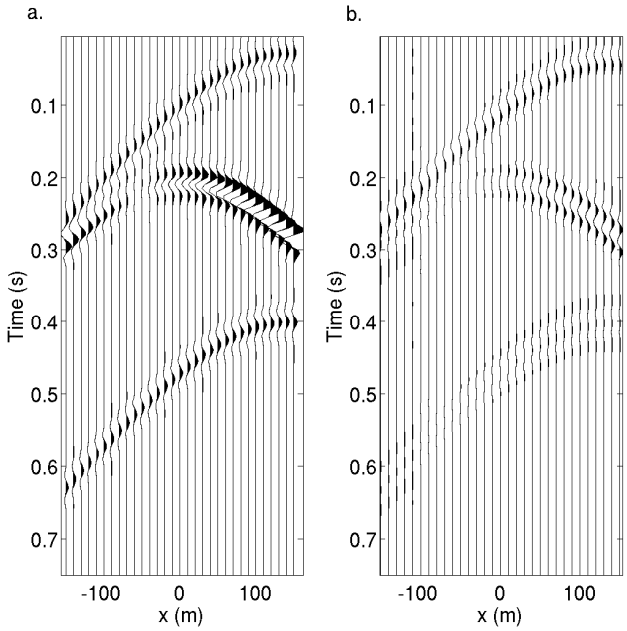

Figure 7.9: As for Figure 7.5 but for the single scatterer example.

corrected gather in Figure 7.4b and the exact gather and plot this in Figure 7.5b: no scaling is applied to this latter plot since the correction factor has already accounted for the amplitude imbalance. This lack of scaling illustrates the effectiveness of the method in this configuration. Note that both plots in Figure 7.5 are scaled such that

they are shown at twice the scale of those in Figure 7.4. It is clear that the proposed algorithm corrects for most of the amplitude imbalance introduced by the non-uniform source strength. Finally to illustrate the fit in more detail, in Figure 7.6 we plot a single trace from Figure 7.4a along with a single trace from Figure 7.4b (using the trace at x equal to 50 m). In Figure 7.6a we use the same gather normalization as in Figure 7.5a, and the misfit can be seen clearly. No additional scaling is applied in Figure 7.6b; note the improved fit.

In the examples we consider, if no amplitude correction is required (i.e., if the scaling function is equal to one) then the use of tapers and stabilization factors will affect the result – correct amplitudes may in fact be incorrectly scaled and numerical noise may be introduced by the tapers and stabilization factors. We avoid this case by ensuring that our desired radiation pattern is scaled such that it is always smaller than the biased estimates, therefore the scale factor is never equal to one.

We now follow the same procedure as for the homogeneous case but use the single-scatterer model in Figure 7.7. To compute scattered wavefields we use a deterministic variant of Foldy's method (Foldy, 1945; Groenenboom and Snieder, 1995; van Manen *et al.*, 2006), where the scattering amplitude is governed by the optical theorem. We assign the imaginary part of each scatterer an equal strength of -3.9 and use the optical theorem to determine the corresponding real part of the scattering amplitude (Groenenboom and Snieder, 1995). The optical theorem ensures that both the back scattered (reflected) and forward scattered (transmitted) waves are modelled with the correct amplitude (which is not true in the linearized Born approximation). In Figure 7.8, 7.10 and 7.11 we reproduce Figure 7.4, 7.6 and 7.7 for this case. We can see that, similarly to the homogeneous case, the amplitudes are well estimated by directional balancing, with only a small residual error.

Notice that we can see non-physical arrivals prior to the first physical arrival in Figure 7.10a (prior to 0.1 s), and these also exist in the corrected estimates in Figure 7.10b. These non-physical arrivals arise due to crosscorrelation of physical waves; later in this chapter we explain why these non-physical arrivals appear in our estimates and propose two methods to identify and remove them.

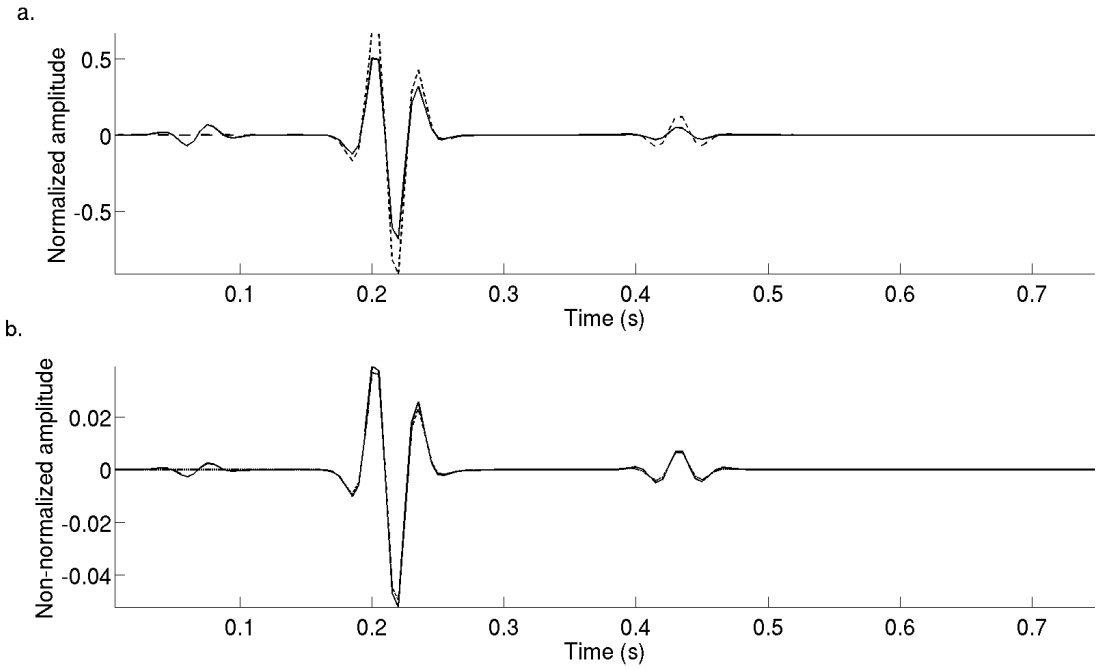

Figure 7.10: As for Figure 7.6 but for the single scatterer example.

We now show results of the algorithm using an example with 12 scatterers (Figure 7.11) in Figure 7.12 and Figure 7.13. Note that we now use a slightly different receiver array, extending from [-120, -88] m to [120, -88] m with a receiver separation of 4 m, and to accentuate the directional bias the boundary source amplitude now has a minimum value of one and a maximum value of four. Here we have used a 1% water level (as opposed to the 5 % discussed above) as we find that results thus improve in this case.

The same non-physical arrivals observed in the previous section are seen here but they are more abundant and occur at different times (both prior to, and after the arrival of the direct wave). Since these errors are also rescaled by the correction factors in the final result we can expect mis-matches between the corrected result and the exact result. Despite this we can see similarities between the corrected result and the exact result in Figure 7.12. For example the region around 0.3 to 0.5 s and 0 to 150 m shows enhanced amplitudes with respect to the original, biased result of interferometry. These are illustrated also in the residual plot in Figure 7.13 (plotted at 3 times the scale of Figure 7.12) which shows that improvements have been made for the physical arrivals, but that in this case the non-physical arrivals are of far larger

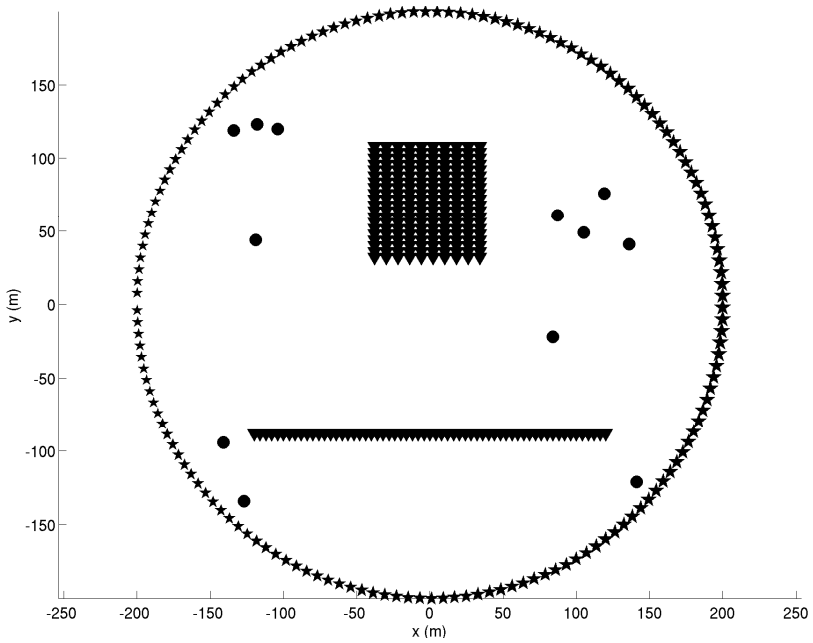

Figure 7.11: Geometry for the multiple-scatterer model. Symbols are as for Figure 7.7.

magnitude than residuals in the physical arrivals. Note that by comparing Figure 7.12c and Figure 7.13b some events in the residual appear to correspond to physical arrivals in the directly modelled data. What we observe is that in more complex media while our method assumes these to be non-physical arrivals it is possible that they contribute physical arrivals. In the examples that we show these arrivals are small and do not have a strong impact on our final results; however, in very complex media these amplitudes may be larger.

Note that the non-physical arrivals prior to the first physical arrivals are much stronger in the corrected estimate than in the biased estimate since they have been magnified by directional balancing. This is because the balancing algorithm is designed to correct amplitudes of *physically-propagating* waves, since the correction factors are determined using only physical waves. Hence, the multiplicative correction factors are inappropriate for the non-physical waves. We can also expect that similarly magnified, non-physical waves arrive *after* the first arrival, but with weaker absolute amplitude (since these non-physical arrivals are related to the weaker, higher-order scattering). This explains why the residual in Figure 7.13b contains so much energy from the non-physical arrivals. We now focus attention on these arrivals and show how they can be predicted and suppressed.

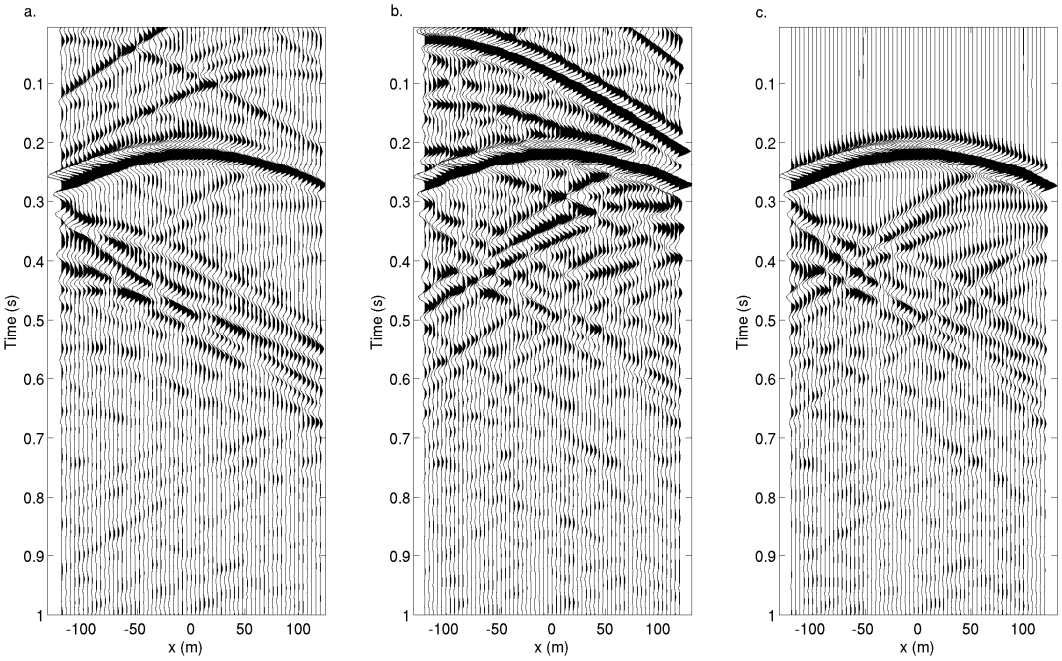

Figure 7.12: As for Figure 7.8 using the multiple scatterer model.

7.3 Non-Physical Arrivals

In all of the heterogeneous examples above we observe that non-physical arrivals are introduced in the biased interferometric estimates. In the examples we consider these non-physical arrivals are most apparent prior to the first physical arrival, where we expect no arrivals at all (e.g., compare Figure 7.12a and c prior to 0.2 seconds). We have suggested that the residuals between the directly modelled results and the corrected results are predominantly due to these non-physical arrivals, i.e., arrivals such as those in Figure 7.13b correspond to non-physical arrivals introduced by the non-uniform amplitude distribution of the sources. We now justify this claim in more detail.

Non-physical (sometimes called *spurious*) arrivals can appear in interferometric estimates when interferometry is applied in non-ideal circumstances, for example by applying interferometry using only surface sources or other spatially limited source geometries (Snieder *et al.*, 2006; Wapenaar, 2006; Vasconcelos and Snieder, 2008a; 2008b; Chapter 4), or by applying interferometry in the presence of attenuation (Wapenaar *et al.*, 2006; Snieder, 2007; Snieder *et al.*, 2007; Chapter 6).

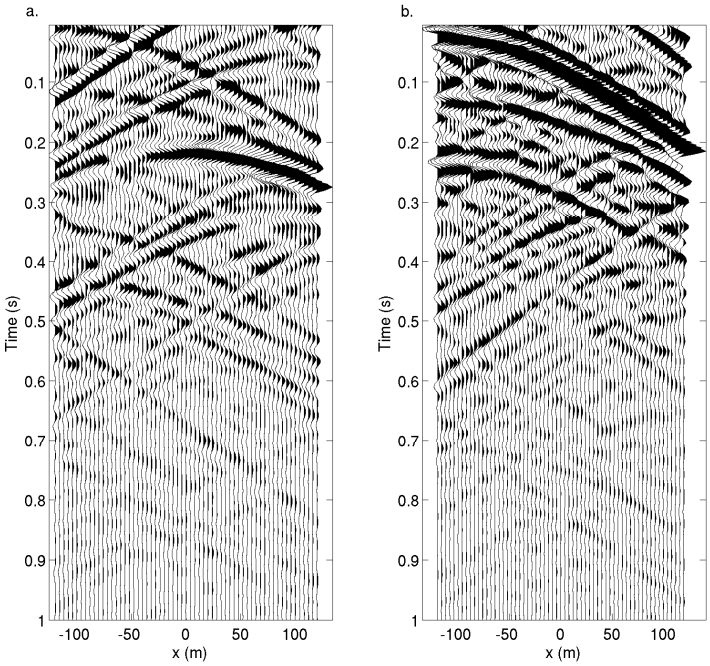

Figure 7.13: As for Figure 7.9 but using the multiple scatterer model.

Non-physical arrivals introduced by non-uniform background source strengths can be understood in a similar manner to the non-physical arrivals introduced for surface waves in Chapter 6 and for acoustic waves by Snieder *et al.* (2008). We briefly summarise the approach for acoustic waves here.

The wavefield is separated into direct waves and scattered waves before interferometry is applied, resulting in four separate contributing terms. These are referred to as T1 to T4, representing the contributions of the crosscorrelation of the direct waves with the direct waves (T1), the direct waves with the scattered waves (T2), the scattered waves with the direct waves (T3), and the scattered waves with the scattered waves (T4). Similar analyses can be found using representation theorems for perturbed media (Vasconcelos *et al.*, 2009) and for deconvolution interferometry (Vasconcelos and Snieder, 2008a, 2008b).

We first define the direct and scattered wavefields between the receiver locations $\mathbf{r}_1$ and $\mathbf{r}_2$ as $G^0(\mathbf{r}_1,\mathbf{r}_2)$ and $G^{sc}(\mathbf{r}_1,\mathbf{r}_2)$ and assume that we wish to estimate these wavefields using interferometry. Terms T1 to T4 provide the following contributions to this estimate:

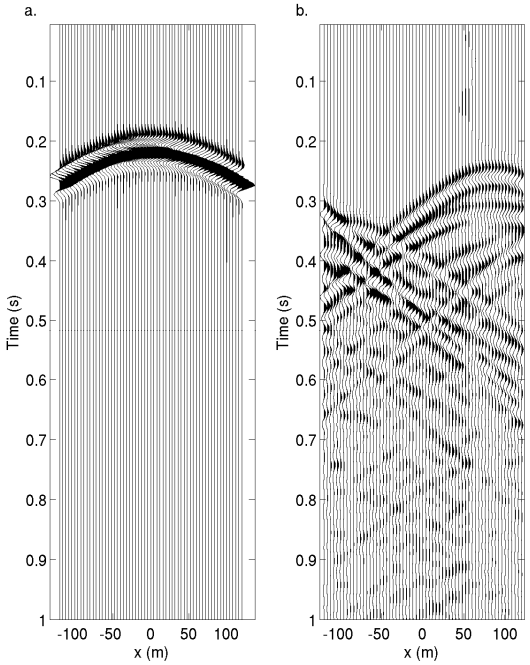

Figure 7.14: (a) Directly modeled direct wavefield between the central receiver of the virtual source array and the receiver line, (b) the equivalent directly modeled scattered wavefield.

$$T1 = G^{0^*}(\mathbf{r}_1, \mathbf{r}_2) - G^{0}(\mathbf{r}_1, \mathbf{r}_2) \tag{7.3}$$

$$T2 = G^{sc^*}(\mathbf{r}_1, \mathbf{r}_2) + G^{np1}(\mathbf{r}_1, \mathbf{r}_2) \tag{7.4}$$

$$T3 = -G^{sc}(\mathbf{r}_1, \mathbf{r}_2) + G^{np2}(\mathbf{r}_1, \mathbf{r}_2) \tag{7.5}$$

$$T4 = -G^{np1}(\mathbf{r}_1, \mathbf{r}_2) - G^{np2}(\mathbf{r}_1, \mathbf{r}_2)\,. \tag{7.6}$$

We have introduced the terms $G^{np1}(\mathbf{r}_1, \mathbf{r}_2)$ and $G^{np2}(\mathbf{r}_1, \mathbf{r}_2)$ to represent the non-physical parts of terms T2 to T4. For the acoustic case Snieder *et al.* (2008) show that when interferometry is applied exactly (i.e., application of Equation (1.2) using a non-biased closed boundary of sources) these non-physical terms cancel when all four terms are summed, and the direct and scattered waves are recovered as desired.

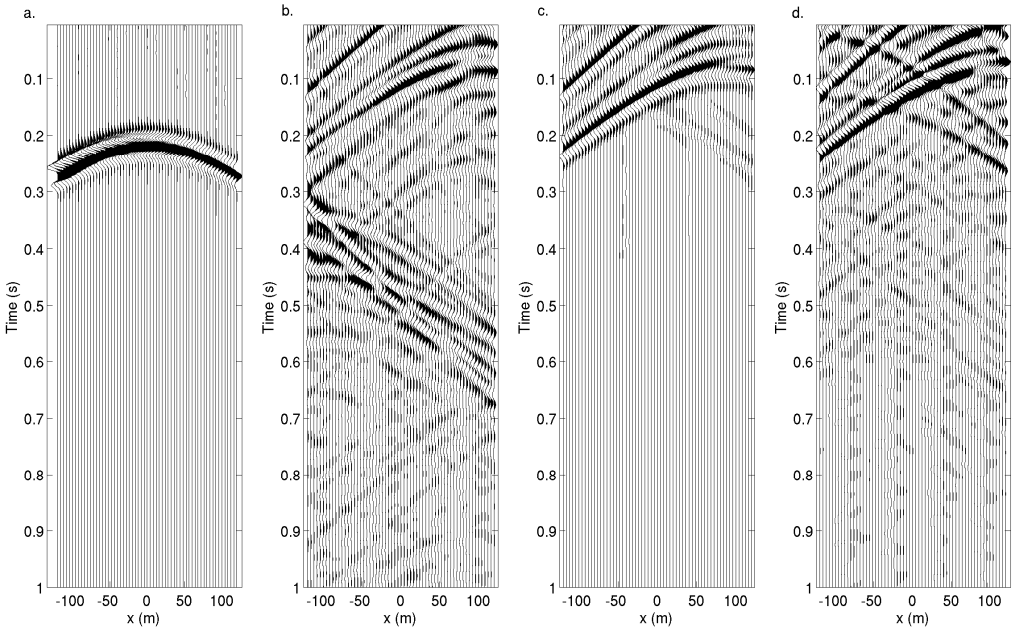

Figure 7.15: Interferometry applied to separated wavefields using a non-uniform source strength. (a) Direct waves cross-correlated with direct waves, (b) direct waves cross-correlated with scattered waves, (c) scattered waves cross-correlated with direct waves, (d) scattered waves cross-correlated with scattered waves.

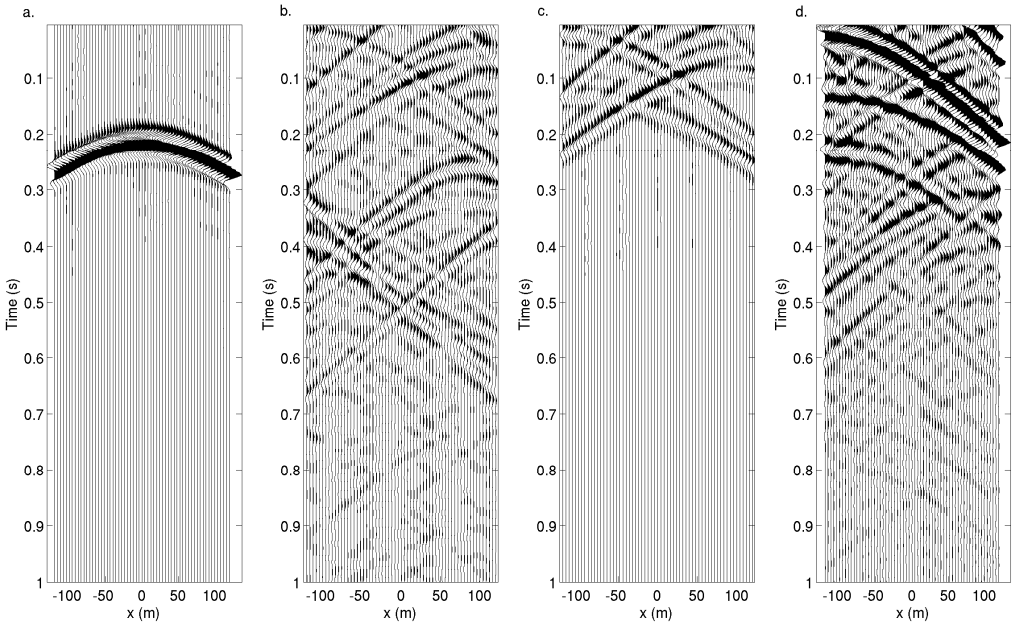

Figure 7.16: As for Figure 7.15, with directional balancing applied.

However, if we consider a non-uniform source strength distribution then the amplitudes of the four different terms will vary, and the non-physical arrivals will

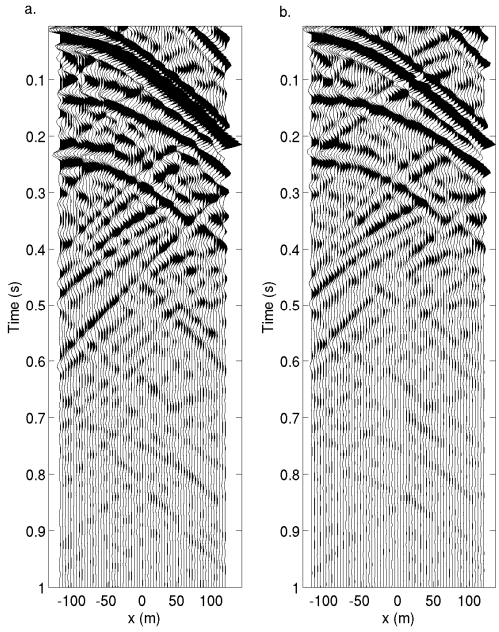

Figure 7.17: (a) Residual from Figure 7.13b, (b) Non-physical term (T4) from Figure 7.16d.

not necessarily cancel, explaining why non-physical arrivals are observed in interferometric estimates. We expect that the amplitudes of the physical parts of the estimate (i.e., the biased estimates $G^{'0}(\mathbf{r}_1,\mathbf{r}_2)$ and $G^{'sc}(\mathbf{r}_1,\mathbf{r}_2)$) can be corrected using the directional-balancing algorithm above (provided that the local Earth model at the virtual source is correct), but that a separate additional approach may be required in order to mitigate for non-cancellation of these non-physical terms. In the remainder of this chapter we present two methods with the potential to predict and isolate the non-physical terms so that they can be removed from the interferometrically-constructed Green's functions.

Wavefield-Separation Based Method

In a first method we predict the non-physical arrivals by assuming that the wavefield can be separated into two components (the direct and scattered waves) and cross-correlate only the scattered waves to find an estimate of term *T*4. Scattered-wavefield separation methods are used by several authors to apply and analyse seismic interferometry (Snieder *et al.*, 2008; Vasconcelos and Snieder, 2008a; 2008b; Chapter 6; Vasconcelos *et al.*, 2009). To test the potential of this method we model

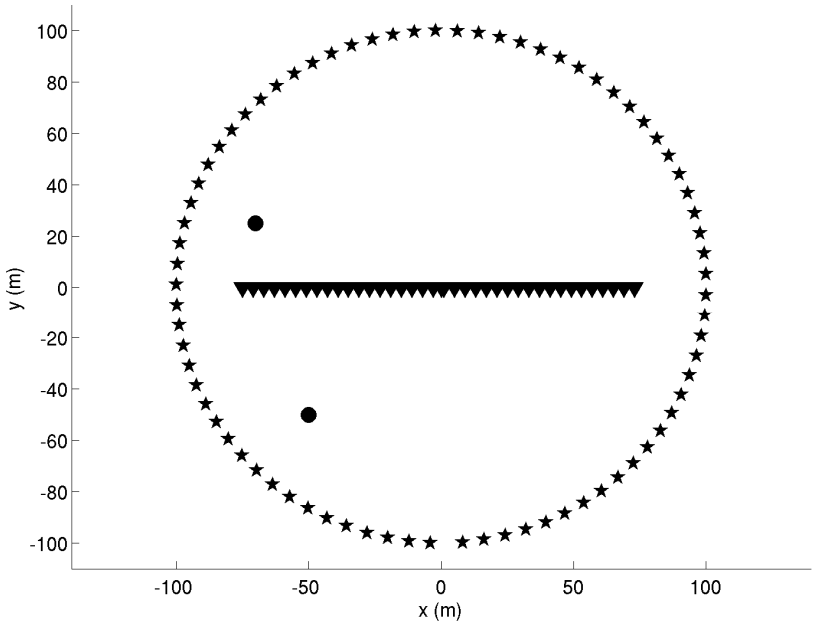

Figure 7.18: Geometry of the two scatterer model. Only every second source and receiver are shown. Symbols are as for Figure 7.11.

the synthetic wavefield in two steps: first determining the direct waves (G^0) and then determining the scattered waves (G^{sc}), allowing us to calculate the four terms above explicitly. In practice, these would have to be separated in real data using time-windowing, *f-k* filtering or some other wavefield-separation scheme. We illustrate the two different parts of the wavefield in Figure 7.14 where we plot the direct waves between the centre point of the virtual-source array and the receiver line (panel a), and the corresponding scattered waves (panel b).

Separating the modelling steps allows interferometric estimates as defined by Equations (7.3) to (7.6) above to be calculated, i.e., we carry out the interferometric estimation process four times, using different input wavefields at each receiver location. Each of these four estimates using the non-uniform source strength are shown in Figure 7.15. Panel (a) shows the result of interferometry using the direct waves recorded at both the first (virtual source) and second receiver (T1), panel (b) shows the result of interferometry using the direct waves recorded at the first receiver and the scattered waves recorded at the second receiver (T2), panel (c) shows the result of interferometry using the scattered waves recorded at the first receiver and

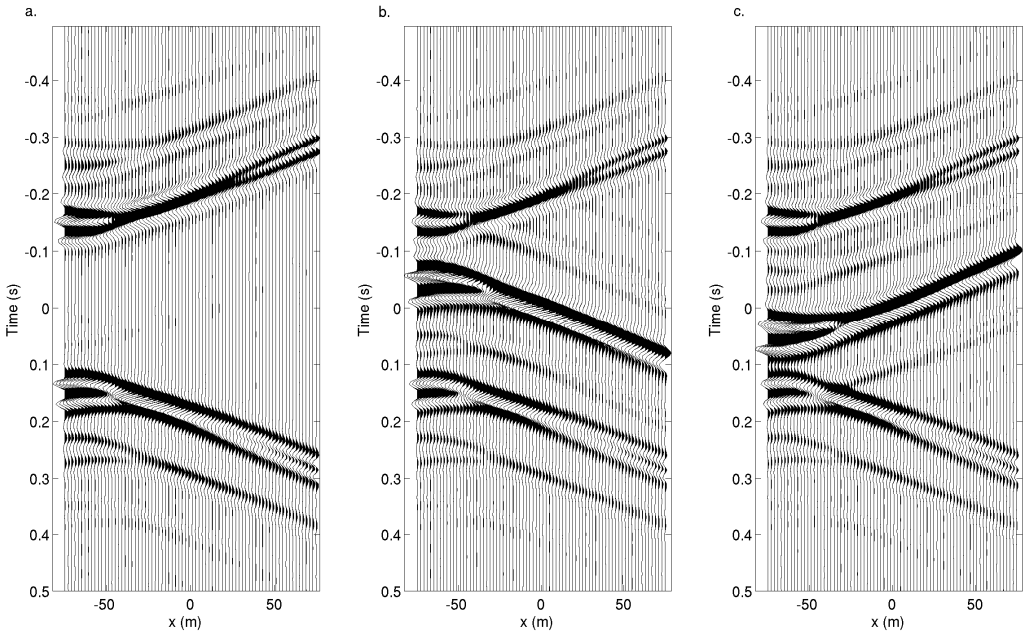

Figure 7.19: (a) Exact scattered surface waves determined using interferometry. Scattered surface waves, including uncancelled non-physical terms (b) using a fixed virtual source and (c) using a fixed receiver.

the direct waves recorded at the second receiver (T3), and panel (d) shows the result of interferometry using the scattered waves recorded at both the first and second receivers (T4). Summing these four gathers results exactly in Figure 7.12a. If the source strength distribution was uniform then we would expect the summation of the four gathers to give the exact result (Figure 7.12c).

We apply the non-uniform directional balancing to each of these four results in turn, using the same bespoke scaling factors in each case, and plot the equivalent corrected seismograms in Figure 7.16. Note that in this configuration of source, receiver and scatterer locations, the dominant contribution to the interferometric estimates comes from panels (a) and (b); panels (c) and (d) predominantly contain non-physical arrivals. Thus, by applying interferometry using separated wavefields we create estimates of the direct waves, scattered waves and the non-physical arrivals.

In Figure 7.17 we compare the residual shown in Figure 7.13b with the non-physical arrival in Figure 7.16d. The residual is similar to the non-physical arrivals,

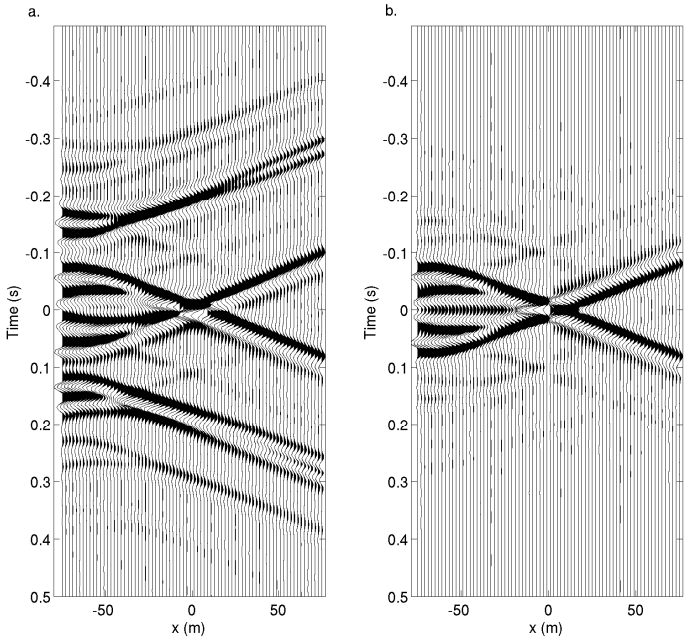

Figure 7.20: (a) Sum of Figure 7.19b and c; (b) Difference of Figure 7.19b and c.

justifying our earlier claim that the residual is dominated by non-physical arrivals. By estimating the non-physical arrivals using wavefield separation we can therefore create an estimate of the residual that remains in the directionally-balanced interferometric estimate.

Symmetry-Based Methods

An alternative approach to identify non-physical arrivals is to use the moveout of waves across source and receiver arrays. By studying the nature of the stationary points that contribute to the non-physical arrivals we have found these arrivals are non-reciprocal. That is, while reversing the role of virtual-source and receiver (i.e., reversing the order of crosscorrelation) in interferometry does not affect the synthesis of the physical arrivals due to source-receiver reciprocity, it does time reverse the non-physical arrivals (in Appendix 7A we prove this to be true using representation theorems for perturbed media (Vasconcelos *et al.*, 2009)). Where appropriate geometries exist, we can use this property to construct an additional method by which non-physical arrivals can be identified.

We illustrate the difference in moveout between physical and non-physical waves using a two-scatterer model. To ensure that these results are not confounded with directional effects, we use a *uniform* source strength distribution around the boundary for this example. We used separated wavefields (as above) and calculate terms T2, T3 and T4 explicitly. We then sum various combinations of them in order to obtain the exact (scattered) result, to focus on non-physical arrivals. A line of receivers with 2 m separation is used to synthesize inter-receiver Green's functions (Figure 7.18). We begin by fixing the central receiver as the virtual source, and calculate the Green's functions between this virtual source and all other receiver locations.

In Figure 7.19a we plot the sum of terms T2, T3 and T4 for a virtual source located at the centre of the receiver line, with receivers at all other locations. This results in the exact virtual source-receiver scattered waves (subject to small numerical implementation errors). This result would be the same if we had reversed the role of virtual source and receiver. In Figure 7.19b we plot only the sum of terms T2 and T3 resulting in non-cancellation of the non-physical term. We illustrate the non-reciprocal nature of the non-physical term by switching the role of virtual source and receiver for each interferometric estimate. This result is shown in Figure 7.19c: note that while the physically-scattered waves (those shown in panel a) are unchanged due to reciprocity, the non-physical arrivals have been time-reversed.

To illustrate how we can further isolate these non-physical arrivals, in Figure 7.20a we plot the sum of Figure 7.19b and c, and in Figure 7.20b we plot the difference between Figure 7.19b and c. Note that in Figure 7.20a the physical arrivals sum constructively, while in panel b the physical arrivals cancel out, leaving the remaining non-physical arrivals, which (apart from phase differences) match those in panel a.

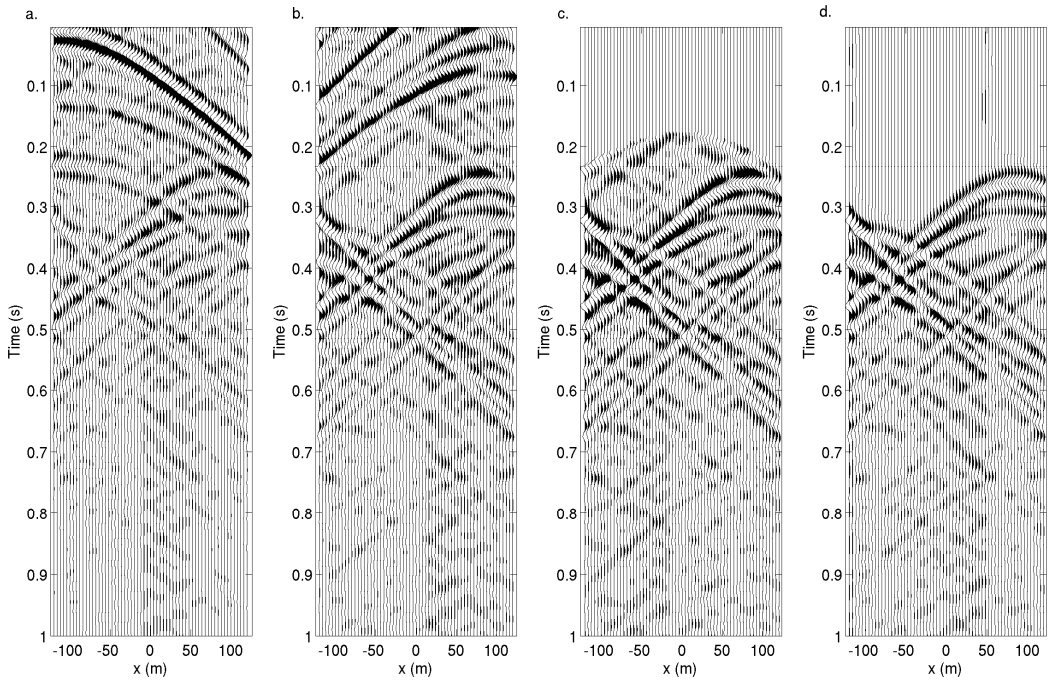

Figure 7.21: (a) The result of the directional balancing algorithm after the removal of the direct arrivals, (b) the result of 2-D helical least squares filtering, (c) result in (b) but with any arrivals prior to the direct wave muted, and (d) the exact result.

Hence, in addition to the wavefield-separation technique above, we find that symmetry-based methods can be used to create complementary indicators of which inter-receiver arrivals are non-physical. Presumably in real-data examples the existence of two methods will help to ensure robustness of the identification process. In the rest of this chapter we use the previous wavefield-separation based method.

7.4 Removing Non-Physical Arrivals

Given methods to predict which arrivals are non-physical, we may treat such arrivals as noise. This noise is superimposed on the real signal (the directionally-balanced Green's function estimates), so the remaining problem is one of signal and noise separation. We now present results of implementing this noise-removal method.

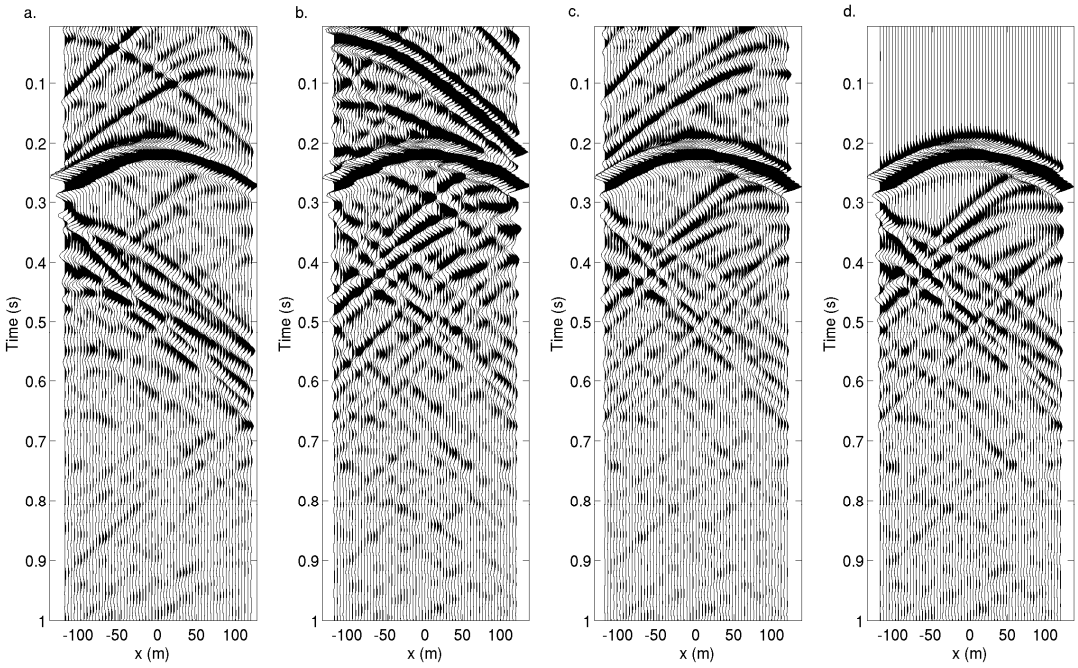

Figure 7.22: Complete gathers for: (a) the non-uniform Green's function estimate; (b) the estimate in (a) after application of the directional balancing; (c) the result of adaptive subtraction of the non-physical arrivals; and (d) the directly modeled Green's functions.

We use a 2-D (*x*,*t*) least-squares filter to match the predicted non-physical arrival in Figure 7.17b to the result of the correction algorithm (Figure 7.12b). Since the direct arrival is dominant we choose to remove this from the problem (i.e., we sum only panels b to d in Figure 7.16, the result of this summation is shown in Figure 7.21a). We use 2-D helical filters (Claerbout, 1998), length 5 in the time direction and length 3 in the *x*-direction. These filters are applied in overlapping windows of 10 traces. We show least-squares filtering results in Figure 7.21b. In Figure 7.21c we show this same result, but we mute any arrivals prior to the arrival time of the direct wave, since we know that these arrivals cannot be physical. This allows the result to be compared to the directly-modelled scattered waves shown in Figure 7.21d, illustrating that a large part of the non-physical energy has been removed, while the physical energy remains relatively unaffected.

Note that we have succeeded in suppressing the dominant non-physical arrivals which move out in the positive direction, yet the non-physical arrivals with conflicting dips have not been suppressed. This is likely to be due to that fact that

these unsuppressed arrivals are weaker than those arrivals that have been suppressed; this results in the least-squares filtering being dominated by the higher-amplitude arrivals.

It might be possible for experienced signal processors to better filter both the non-physical arrivals dipping in the positive direction, and those dipping in the negative direction. The non-physical arrival estimate could be split into positive and negative velocities and these could be removed individually using least-squares filters, for example using curvelet-domain filtering (Hermann *et al.*, 2008).

Finally we put together all of the different processing steps. In Figure 7.22 we show (from left to right): the original Green's function estimates using the non-uniform source strength; the result of the directional balancing algorithm; the result of the adaptive subtraction of the non-physical arrivals – here we have subtracted the non-physical arrival from the entire wavefield (rather than from the scattered wavefield only, as shown in Figure 7.21b above); and the directly modelled result. As we move from left to right (a to c) we can see that the interferometric estimates more closely resemble the directly modelled (desired) Green's function in (d).

7.5 Discussion

Using acoustic-scattering examples we have illustrated the application of a new algorithm to correct for directional bias due to non-uniform source-strength distribution in seismic interferometry. While these examples are illustrative of the method there are challenges remaining before the algorithm can be applied to correct for bias in seismic interferometry applied to real data, especially for the improved recovery of body-wave arrivals.

In our examples the method is applied to cases where the boundary of sources is totally enclosing and well sampled. In many applications this configuration will not exist, the source strength distribution is not likely to be smooth and the strength of some sources will drop to zero: this will result in gaps in the radiation pattern of the virtual source. In heterogeneous media we would expect scattered waves to act as secondary sources to 'fill in' the gaps in the source boundary; nevertheless it remains to be seen how stable the algorithm is in the presence of a limited-source boundary.

Indeed, in cases where the method does remain stable when correcting for directional bias due to gaps in the source boundary, it may be useful when applying interferometry using both passive sources and active sources.

We also use relatively large arrays in our examples. The array used is not optimised in any way. In practice it may be possible to find an optimized array design that provides a sensitivity to many directional components using fewer receivers. The use of a 2D array also means that the method can only be applied exactly to waves propagating in 2D. For example, this configuration could be used when receivers are placed on the surface of the Earth to construct inter-receiver surface-wave seismograms. However, the potential of methods such as this is that they can correct for bias in reflected wavefields, allowing conventional imaging and inversion algorithms to be applied to the interferometric estimates as if they were conventional source-receiver records. It seems likely that in 3D media, 2D arrays at the surface of the Earth could allow a slowness transform to distinguish waves arriving at different angles to the horizontal, and hence correction factors can be applied to reflections as a function of 3D directions of arrival.

The modelling step used in the algorithm is very important. If the model is wrong then the directionality-correction algorithm will fail. However, since the model is only required for the region of the Earth immediately at the receiver array it is far easier to constrain than larger Earth models. Since we only model the first few time steps in the area immediately around the receiver (virtual-source) array the modelling step is not particularly time consuming or computationally expensive.

In the steps used to remove the non-physical arrivals from our corrected estimates we used a method that takes advantage of separated direct and scattered wavefields. In practical applications this requires that we separate the direct wave from the scattered (or reflected) wavefields. In the presence of dispersion and multiple scattering this separation process may not be straightforward, however we expect that in most cases a combination of *f-k* (or *f-x*) filtering and time windowing would allow for an adequate estimate of the direct wave to be separated from the scattered wave field.

Finally, we note that the forward modelling steps of the directional-balancing algorithm may in fact approximately account for any other errors that cause the

interferometric Green's function to be inconsistent with an exact, synthetic source radiating from the virtual-source point. This may, for example, correct errors incurred due to approximations involved in using the monopolar version of the exact Equation (1.2). It is also possible to use different source-radiation patterns in the forward-modelling process. Thus the directional-balancing algorithm may also allow interferometric estimates to be processed to represent cases using those different radiation patterns (for example the balancing algorithm could 'steer' the virtual source radiation in certain directions, or give the source a particular radiation character e.g., that of a dipole rather than monopole source).

7.6 Conclusions

The directional-balancing algorithm proposed here corrects interferometric estimates that are biased due to a non-uniform pattern of virtual-source directionality. In our implementation we also employed interferometry in the forward modelling step of the directional balancing algorithm. The modelling results are thus diffraction-limited and can be compared directly to the data-derived interferometric Green's functions estimates. To illustrate the method we have used a series of examples of varying complexity. We find that the directional-balancing algorithm does provide better interferometric estimates of the Green's functions in that they are closer to the true source-receiver data, and hence more suitable for seismic data processing and inversion. While we have considered acoustic-wave propagation the algorithm can be applied to other wave-propagation regimes, including elastic and electromagnetic wave propagation. Note that the examples shown here only consider amplitude anomalies: further work will include analysis of the algorithm's ability to correct for discrepancies in both phase and amplitude.

We found that the dominant residual after application of the algorithm consists of arrivals from non-physical waves. We cast the remaining problem as one of signal and noise separation, where we refer to physical arrivals as signal, and to non-physical arrivals as noise. We illustrated this signal and noise separation problem using a simple 2-D least-squares filter. Dominant non-physical arrivals dipping in the

positive x-direction are suppressed, preserving the physical arrivals with which they interfere.

Finally, our analysis of non-physical arrivals also shows that the move-out of the physical arrivals is different to the move-out of the non-physical arrivals, and in particular that the former do not satisfy reciprocity with respect to the exchange of sources and receivers. This difference in move-out is even more apparent when they are observed over two (spatial) dimensions. Hence, we expect that 3-D (x,y,t) filters should provide better removal of the non-physical arrivals.

8. Interferometric ground-roll removal: Attenuation of scattered surface waves in single-sensor data

Land seismic data are contaminated by surface waves (or ground roll). These surface waves are a form of source-generated noise and can be strongly scattered by near-surface heterogeneities. The resulting scattered ground roll can be particularly difficult to separate from the desired reflection data. We use seismic interferometry to estimate scattered surface waves, recorded during an exploration seismic survey, between pairs of receiver locations. Where sources and receivers coincide these inter-receiver surface wave estimates can be adaptively subtracted from the data. We show that this predictive-subtraction process can successfully attenuate scattered surface waves, forming a new scattered-noise removal algorithm: we refer to this as interferometric ground-roll removal.

8.1 Introduction

In exploration seismology, surface waves (or ground roll) constitute a form of source-generated noise. Ground roll travels laterally through the near surface of the Earth and contains little or no information about the deeper subsurface. These arrivals are characterised by a high amplitude and low frequency content and they often obscure recordings of body waves reflected by deeper subsurface targets. Conventionally, ground roll is removed using frequency-wavenumber (*f*-*k*) or frequency-offset (*f*-*x*) methods (e.g., Yilmaz, 2001). However, when near surface heterogeneities cause ground roll to be scattered in the cross-line direction these conventional techniques can prove to be ineffective; cross-line scattered ground roll can occupy the same regions of *f*-*k* and *f*-*x* space as the reflected waves that we wish to preserve.

Methods focusing on the removal of these scattered surface waves exist and can be separated into two categories: acquisition-based suppression schemes are based on the use of recording arrays (e.g., Regone, 1998; Özbek, 2000a), whereas prediction-removal suppression schemes estimate and subtract scattered surface waves using either modelling based (Blonk *et al.*, 1995; Blonk and Herman, 1996; Ernst *et al.*, 2002a; Ernst *et al.*, 2002b) or data driven (Herman and Perkins, 2006) inverse-scattering series. The use of extensive stacked arrays in acquisition-based schemes can compromise data resolution, and on the other hand current prediction-removal schemes rely on time consuming iterative inversions using the Born (single-scattering) approximation. In areas with strongly heterogeneous near-surface properties a Born approximation may not be valid and the inverse-scattering series may identify reflected waves as scattered events, hence these may be removed erroneously from the data.

In this chapter we consider a prediction-removal suppression scheme that is based on the use of seismic interferometry (e.g., Wapenaar, 2003, 2004; van Manen *et al.*, 2005; Curtis *et al.*, 2006) and adaptive filtering (e.g., Claerbout, 2004). This scheme is naturally applied to single-sensor data (since seismic interferometry is naturally applied to single sensors) and it does not rely on array-based acquisition, single-scattering (Born) approximations or the use of costly modelling and inversion processes. We show that this method is capable of removing complex and strongly-scattered ground roll.

Inter-receiver surface wave signals can be estimated using seismic interferometry by performing a simple process of cross-correlation (or cross-convolution) and summation of the wavefields observed at the receivers (e.g., see Chapters 1, 2, and 3). If each source location within an exploration survey is located near a receiver position then surface-wave estimates can be created for each source-receiver pair. These estimates can be adaptively subtracted from the directly-recorded full wavefield. We refer to this technique as interferometric ground-roll removal.

While it is desirable to be able to produce estimates using recordings of background noise, for the ground-roll removal application we require the bandwidth of the estimates to match those of the active-source data. The only way to ensure this is to use active-source data, as we cannot guarantee that background-noise sources

will excite the frequencies of interest (e.g., in Chapter 3 it was shown that in one particular setting the results of passive interferometry are dominated by a lower-frequency content than active-source data).

In this chapter we first review interferometric theory for scattered waves and develop a workflow for the prediction of scattered surface waves by seismic interferometry. We then introduce a subset of a single-sensor land-seismic survey where we observe strong lateral scattering. We apply both correlation-type and convolution-type interferometry to these data and illustrate the adaptive subtraction of scattered surface-wave estimates from the appropriate source-receiver recordings. Finally, we show how the two approaches may be combined to allow the method to be applied to an entire shot gather, and hence the method can be used as part of a conventional seismic processing flow.

8.2 Seismic interferometry: scattered surface-wave isolation

Seismic interferometry is applied by solving a so-called interferometric integral. Such an integral requires integration across a bounding surface of sources, *S*. In their most complicated form interferometric integrals require that various source types exist on the bounding surfaces. However since in practice source types are limited we can use approximations to reduce these integrals to more practical forms. For example, Wapenaar and Fokkema (2006) reduce the interferometric integral to include a summation over P- and S-wave sources by assuming that the surface *S* is a sphere with large radius and that the medium at and around the surface is homogeneous. Further, for surface waves, in Chapter 4 it was shown that it is reasonable to replace these P- and S-wave sources with point forces, i.e.,

$$G^{*}_{im}(\mathbf{r}_A,\mathbf{r}_B) - G_{im}(\mathbf{r}_A,\mathbf{r}_B) \approx \frac{C(\omega)}{|S(\omega)|^2}\int_{\mathbf{r}_S\in S} G_{in}(\mathbf{r}_A,\mathbf{r}_S)G^{*}_{mn}(\mathbf{r}_B,\mathbf{r}_S)dS\,, \qquad (8.1)$$

where $G_{im}(\mathbf{r}_A,\mathbf{r}_B)$ denotes the Green's function representing the *i*th component of particle displacement at location $\mathbf{r}_A$ due to a uni-directional, impulsive, point force in the *m* direction at $\mathbf{r}_B$, superscript * denotes complex conjugation and the surface S

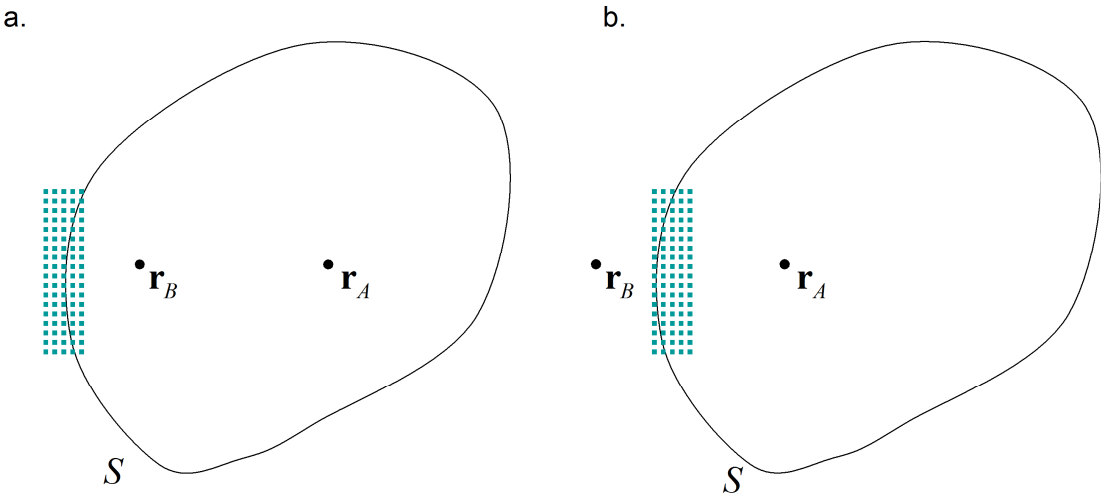

Figure 8.1: Configurations for (a) correlation-type interferometry and (b) convolution-type interferometry. In practice it is not possible to form enclosing source boundaries *S* as shown here. Instead portions of the source boundary can be formed using available source distributions. Grey squares indicate distributions of sources that may replace the surface integral in practice.

encloses the locations $\mathbf{r}_A$ and $\mathbf{r}_B$ (see Figure 8.1a). Einstein's summation convention applies for repeat indices and $S(\omega)$ is the source signature of the boundary sources. The scale factor $C(\omega)$ occurs due to the approximations involved in relaxing the required source types. This can be related to frequency, the elastic properties at the source location, and the geometry of the source boundary (Wapenaar and Fokkema, 2006). On the left hand side of Equation (8.1) there are both forward-time and reverse-time parts. In practice Equation (8.1) is applied by summing over available source locations rather than solving an integral equation:

$$G^*_{im}(\mathbf{r}_A,\mathbf{r}_B) - G_{im}(\mathbf{r}_A,\mathbf{r}_B) \approx \frac{C(\omega)}{|S(\omega)|^2}\sum_S G_{in}(\mathbf{r}_A,\mathbf{r}_S)G^*_{mn}(\mathbf{r}_B,\mathbf{r}_S)\,. \qquad (8.2)$$

Finally, we assume that the vertical components dominate (as assumed for surface waves by Blonk *et al.* (1995)):

$$G_{33}^{*}(\mathbf{r}_A,\mathbf{r}_B)-G_{33}(\mathbf{r}_A,\mathbf{r}_B)\approx\frac{C(\omega)}{\left|S(\omega)\right|^2}\sum_S G_{33}(\mathbf{r}_A,\mathbf{r}_S)G_{33}^{*}(\mathbf{r}_B,\mathbf{r}_S)\,. \tag{8.3}$$

Equation (8.3) is similar to Equation (5) of Bakulin and Calvert (2006) on which they base their Virtual Source Method. Bakulin and Calvert (2006) find that their results are reliable, despite the approximations required. In Dong *et al.* (2006), Chapter 2, and Chapter 3 only vertical force sources are used when applying interferometry to surface-wave data and it is shown that the (direct) surface-wave estimates are reliable. We expect that such source types can also produce estimates of scattered surface waves.

The theory of correlation-type interferometry (as represented by Equations (8.1) to (8.3)) dictates that the medium through which the waves propagate must be lossless. The presence of losses can introduce amplitude errors and non-physical arrivals into the interferometric estimates (Draganov *et al.*, 2008). Interferometry can also be applied using convolution. This approach places no restrictions on the attenuation properties of the medium (Slob *et al.*, 2007; Slob and Wapenaar, 2007; Wapenaar, 2007; Chapter 6) and we expect convolution applications to be less sensitive to non-physical arrivals introduced by attenuation and limited aperture. In Chapter 6 it was shown show why the convolution results are better than those using correlation when trying to estimate scattered surface waves. The stationary-phase analysis reveals that there are mutually-cancelling contributions in correlation-type interferometry that do not exist in convolution-type interferometry. When interferometry is applied in attenuative media or with limited aperture (or indeed both), the mutual cancellation may not necessarily occur and artefacts (non-physical wave energy) are introduced into the interferometric estimates. This effect has also been observed for acoustic scattering (Snieder *et al.*, 2008) and for reflected wavefields (Draganov *et al.*, 2008).

For this convolution case we simply remove the complex conjugate from Equation (8.3):

$$G_{33}(\mathbf{r}_A,\mathbf{r}_B)\approx\frac{C(\omega)}{S(\omega)S(\omega)}\sum_S\; G_{33}(\mathbf{r}_A,\mathbf{r}_S)\; G_{33}(\mathbf{r}_B,\mathbf{r}_S)\,, \tag{8.4}$$

and require that one of the receivers be located out-with the boundary of sources (i.e., we require that the inter-receiver line is dissected by the boundary of sources, Figure 8.1b).

In the following we assume that the surface waves propagate in 2-dimensions across the surface of the Earth, and as such we only consider sources and receivers located on (or just below) the free surface. In Chapter 4 it was shown that surface wave estimates can be made using such source geometries provided no strong higher modes exist (or by isolating each mode and applying interferometry to the individual modes). By splitting the surface waves into direct and scattered parts in Chapter 6 a stationary-phase analysis was applied and it was found that the scattered surface waves can be estimated by correlating (or convolving) the direct surface waves at the virtual source with the scattered surface waves at the second receiver. (Stationary-phase analysis assumes that the major contributions to an integral come from those points at which the phase of the integral is stationary; by applying this method to seismic interferometry it is possible to locate those regions of the surface *S* from which the major contributions to interferometry come.) For the separation of wavefields, similar results have been found for acoustic-wave propagation by Snieder *et al.* (2008) and Vasconcelos *et al.* (2009). In the cross-correlation case those studies show that non-physical (or spurious) arrivals can be introduced when cross-correlating only direct and scattered waves and these may be accentuated by the presence of attenuation.

For each source on the boundary *S*, we separate the surface-wave signals into two parts, one approximating the direct surface waves ($G_{33}^{d}(\mathbf{r}_A,\mathbf{r}_S)$), and another approximating the scattered surface waves ($G_{33}^{sc}(\mathbf{r}_A,\mathbf{r}_S)$). As discussed above and in Chapter 6, we can then consider the application of interferometric equations of the form,

$$\begin{aligned}\tilde{G}_{33}^{sc*}(\mathbf{r}_A,\mathbf{r}_B)-\tilde{G}_{33}^{sc}(\mathbf{r}_A,\mathbf{r}_B)\\ \approx\sum_S G_{33}^{d}(\mathbf{r}_B,\mathbf{r}_S)G_{33}^{sc*}(\mathbf{r}_A,\mathbf{r}_S)+\sum_S G_{33}^{sc}(\mathbf{r}_B,\mathbf{r}_S)G_{33}^{d*}(\mathbf{r}_A,\mathbf{r}_S),\end{aligned}\qquad(8.5)$$

and

$$\tilde{G}_{33}^{sc}(\mathbf{r}_A,\mathbf{r}_B) \approx \sum_S G_{33}^{d}(\mathbf{r}_B,\mathbf{r}_S)G_{33}^{sc}(\mathbf{r}_A,\mathbf{r}_S) + \sum_S G_{33}^{sc}(\mathbf{r}_B,\mathbf{r}_S)G_{33}^{d}(\mathbf{r}_A,\mathbf{r}_S), \quad (8.6)$$

for cross-correlation and cross-convolution, respectively. Note that the scattered surface-wave Green's function components on the left hand side of Equations (8.5) and (8.6) are estimates that may contain both physical and non-physical events and we have included the scale factor, $C(\omega)$, and source term, $S(\omega)$, within these Green's function estimates. We differentiate these from the exact scattered surface-wave component of the Green's function by using a tilda (~). In practice we do not make estimates of the scattered surface waves, rather we make a 'best guess' of the scattered waves by removing the direct surface waves and time windowing the earlier arrivals, resulting in an estimate of the scattered surface waves that includes body-wave arrivals. This process is discussed in more detail below.

Note that Equations (8.5) and (8.6) are very similar to Equations (16) and (22) of Vasconcelos *et al.* (2009). While we have derived these equations using observations from a stationary-phase analysis, those authors derive similar expressions for acoustic-wave propagation using representation theorems for perturbed media. Similar wavefield-separation techniques are proposed and used successfully by Mehta *et al.* (2007) and Vasconcelos and Snieder (2008a). In practice it is unlikely that the available sources will form a closed boundary; nevertheless we can select sources to be considered in the same manner as these boundary sources. For example in the following we consider a thick boundary of sources concentrated around the inter-receiver line (indicated by grey dotted area in Figure 8.1).

In the results presented here we only consider the application of one of the summations on the right hand side of Equations (8.5) and (8.6). We isolate the direct surface waves at the virtual receiver and cross-correlate, or cross-convolve these estimates with the isolated scattered waves at the second receiver. In the specific case that we consider we find that the other summation does not contribute to the scattered surface wave estimate.

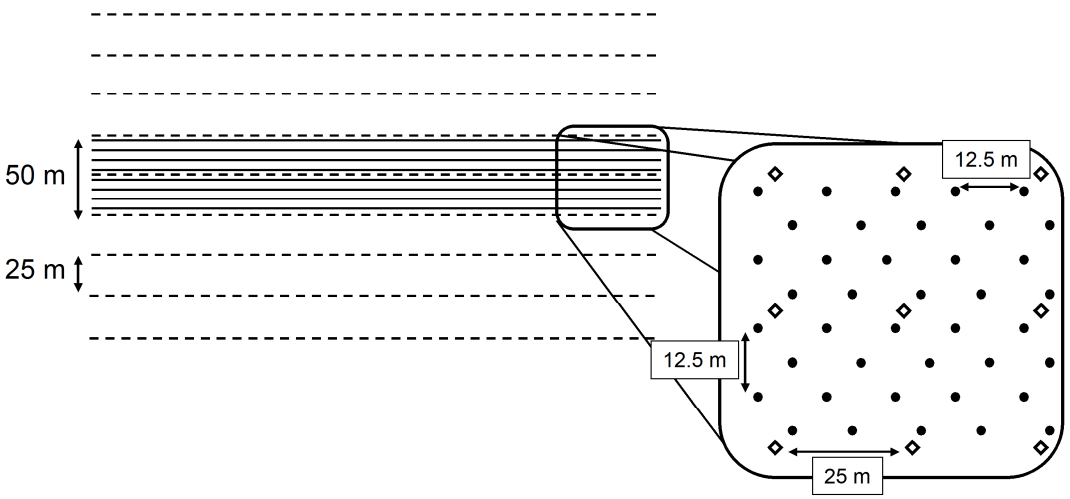

Figure 8.2: Sketch of survey geometry. Dashed lines indicate source lines, solid lines indicate receiver lines. Inset shows source (diamond) and receiver (circle) geometries.

8.3 Data set geometry and pre-processing for interferometry

We use a subset of single-sensor single-source data that was recorded as part of a test line in a desert. This subset consists of 8 parallel lines of single-sensor receiver stations and 9 parallel lines of Vibroseis source stations (Figure 8.2). The 8 receiver lines have a cross-line separation of 6.25 m and an in-line receiver separation of 12.5 m (in a staggered pattern, sketched in the inset in Figure 8.2). The 9 source lines have a cross-line and in-line separation of 25 m. The data themselves consists of 6 second records of correlated vibrator data, sampled at 4 ms. Apart from the vibroseis correlation, pre-processing also includes the application of a noise-attenuation algorithm, which uses a spatial median filter to identify anomalous amplitudes.

The dataset is recorded in an area with a relatively strongly-varying near surface (both topographic and lithological variations) and clear scattered ground-roll arrivals can be identified. In many parts of the data strong in-line (i.e., linear) and cross-line (i.e., hyperbolic) scattered surface-wave arrivals can be identified. For example, in Figure 8.3 below we show an example of particularly strong cross-line scattered ground roll (around 1.5 s).

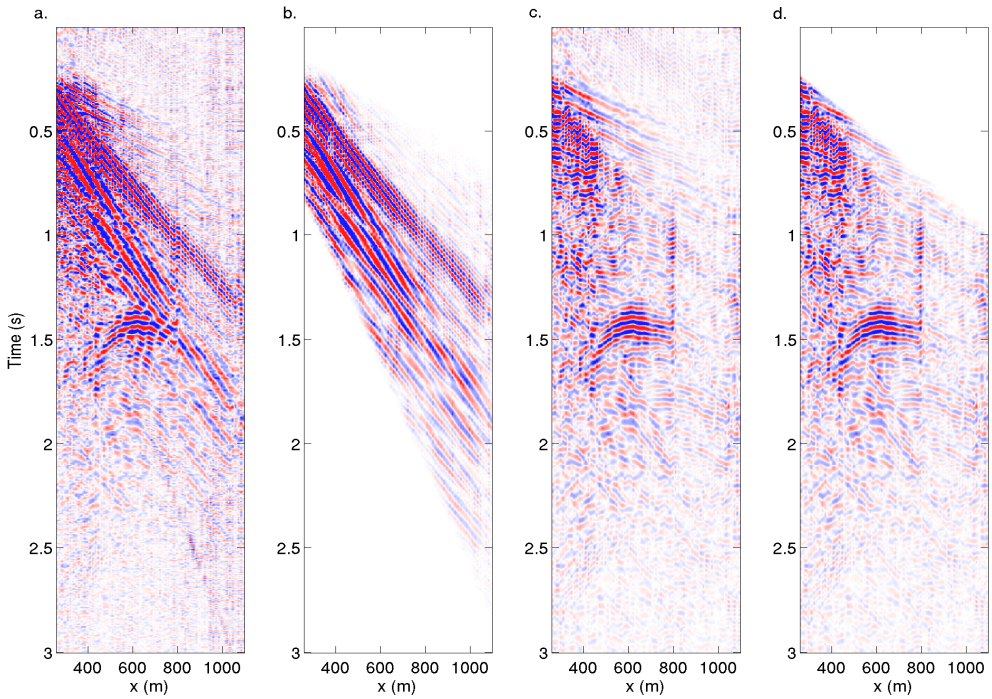

Figure 8.3: (a) Selection of a raw gather from the central source line and receiver lines, recorded on the 5th receiver line, (b) direct surface waves isolated using *f-k* filtering and time-windowing, (c) removal of (b) from (a) after band-pass filtering, and (d) zero-ing of early arrivals in (c). x (m) is the source-detector distance in meters, this and all subsequent x-axes are interpolated by a factor of 4 to smooth the plots.

In order to apply interferometry to isolate the scattered surface waves we require estimates of the separated wavefields $G_{33}^{d}(\mathbf{r}_A, \mathbf{r}_S)$ and $G_{33}^{sc}(\mathbf{r}_A, \mathbf{r}_S)$. This approximate separation of wavefields has two advantages: (i) it allows us to apply interferometry in the framework laid out for the estimation of only scattered events (Equations (8.5) and (8.6)), and (ii) the pre-processing steps remove as much body-wave energy from the recording as possible. Therefore this can also be considered to be a signal preservation procedure. We apply the following workflow to estimate the inter-receiver surface waves:

1. Isolate the direct surface waves using a combination of *f-k* or *f-x* methods and time windowing.

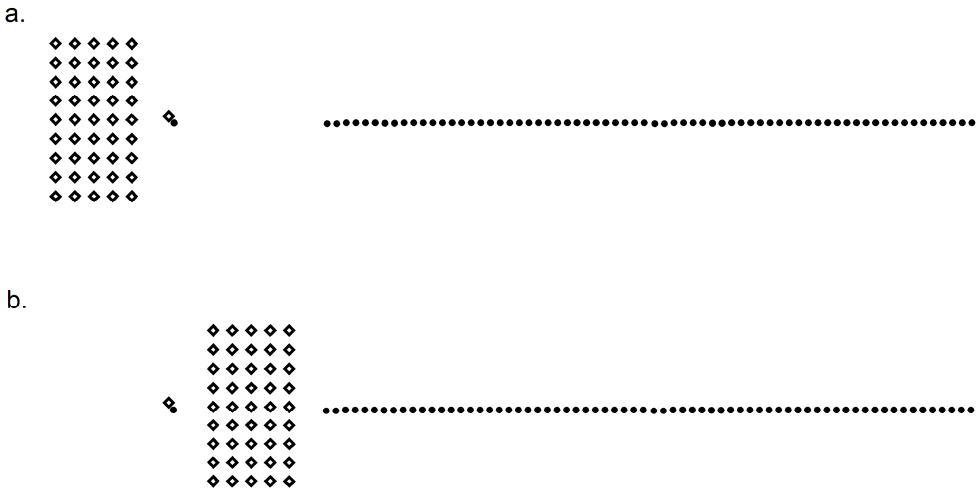

Figure 8.4: Geometries used to create scattering estimates in Figure 8.5. (a) Geometries for correlation-type interferometry and (b) geometries for convolution-type interferometry. Circles indicate receivers, diamonds indicate sources. The virtual-source real-source pair is indicated by the neighbouring circle and diamond, respectively.

2. Remove any data that we can identify as not being scattered surface waves, i.e., remove the direct surface wave estimate from the data and zero any arrivals prior to the first arrival time of the direct surface wave.
3. Select appropriate source geometries and apply either Equation (8.5) or (8.6) for convolution-type or correlation-type interferometry, respectively.

We choose a receiver as the virtual source location and show the source gather from the closest source to this receiver in Figure 8.3a. To begin processing the data using interferometry as described above we make estimates of the direct surface wave and the scattered surface waves. We apply a 1 to 30 Hz band-pass filter to the data as this is the frequency band where the surface waves are dominant. The direct surface waves separated by using *f-k* filters and time-windowing are shown in Figure 8.3b. We then remove the direct surface wave from the full-wavefield data (Figure 8.3c) and set the data equal to zero prior to the first surface-wave arrival (Figure 8.3d). The data in Figure 8.3b and d are representative of the data we use as the input to the interferometric estimation (i.e., these are estimates of $G_{33}^{d}(\mathbf{r}_A,\mathbf{r}_S)$ and $G_{33}^{sc}(\mathbf{r}_A,\mathbf{r}_S)$, respectively). This is the first step in our interferometric estimation

process, and this step is repeated for all sources chosen to be treated as boundary sources.

8.4 Comparison of approaches: correlation or convolution?

In Section 8.2 above we discussed the differences between the application of correlation-type interferometry and convolution-type interferometry. We now consider the application of both of these methods to estimate scattered surface waves.

We choose a selection of sources that act as part of the integration boundary when applying Equations (8.5) and (8.6); see the dotted areas in Figure 8.1. While this part of the boundary may not contain all sources required to construct all scattered events, in the following we show that it is still significant to construct the dominant scattering events observed in the dataset.

In Chapter 6 it was shown that the results of interferometry for scattered surface-wave recovery can vary greatly depending on source geometries and the type of interferometry applied. For correlation-type interferometry we require sources outside the virtual source (locations out-with the virtual source-receiver pairs). We found that when applying interferometry to the closest sources to our chosen virtual source the estimates were more reliable than when the sources closest to the second receiver were used. For convolution-type interferometry we require sources inside the virtual source (locations between the virtual source-receiver pairs). Provided that we choose sources in this way we found that the convolution-type interferometric estimates were reliable. In Appendix 8A we include a further discussion on the selection of sources in light of the stationary-phase analysis presented in Chapter 6. In this discussion we explain how by applying interferometry using the limited source geometries available we can expect to reconstruct the physical scattered surface waves.

We now apply interferometry to estimate the scattered surface waves in the gather in Figure 8.3c. The geometries used are shown in Figure 8.4a and b for correlation-type interferometry and convolution-type interferometry, respectively. We find that results are good when we choose a 5 by 9 patch of sources to be the boundary

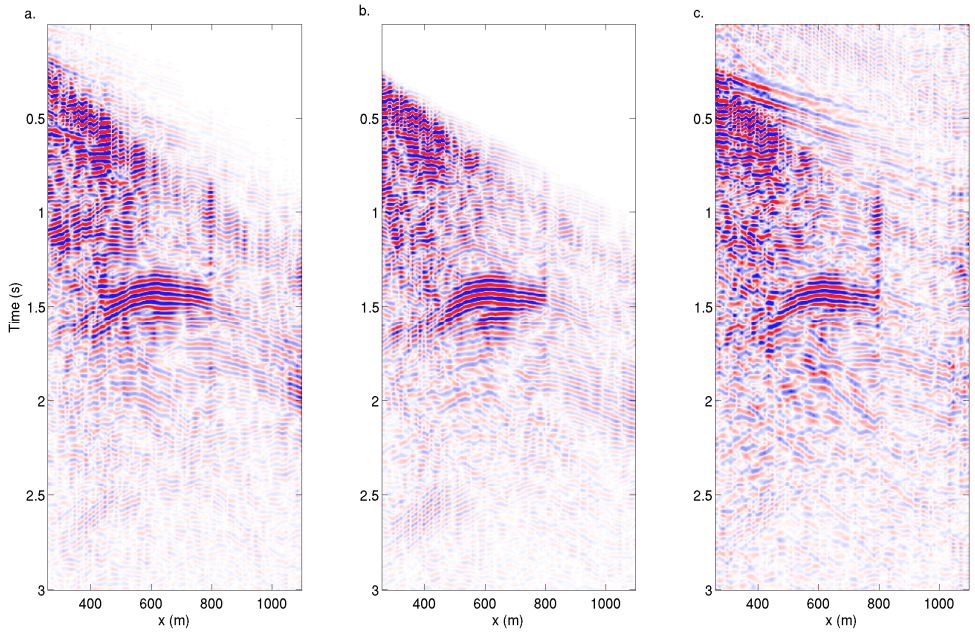

Figure 8.5: Interferometric estimates using (a) correlation-type interferometry and (b) convolution-type interferometry. (c) Data from Figure 8.3c for comparison.

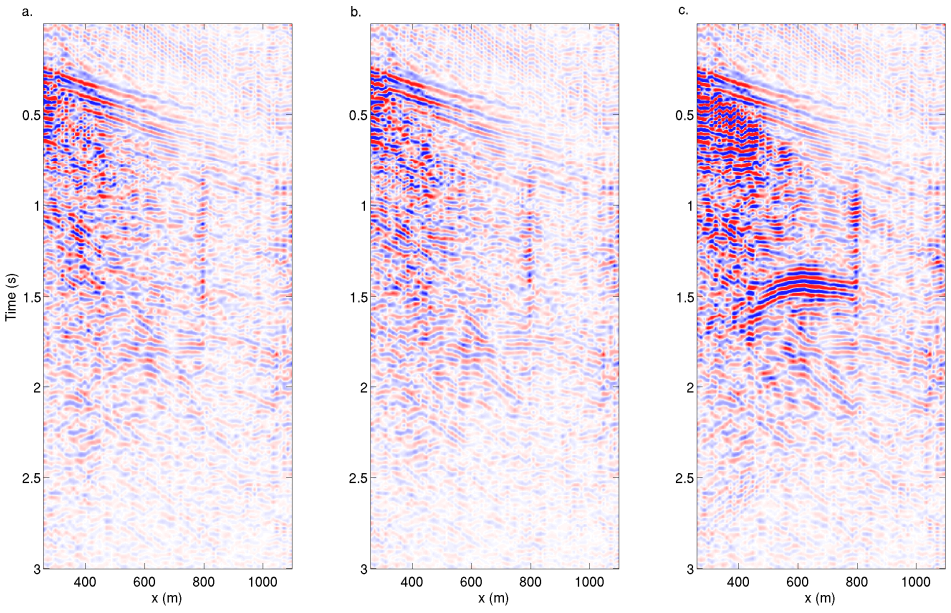

Figure 8.6: Adaptive subtraction of interferometric estimates in Figure 8.5 (a) and (b) from data in Figure 8.5 (c). Again the real data from Figure 8.3c are shown for comparison (c).

sources for interferometry. As a rule of thumb we choose sources to be 75 m outside (for correlation) or inside (for convolution) the virtual source.

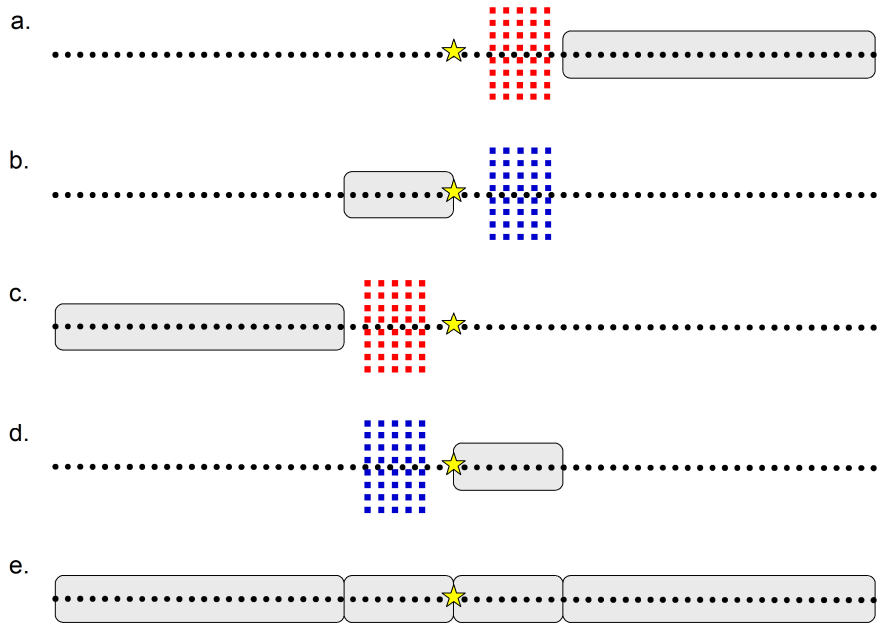

Figure 8.7: Sketch showing application of interferometry for a full gather. Red and blue squares indicate sources used for convolution and correlation respectively, the yellow star is the position of the real and virtual source and black dots indicate the receiver line. Shaded boxes indicate the receivers considered in each step. (a) Convolution for forward offsets, (b) correlation for backward offsets, (c) convolution for backward offsets and (d) correlation for forward offsets. Finally, (e) shows the combination of the four shaded regions in (a) to (d).

The processing sequence to generate the interferometric gathers is as follows. At the virtual-source location ($\mathbf{r}_B$) we sort the data into a common-receiver gather containing the isolated direct waves ($G_{33}^{d}(\mathbf{r}_B,\mathbf{r}_S)$ in Equations (8.5) and (8.6)) between each boundary source and the virtual receiver, and for every other receiver of interest ($\mathbf{r}_A$) we sort the data into a common-receiver gather containing the isolated scattered (and body) waves ($G_{33}^{sc}(\mathbf{r}_A,\mathbf{r}_S)$ in Equations (8.5) and (8.6)). Since $\mathbf{r}_B$ is the virtual-source position we fix this as the reference trace and for all other receivers $\mathbf{r}_A$ we cross-correlate (or cross-convolve) the two common-receiver gathers and sum the resulting traces, resulting in estimates of the scattered waves between a virtual source at $\mathbf{r}_B$ and all other receivers $\mathbf{r}_A$.

For correlation-type interferometry we use the source geometries illustrated in Figure 8.4a, with the resulting scattered surface wave estimate shown in Figure 8.5a.

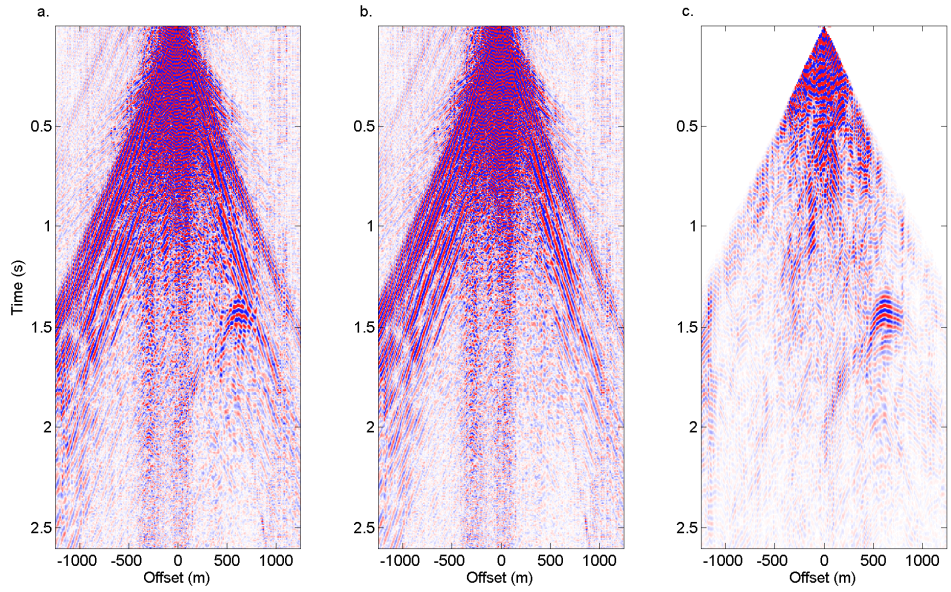

Figure 8.8: Example of interferometric ground roll removal applied to full gathers, while preserving the direct ground roll. (a) Raw data, (b) results of interferometric ground roll removal, and (c) the subtracted (scattered) ground roll. The offset is measured between the source and receivers.

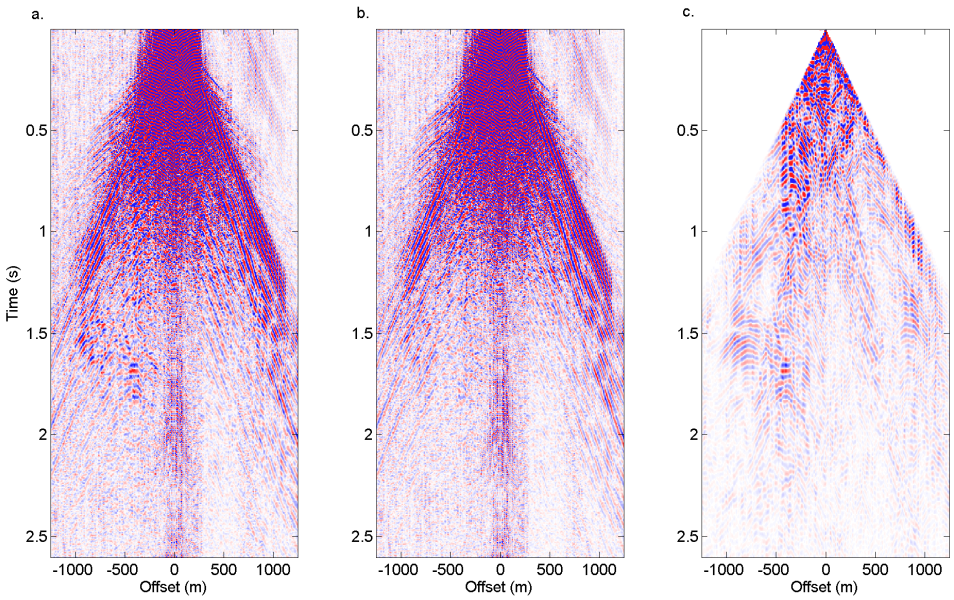

Figure 8.9: As for Figure 8.8 but using a different shot gather.

For convolution-type interferometry we use the source geometries illustrated in Figure 8.4b, with the resulting scattered surface wave estimate shown in Figure 8.5b. In Figure 8.5c we show the data from the real source (with the direct ground roll

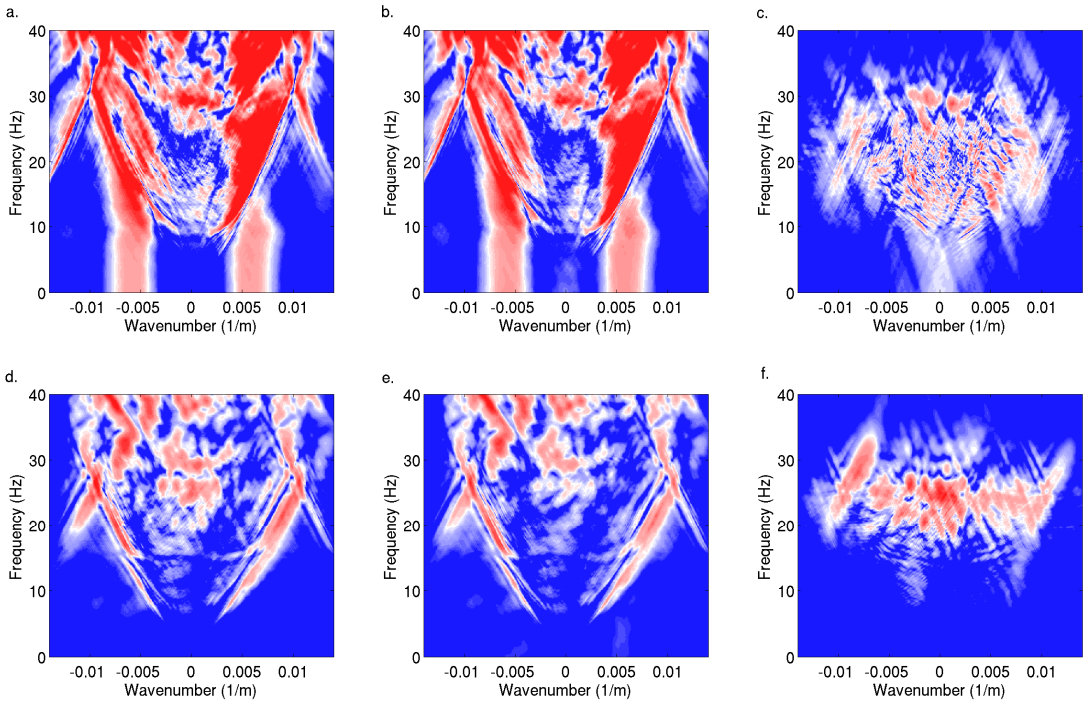

Figure 8.10: Frequency wave-number plots corresponding to Figure 8.8a, b, and c (panels a, b, and c respectively) and those corresponding to Figure 8.9a, b, and c (panels d, e, and f respectively).

removed). Comparing the results it is clear that both correlation- and convolution-type interferometry estimates many of the dominant scattered surface wave events (for example the dominant scatterer in the centre of the gather, and other weaker scattering events at [400 m, 2.6 s]). We do expect losses due to attenuation to affect the correlation-type estimates, but since we consider sources that are close to the pair of receivers these losses are minimal. We can however identify subtle differences between the plots. At [600 m, 2 s] there is an apex of a weak hyperbolic event in the convolution estimate that is not present in the correlation estimate. At [300m, 2.3s] the flank of the same hyperbolic event can be seen on both the convolution estimate and the real data, but not in the correlation estimate.

As the final part of our comparison we consider the adaptive subtraction of these scattered surface wave estimates from the real data. For more on adaptive filtering see Claerbout (2004). To perform the adaptive subtraction we find some matching filter, $\mathbf{f}$, that minimises the difference between the real data (without the direct

ground roll), $\mathbf{G}^{nd}$, and the estimated scattered surface waves, $\mathbf{G}^{sc}$. That is we solve the following minimisation problem for $\mathbf{f}$:

$$\min_{\mathbf{f}} \left\| \mathbf{G}^{nd} - \mathbf{f}\mathbf{G}^{sc} \right\| . \tag{8.7}$$

In the following we solve Equation (8.7) in overlapping 2D windows (width 5 traces, length 0.25 s), using iterative least squares with a conjugate-gradient algorithm to design 2D matching filters (with a maximum spatial lag of ±2 traces and a maximum time lag of ±5 samples). The scatterer-free seismic data, $\mathbf{G}^{nsd}$, are then generated using,

$$\mathbf{G}^{nsd} = \mathbf{G}^{nd} - \mathbf{f}\mathbf{G}^{sc} . \tag{8.8}$$

Later in the chapter we wish to remove the scattered waves while preserving the direct ground roll (such that the resulting scatterer-free data can be used in a conventional seismic processing flow). To do this we simply modify Equation (8.8) such that the filtered data are subtracted from the full raw gather, $\mathbf{G}$, to give the raw data without scattered surface waves,

$$\mathbf{G}^{nsc} = \mathbf{G} - \mathbf{f}\mathbf{G}^{sc} , \tag{8.9}$$

where $\mathbf{G}^{nsc}$ is the raw data without scattered surface waves but with the direct surface waves intact.

We use this least squares approach to match the scattered estimates in Figure 8.5a and b to the data shown in Figure 8.3d, and subtract the filtered estimates using Equation (8.8). These results are shown in Figure 8.6a and b, again showing the data from Figure 8.3c for comparison in Figure 8.6c. We have used the same filter parameters for each adaptive subtraction and both of the estimates give a similar result after this subtraction. It is likely that the adaptive filter accounts for the differences seen between the estimates in Figure 8.5a and b.

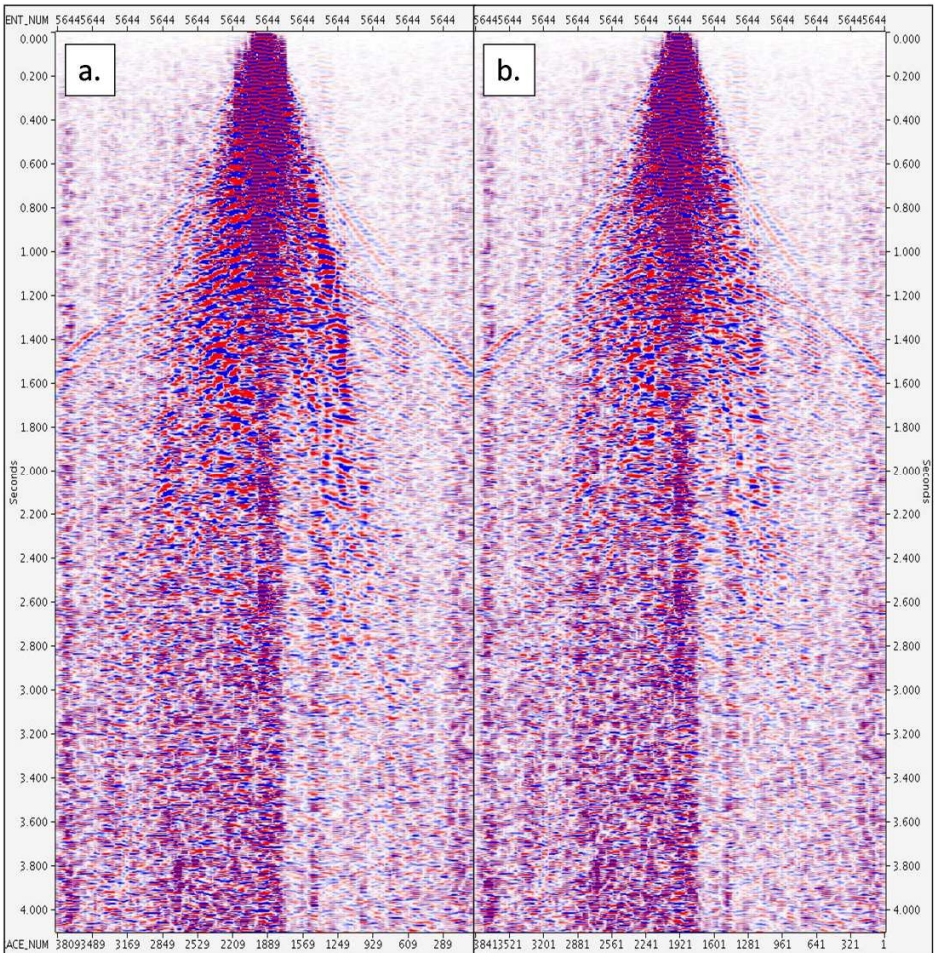

Figure 8.11: Results of digital group forming (DGF) for the source gather shown in Figure 8.9 (using the 8 neighbouring receiver lines illustrated in Figure 8.2). (a) DGF without the application of interferometric ground-roll removal, and (b) DGF using the data after application of interferometric ground-roll removal.

While the results using convolution are expected to be better than those using correlation, one drawback of the convolution method is that we cannot make convolution estimates at short offsets since we require a gap for the boundary sources. In the following we illustrate that by filling this gap using the correlation approach, it is possible to create scattered surface-wave estimates for the whole gather, preparing the data for conventional processing techniques.

We use cross-correlation up to a source-receiver offset of 300 m, and beyond 300 m we use cross-convolution. We also split the data into positive and negative offsets, since we require different sources when applying interferometry to positive and negative offsets. A schematic of the combination of geometries is shown in

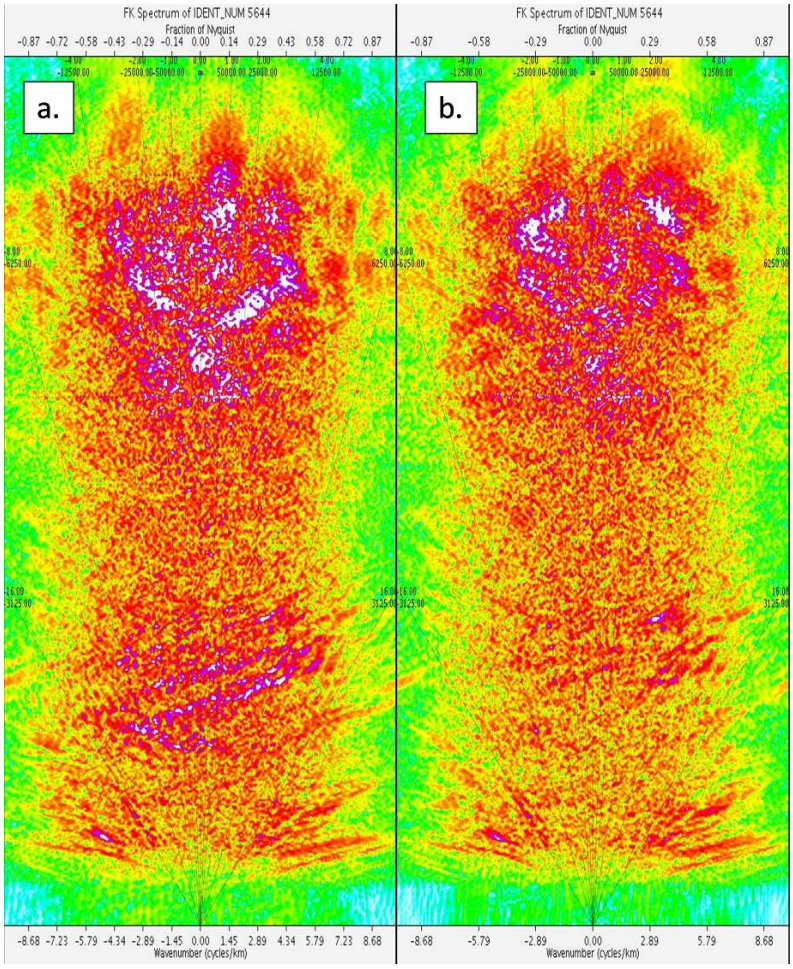

Figure 8.12: Frequency wave-number plots corresponding to Figure 8.11a, and b respectively.

Figure 8.7. We estimate the scattering using the same process as above and adaptively subtract these estimates from the full wavefield using Equations (8.7) and (8.9). We preserve the direct ground roll in these estimates such that it can be removed using existing methods (e.g., *f-k* or *f-x* methods) which may also remove any residual in-line scattered waves. In Figure 8.8 and Figure 8.9 we show two gathers before (panel a) and after (panel b) the application of the interferometric method, along with the removed scattered ground-roll (panel c). These examples illustrate the removal of scattered ground roll while preserving the direct ground roll. We use convolution-type interferometry where possible, since as discussed in Section 8.4 and in Appendix 8A, we have previously identified that this approach is less sensitive to non-physical arrivals and attenuation. While we have not observed a large difference between the cross-correlation and cross-convolution approaches in

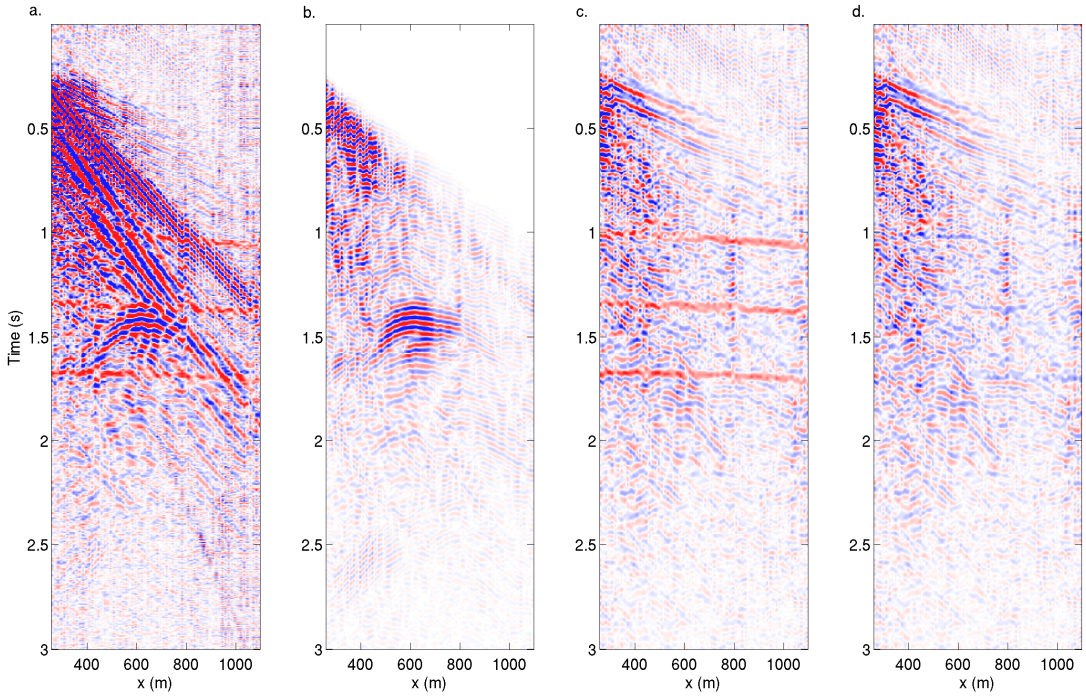

Figure 8.13: Results for convolution interferometry after introducing three synthetic reflections. (a) Raw gather, (b) interferometric estimate of the scattered ground roll (c) result of *f-k* filtering of the direct ground roll and interferometric ground roll removal, and (d) residual after subtraction of modelled reflections.

this case, it may be that different scatterer distributions are more susceptible to these changes. In Figure 8.10 we show the equivalent *f-k* plots corresponding to Figure 8.8a, b, and c (panels a, b, and c) and Figure 8.9a, b, and c (panels d, e, and f). These *f-k* plots illustrate the operation of the interferometric method inside the pass-zone of a conventional *f-k* filter.

To further illustrate the method we consider digital group forming (DGF) using the shot gathers shown in Figure 8.9a and b considering all eight receiver lines shown in Figure 8.2. DGF is a process that allows the application of optimally designed noise-attenuation filters to single-sensor data before group forming, rather than simply stacking recording arrays in the field (as in conventional array-based acquisition). Figure 8.11a and Figure 8.12a illustrate the data after DGF in the time-offset and *f-k* domains, respectively, for the data without the application of interferometric ground-roll removal, and Figure 8.11b and Figure 8.12b show the equivalent plots with the application of interferometric ground-roll removal. The

improvement using interferometry is clear to see in the group-formed data. In the time domain (Figure 8.11) clear improvements can be seen within the noise cone, especially around 1.2s where the strong reflection event has greater continuity across the noise cone, and also in the *f-k* domain where significant energy is removed from around the zero wave-number axis at lower frequencies (note these *f-k* plots are generated without amplitude preservation, hence the apparent differences between the two *f-k* plots at higher frequencies).

8.6 Discussion

Our results indicate that interferometric ground-roll removal may be a solution to the problem of scattered ground roll. As is typical of single-sensor data it is difficult to identify strong reflection events in the raw data, although some reflection events can be observed in the digital group formed data and the interferometric approach appears to improve the continuity of these reflection events across the noise cone. In the time-scale of this study it was not possible to process the whole test-line up to stack. However, to test whether reflection energy is at all attenuated by our method we have repeated the process involved in creating Figure 8.6b but with the inclusion of three synthetic reflection events in all data used in the processing. In Figure 8.13 we show the raw data with synthetic reflections (panel a), the interferometric estimate (panel b), the data after *f-k* filtering of the direct ground roll and adaptive subtraction of the interferometric estimate (panel c), and the data in (c) after subtraction of the original modelled reflections (panel d). The lack of a strong residual in panel (d) suggests that these strong synthetic reflection events have been preserved during interferometric ground-roll removal. There is a small residual, but the residual is not present in the interferometric estimate (panel b). It is therefore likely that the residual is a signal-processing artefact from the adaptive subtraction rather than an artefact introduced by interferometry.

The geometries in the test dataset appear to be suitable to estimate the scattering observed here. However this is not a typical source geometry and it may be that a change of geometry is required for the interferometric method to be fully applied in exploration and production. Typically source lines are coarsely spaced (Vermeer,

2002) and the application of interferometry may not be as successful (for example, we may have to consider interpolating sources over significant distance). There is scope for further work in determining if the method can be applied to conventional datasets and to find an optimal geometry for the application of the method.

There are other advantages to having estimates of the scattered waves, even if it is not possible to adaptively subtract them from all source gathers. For example, interferometric estimates may help to characterize near-surface scattering: since the estimates contain predominantly scattered waves it may be relatively easy to distinguish which arrivals are scattering events. Additionally the estimates of scattered waves may also be used in near-surface imaging algorithms (e.g., Campman and Riyanti, 2007; Kaslilar, 2007), hence a combination of our method and model-based ground-roll removal may bear fruit in future.

Recent advances have also shown that interferometry can be adapted such that cross-correlation is replaced with deconvolution, an approach that may also account for intrinsic attenuation. Multi-dimensional deconvolution (MDD) has been proposed by Wapenaar *et al.* (2008a, 2008a) and is a method which uses arrays of receivers and a matrix inversion to extract array-receiver (or array-array) Green's functions. It is expected that MDD will be less sensitive to non-uniform source distributions and to the presence of attenuation. Additionally, Vasconcelos and Snieder (2008a) consider the use of deconvolution interferometry applied to direct and scattered wavefields. Vasconcelos *et al.* (2008) discuss the use of deconvolution interferometry to predict and subtract scattered surface waves, suggesting that the deconvolution version of the method may also be powerful tool in predicting and subtracting scattered ground roll.

There are also several opportunities to improve the interferometric estimates. For example in the presence of directional bias, directional-balancing algorithms exist which allow for (correlation-type) interferometric Green's function estimates to be altered to more closely resemble those from isotropic point-sources, and algorithms have been proposed that remove non-physical arrivals (Wapenaar *et al.*, 2008a; Chapter 7; van der Neut and Bakulin, 2009). It is also possible to apply damping factors to account for the presence of attenuation when using correlation-type interferometry (Draganov *et al.*, 2008).

Finally, in future we may also consider other adaptive subtraction schemes such as pattern matching (Guitton *et al.*, 2007) or the use of 3-D (*x*,*y*,*t*) filters (Claerbout, 1998).

However, this work already demonstrates the ability of interferometry to predict and subtract scattered ground roll without adapting the interferometric processing schemes (which may make the method more computationally expensive), or without more advanced adaptive-subtraction schemes.

8.7 Conclusions

We have shown that scattered surface waves can be successfully predicted using both correlation-type and convolution-type interferometric approaches. These interferometric estimates are consistent with our previous work on surface-wave interferometry, and for the first time we have used both correlation-type and convolution-type interferometric estimates of scattered surface waves as part of a scattered ground-roll removal algorithm (interferometric ground-roll removal).

Our results illustrate the ability of this new method to successfully suppress scattered ground-roll energy, allowing for the further processing of better quality data. We have also shown that better continuity of reflection events in group-formed data results from the application of the method. Applying the method to data with synthetic reflections added to the raw data suggests that the method does not attenuate reflection data significantly. Future work on the method will include further processing to assess the effect of the method on stacked seismic data. The method could potentially form a vital part of the processing sequence for land-seismic data in the same way that surface-related multiple elimination has become a vital part of the processing sequence for marine data.

The dataset geometry that we consider is not typical of a land-seismic survey; it may be that a change in survey design is required in order to fully apply the method in exploration and production. Further research must also be undertaken to investigate the effect of different acquisition geometries, and to assess the method in regions with different near-surface scattering characteristics.

9. Virtual Seismometers in the Subsurface of the Earth from Seismic Interferometry

Seismologists image the Earth's interior by analysing recordings of propagating seismic waves. The global array of permanent seismometers that record seismic energy is confined almost exclusively to accessible and secure, land-based sites, while the spatial distribution of global earthquakes is highly heterogeneous and is often most dense beneath the oceans. This limits the resolution of subsurface images, and results in relatively few local measurements from areas of great geological and tectonic interest such as mid-ocean ridges, the Tibetan and Andean plateaus, and subduction zones. Seismic interferometry allows the Earth to be imaged using ambient-seismic energy always propagating in the subsurface, but the current and planned future global seismometer distribution remains a serious cause of bias in our knowledge of the subsurface. Here we show that a different form of interferometry can be used to construct an artificial or 'virtual' sensor from any energy source, and demonstrate this by turning earthquakes in Alaska and south-west USA into virtual seismometers located beneath the Earth's surface. Such sensors inherit the spatio-temporal response function from the radiation pattern of the original energy source; i.e. since earthquakes impart strain, the virtual seismometers measure the strain created by passing seismic waves. By definition earthquakes are located within the Earth's solid interior, so virtual seismometers can be located non-invasively inside solid bodies. Earthquakes occur precisely within many tectonically active areas of most interest in which there are often no real seismometers; their corresponding virtual seismometers provide local windows into such geological phenomena. This may allow for real-time sub-surface monitoring, and studies of earthquake triggering in those areas.

9.1 Introduction

To interrogate the Earth's subsurface at greater than a few kilometres depth, traditional seismology analyses seismic-wave energy from earthquakes. Other energy recorded in seismograms, such as ambient Earth oscillation, is considered noise and is excluded from analysis. Since 2003, however, methods of seismic interferometry (generally, the cross-correlation of seismic wavefields) have been used to synthesise impulsive-source seismograms from ambient noise recorded at two seismic receivers (Campillo and Paul, 2003). These seismograms simulate the situation where energy from a relatively impulsive, imagined or 'virtual' source occurring at the location of one receiver was recorded at the other.

To this point, the work considered in this thesis considers recordings of a series of boundary sources at a pair of receivers that are cross-correlated, then integrated (summed) over all sources (e.g., Equation 1.2). Given a suitable receiver geometry, interferometry obviates the need for actual earthquake sources to image the Earth (Claerbout, 1968; Campillo and Paul, 2003; Wapenaar, 2003; Wapenaar and Fokkema, 2004; Wapenaar *et al.*, 2004; Wapenaar and Fokkema, 2006).

Although in principle interferometry frees seismologists from constraints imposed by the global distribution of earthquakes which is strongly biased towards active margins and mid-ocean ridges, the global receiver distribution is also strongly biased (Figure 9.1). More than two-thirds of the Earth's surface is covered by liquid water or ice, rendering receiver installation difficult and expensive. Even many land-based areas have few receivers due to geographical or political inhospitability (e.g., Tibetan and Andean plateaus, Central Africa – Figure 9.1). Hence, most of the Earth's subsurface can only be interrogated using long earthquake-to-receiver, or receiver-to-receiver paths of energy propagation. This provides relatively poor spatial resolution of some of the most intriguing tectonic, geological and geophysical phenomena such as mid-ocean ridges and plate convergence zones, and consequently there is a need for data to be recorded locally to investigate such phenomena.

By taking the reciprocal of its usual form, here we show that interferometry can also be used in the opposite sense: to turn any energy *source* into a *virtual sensor*. In this form, we apply interferometry using sources enclosed within a boundary of receivers (interchange all sources and receivers in Figure 1.1a). The results of

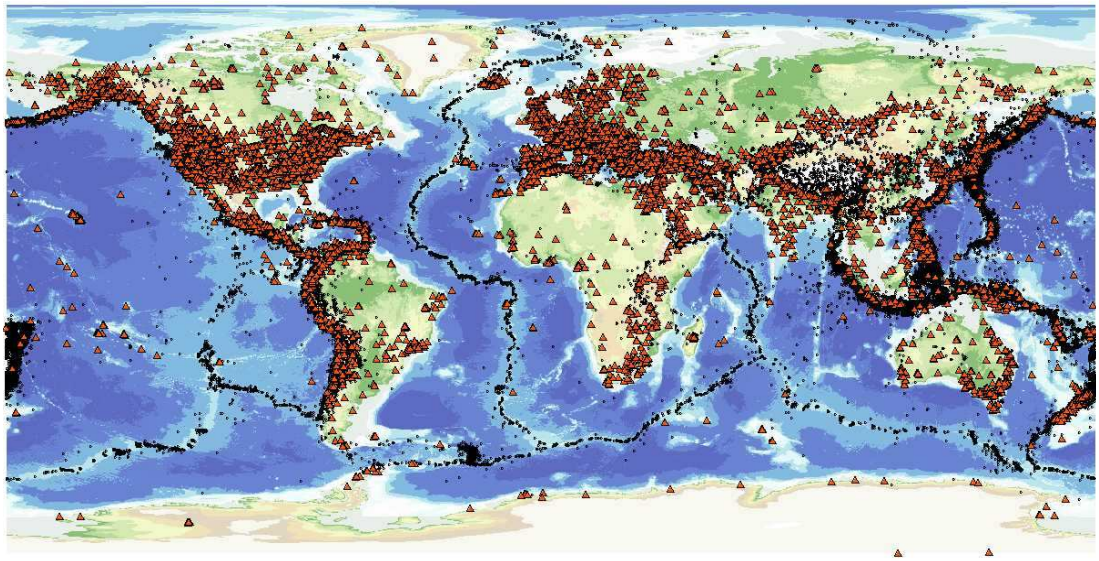

Figure 9.1: Global distribution of earthquakes of magnitude > 5 since 1973 (circles) and 13,000 NEIC-listed seismometers (triangles).

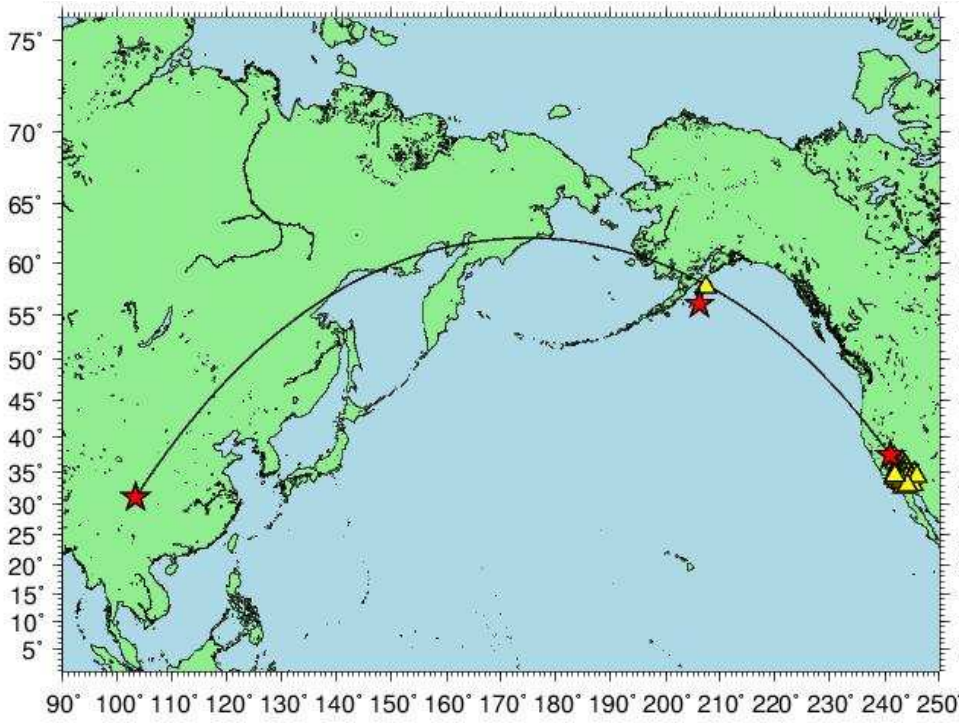

Figure 9.2: Location Map. Earthquakes (red stars); seismic stations (yellow triangles); great circle path (solid, black line).

Snieder (2004a) and those in Chapters 4 and 6 imply that it is not always necessary to have an entire enclosing boundary, provided sources are located on the extension

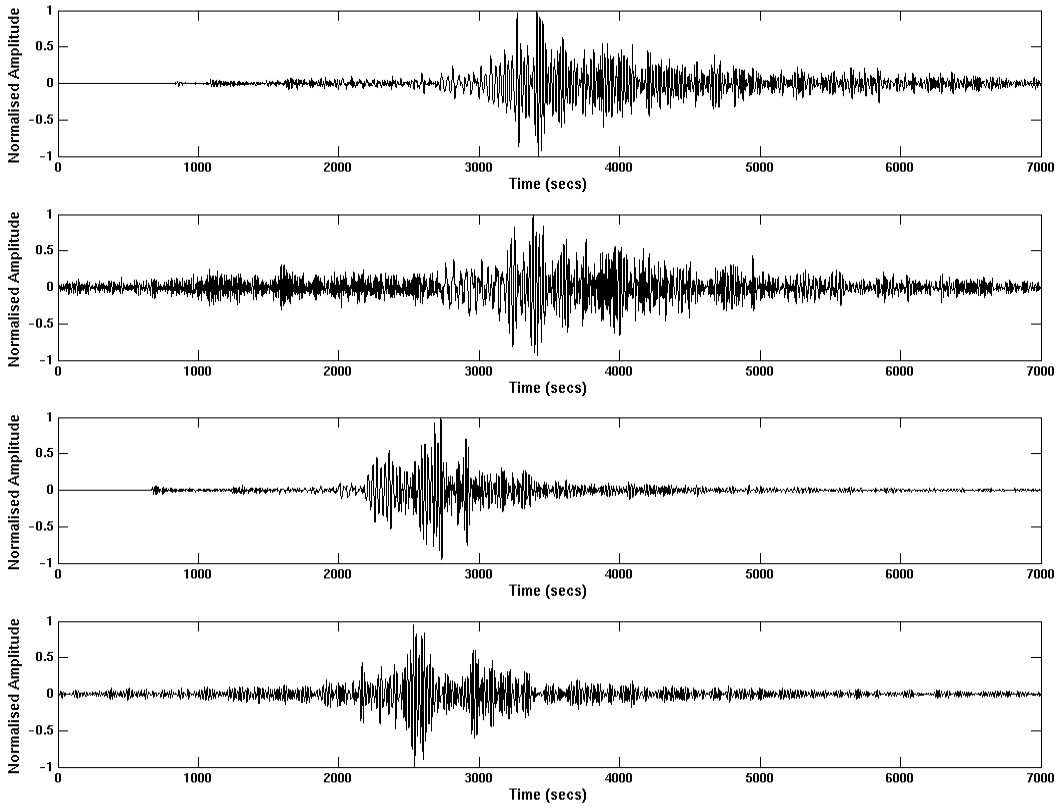

Figure 9.3: Comparison of virtual and real receiver recordings of the 2008 Sichuan earthquake using the configuration in Figure 3. (a) Real recording at MLAC in California; (b) virtual receiver recording at event within 40km of MLAC; (c) real recording at KDAK in Alaska; (d) virtual receiver recording at event within 260km of KDAK. All vertical component.

of the inter-event path. Either of the sources can then be used as a virtual receiver, to record energy from the other.

To illustrate our method simply we use real-station recordings of the 2008 Sichuan earthquake from the Caltech Regional Seismic Network to construct seismograms recorded by two virtual receivers, in the Alaskan subduction zone and in California, respectively. These virtual receivers and real stations lie approximately on a great circle with the Sichuan earthquake (Figure 9.2). It is assumed that seismic energy will travel along this path between the various chosen locations. For each Californian station located around the great circle path (i.e., those in the regions of stationary phase) the seismograms for the Sichuan and virtual-receiver earthquakes are cross-correlated, then the resulting cross-correlations are summed. In Figure 9.3 we show the real recordings of the Sichuan earthquake at stations located close to

each virtual receiver (top and second from bottom), and the resulting virtual receiver records (second from top and bottom).

The real and virtual traces should not be exactly the same since the virtual-receiver records strain whereas real receivers measure displacement (see below). In addition, the stations used for comparison are not co-located with the virtual receivers. Nevertheless, the similarity between the real and virtual receiver recording is clear to see, especially for the Californian virtual receiver.

In Section 9.2 we present a general acoustic and elastic formulation for constructing virtual sensors in this way. We also develop theory for the particular case of an earthquake double-couple moment tensor source radiating Rayleigh- and Love-surface waves, since to-date seismic interferometry has derived useful information largely from the reconstruction of surface waves. We thus derive precisely which components of surface-wave strain are recorded by virtual receiver response functions constructed from canonical normal, thrust and strike-slip earthquakes, allowing verification of the method by comparison with directly recorded seismograms in these cases (see Table 9.1).

9.2 Theoretical approach

Here we derive the theory of virtual receivers for acoustic and elastic media using methods similar in part to those of Wapenaar (2004), Wapenaar and Fokkema (2006) and van Manen *et al.* (2005; 2006). It seems straightforward to extend the theory in various forms to attenuative media, to diffusive propagation, and to other wave propagation regimes (Slob *et al.*, 2007; Slob and Wapenaar, 2007; Snieder, 2007; Snieder *et al.*, 2007).

In time-reversed acoustics, invariance of the wave equation for time-reversal can be exploited to focus a wavefield through a highly-scattering medium on an original source point (Derode *et al.*, 1995). Cassereau and Fink (1992, 1993) realized that the acoustic representation theorem (Wapenaar and Fokkema, 2004) can be used to time-reverse a wavefield in a volume by creating secondary sources (monopole and dipole) on a surface surrounding the medium such that the boundary conditions correspond to the time-reversed components of a wavefield measured there. In an

acoustic medium, the expression for the time-reversed pressure field $P_{TR}(\boldsymbol{x},t)$ at location $\boldsymbol{x}$ and time t radiated from the boundary S can be written as:

$$P_{TR}(\mathbf{r},t) = \oint_{\mathbf{r}'\in S} \frac{1}{\rho}\left[G(\mathbf{r},\mathbf{r}',t) * \nabla' P(\mathbf{r}',-t) - P(\mathbf{r}',-t) * \nabla' G(\mathbf{r},\mathbf{r}',t)\right]\cdot \mathbf{n}\, dS \qquad (9.1)$$

where $G(\mathbf{r},\mathbf{r}',t)$ denotes the Green's function of the medium, $\nabla' G(\mathbf{r},\mathbf{r}',t)$ denotes its gradient with respect to primed coordinates, and star denotes convolution. The medium density at the boundary and the outward normal to the boundary are denoted by ρ and $\mathbf{n}$, respectively. $P(\mathbf{r}',-t)$ and $\nabla' P(\mathbf{r}',-t)$ denote the time-reversal of the pressure field and its gradient. These secondary sources give rise to the back-propagating, time-reversed wavefield inside the medium that collapses onto itself at the original source location. Note that since there is no source term absorbing the converging wavefield in the original source location, it will immediately begin diverging again.

Say the initial pressure wavefield $P(\mathbf{r}',-t)$ and its gradient $\nabla' P(\mathbf{r}',-t)$ were those recorded on S from an impulsive source at some point $\mathbf{r}_1$ within the interior of S. Equation (9.1) reverses the entire wavefield throughout the interior of S, and hence can be used to compute the time-reversed wavefield (including all high-order interactions) at any such location, not only the original source location. By measuring the time-reversed wavefield in a second location $\mathbf{r}_2$, the Green's function and its time reverse (due to the expansion of the time-reversed source field after convergence at $\mathbf{r}_1$) between the source point $\mathbf{r}_1$ and the second point $\mathbf{r}_2$ is observed (Derode *et al.*, 2003b):

$$G(\mathbf{r}_2,\mathbf{r}_1,t) - G(\mathbf{r}_2,\mathbf{r}_1,-t) = \oint_{\mathbf{r}'\in S} \frac{1}{\rho}\left[G(\mathbf{r}_2,\mathbf{r}',t) * \nabla' G(\mathbf{r}',\mathbf{r}_1,-t) - \nabla' G(\mathbf{r}_2,\mathbf{r}',t) * G(\mathbf{r}',\mathbf{r}_1,-t)\right]\cdot \mathbf{n}\, dS\,. \qquad (9.2)$$

Source-receiver reciprocity gives $G(\mathbf{r}',\mathbf{r}_1,-t)=G(\mathbf{r}_1,\mathbf{r}',-t)$, so we can rewrite Equation (9.2) so that it involves only sources on the boundary enclosing the medium:

$$G(\mathbf{r}_2,\mathbf{r}_1,t)-G(\mathbf{r}_2,\mathbf{r}_1,-t)= \oint_{\mathbf{r}'\in S}\frac{1}{\rho}\left[G(\mathbf{r}_2,\mathbf{r}',t)*\nabla' G(\mathbf{r}_1,\mathbf{r}',-t)-\nabla' G(\mathbf{r}_2,\mathbf{r}',t)*G(\mathbf{r}_1,\mathbf{r}',-t)\right]\cdot\mathbf{n}\,dS\,. \quad (9.3)$$

Thus the Green's function between two points $\mathbf{x}_1$ and $\mathbf{x}_2$ can be calculated once the Green's functions between the enclosing boundary and these points are known. Following the same reasoning for the acoustic case, a similar treatment for elastic waves is possible (van Manen *et al.*, 2006; Wapenaar and Fokkema, 2006). Elastic equivalents of Equations (9.2) and (9.3) are found to be:

$$G_{im}(\mathbf{r}_2,\mathbf{r}_1,-t)-G_{im}(\mathbf{r}_2,\mathbf{r}_1,t)= \oint_{\mathbf{r}'\in S}\Big[G_{in}(\mathbf{r}_2,\mathbf{r}',t)*n_j c_{njkl}\partial'_k G_{lm}(\mathbf{r}',\mathbf{r}_1,-t) - n_j c_{njkl}\partial'_k G_{il}(\mathbf{r}_2,\mathbf{r}',t)*G_{nm}(\mathbf{r}',\mathbf{r}_1,-t)\Big]dS\,, \quad (9.4)$$

and

$$G_{im}(\mathbf{r}_2,\mathbf{r}_1,-t)-G_{im}(\mathbf{r}_2,\mathbf{r}_1,t)= \oint_{\mathbf{r}'\in S}\Big[G_{in}(\mathbf{r}_2,\mathbf{r}',t)*n_j c_{njkl}\partial'_k G_{lm}(\mathbf{r}_1,\mathbf{r}',-t) - n_j c_{njkl}\partial'_k G_{il}(\mathbf{r}_2,\mathbf{r}',t)*G_{nm}(\mathbf{r}_1,\mathbf{r}',-t)\Big]dS\,, \quad (9.5)$$

respectively. Here c is the elastic stiffness tensor, $\mathbf{n}$ is the outward normal vector to surface S, $G_{ij}(\mathbf{r}_1,\mathbf{r}',t)$ is the ith component of the particle-displacement Green's tensor at location $\mathbf{r}_1$ for a unidirectional point force in direction j at location $\mathbf{r}'$, and $\partial'_k G_{ij}(\mathbf{r}_1,\mathbf{r}',t)$ is the partial derivative of the Green's tensor in the k direction with

respect to primed coordinates. In what follows there are significant differences in methodology between acoustic and elastic cases so we address each separately.

Acoustic case

Equation (9.3) represents the Green's state with impulsive sources at locations $\mathbf{r}'$ on the surface *S* recorded at locations $\mathbf{r}_1$ and $\mathbf{r}_2$. Now, say instead an impulsive source was fired at location $\mathbf{r}_2$, and the resulting pressure signals $\tilde{G}(\mathbf{r}', \mathbf{r}_2, t)$ and $\nabla'\tilde{G}(\mathbf{r}', \mathbf{r}_2, t)$ were recorded at points $\mathbf{r}'$ on *S* (using tilde to denote quantities derived directly from measured data in practice). By reciprocity, we would record the same signals as the case where the source occurred at $\mathbf{r}'$ and was recorded at $\mathbf{r}_2$, i.e., $G(\mathbf{r}_2, \mathbf{r}', t) = \tilde{G}(\mathbf{r}', \mathbf{r}_2, t)$ and $\nabla' G(\mathbf{r}_2, \mathbf{r}', t) = \nabla'\tilde{G}(\mathbf{r}', \mathbf{r}_2, t)$. If a second source fires at location $\mathbf{r}_1$ we obtain similarly $G(\mathbf{r}_1, \mathbf{r}', t) = \tilde{G}(\mathbf{r}', \mathbf{r}_1, t)$ and $\nabla' G(\mathbf{r}_1, \mathbf{r}', t) = \nabla'\tilde{G}(\mathbf{r}', \mathbf{r}_1, t)$. Hence, by applying reciprocity to either of the acoustic Equations (9.2) or (9.3) we obtain the result,

$$G^h(\mathbf{r}_2, \mathbf{r}_1, t) = \oint_{\mathbf{r}' \in S} \frac{1}{\rho}\left[\tilde{G}(\mathbf{r}', \mathbf{r}_2, t) * \nabla'\tilde{G}(\mathbf{r}', \mathbf{r}_1, -t) - \nabla'\tilde{G}(\mathbf{r}', \mathbf{r}_2, t) * \tilde{G}(\mathbf{r}', \mathbf{r}_1, -t)\right] \cdot \mathbf{n}\, dS \quad (9.6)$$

which in the frequency domain becomes (dropping angular frequency dependence from the notation),

$$G^h(\mathbf{r}_2, \mathbf{r}_1) = \oint_{\mathbf{r}' \in S} \frac{1}{\rho}\left[\tilde{G}(\mathbf{r}', \mathbf{r}_2)\nabla'\tilde{G}^*(\mathbf{r}', \mathbf{r}_1) - \nabla'\tilde{G}(\mathbf{r}', \mathbf{r}_2)\tilde{G}^*(\mathbf{r}', \mathbf{r}_1)\right] \cdot \mathbf{n}\, dS\,. \quad (9.7)$$

The left side of Equations (9.6) and (9.7) is the so-called homogenous Green's function, $G^h(\mathbf{r}_2, \mathbf{r}_1) = G(\mathbf{r}_2, \mathbf{r}_1) - G^*(\mathbf{r}_2, \mathbf{r}_1)$ in the frequency domain, between the two source locations, and is obtained using Green's functions from $\mathbf{r}_1$ and $\mathbf{r}_2$ to the boundary location $\mathbf{r}'$.

Elastic case

Equation (9.5) represents the Green's state in which impulsive, unidirectional, force sources at locations $\mathbf{r}'$ on the surface *S* are recorded at locations $\mathbf{r}_1$ and $\mathbf{r}_2$. Now, say three impulsive, unidirectional force sources in coordinate directions *j* were fired at location $\mathbf{r}_2$, and for each the three resulting particle displacement vectors in directions *i*, $\tilde{G}_{ij}(\mathbf{r}',\mathbf{r}_2,t)$ and $\partial'_k\tilde{G}_{ij}(\mathbf{r}',\mathbf{r}_2,t)$, were recorded at points $\mathbf{r}'$ on *S*. We can obtain the Green's functions used in Equation (9.5) by reciprocity: $G_{ji}(\mathbf{r}_2,\mathbf{r}',t)=\tilde{G}_{ij}(\mathbf{r}',\mathbf{r}_2,t)$ and $\partial'_k G_{ji}(\mathbf{r}_2,\mathbf{r}',t)=\partial'_k\tilde{G}_{ij}(\mathbf{r}',\mathbf{r}_2,t)$. If a second source fires at location $\mathbf{r}_1$ we obtain similarly $G_{ji}(\mathbf{r}_1,\mathbf{r}',t)=\tilde{G}_{ij}(\mathbf{r}',\mathbf{r}_1,t)$ and $\partial'_k G_{ji}(\mathbf{r}_1,\mathbf{r}',t)=\partial'_k\tilde{G}_{ij}(\mathbf{r}',\mathbf{r}_1,t)$. Hence, by applying reciprocity to either of Equations (9.3) or (9.5) we obtain the result,

$$G^h_{im}(\mathbf{r}_2,\mathbf{r}_1,t)= \oint_{\mathbf{r}'\in S}\Big[\tilde{G}_{ni}(\mathbf{r}',\mathbf{r}_2,t)*n_j c_{njkl}\partial'_k\tilde{G}_{lm}(\mathbf{r}',\mathbf{r}_1,-t) - n_j c_{njkl}\partial'_k\tilde{G}_{li}(\mathbf{r}',\mathbf{r}_2,t)*\tilde{G}_{mn}(\mathbf{r}',\mathbf{r}_1,-t)\Big]dS \qquad (9.8)$$

which in the frequency domain becomes (dropping angular frequency dependence from the notation),

$$G^h_{im}(\mathbf{r}_2,\mathbf{r}_1)= \oint_{\mathbf{r}'\in S}\Big[\tilde{G}_{ni}(\mathbf{r}',\mathbf{r}_2)n_j c_{njkl}\partial'_k\tilde{G}^*_{lm}(\mathbf{r}',\mathbf{r}_1) - n_j c_{njkl}\partial'_k\tilde{G}_{li}(\mathbf{r}',\mathbf{r}_2)\tilde{G}^*_{nm}(\mathbf{r}',\mathbf{r}_1)\Big]dS\,. \qquad (9.9)$$

the left side of Equations (9.8) and (9.9) is the elastic homogenous Green's function, $G^h_{im}(\mathbf{r}_2,\mathbf{r}_1)=G_{im}(\mathbf{r}_2,\mathbf{r}_1)-G^*_{im}(\mathbf{r}_2,\mathbf{r}_1)$ in the frequency domain, between the two source locations.

Acoustic and Elastic case

The right side of Equations (9.6) and (9.7) [(9.8) and (9.9)] involve only time-domain cross-correlation (frequency-domain multiplications with the complex conjugate) of Green's functions recorded on the surface *S* with sources at $\mathbf{r}_1$ and $\mathbf{r}_2$. The left side, on the other hand, gives the homogenous Green's function between the two source locations. That is, these equations convert the recorded data into the data that *would have been recorded if the previous source location* $\mathbf{r}_2$ *had in fact been a receiver location*. This is achieved without any approximations, and without any synthetically-modelled Green's functions. For each source point the equations require one (pressure) source in the acoustic case, and three (unidirectional force) sources in the elastic case. It also seems that derivative (dipole) sources are required, but below we will show that these can be dispensed with while still obtaining good approximations to the results.

Non-Impulsive Sources

Now say the two sources at $\mathbf{r}_1$ and $\mathbf{r}_2$ emitted a wavefield with source signatures represented by the temporal-frequency spectra $W_1(\omega)$ and $W_2(\omega)$, respectively. In the acoustic case, recordings on *S* would take forms similar to $\tilde{G}(\mathbf{r}', \mathbf{r}_i) = W_i\, G(\mathbf{r}', \mathbf{r}_i)$ for *i*=1,2, and the cross-correlation operation in Equation (9.7) gives,

$$W_2 W_1^*\, G_h(\mathbf{r}_2, \mathbf{r}_1) = \oint_{\mathbf{r}' \in S} \frac{1}{\rho} \left[\tilde{G}(\mathbf{r}', \mathbf{r}_2) \nabla' \tilde{G}^*(\mathbf{r}', \mathbf{r}_1) - \nabla' \tilde{G}(\mathbf{r}', \mathbf{r}_2) \tilde{G}^*(\mathbf{r}', \mathbf{r}_1) \right] \cdot \mathbf{n}\, dS \,. \qquad (9.10)$$

In the time domain then, the same cross-correlation operation gives the homogeneous Green's function convolved with the cross-correlation of the two source wavelets.

In the elastic case, if all three components of each of the two sources are excited with the same source temporal-frequency signature, $W_1(\omega)$ and $W_2(\omega)$ respectively for sources 1 and 2, then the cross-correlation operations in Equation (9.9) give,

$$W_2 W_1^* \, G^h_{im}(\mathbf{r}_2, \mathbf{r}_1) = \oint_{\mathbf{r}' \in S} \left[\tilde{G}_{ni}(\mathbf{r}', \mathbf{r}_2) n_j c_{njkl} \partial'_k \tilde{G}^*_{lm}(\mathbf{r}', \mathbf{r}_1) - n_j c_{njkl} \partial'_k \tilde{G}_{li}(\mathbf{r}', \mathbf{r}_2) \tilde{G}^*_{nm}(\mathbf{r}', \mathbf{r}_1) \right] dS \, . \quad (9.11)$$

Again, in the time domain, the same cross-correlation operation gives the homogeneous Green's function convolved with the cross-correlation of the two source wavelets.

Moment Tensor Sources

We wish to apply the above theory to recordings of earthquake sources from within the earth. This requires that we create corresponding expressions from moment tensor-style sources rather than unidirectional force sources. It also requires that we develop approximations for cases where we do not have separate records for each individual component of the Green's function but instead have a set of recordings from a single source comprising a combination of different source components. In order to adapt the interferometric formulae to include moment tensors we must first apply changes that allow for the inclusion of strain sources, which correspond to single components of the moment-tensor. To do this we apply spatial derivatives to each of the source locations in Equation (9.9), i.e.,

$$\partial_p \partial_q G^h_{im}(\mathbf{r}_2, \mathbf{r}_1) = \oint_{\mathbf{r}' \in S} \left[\partial_p \tilde{G}_{ni}(\mathbf{r}', \mathbf{r}_2) n_j c_{njkl} \partial'_k \partial_q \tilde{G}^*_{lm}(\mathbf{r}', \mathbf{r}_1) - n_j c_{njkl} \partial'_k \partial_p \tilde{G}_{li}(\mathbf{r}', \mathbf{r}_2) \partial_q \tilde{G}^*_{nm}(\mathbf{r}', \mathbf{r}_1) \right] dS \, . \quad (9.12)$$

where ∂_p is the spatial derivative applied at $\mathbf{r}_2$ and ∂_q is the spatial derivative applied at $\mathbf{r}_1$. Note that the resulting Green's function is the elastic homogeneous Green's function modulated by two independent spatial derivatives.

We can consider these strain components to represent single force couples (i.e., a pair of opposing forces defined as M_{ij}, acting in the *i*-direction, separated in the *j*-

direction). If the sources at $\mathbf{r}_1$ and $\mathbf{r}_2$ consist of single couples then we may use Equation (9.12) to construct spatial derivatives of the homogeneous Green's function. However, if the source consists of a combination of couples (e.g., a double-couple Earthquake source, or an explosion) then we must make alterations to Equation (9.12). For such sources we define a moment tensor **M**,

$$\mathbf{M} = \begin{bmatrix} M_{11} & M_{12} & M_{13} \\ M_{21} & M_{22} & M_{23} \\ M_{31} & M_{32} & M_{33} \end{bmatrix}, \tag{9.13}$$

and from Aki and Richards (2002) the displacement at $\mathbf{r}_1$ due to this moment tensor source at $\mathbf{r}_2$ is given by $M_{pq}\partial_q \widetilde{G}_{ip}(\mathbf{r}_2, \mathbf{r}_1)$, where Einstein's summation convention applies. This Green's function is the *i*th component of displacement, $u_i(\mathbf{r}_2, \mathbf{r}_1)$ at $\mathbf{r}_2$ due to a moment tensor source at $\mathbf{r}_1$.

For the case where we would like to obtain the Green's function between two earthquake sources we alter Equation (9.12) by inserting moment tensors, $\mathbf{M}^1$ and $\mathbf{M}^2$ at the corresponding source positions $\mathbf{r}_1$ and $\mathbf{r}_2$:

$$\begin{aligned} M^2_{ip} M^1_{mq} \partial_p \partial'_q G^h_{im}(\mathbf{r}_2, \mathbf{r}_1) = \\ \int_{\mathbf{r}' \in S} \Big\{ & M^2_{ip} \partial_p \widetilde{G}_{ni}(\mathbf{r}', \mathbf{r}_2) \; n_j c_{njkl} \partial'_k M^1_{mq} \partial_q \widetilde{G}^*_{lm}(\mathbf{r}', \mathbf{r}_1) \\ & - n_j c_{njkl} \partial'_k M^2_{ip} \partial_p \widetilde{G}_{li}(\mathbf{r}', \mathbf{r}_2) \; M^1_{mq} \partial_q \widetilde{G}^*_{nm}(\mathbf{r}', \mathbf{r}_1) \Big\} \, dS \,. \end{aligned} \tag{9.14}$$

The resulting interferometric Green's functions are modulated by both of these moment tensors. The term $n_j c_{njkl} \partial'_k M^1_{mq} \partial_q \widetilde{G}_{lm}(\mathbf{r}', \mathbf{r}_1)$ is the *n*th component of traction, $T_n(\mathbf{r}', \mathbf{r}_1)$ at the boundary due to a moment tensor source. Using this definition, and the definition of displacement above we re-write Equation (9.14) in terms of displacement and traction,

$$M_{ip}^{2} M_{mq}^{1} \partial_p \partial'_q G_{im}^{h}(\mathbf{r}_2, \mathbf{r}_1) =$$

$$\int_{\mathbf{r}' \in s} \left\{ u_n(\mathbf{r}', \mathbf{r}_2) \cdot T_n^*(\mathbf{r}', \mathbf{r}_1) - T_n(\mathbf{r}', \mathbf{r}_2) \cdot u_n^*(\mathbf{r}', \mathbf{r}_2) \right\} dS \,. \tag{9.15}$$

Monopole Seismometers

The right hand side of Equation (9.15) requires both monopole (displacement, u_n) and dipole (traction, T_n) recordings of the energy from both moment tensor sources. Real-world seismometers only record displacement (or a time derivative thereof). In the case of particle-displacement seismometers one can usually approximate Equation (9.15) as

$$M_{ip}^{2} M_{mq}^{1} \partial_p \partial'_q G_{im}^{h}(\mathbf{r}_2, \mathbf{r}_1) \;=\; iK\omega \int_{\mathbf{r}' \in s} u_n(\mathbf{r}', \mathbf{r}_2)\, u_n^*(\mathbf{r}', \mathbf{r}_1)\, dS \tag{9.16}$$

for some constant *K*. This is similar to approximations made in virtual-source interferometry where only monopole sources are typically available (for example, in Chapter 4 it is shown how such an approximation can be made for surface waves, and a value of *K* specific to that case is derived).

If particle-velocity seismometers are used, the time-derivatives $\dot{u}_n$ of each of the displacements u_n on the right of Equation (9.16) are measured. The left side of Equation (9.16) is then obtained by taking minus (due to the complex conjugate in $u_n^*(\mathbf{x}' \,|\, \mathbf{x}_1)$) a double integration in time of the right side, giving

$$M_{ip}^{2} M_{mq}^{1} \partial_p \partial'_q G_{im}^{h}(\mathbf{r}_2, \mathbf{r}_1) \;=\; -\frac{K}{i\omega} \int_{\mathbf{r}' \in s} \dot{u}_n(\mathbf{r}', \mathbf{r}_2)\, \dot{u}_n^*(\mathbf{r}', \mathbf{r}_1)\, dS \,. \tag{9.17}$$

Equivalently we obtain the *strain rate* on the left using,

$$M_{ip}^{2} M_{mq}^{1} \partial_p \partial'_q \dot{G}_{im}^{h}(\mathbf{r}_2, \mathbf{r}_1) \;=\; -K \int_{\mathbf{r}' \in s} \dot{u}_n(\mathbf{r}', \mathbf{r}_2)\, \dot{u}_n^*(\mathbf{r}', \mathbf{r}_1)\, dS \,. \tag{9.18}$$

Surface waves

We illustrate the above in the particular case of surface waves since to-date most applications have used that wave type.

Surface Wave Green's Functions

We assume that the portion of the earth in which we are interested can be approximated by a lossless, horizontally layered medium, and that in this medium the wavefield is dominated by (or can be represented by) surface waves. Further, to simplify our expressions by avoiding cross-mode intercorrelations we assume that only a single surface wave mode is present or dominant (or that modes have been separated prior to any application of interferometry as discussed in Chapter 4). We use a strain operator $\mathbf{E}^{\nu}$ to define the spatial derivatives,

$$\mathbf{E}^{\nu}(\varphi) = \begin{pmatrix} ik_{\nu}\cos\varphi \\ ik_{\nu}\sin\varphi \\ \dfrac{\partial}{\partial z} \end{pmatrix}, \tag{9.19}$$

where k_{ν} is the wavenumber associated with the νth surface wave mode and φ is the azimuth of the horizontal projection of the source-receiver path (Figure 4.2). The Green's function representing a single force couple is given by applying the strain operator to Equation (14) of Snieder (2002b),

$$\partial_q G_{im}(\mathbf{r}_2, \mathbf{r}_1) = p_i^{\nu}(z_2, \varphi) E_q^{\nu *} p_m^{\nu *}(z_1, \varphi) \frac{e^{i\left(k_{\nu}X + \frac{\pi}{4}\right)}}{\sqrt{\frac{\pi}{2}k_{\nu}X}}, \tag{9.20}$$

where z is positive downwards. Here p_i^{ν} is the ith component of the polarisation vector, given for Rayleigh waves as

$$\mathbf{p}^{\nu R}(z,\varphi)=\begin{pmatrix} r_1(z)\cos\varphi \\ r_1(z)\sin\varphi \\ ir_2(z) \end{pmatrix}, \tag{9.21}$$

and for Love waves as

$$\mathbf{p}^{\nu L}(z,\varphi)=\begin{pmatrix} -l_1(z)\sin\varphi \\ l_1(z)\cos\varphi \\ 0 \end{pmatrix}, \tag{9.22}$$

where X is the horizontal offset between the locations $\mathbf{r}_1$ and $\mathbf{r}_2$, $r_1^{\nu}(z)$ and $r_2^{\nu}(z)$ are the horizontal and vertical Rayleigh-wave eigenfunctions, respectively, and $l_1^{\nu}(z)$ is the horizontal Love wave eigenvector. To simplify the expression the modal normalization $8c^{\nu}U^{\nu}I_1^{\nu}=1$ is again assumed (Snieder, 2002b), where c^{ν}, U^{ν}, and I_1^{ν} are the phase velocity, group velocity and kinetic energy for the current mode respectively. This Green's function is for a single frequency, and in the following we assume summation over the relevant frequency range. Note that when we refer specifically to Rayleigh waves or Love waves we use superscripts *R* and *L*, as in Equations (9.21) and (9.22).

First we use Equation (9.20) to define the surface wave Green's function representing the particle displacement $\mathbf{u}(\mathbf{r}_2,\mathbf{r}_1)$ at $\mathbf{r}_2$ due to the general moment tensor source at $\mathbf{r}_1$. For Rayleigh waves this is $\mathbf{u}^R(\mathbf{r}_2,\mathbf{r}_1)$ with components

$$\begin{aligned} u_1^R(\mathbf{r}_2,\mathbf{r}_1) &= M_{mq}^1\partial_q G_{1m}^R(\mathbf{r}_2,\mathbf{r}_1) \\ &= r_1(z_2)\cos\varphi M_{mq}^1 E_q^{\nu *} p_m^{\nu *}(z_1,\varphi)\frac{e^{i\left(k_\nu X+\frac{\pi}{4}\right)}}{\sqrt{\frac{\pi}{2}k_\nu X}}, \end{aligned} \tag{9.23}$$

$$u_2^R(\mathbf{r}_2,\mathbf{r}_1) = M_{mq}^1 \partial_q G_{2m}^R(\mathbf{r}_2,\mathbf{r}_1)$$

$$= r_1(z_2)\sin\varphi M_{mq}^1 E_q^{\nu *} p_m^{\nu *}(z_1,\varphi)\frac{e^{i\left(k_\nu X+\frac{\pi}{4}\right)}}{\sqrt{\frac{\pi}{2}k_\nu X}}, \tag{9.24}$$

$$u_3^R(\mathbf{r}_2,\mathbf{r}_1) = M_{mq}^1 \partial_q G_{3m}^R(\mathbf{r}_2,\mathbf{r}_1)$$

$$= i r_2(z_2) M_{mq}^1 E_q^{\nu *} p_m^{\nu *}(z_1,\varphi)\frac{e^{i\left(k_\nu X+\frac{\pi}{4}\right)}}{\sqrt{\frac{\pi}{2}k_\nu X}}, \tag{9.25}$$

and where G^R denotes the Rayleigh wave component of the Green's function. For Love waves the equivalent displacements $\mathbf{u}^L(\mathbf{r}_2,\mathbf{r}_1)$ are defined as

$$u_1^L(\mathbf{r}_2,\mathbf{r}_1) = M_{mq}^1 \partial_q G_{1m}^L(\mathbf{r}_2,\mathbf{r}_1)$$

$$= -l_1(z_2)\sin\varphi M_{mq}^1 E_q^{\nu *} p_m^{\nu *}(z_1,\varphi)\frac{e^{i\left(k_\nu X+\frac{\pi}{4}\right)}}{\sqrt{\frac{\pi}{2}k_\nu X}}, \tag{9.26}$$

$$u_2^L(\mathbf{r}_2,\mathbf{r}_1) = M_{mq}^1 \partial_q G_{2m}^L(\mathbf{r}_2,\mathbf{r}_1)$$

$$= l_1(z_2)\cos\varphi M_{mq}^1 E_q^{\nu *} p_m^{\nu *}(z_1,\varphi)\frac{e^{i\left(k_\nu X+\frac{\pi}{4}\right)}}{\sqrt{\frac{\pi}{2}k_\nu X}}, \tag{9.27}$$

$$u_3^L(\mathbf{r}_2,\mathbf{r}_1) = M_{mq}^1 \partial_q G_{3m}^L(\mathbf{r}_2,\mathbf{r}_1) = 0. \tag{9.28}$$

where G^L denotes the Love wave component of the Green's function, and the terms on the seconds lines of Equations (9.23) to (9.27) are described in Chapter 4.

Surface Wave Interferometry

We can now define the forward time part of the interferometric surface wave Green's function (the left side of Equation (9.17)) as,

$$M_{ip}^{2} M_{mq}^{1} \partial_p \partial_q G_{im}(\mathbf{r}_2, \mathbf{r}_1) =$$

$$\left[M_{ip}^{2} E_p^{\nu} p_i^{\nu}(z_2, \varphi) \right] \left[M_{mq}^{1} E_q^{\nu *} p_m^{\nu *}(z_1, \varphi) \frac{e^{i\left(k_\nu X + \frac{\pi}{4}\right)}}{\sqrt{\frac{\pi}{2} k_\nu X}} \right]. \qquad (9.29)$$

On the right side of this equation, the right square bracket is equal to the displacement **u** of the appropriate surface wave. The left square bracket shows that the virtual receiver strain-response function is represented by all M_{ip}^{2}, the components of the moment tensor of event 2, since $E_p^{\nu} p_i^{\nu}(z_2, \varphi)$ is simply the *p,i* component of strain. Hence, the virtual receiver measures the same components of strain as occurred in the original earthquake source mechanism.

Using Equation (9.29) we can predict phase differences between interferometric estimates using different source types of moment tensor form $\mathbf{M}^1$ and $\mathbf{M}^2$, since we know the form of the strain operator (Equation (9.19)). While we may not necessarily know the different eigenvectors required to define $\mathbf{p}^{\nu}(z_1, \varphi)$ and $\mathbf{p}^{\nu}(z_2, \varphi)$ the above equation also shows their effect on the phase of the surface wave.

To give a feeling for what recordings at virtual sensors detect, we consider a general moment tensor source $\mathbf{M}^1$ at location $\mathbf{r}_1$ recorded at a virtual receiver at location $\mathbf{r}_2$ constructed from a range of canonical example moment-tensor sources. This range includes a strike-slip, a thrust, and a normal earthquake event. For a fault oriented in the North-South direction we derive explicit expressions for both Love and Rayleigh waves from an event with a general moment tensor recorded at a virtual receiver with the three different source types. Although we have fixed the orientation of the fault plane to be North-South trending, we allow a general azimuth of the (horizontal projection of the) virtual receiver–to-source path. All of the following equations can therefore be applied to any fault plane geometry simply by rotating the co-ordinate axes such that the fault-plane at the virtual receiver lies in the i_2 direction.

Strike-Slip Virtual Sensor

The scalar moment tensor for a pure left-lateral strike-slip event on a North-South trending fault (denoted $\mathbf{M}^{SS}$) is then given by $M_{12}=M_{21}=1$ with all other $M_{ij}=0$. Equation (9.29) then becomes,

$$\mathbf{M}^{ss} M^1_{mq} \partial_p \partial_q G^R_{im}(\mathbf{r}_2, \mathbf{r}_1) =$$

$$2ik_\nu r_1(z_2) \cos\varphi \sin\varphi \; M^1_{mq} E^{\nu\,*}_q p^{\nu\,*}_m(z_1, \varphi) \frac{e^{i\left(k_\nu X + \frac{\pi}{4}\right)}}{\sqrt{\frac{\pi}{2} k_\nu X}}. \qquad (9.30)$$

Hence, a virtual receiver constructed from such a strike-slip event (left side of the above equation) measures the quantity on the right side, which is a scaled version of one of the horizontal components of particle displacement at location $\mathbf{r}_2$, i.e.,

$$\mathbf{M}^{ss} M^1_{mq} \partial_p \partial_q G^R_{im}(\mathbf{r}_2, \mathbf{r}_1) \; = \; \left[2ik_\nu \sin\varphi\right] \; u^R_1(\mathbf{r}_2, \mathbf{r}_1), \qquad (9.31)$$

or

$$\mathbf{M}^{ss} M^1_{mq} \partial_p \partial_q G^R_{im}(\mathbf{r}_2, \mathbf{r}_1) \; = \; \left[2ik_\nu \cos\varphi\right] \; u^R_2(\mathbf{r}_2, \mathbf{r}_1). \qquad (9.32)$$

The terms $ik_\nu \cos\varphi$ and $ik_\nu \sin\varphi$ correspond to horizontal spatial derivatives (cf. Equation (9.19)). Hence, the resulting surface waves in the preceding two equations are spatial derivatives in the i_2 (i_1) direction of the horizontal component of particle displacement in the i_1 (i_2) direction, respectively. In terms of strain, the equations represent recordings of twice the e_{12} and e_{21} components at the virtual receiver, respectively.

For Love waves we obtain

$$\mathbf{M}^{ss} M^1_{mq} \partial_p \partial_q G^L_{im}(\mathbf{x}_2 \,|\, \mathbf{x}_1) = \left[ik_\nu \cos\varphi\right] \; u^L_2(\mathbf{x}_2 \,|\, \mathbf{x}_1) + \left[ik_\nu \sin\varphi\right] \; u^L_1(\mathbf{x}_2 \,|\, \mathbf{x}_1). \qquad (9.33)$$

Hence, for Love waves the virtual receiver measures the sum of the horizontal derivative in the i_1 direction of the particle displacement in the i_2 direction, with the horizontal derivative in the i_2 direction of the particle displacement in the i_1 direction. Again, this corresponds to the sum of the e_{12} and e_{21} components of strain at the virtual-receiver position.

Thus the strike-slip vertical receiver for this fault configuration is equivalent to recording various combinations of horizontal strain for both Love and Rayleigh waves.

Thrust Virtual Sensor

The moment tensor ($\mathbf{M}^{\mathrm{TF}}$) for a thrust event on a North-South trending fault is given by M_{11}=-1 and M_{33}=1 with all other M_{ij}=0. For Rayleigh waves we then obtain,

$$\mathbf{M}^{\mathbf{TF}} M^1_{mq} \partial_p \partial_q G^R_{im}(\mathbf{r}_2, \mathbf{r}_1) = \left(\frac{\partial}{\partial z} i r_2(z_2) - i k_\nu r_1(z_2) \cos^2 \varphi \right) M^1_{mq} E^{\nu *}_q p^{\nu *}_m(z_1, \varphi) \frac{e^{i\left(k_\nu X + \frac{\pi}{4}\right)}}{\sqrt{\frac{\pi}{2} k_\nu X}}, \qquad (9.34)$$

and from Equation (9.23) and (9.25) this is equivalent to

$$\mathbf{M}^{TF} M^1_{mq} \partial_p \partial_q G^R_{im}(\mathbf{r}_2, \mathbf{r}_1) = \frac{\partial}{\partial z} u^R_3(\mathbf{r}_2, \mathbf{r}_1) - k_\nu \cos\varphi \, u^R_1(\mathbf{r}_2, \mathbf{r}_1). \qquad (9.35)$$

So in this configuration, a virtual receiver constructed from a reverse fault measures the difference between the e_{33} and e_{11} components of strain.

For Love waves on the other hand we obtain,

$$\mathbf{M}^{TF} M^1_{mq} \partial_p \partial_q G^L_{im}(\mathbf{r}_2, \mathbf{r}_1) = -\left[i k_\nu (\cos\varphi) \right] u^L_1(\mathbf{r}_2, \mathbf{r}_1), \qquad (9.36)$$

or

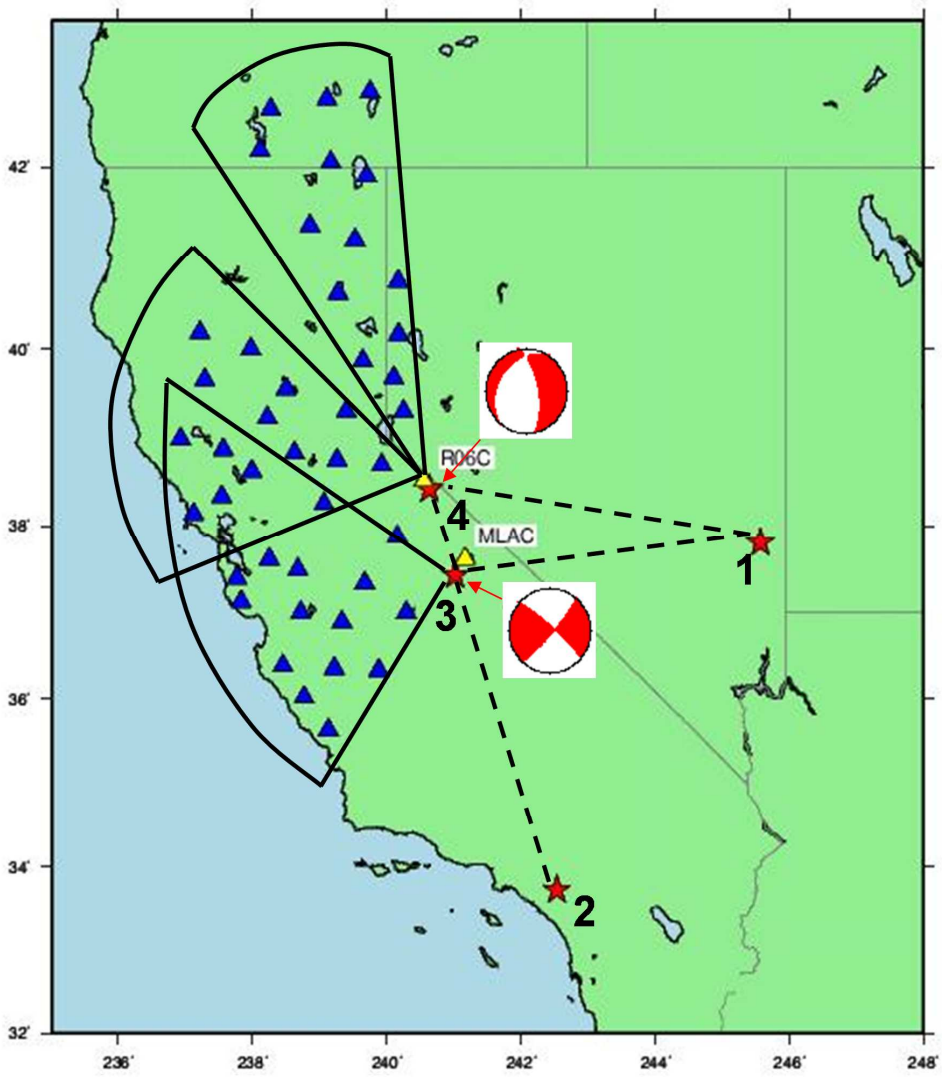

Figure 9.4: Location Map. Earthquakes (red stars) numbered 1 to 4; seismic stations used in interferometry (blue triangles); seismic stations for comparison (yellow triangles); focal mechanisms of virtual receivers are shown as standard lower-hemisphere projections near to their locations. Dashed lines indicate inter-Earthquake paths, solid lines connected by arcs indicate the region within which receivers were located for each Earthquake pair.

$$\mathbf{M}^{TF} M^{1}_{mq} \partial_p \partial_q G^{L}_{im}(\mathbf{r}_2, \mathbf{r}_1) = \left[ik_\nu (\sin\varphi)\right]\ u^{L}_{2}(\mathbf{r}_2, \mathbf{r}_1), \tag{9.37}$$

which is equivalent to recording the $-e_{11}$ or e_{22} components of strain. This is because there is no component corresponding to M_{33} in the Love wave Green's function in a horizontally-layered, isotropic, 1-dimensional medium, and in this case $e_{22} = -e_{11}$.

Thus the thrust vertical receiver for this fault configuration is equivalent to recording various combinations of horizontal and vertical strains for Love and Rayleigh waves.

Normal Virtual Sensor

The moment tensor for a normal fault is simply the negative of that for the thrust fault. Hence, by applying sign reversals to the above moment tensors we obtain the results for a normal virtual sensor.

Exploding virtual receiver

Finally we consider the case of a virtual receiver constructed from an explosive source. The moment tensor, $\mathbf{M}^{EX}$, then has $M_{11} = M_{22} = M_{33} = 1$, with all other $M_{ij} = 0$. The result is simply the sum of the diagonal components of the strain tensor $e_{11}+e_{22}+e_{33}$, i.e.,

$$\mathbf{M}^{EX} M^{1}_{mq} \partial_p \partial_q G^{R}_{im}(\mathbf{r}_2, \mathbf{r}_1) = \left[ik_\nu \cos\varphi\right] u_1^R(\mathbf{r}_2, \mathbf{r}_1) + \left[ik_\nu \sin\varphi\right] u_2^R(\mathbf{r}_2, \mathbf{r}_1) + \frac{\partial}{\partial z} u_3^R(\mathbf{r}_2, \mathbf{r}_1), \tag{9.38}$$

for Rayleigh waves and,

$$\mathbf{M}^{EX} M^{1}_{mq} \partial_p \partial_q G^{L}_{im}(\mathbf{r}_2, \mathbf{r}_1) = \left[ik_\nu \cos\varphi\right] u_1^L(\mathbf{r}_2, \mathbf{r}_1) + \left[ik_\nu \sin\varphi\right] u_2^L(\mathbf{r}_2, \mathbf{r}_1), \tag{9.39}$$

for Love waves (since again there is no component corresponding to M_{33} in this Love wave Green's function).

Moment Tensor Summary

The above examples illustrate how we can use theoretical Green's functions to investigate the effect of cross-correlating recordings from two sources that can be represented by moment tensors. We find that, by using moment-tensor sources at virtual-receiver locations, the resulting surface-wave estimates can be considered to

Thrust Fault Earthquake	$e_{33} - e_{11}$
Normal Earthquake	$e_{11} - e_{33}$
Strike-Slip Earthquake	$e_{12} + e_{21}$
Isotropic Explosion	$e_{11} + e_{22} + e_{33}$

Table 9.1: Combinations of strain components e_{ij} measured for each canonical source mechanism. We use the Aki and Richards left-handed coordinate system with axes 1, 2 and 3 pointing East, North and down, respectively. The earthquake fault plane is assumed to be oriented (strike) Northwards, the strike-slip fault plane is vertical while the thrust and normal fault planes have 45 degrees dip. No fault is assumed for the explosion.

be combinations of spatial derivatives of particle displacement (i.e., strain sensors). Moment tensors are readily available for most sizeable earthquakes, hence similar analysis to the above can be used to understand the different Green's functions estimated using virtual-receiver seismic interferometry for real earthquakes. This may be important as in conventional earthquake seismology, data contain a receiver-response function and a moment tensor source function. However, in virtual-receiver interferometry the moment tensor at the virtual-receiver location becomes a moment-tensor sensor. Conventional approaches to data analysis may therefore require some development in order to use this new data type.

9.3 Verification

The matches in Figure 9.3 are not perfect so we consider a test case using earthquake and receiver geometries that allow more in-depth analysis of the method. A potential problem in verifying virtual receiver seismograms is that no direct seismic-frequency strain sensors exist in the Earth close to earthquakes for comparison. To make direct comparisons possible, in principle one could construct horizontal-strain measurements by computing scaled differences between closely-spaced seismometers (Curtis and Robertsson, 2002), but in the frequency range considered here (15s-33s period) across south-west USA this is generally not possible since the

seismometer distribution is spatially aliased. Instead we derive estimates of the scaled horizontal strain in a direction in-line with the source-to-seismometer path by taking time-derivatives of measured seismograms. This results in frequency-domain multiplication by $i\omega = ick$, where ω and k are temporal and in-line spatial frequencies, respectively, and c is phase velocity. Thus we approximate a spatial derivative (multiplication by ik) assuming that the unknown phase velocity c does not change rapidly within the frequency band considered. There is no equivalent operation to approximate vertical strains in this case, so vertical strain measurements from virtual receivers constitute new information about Earth vibrations.

If an earthquake is considered to be temporally-impulsive with moment tensor $\mathbf{M}_1$, and is recorded by a virtual sensor constructed from another earthquake with moment tensor $\mathbf{M}_2$, the data consist of a sum of strain Green's functions between the locations of the two earthquakes, scaled by the product of the respective moment-tensor components (Equations (9.15) to (9.18)). However, earthquake sources are also generally non-impulsive. If $W_i(\omega)$ is the frequency domain representation of the source time function of earthquake i, the seismograms recorded at the virtual sensor are modulated by $W_2 W_1^*$ (Equations (9.10) and (9.11)). Hence, if for example the two source-time functions were similar, $W_2 \approx W_1$, the recorded data would consist of inter-earthquake strain Green's functions modulated by the autocorrelation of the source time function, shifted in time by $t_2 - t_1$, where t_i is the origin time of earthquake i. We remove that time shift in the results that follow. As a consequence, compared to a zero-phase seismometer, residual phase shifts in the virtual-sensor records are caused by differences between the two source time functions W_1 and W_2.

Since virtual sensors inherit the spatio-temporal response function of the original source, those constructed from purely normal and purely thrust earthquakes measure strains in a vertical-horizontal plane, while those from strike-slip earthquakes measure strain in the purely horizontal plane. Those constructed from subsurface explosions or implosions measure volumetric expansion of the rock mass, the solid-body equivalent of a pressure sensor in a fluid (Curtis and Robertsson, 2002). Table 9.1 summarises the strain components measured for each canonical earthquake or explosive source mechanism.

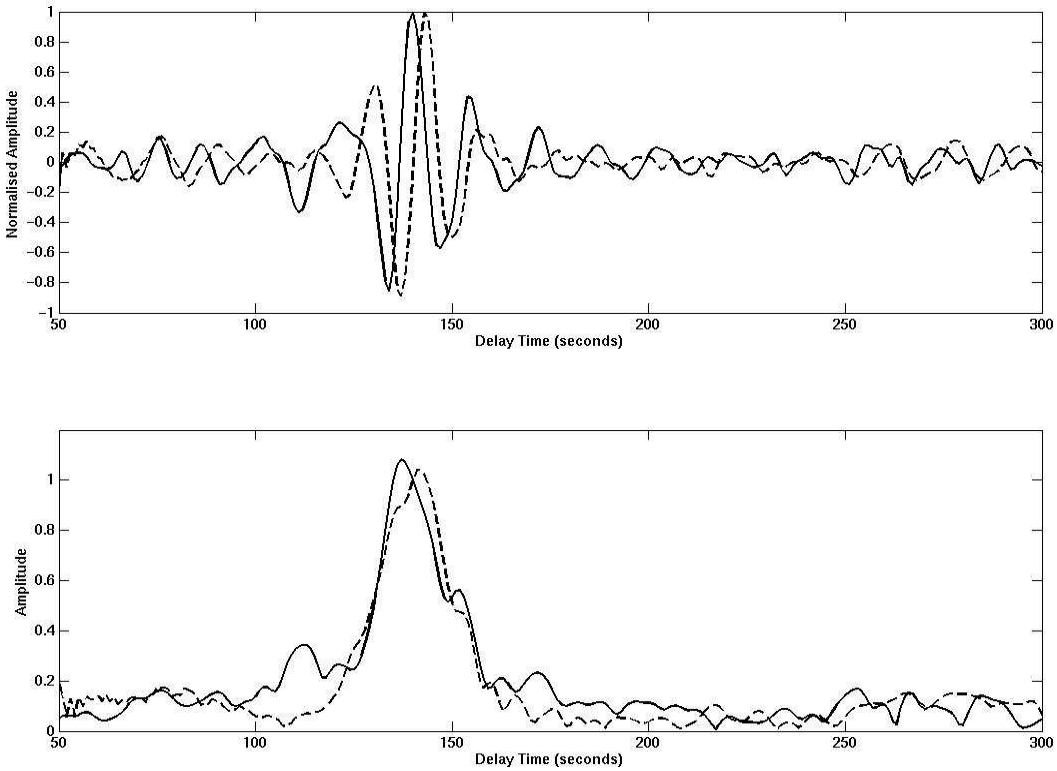

Figure 9.5: Compares recordings of earthquake 1 by the strike-slip virtual receiver 3 and the real seismometer MLAC: seismograms (top) and envelope functions (bottom) recorded at the virtual receiver (solid line) and the inverted time-derivative of the radial-component seismogram from MLAC (dashed). Signals are constructed by cross-correlation and stacking of 20 stations from the USArray and Berkeley seismic networks. Amplitudes are normalised and all traces are band-passed between 15 and 33 seconds.

Figure 9.4 shows earthquakes and stations used. Two earthquakes with approximately canonical (strike-slip and normal) moment-tensor sources were chosen to be converted into virtual sensors because *(i)* seismometers (MLAC and R06C) exist in their local vicinity for comparison, *(ii)* they had a well-constrained moment-tensor source mechanism, *(iii)* they had lowest possible magnitude subject to constraints *(i)* and *(ii)* and hence are as spatially and temporally localised as possible, reducing associated relative phase differences between recordings on seismometers and virtual sensors. Source times used for the seismometer recordings are those from the International Seismology Centre (ISC) catalogue; no Centroid Moment Tensor (CMT) source mechanism and timing was available. We also chose

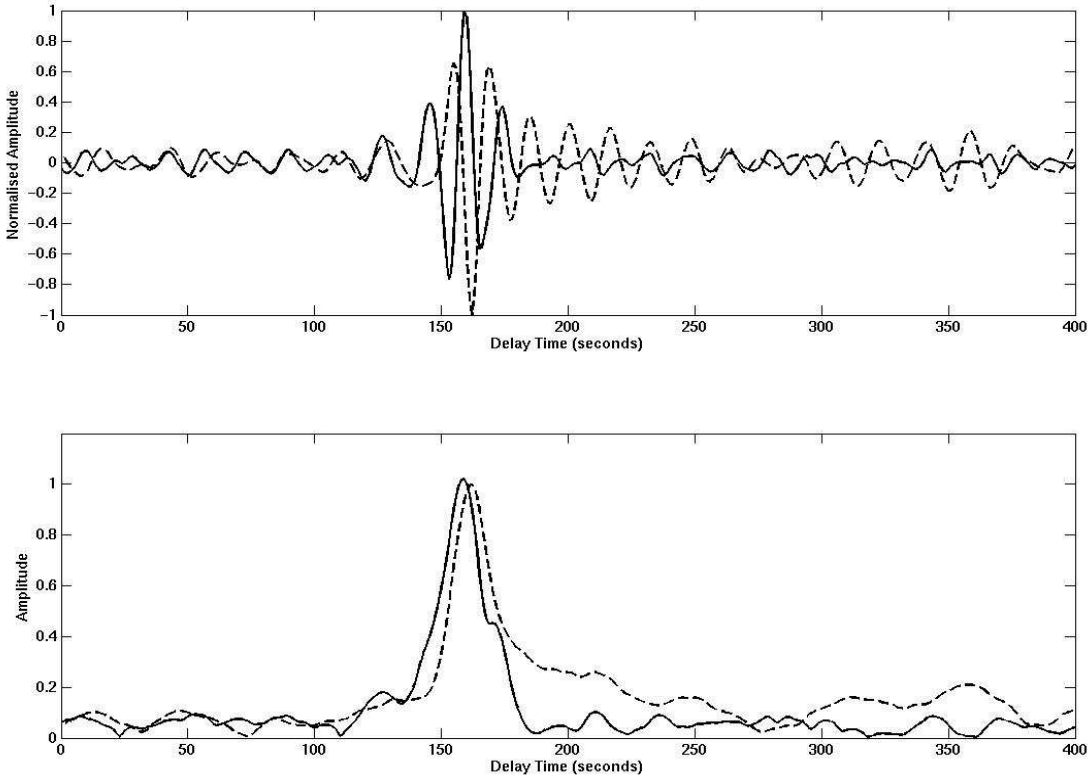

Figure 9.6: Similar to Figure 9.5, but here using the normal virtual receiver 4 (solid), and the direct recording is the inverted, vertical-component seismogram from seismometer R06C (dashed). Virtual receiver records are constructed using 15 stations from the USArray and Berkeley seismic networks.

a strike-slip event oriented at 45 degrees (striking NE) to the normal event (striking N).

We analysed recordings of two other earthquakes recorded on these virtual sensors, one chosen to have source-to-virtual sensor path aligned roughly east-west, the other chosen to have a roughly perpendicular path. We compare strain recordings of these events on the virtual sensors with recordings of particle velocity from the neighbouring seismometers.

Virtual sensors were constructed by integrating (summing) un-weighted recordings at a subset of other available seismometers that did not include either comparison seismometer (Equation 9.18). Each subset consisted of seismometers within a cone around the propagation path direction at the virtual sensor (Figure 9.4), since these are expected to record the main energy that integrates constructively within the virtual receiver seismogram (Snieder, 2004a). Conclusions herein are

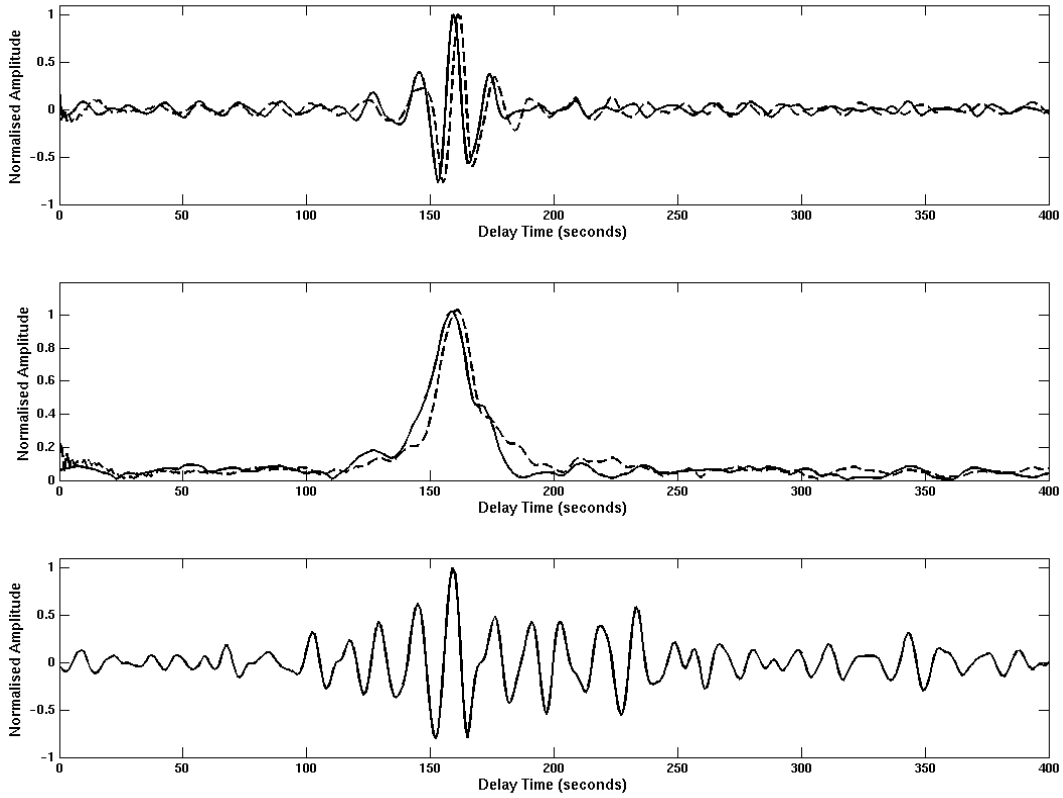

Figure 9.7: Top two panels similar to Figure 9.6, but here the direct recording (dashed) is the inverted, time derivative of the radial-component measurements from seismometer R06C. Solid line is identical to that in Figure 9.6. Lower panel is the equivalent result obtained from the method of Hong and Menke (2006).

robust to changes in the subtending angle. We also took account of the azimuth of propagation, which in this case changes the sign of the horizontal strain recordings.

A strike-slip virtual receiver records the sum of the e_{12} and e_{21} components of strain (Equations (9.30) to (9.33)). For a strike-slip orientation at 45 degrees to the East-West propagation path, a scaled strain measurement can be calculated from the neighbouring seismometer by taking the (negative of the) time-derivative of the radial component of velocity. Figure 9.5 shows a comparison between this time derivative and the virtual receiver record. The group arrival of the main energy matches to within 5s, as does the phase. A phase mismatch of 5s is easily accounted for by the difference between temporal responses of virtual and real seismometers discussed above.

Figure 9.6 shows the same event recorded by the virtual sensor constructed from the N-S oriented normal-fault. This virtual receiver measures the difference between the e_{33} and e_{11} components of strain. There is no easy way to construct a comparison measurement for the e_{33} component from the real seismometer so in Figure 9.6 the comparison seismogram is simply the vertical component of particle velocity. As expected, while the energy group arrival times are again well matched, the phases differ markedly.

We can construct a comparison seismogram for the e_{11} component, however, by again taking the time derivative of the radial particle velocity at the seismometer (Figure 9.7). The fit is excellent, showing that for this event at this station, the signal is probably dominated by the horizontal-strain component. Since the vertical-strain component is approximately related to the derivative of the Rayleigh-wave eigenfunctions with depth beneath the virtual receiver, we infer that that eigenfunction is likely to be approximately constant with depth at the earthquake location.

Previously, Hong and Menke (2006) attempted to create virtual seismograms by a different method. They added active source recordings together to generate pseudo-noise sequences, then applied the *passive-noise* form of interferometry to estimate inter-source responses (i.e., they sum over receivers, then cross-correlate). In Figure 9.7 we also show that their method produces relatively inaccurate seismogram approximations. This is expected because accurate seismogram construction from noise requires much longer time series than are afforded by typical earthquake seismograms. Our approach is different: we use the *impulsive source* form of interferometry by first cross-correlating responses and only then summing over receivers, requiring only the actual, recorded seismograms at each receiver. Figure 9.7 illustrates that this is a key advance, providing a step-change in construction accuracy.

Vertical strains are fundamentally new measurements provided by the virtual sensors. We can isolate the vertical derivative measurement by looking at seismograms from earthquakes occurring along-strike of the normal virtual sensor. In this geometry the e_{11} component is zero, leaving only the e_{33} component (Equation 9.35).

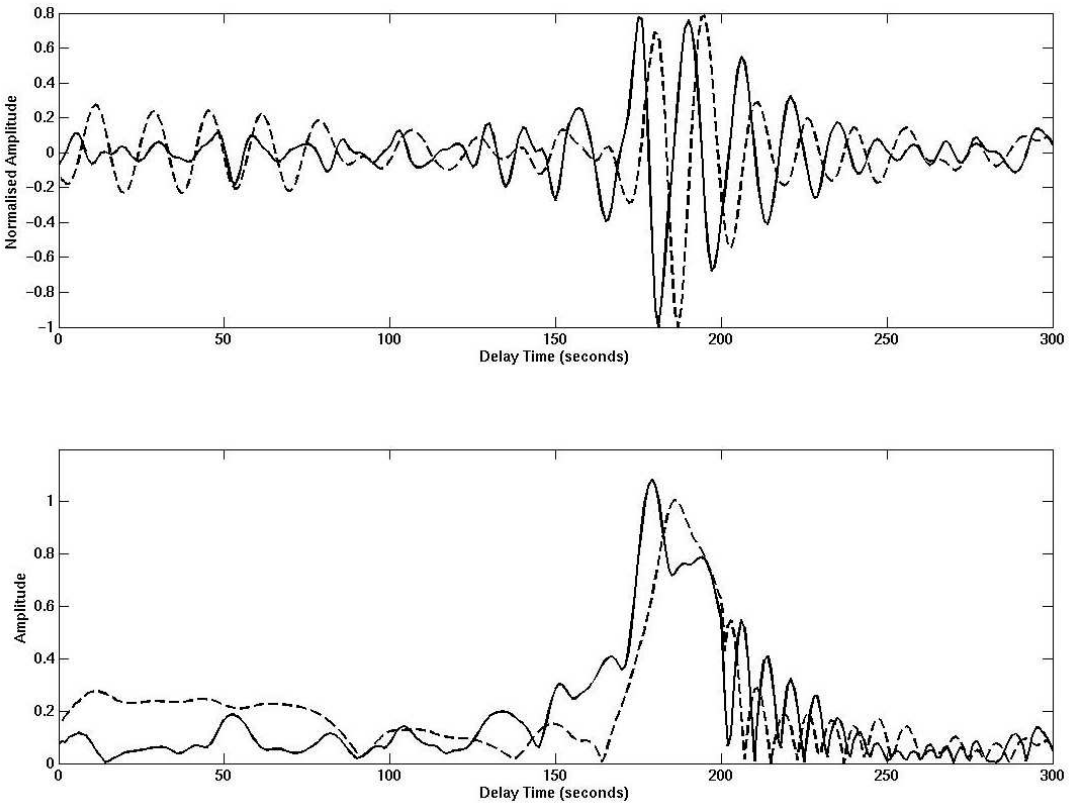

Figure 9.8 shows the vertical strain seismogram recorded on the normal virtual receiver from the southernmost earthquake in Figure 9.4. Again, the energy group arrival time is reasonable given that observed on the vertical particle velocity record, while the phase of the vertical strain represents a new measurement.

9.4 Conclusions

Although we formulated theory only for acoustic and elastic wave propagation, this can be extended into forms appropriate for diffusive, attenuating, electromagnetic or electro-kinetic energy propagation (Slob *et al.*, 2007; Slob and Wapenaar, 2007; Snieder, 2007; Snieder *et al.*, 2007). It is applied here to earthquake sources, but we could equally construct virtual sensors from fractures occurring in stressed solid material in a laboratory, or from impulsive pressure sources in liquid or gas, provided energy from such sources is recorded at an appropriately placed array of receivers.

The inter-earthquake seismogram is obtained by back-projecting data recorded from one earthquake through empirically-recorded Green's functions from another,

an explicit elastic expression of the acoustic time-reversal experiment of Derode *et al*. (2003b). However, the method also converts the data from particle displacement (or time derivatives thereof) at the real seismometers to strain due to seismic waves at the subsurface locations to match the type of the original source.

In the exploration industry seismic-frequency strain recordings have been shown to be particularly useful for wavefield analysis and subsurface imaging (Robertsson and Curtis, 2002). Vertical strains are available on the seabed using combinations of velocity and pressure sensors. However, no such measurement has been available in a solid without taking the difference between displacement measurements from separated sensors, requiring, for example, a receiver to be buried invasively at a depth equal to a significant fraction of a vertical wavelength if vertical derivatives are to be estimated (Curtis and Robertsson, 2002). The direct, non-invasive sensitivity to strain provided by the virtual seismometers introduced here is the first such measurement within a solid. It holds the promise to analyse stress- or strain-triggering of earthquakes by passing seismic waves, for example, since no other method has the potential to provide such deep, or such widely distributed measurements of the strain field in the Earth's subsurface.

Finally, since this method essentially back-projects recordings to the virtual-sensor location, it is equally possible to back-project other signals such as passive-noise recordings to either or both of the pair of subsurface source locations. This offers the possibility to monitor inter-earthquake Green's functions as a function of time either before or after the original earthquakes occurred, by using standard passive-noise interferometry (Campillo and Paul, 2003; Shapiro and Campillo, 2004; Shapiro *et al.*, 2005; Gertstoft *et al.*, 2006; Moschetti *et al.*, 2007). If both earthquakes occurred in the same fault zone for example, this would allow local, non-invasive, subsurface monitoring of the intra-fault zone Green's functions for the first time.

10. Discussion

Throughout this thesis we have considered a number of different topics centred around the theme of surface-wave interferometry. While the focus of the thesis was the application of seismic interferometry to ground-roll removal in land-seismic exploration (Chapter 8), several other avenues of research were also investigated. These included optical theorems for surface waves (Chapter 5), correcting for directional bias and the attenuation of non-physical arrivals in interferometric estimates (Chapter 7), and estimating Green's functions between pairs of sources, rather than pairs of receivers (Chapter 9). In this final chapter we outline potential topics for future work in a number of different fields in seismology and physics relating to the range of topics covered in this thesis.

In Chapter 8 we successfully tested the application of seismic interferometry to ground-roll removal. However there are still a number of question to be answered regarding the application of the method to more typical seismic-acquisition geometries. In the first part of this chapter we consider some aspects of the interferometric ground-roll removal method when applying the method to different acquisition geometries. In the second part of this chapter we further discuss the non-physical arrivals considered in Chapters 4, 6, and 7, drawing on our own work and the work of others to suggest potential uses for the non-physical arrivals, and potential enhancements to the non-physical attenuation algorithm proposed in Chapter 7. Finally we discuss the link between seismic interferometry and optical theorems. We briefly considered the surface-wave optical theorem in Chapter 5, however there are many avenues of further research which could be pursued as a consequence of that work and recent work by other authors.

Note that we do not discuss the further use of the virtual-receiver method as introduced in Chapter 9. Since this work is the reciprocal of the virtual-source case

all of the issues discussed in this thesis regarding the application of the virtual-source configuration may equally apply to the virtual-receiver configuration.

10.1 Data acquisition and survey design for ground-roll removal

In Chapter 8 we considered the application of seismic interferometry to ground-roll removal. The data set geometries used in this example are not typical of those found in conventional seismic surveys; both the source and receiver distributions are much denser than those encountered in typical 2D and 3D surveys (e.g., see Vermeer, 2002). This source distribution allowed the method to be applied successfully, and source distribution and sampling is one of the more important aspects of interferometric ground-roll removal. This topic requires further attention and we now discuss some aspects of acquisition and survey design for ground-roll removal.

The test geometry meets the following requirements that are important for application of the interferometric ground roll removal method:

1. Approximately coinciding source and receiver stations for all sources allowing a virtual source to be constructed for each real source
2. Dense distribution of sources that (i) cover the stationary points for dominant scattered waves, and (ii) allow application of both correlation-type and convolution-type interferometry.

In more typical 3D acquisition geometries conditions (1) and (2) are rarely met. It is unlikely that such a dense carpet of sources and receivers will be deployed on the scale of a 3D seismic survey. In Figure 10.1 we show sketches of three survey geometries. In Figure 10.1a we show a 2-D seismic line: this geometry is suitable for estimating direct and in-line scattered surface waves (see Chapter 2, Chapter 3, Dong *et al.*, 2006; Vasconcelos *et al.*, 2008). In Figure 10.1b we show a ‘fat’ 2D seismic line similar to that used in Chapter 8: we have shown that this geometry is suitable for estimating scattered surface waves. Finally in Figure 10.1c we show a cross-line 3D geometry, where source lines and receiver lines are deployed in an orthogonal pattern. Only a limited number of sources have a coinciding receiver, and the

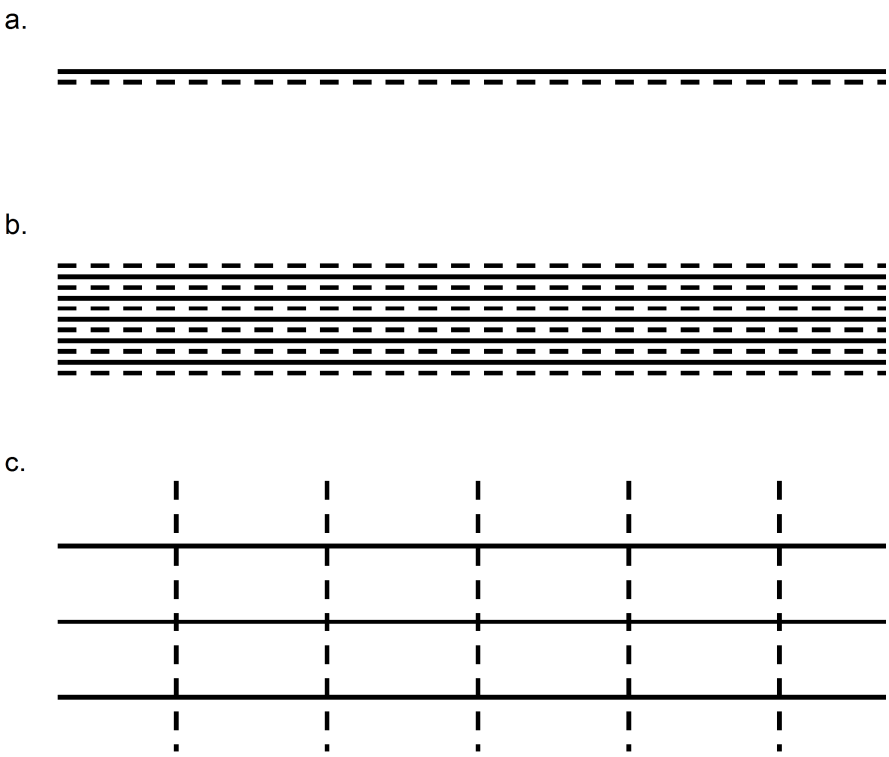

Figure 10.1: Survey geometries for (a) a 2D seismic line, (b) a 'fat' 2D seismic line and (c) a 3D orthogonal geometry. Solid lines indicate receiver lines and dashed lines indicate source lines.

application of the interferometric ground-roll removal method becomes more difficult.

This highlights an interesting problem to determine the **optimum survey design for interferometric ground-roll removal**, especially for 3D surveys. Survey design of this kind could involve the use of near surface characterization (e.g., Laake *et al.*, 2008); dominant scatterers can be identified and used as part of a stationary-phase survey-design algorithm. By applying a similar reasoning as in Appendix 8A it could be possible to minimise the source effort required for interferometry. For example, it may be possible to limit the application of interferometry to only those regions of a survey area where scattering is expected to be dominant, or near-surface characterisation could be used to establish the range of azimuths that may be expected within the scattered surface-wave arrivals, this in turn allowing a suitable distribution of sources to be deployed.

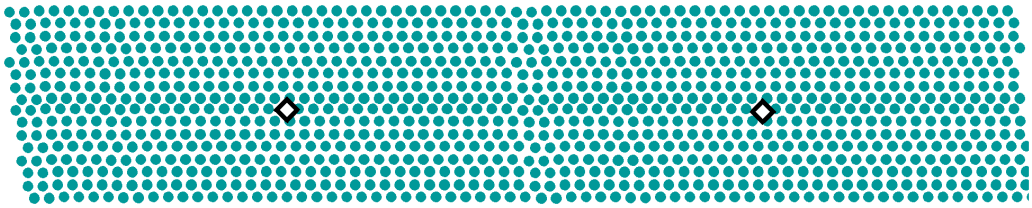

Figure 10.2: Sketch showing a possible configuration allowing for the generation of stationary-phase kernels (SPKs). The response between the two sources (diamonds) can be determined by cross-convolution or cross-correlation of the recordings from both sources at each receiver (grey circles). The kernel can be generated by considering the contribution from each receiver at a given time.

Continuing with the survey design theme, we now briefly consider the generation of **stationary-phase kernels** (SPKs). In the test geometry used in Chapter 8, in addition to the 8 receiver lines considered, there were an additional 24 receiver lines that we did not use. Such a dense receiver array could be used to analyse the distribution of stationary-points for different arrivals. We show a sketch of this configuration in Figure 10.2, where two sources are located within the dense spread of receivers. In the virtual-receiver configuration (see Chapter 9) the contribution of each receiver to the interferometric estimate of the wavefield between the two sources can be used to determine the SPK. This is done by simply plotting a map of these contributions for a given time (or the sum over a time-window for an arrival of interest). This map would then represent the stationary-phase regions for the contribution to the interferometric integral at that specific time (or time period). Knowledge of the stationary-phase regions for dominant arrivals could aid survey design for interferometric ground-roll removal. In an initial test phase this would only require a few shot locations located within a dense spread of receivers, or this could be done synthetically.

To illustrate this we use a simple 2-D acoustic model (the same model used in Chapter 1 to illustrate interferometry), but rather than using an enclosing boundary of sources we consider a source at each point in a 400 by 200 m plane with a source-grid spacing of 4 m. In Figure 10.3 we plot the SPKs for the time corresponding to the peak of the direct-wave arrival for (a) the acausal cross-correlation estimate, (b)

the casual cross-correlation estimate, and (c) the causal cross-convolution estimate. These SPKs show the regions of stationary phase contributing to the interferometric estimate at the time of the peak direct-wave arrival. Sources within the non-zero regions contribute, while sources in the zero regions do not contribute to the arrival. By performing interferometry with sources within those regions we can be sure that the chosen arrival of interest will be illuminated in the interferometric process. We show a second example in Figure 10.4 where we consider a single scatterer and show the SPK at the peak arrival time of the scattered wave. The results are similar to the case for the direct wave, however we can see how the stationary-phase regions align with respect to the scatterer (the circle plotted in Figure 10.4).

In Chapters 5 and 6 we considered that the interferometric integral is stationary at isolated points, whereas here we show that these are actually stationary regions. Note that these stationary-phase regions are finite-frequency effects. Had we computed these with unlimited band width the stationary-phase regions would be straight lines. Seismic data are frequency-band limited resulting in a wider stationary-phase region. This suggests that seismic interferometry for band-limited data may be relatively insensitive to errors in source placement. Finally, note that for the convolution case it is far easier to constrain the source position, since the stationary-phase kernel is closed. In contrast the cross-correlation SPK is not closed, and any number of source positions could contribute in this case.

For 3D geometries it is likely that interferometric estimates may only be available for a limited number of shot gathers (see Figure 10.1c). In that case it may be possible to use an **interpolation** technique to map the scattered waves that we would expect at source positions where we do not have interferometric estimates. For example, Stolt (2002) discusses data mapping and reconstruction to fill in gaps in seismic data; it may be possible to develop a similar approach to fill gaps in the surface wave estimates.

Interpolation may only be possible if the near-surface scattering is well behaved and does not vary greatly from source to source. This may be the case if the dominant scattering energy is single scattered. If the scattered wavefield varies greatly from source to source the interpolation becomes more difficult, for example in the presence of strong multiple scattering it is unlikely that an interpolation

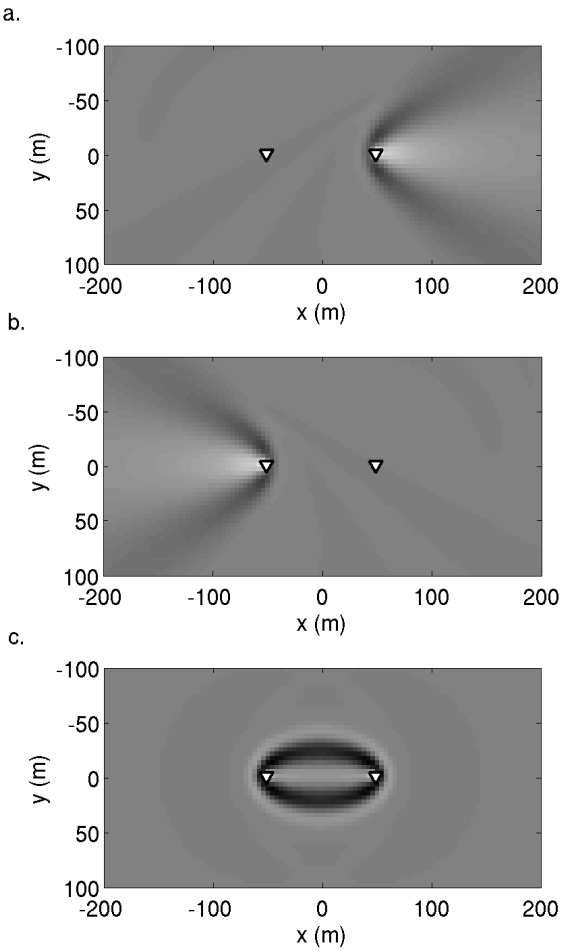

Figure 10.3: Stationary-phase kernels for a 2D homogeneous acoustic example. The kernels are shown to correspond with the time of the peak arrival of the direct wave. (a) Acausal cross-correlation kernel, (b) causal cross-correlation kernel, and (c) causal convolution kernel.

algorithm could successfully interpolate scattered surface waves over distances of several hundred meters.

Something that we have not considered in this thesis is the use of **noise sources** for ground-roll removal. In Chapter 3 we observed that the background noise sources used to create surface wave estimates had a different band width to the active-source estimates at the same location. For near-surface imaging and characterisation this difference in band width is desirable; a wider range of frequencies allows for a greater penetration in depth when imaging with surface waves. For ground-roll removal this is not desirable, since those passive surface-wave estimates cannot then be removed from the higher-frequency active-source data. However, for interferometric ground-roll removal it may be possible to design pseudo-noise

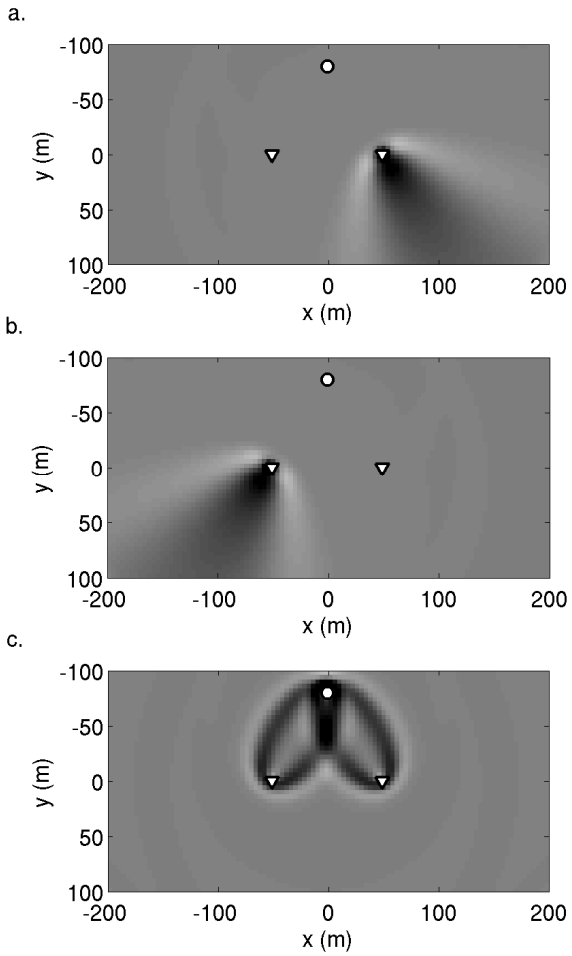

Figure 10.4: As for Figure 10.3 but SPKs are plotted for a single-scattered example.

sources: man-made sources with a controlled frequency-band width. These sources could be used to rapidly illuminate all receiver positions of interest from a wide range of azimuths. This may allow for the estimation of scattered surface waves without the need for many individual source positions. It would also require a different processing strategy, since noise recordings require integration over many time windows, rather than integration over many source positions.

10.2 Non-physical arrivals

In this thesis we have considered two types of non-physical arrivals. There are those that come from stationary points on the integration surface (i.e., the non-physical arrivals in Chapter 6 that are generated by the cross-correlation of direct and

scattered waves) and those that are not stationary on the integration surface (i.e., the cross-mode terms in Chapter 4). We now discuss some further aspects of these non-physical arrivals.

The **stationary non-physical arrivals** are well understood: for the scattered surface wave case we have derived a physical representation for these arrivals. We show that these arrivals are related to the generalized optical theorem for surface waves (Chapters 5 and 6). Snieder *et al.* (2008) show a similar result for acoustic scattering, and Vasconcelos *et al.* (2009) provide representation theorems for perturbed media that describe these non-physical arrivals in a more general way.

In Chapter 7 we proposed a method by which these arrivals can be attenuated. However, in those examples we used non-attenuating media and had a perfectly enclosing boundary of sources. While our examples in Chapter 7 dealt with a non-uniform source strength distribution, the approaches proposed in that chapter may need to be modified to account for a non-uniform source distribution (i.e., missing sources, rather than variable sources strength) and attenuation, since the spurious arrivals observed in Chapter 6 are due to the presence of attenuation. Draganov *et al.* (2008) observe the effect of the latter on seismic interferometry for reflected and transmitted wavefields. They show that non-physical arrivals are introduced both when the medium is attenuating, and when the medium is attenuating and interferometry is applied with a limited source distribution. They introduce a method that can correct for the non-physical arrivals introduced due to attenuation, but this method cannot correct for the non-physical arrivals introduced due to the non-uniform source distribution. It may be the case that some combination of our method for correcting for directional bias, and Draganov *et al.*'s method for correcting for attenuation, may allow for the removal of both types of error. However, it remains to be seen if our directional-balancing algorithm can correct for non-uniform source distribution, as well as non-uniform source-strength distribution.

Vasconcelos *et al.* (2009) also show that it is possible to isolate either these non-physical arrivals or the physical arrivals by applying different boundary conditions. Those authors introduce correlation forms of scattering series with terms that are cross-correlation forms of well known scattering integrals such as the Lippman-Schwinger equation (Snieder, 2002a). These scattering series could be used to extract

information from isolated non-physical waves. For near-surface characterization this means that it may be possible to use the non-physical arrivals to invert for near-surface scattering properties in a similar fashion to Campman and Riyanti (2007) and Kaslilar (2007).

We also observe non-physical arrivals that change with boundary source position; we refer to these as **non-physical non-stationary arrivals**. This is what we observe in Chapter 4, where we show that non-physical arrivals are introduced by cross-correlating different surface-wave modes when there is not an enclosing boundary of sources. Those non-physical arrivals cancel exactly when we integrate in depth and in Chapter 4 we also observe that they also cancel in practice when we integrate across a plane at the surface of the Earth. They may be simpler to deal with than the stationary non-physical arrivals, since a brute force approach (i.e., using many source positions) can reduce the impact of these arrivals. The phase of the arrival changes with the position of the boundary source, hence when the contributions from many sources are summed together these arrivals can cancel destructively. Similar cancellation of non-physical arrivals is also illustrated by Draganov *et al.* (2004), who use an irregular source boundary to mitigate for this type of non-physical arrival.

However, we may also use these surface-wave cross-mode terms to constrain the near-surface properties of the Earth. If we only integrate along a line of surface sources we expect cross-mode terms to be introduced (e.g., Chapter 4, Figure 4.6). These cross-mode terms can be represented in the framework of surface wave theory (Chapter 4, Equation 4.21) and could be used in an inversion procedure to constrain subsurface properties of the Earth, for example by using an approach similar to that of Lai and Rix (1998). In Chapter 4 we propose a method by which we can eliminate these cross-mode terms, but we can also use the same method to *generate* cross-mode terms. By isolating the modes and cross-correlating the different modes we can generate the cross-mode terms in addition to the physical waves. This is illustrated in Figure 4.6c, where we show the result of applying interferometry to separate modes. Hence these may form a new and useful data type.

10.3 Optical theorems and seismology

> *"…the relation between the scattered energy and the amplitude decay of a propagating wave is formulated by the 'optical theorem'… …surprisingly these results have not been used in geophysical applications, where usually linearized scattering theory is used to study the effects of scattering…"*
>
> Snieder, R., 1988, The optical theorem for surface waves and the relation with surface-wave attenuation, *Geophysical Journal*, Vol. 95, 293-302.

In 1988 Roel Snieder made the above statement in a paper on the optical theorem for surface waves. Strangely, this statement is still true today; the optical theorem is under used (if used at all) in both global and exploration seismology. The Born approximation remains a corner-stone of seismic imaging and inversion, yet this approximation does not conserve energy in the way the optical theorem does. Existing optical theorems describe the conservation of energy in scattering problems, where the scatterers are embedded in homogeneous media or homogeneous half-spaces (Glauber and Schomaker, 1953; Newton, 1968, 1976; Tan, 1977; Budreck and Rose, 1992; Carney and Wolf, 1997; Marston, 2001; Snieder *et al.*, 2008). To the best of our knowledge, Snieder's paper was the first attempt to apply the optical theorem in seismology. By using scattered surface waves Green's functions he was able to study the effect of scatterers on the propagation of surface waves. Brandenburg and Snieder (1989) published a similar paper on the same topic soon after. Whereas these two papers concentrate on more specific versions of the optical theorem for surface waves, the generalized optical theorem for surface waves that we derive in Chapter 6 may allow for more wide-spread application of optical theorems in seismology. Further, the link that has been exposed between interferometry and the optical theorem may encourage others to look into the potential of the optical theorem in seismology.

In the final part of this thesis we look at potential imaging applications of the generalized optical theorem for surface waves, before considering how we might

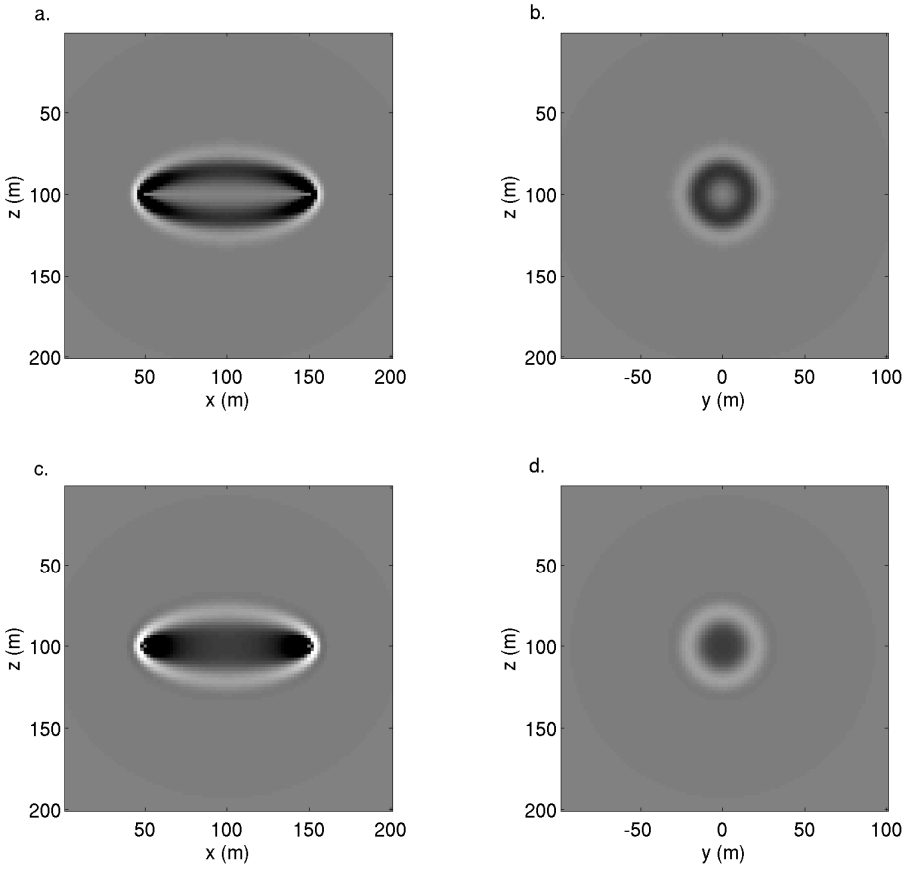

Figure 10.5: Travel-time sensitivity kernel for homogeneous, acoustic, 3D media. 2D slices of the kernels are shown in both the x-z plane (located at y = 0 m) and the y-z plane (located at x = 100 m). (a) Born scattering, x-z plane, (b) Born scattering, y-z plane, (c) optical theorem scattering, x-z plane, and (d) optical theorem scattering, y-z plane. The background grey is zero, blacker shades are positive and lighter shades are negative.

derive a unified generalized optical theorem for diffusion, flow and wave phenomena in an approach similar to that of Wapenaar *et al*. (2006) and Snieder *et al*. (2007) who consider unified Green's function retrieval for diffusion, flow and wave phenomena. Such a unified form for the optical theorem may also allow the optical theorem to be applied in background media with a more complex form than the layered elastic case that we have considered for surface waves.

The generalized optical theorem for surface waves derived in Chapter 6 has potential applications in **imaging and inversion** using seismic waves. The optical theorem places constraints on scattering amplitude that relates to perturbations of some background model. In seismic imaging, perturbations to background models

are used to represent heterogeneities in the subsurface structure of the Earth, and those are estimated based on recordings of scattered energy. For example, surface-wave scattering theory is used in so-called diffraction tomography, where the Born (single-scattering) approximation is used to derive a sensitivity kernel (a kernel showing the sensitivity of a finite-frequency travel time or amplitude difference, between an observed and synthetic seismogram, to perturbations to the synthetic Earth model). An interesting result of using the Born approximation is that this results in the kernel having a 'banana-doughnut' shape. That is, the kernel surrounds the path along which one would expect the ray to propagate, but on the ray itself the kernel is zero. We illustrate the nature of this kernel in a homogeneous acoustic medium using a constant wave propagation velocity of 200 m/s. For each point in space we calculate the waveform sensitivity kernel $K_u(\mathrm{r},t)$,

$$K_u(\mathbf{r},t) = \int_0^\infty \frac{\exp i\left(k(\omega)|\mathbf{r}_2 - \mathbf{r}|\right)}{4\pi|\mathbf{r}_2 - \mathbf{r}|} V(\mathbf{r}) \frac{\exp i\left(k(\omega)|\mathbf{r} - \mathbf{r}_1|\right)}{4\pi|\mathbf{r} - \mathbf{r}_1|} \exp(-i\omega t) d\omega . \qquad (10.1)$$

This is the 3D acoustic version of the waveform sensitivity kernel for surface waves used by Marquering et al. (1999). $k(\omega)$ is the wavenumber, $\mathbf{r}$ is the position of a single scatterer, $\mathbf{r}_1$ is the position of the source and $\mathbf{r}_2$ is the position of the receiver. $V(\mathbf{r})$ is the scattering matrix which describes the scattering of the incident wave.

This formulation is for single-scattered waves and a real-valued scattering matrix, i.e., the Born approximation. We use a scattering matrix that is a function of k^{-1}, the reasons for which are made clear below. We use $\mathbf{r}_1 = [50,0,100]$ and $\mathbf{r}_2 = [150,0,100]$ and $K_u(\mathbf{r},t)$ is determined for points **r,** separated at 2 m intervals on the x-z plane intersecting the two receiver points (i.e., y = 0 m) and on the y-z plane at x = 100 m. We then determine the travel-time sensitivity kernel, $K_T(\mathbf{r})$ using Equation (14) of Marquering *et al.* (1999),

$$K_T(\mathbf{r}) = \frac{\int_{t_1}^{t_2} \dot{u}(t) K_u(\mathbf{r},t) dt}{\int_{t_1}^{t_2} u(t)\ddot{u}(t) dt} . \qquad (10.2)$$

Here $u(t)$ is the wave propagating between source and receiver in the unperturbed model, the integration limits t_1 and t_2 correspond to the beginning and end of a time-window enclosing the arrival of interest (in our case this is the direct-wave arrival), and the dot indicates the time-derivative. Marquering *et al.* (1999) describe the quantity $K_T(\mathbf{r})$ as the sensitivity kernel of a finite-frequency travel-time shift measured by cross-correlation of an observed and synthetic seismogram. In Figure 10.5a and b we show the x-z and y-z planes respectively. In the x-z plane we show the banana shape of the kernel. Note that the banana is straight because the ray-path between source and receiver is a straight line in this homogeneous case. In practice the banana shape would arise due to the curvature of the ray in the presence of the Earth's velocity gradient. It is clear in the x-z plane that the sensitivity in the centre of the kernel approaches zero. The y-z plane shows the doughnut shape, and again towards the centre of the kernel the sensitivity approaches zero. This zero sensitivity is the doughnut hole.

The presence of this doughnut hole was particularly controversial. Several researchers questioned the validity of such a hole and this resulted in a very public debate which took the form of a series of papers, comments to the authors, and replies to comments (Dahlen and Nolet, 2005; de Hoop and van der Hilst, 2005a, 2005b; van der Hilst and de Hoop, 2005). One thing that was not debatable about the new imaging method was that it provided significantly different results to conventional ray-tracing seismology; for example the method suggested that a two-layer convection model existed in the Earth's mantle (Montelli *et al.*, 2004a, 2004b).

The doughnut hole is simply a result of using Born-scattering theory. If we consider the travel-time sensitivity for a scatterer on a ray-path, Born theory does not affect the phase of the arrival, only the amplitude, i.e., there is zero travel-time sensitivity to a scatterer on the ray-path. We expect that the generalized optical theorem for surface waves is more accurate than the Born method. First it accounts for the conservation of energy at the scatterer, and second as a consequence of the conservation of energy, it introduces a phase shift even for scatterers on the ray path. Waveform and travel-time sensitivity kernels may therefore be affected by using the generalized optical theorem to derive the sensitivity kernels. This has not been possible before, as no generalized optical theorem existed that could be applied using

surface wave theory for layered media (or any other heterogeneous background media). We illustrate the changes the optical theorem introduces by using a scatterer with a scattering amplitude governed by the optical theorem (herein referred to as optical scattering), rather than Born scattering. We again use the simple homogeneous case; while this is overly simple for problems in the Earth, it clearly illustrates changes that can be expected by using the optical theorem to constrain scattering amplitudes.

Following Groenenboom and Snieder (1995) we find the constraint that the optical theorem places on the scattering amplitude of a point scatterer, embedded in homogeneous, 3D acoustic media:

$$\mathrm{Re}V = \sqrt{-\mathrm{Im}V\left(\frac{2}{k} + \mathrm{Im}V\right)}. \qquad (10.3)$$

V has no dependence on the azimuth of the incident or scattered waves. Equation (10.3) places the constraint $-2/k \leq \mathrm{Im}\ V \leq 0$ on the imaginary part of the scattering amplitude. We set Im V equal to $-1.99/k$. This results in the real part of the scattering amplitude being dependent on k^{-1} (explaining the use of the same dependence in the Born example above). In Figure 10.5c and d we show the equivalents to Figure 10.5a and b, but using the optical scatterer constrained by Equation (10.3). Note that while the kernels have the same outline, the optical theorem has filled in the doughnut hole. Also note the similarity between Figure 10.4c: is there some link between convolution interferometry and the banana-doughnut kernel? Kinematically the two cases are similar, each scatterer **r** in Equation (10.1) above acts as a secondary or Huygens' source, likewise each boundary source in convolution interferometry also acts like a Huygens' source.

For a scatterer on the ray-path the optical theorem applies a phase shift and an amplitude change to the propagating wave. This is in contrast to the Born approximation which only applies an amplitude change. The optical theorem for surface waves has a similar effect on wavefields propagating in layered media and we expect similar 'doughnut-less' kernels in layered media (i.e., using models more

representative of Earth structure) by using the optical theorem for surface waves, rather than simply using Born scattering.

Currently it is difficult to say what kind of difference such kernels would make. Generally much spatial smoothing and averaging takes place during tomography, so the effects of changing the central part of the kernels may be smaller than one might expect. However, we would expect differences to be larger when multiple scattering is taken into account (since more energy is lost due to the multiple interactions of waves with each scatterer). However this would require the computation of kernels using higher-order scattering series (of which the Born approximation is the first order term), greatly increasing the computational cost of tomographic algorithms.

One outcome of the derivation of the generalized optical theorem for surface waves is that a link between the optical theorem and seismic interferometry has been exposed. Both the optical theorem that we derive and the optical theorem of Snieder *et al.* (2008) are derived using an interferometric approach, indicating that these theorems are somehow intertwined with interferometric theory. Indeed since interferometric formulae exist that describe the extraction of electromagnetic, acoustic, diffusion-phenomena and seismo-electric Green's functions (Wapenaar *et al.*, 2006; Snieder *et al.*, 2007), this suggests that interferometry itself could be a method by which one could derive a **unified generalized optical theorem** for many different types of energy or material propagation. Using the same approach as in Chapter 5 and in Snieder *et al.* (2008) it should be possible to derive optical theorems for all of these phenomena.

One limiting factor of our approach is the reliance on a stationary-phase analysis, which may not always be possible when considering, for example, diffusion phenomena. Another potential way to derive a unified generalized optical theorem is to use scattering representation theorems. Vasconcelos *et al.* (2009) have carried out work in studying representation theorems for perturbed media. Equation (28) of Vasconcelos *et al.* relates the surface integral of cross-correlated wavefield perturbations to a volume integral of cross-correlations between unperturbed and perturbed waves:

$$\oint_{\mathbf{r}\in\partial\mathcal{V}} \left[G_S(\mathbf{r},\mathbf{r}_A)\nabla G_S^*(\mathbf{r},\mathbf{r}_B) + G_S^*(\mathbf{r},\mathbf{r}_B)\nabla G_S(\mathbf{r},\mathbf{r}_A) \right] \cdot dS$$

$$= \int_{\mathbf{r}\in V} \frac{1}{i\omega\rho}\left[G_0(\mathbf{r},\mathbf{r}_A)V(\mathbf{r})G_S^*(\mathbf{r},\mathbf{r}_B) - G_S(\mathbf{r},\mathbf{r}_A)V(\mathbf{r})G_0^*(\mathbf{r},\mathbf{r}_B)\right]dV. \qquad (10.4)$$

Here $G_0(\mathbf{r},\mathbf{r}_A)$ is the Green's function in the unperturbed background medium describing the pressure response at $\mathbf{r}_A$ due to a monopole source at $\mathbf{r}$, $\nabla G_0(\mathbf{r},\mathbf{r}_A)$ is the equivalent dipole response, and $G_S(\mathbf{r},\mathbf{r}_A)$ and $\nabla G_S(\mathbf{r},\mathbf{r}_A)$ are the equivalent Green's functions describing the wave propagation due to perturbations in the background medium. This equation describes the same mutual cancellation that allowed us to derive the generalized optical theorem for surface waves in Chapter 5; in relation to the work in Chapters 5, 6, and 7, the left hand side is equivalent to term *T4* and the ride hand side is equivalent to terms T2 and T3. For the acoustic case this representation theorem can be viewed as a more generalised form of the optical theorem. This equation was derived without any assumptions on the form of the Green's function (i.e., no analytical Green's functions were used), and no stationary-phase analysis was required. An optical theorem expressed in this way places no assumptions on the homogeneity of the background media in which the scatterers are embedded. Hence such an optical theorem could be used to constrain the scattering amplitudes of scatterers embedded in any media.

This new approach may therefore find useful applications in inverse scattering or full wave-form inversion problems where background models may be complex, thus ruling out the use of existing optical theorems which rely on homogeneous or (in the case of our surface-wave theorem) layered background media. By unifying the approach of Vasconcelos *et al.* (2009) in a similar way to the unified approach of Wapenaar *et al*. (2006) and Snieder *et al.* (2007) it should be possible to derive a truly generalized optical theorem for diffusion, flow, and wave phenomena.

To further investigate the relationship between seismic interferometry and the optical theorem, or indeed the applicability of the optical theorem in seismology is beyond the scope of this thesis. However, given that seismic interferometry is a field of particularly active research, the creation of a link between the optical theorem and seismic interferometry may encourage seismologists to begin further research on the use of the optical theorem in seismology.

After taking decades to prove Claerbout's conjecture, the influence of seismic interferometry continues to grow far beyond the extraction of Green's functions. In this thesis alone we have touched on a wide range of topics including noise attenuation, near-surface characterisation, optical theorems, mantle tomography, the banana-doughnut debate, and quantum physics. Despite the advances made in recent years, and the vast volume of literature that now exists, one can't help feeling that we have still only scratched the surface of what is to come.

Appendices

Appendix 4A: Deformation-rate-tensor surface wave Green's functions

Equation (4.1) requires the Green's functions representing particle displacement arising from both point-force sources and deformation-rate-tensor sources. Snieder (2002b, eqs. 14 and 23) gives the particle displacement-point force Green's function (Equation 4.2), and the spatial derivative of this Green's function

$$\partial_k G_{im}(\mathbf{r}_B,\mathbf{r}_A) = \sum_\nu p_i^\nu(z_B,\varphi)\ \left\{E_k^\nu\, p_m^\nu(z_A,\varphi)\right\}^* \frac{e^{i\left(k_\nu X+\frac{\pi}{4}\right)}}{\sqrt{\frac{\pi}{2}k_\nu X}} \tag{A4.1}$$

where E_k^ν is the kth component of the strain operator for the ν th mode

$$\mathbf{E}^\nu = \begin{pmatrix} ik_\nu\cos\varphi \\ ik_\nu\sin\varphi \\ \dfrac{\partial}{\partial z} \end{pmatrix}. \tag{A4.2}$$

As discussed by van Manen *et al.* (2006) the term $n_j c_{njkl}\partial_k G_{ml}(\mathbf{r}_B,\mathbf{r}_A)$ in Equation (4.1) corresponds to the response due to deformation-rate-tensor sources. For surface waves we write this response as

$$n_j c_{njkl}\partial_k G_{ml}(\mathbf{r}_B,\mathbf{r}_A) = n_j c_{njkl}\sum_\nu p_m^\nu(z_B,\varphi)\ \left\{E_k\, p_l^\nu(z_A,\varphi)\right\}^* \frac{e^{i\left(k_\nu X+\frac{\pi}{4}\right)}}{\sqrt{\frac{\pi}{2}k_\nu X}}, \tag{A4.3}$$

or

$$n_j c_{njkl} \partial_k G_{ml}(\mathbf{r}_B, \mathbf{r}_A) = \sum_\nu p_m^\nu(z_B, \varphi)\ T_n^{\nu *}(z_A, \varphi) \frac{e^{i\left(k_\nu X + \frac{\pi}{4}\right)}}{\sqrt{\frac{\pi}{2} k_\nu X}}, \tag{A4.4}$$

where, the traction $T_n^\nu(z, \varphi)$ associated with the νth mode is

$$T_n^\nu(z, \varphi) = n_j c_{njkl} \left\{ E_k^\nu\, p_l^\nu(z, \varphi) \right\}. \tag{A4.5}$$

Incorporating the isotropic elasticity tensor this matrix consists of the 9 components of stress

$$\mathbf{T}^\nu(z, \varphi) = \begin{pmatrix} \tau_{xx}^\nu & \tau_{xy}^\nu & \tau_{xz}^\nu \\ \tau_{yx}^\nu & \tau_{yy}^\nu & \tau_{yz}^\nu \\ \tau_{zx}^\nu & \tau_{zy}^\nu & \tau_{zz}^\nu \end{pmatrix} n_j\,. \tag{A4.6}$$

These stress components are given by

$$\tau_{xx}^\nu = ik_\nu \left[\lambda r_1^\nu(z) + i \frac{\lambda}{k_\nu} \frac{\partial}{\partial z} r_2^\nu(z) + 2\mu r_1^\nu(z) \cos^2 \varphi \right], \tag{A4.7}$$

$$\tau_{xy}^\nu = \tau_{yx}^\nu = ik_\nu \left[2\mu r_1^\nu(z) \cos\varphi \sin\varphi \right], \tag{A4.8}$$

$$\tau_{xz}^\nu = \tau_{zx}^\nu = k_\nu \left[-\mu r_2^\nu(z) \cos\varphi + \frac{\mu}{k_\nu} \frac{\partial}{\partial z} r_1^\nu(z) \cos\varphi \right], \tag{A4.9}$$

$$\tau_{yy}^\nu = ik_\nu \left[\lambda r_1^\nu(z) + i \frac{\lambda}{k_\nu} \frac{\partial}{\partial z} r_2^\nu(z) + 2\mu r_1^\nu(z) \sin^2 \varphi \right], \tag{A4.10}$$

$$\tau_{yz}^\nu = \tau_{zy}^\nu = k_\nu \left[-\mu r_2^\nu(z) \sin\varphi + \frac{\mu}{k_\nu} \frac{\partial}{\partial z} r_1^\nu(z) \sin\varphi \right], \tag{A4.11}$$

$$\tau_{zz}^\nu = ik_\nu \left[\lambda r_1^\nu(z) + i \frac{\lambda}{k_\nu} \frac{\partial}{\partial z} r_2^\nu(z) + 2 \frac{\mu}{k_\nu} \frac{\partial}{\partial z} r_2^\nu(z) \right]. \tag{A4.12}$$

Thus the Rayleigh-wave response to a deformation-rate-tensor source can be determined from the earth properties (λ and μ), the azimuth of the propagation path (φ), the Rayleigh-wave eigenvectors ($r_1^{\nu}(z)$ and $r_2^{\nu}(z)$) and the set of wavenumbers, k_{ν} for all surface wave modes, *v*.

Appendix 4B: Stationary phase evaluation of the interferometric integral

In this appendix we show the details of the stationary-phase analysis required to solve the interferometric integral for surface waves. First we derive the stationary-phase condition, important in the analysis of Equation (4.10) in Chapter 4. We then illustrate the steps necessary to solve for the exact inter-receiver surface waves (i.e., we show the steps involved in reaching Equation (4.16) from Equation (4.15)).

To solve the integral in Equation (4.15) using the stationary phase approximation we follow Snieder (2004a). We define the locations, $\mathbf{r}$, $\mathbf{r}_B$, and $\mathbf{r}_A$ as (x, y, z) , (0, 0, 0), and (R, 0, 0) respectively, the lengths X_A and X_B are defined as

$$X_B = \sqrt{x^2 + y^2}\,, \tag{A4.13}$$

$$X_A = \sqrt{(x-R)^2 + (y)^2}\,, \tag{A4.14}$$

and the first derivatives are defined as

$$\frac{\partial X_A}{\partial y} = \frac{y}{X_A} = \sin\varphi_B\,, \tag{A4.15}$$

$$\frac{\partial X_B}{\partial y} = \frac{y}{X_B} = \sin\varphi_A\,. \tag{A4.16}$$

$$\frac{\partial X_A}{\partial x} = \frac{x}{X_A} = \cos\varphi_B\,, \tag{A4.17}$$

$$\frac{\partial X_B}{\partial x} = \frac{x-R}{X_B} = \cos\varphi_A\,. \tag{A4.18}$$

The integral is stationary when $0 = \partial(X_B - X_A)/\partial x$ and when $0 = \partial(X_B - X_A)/\partial y$ i.e. when $\varphi = \varphi_A = \varphi_B$. This condition is applied to Equation (4.10):

$$G^*_{im}(\mathbf{r}_B,\mathbf{r}_A)-G_{im}(\mathbf{r}_B,\mathbf{r}_A)=\sum_\nu \int_S \frac{e^{ik_\nu(X_B-X_A)}}{\frac{\pi}{2}k_\nu\sqrt{X_A X_B}}\; p_i^\nu(z_B,\varphi)\;\; p_m^{\nu\,*}(z_A,\varphi)$$

$$\times\Big(\;\; p_n^{\nu\,*}(z,\varphi)T_n^\nu(z,\varphi)-T_n^{\nu\,*}(z,\varphi)p_n^\nu(z,\varphi)\;\;\Big)\;dS\,, \qquad \text{(A4.19)}$$

from here it is then simpler to analyse the term in brackets on the right hand side of Equation (4.10).

Following Equations (4.10) to (4.15) we reach

$$G^*_{im}(\mathbf{r}_B,\mathbf{r}_A)-G_{im}(\mathbf{r}_B,\mathbf{r}_A)=\sum_\nu \frac{ik_\nu}{\pi}\int_S \frac{e^{ik_\nu(X_B-X_A)}}{k_\nu\sqrt{X_A X_B}}\; p_i^\nu(z_B,\varphi)\;\; p_m^{\nu\,*}(z_A,\varphi)dS$$

$$\times\;\;(\cos\varphi n_x^{sp}+\sin\varphi n_y^{sp})\;\;. \qquad \text{(A4.20)}$$

The integral now consists of the sum of the horizontal components of the normal to the boundary. Having already determined the stationary-phase condition, we continue to evaluate each component using the stationary phase approach of Snieder (2004a). First we evaluate the part dependent on the *x*-component of the normal

$$C_{n_x}=\frac{1}{2}\sum_\nu \frac{ik_\nu}{\pi}\int_S \frac{e^{ik_\nu(X_B-X_A)}}{k_\nu\sqrt{X_A X_B}}\; p_i^\nu(z_B,\varphi)\;\; p_m^{\nu\,*}(z_A,\varphi)\;\cos\varphi\; dy\,. \qquad \text{(A4.21)}$$

In order to evaluate the integral we require the second derivates at this stationary point

$$\frac{\partial^2 X_B}{\partial x^2}=\frac{\cos^2\varphi_B}{X_B}\,, \qquad \text{(A4.22)}$$

$$\frac{\partial^2 X_A}{\partial x^2}=\frac{\cos^2\varphi_A}{X_A}\,. \qquad \text{(A4.23)}$$

Following Snieder (2004a, 2004b) and Snieder *et al* .(2006) the integral is equal to

$$C_{n_x} \approx \frac{1}{2}\sum_{\nu}\frac{ik_\nu}{\pi}\frac{e^{ik_\nu(X_B-X_A)}}{k_\nu\sqrt{X_A X_B}}\, p_i^\nu(z_B,\varphi)\;\; p_m^{\nu\,*}(z_A,\varphi)\cos\varphi$$

$$\times e^{-i\frac{\pi}{4}}\sqrt{\frac{2\pi}{k_\nu}}\frac{1}{\sqrt{\cos^2\varphi\left(\frac{1}{X_B}-\frac{1}{X_A}\right)}}, \qquad \text{(A4.24)}$$

after some manipulation

$$C_{n_x} \approx -\frac{\eta}{2}\sum_{\nu}\frac{e^{i\eta\left(k_\nu X+\frac{\pi}{4}\right)}}{\sqrt{\frac{\pi}{2}k_\nu X}}p_i^\nu(z_B,\varphi)\;\; p_m^{\nu\,*}(z_A,\varphi), \qquad \text{(A4.25)}$$

where X is the horizontal offset between $\mathbf{r}_A$ and $\mathbf{r}_B$. There are two types of stationary points, one where $X_A > X_B$ and one where $X_A < X_B$, these two cases are denoted by $\eta = -1$ and $\eta = 1$ respectively.

The treatment of the integral over the *x*-coordinate is similar to the treatment of the integration over the *y* coordinate but with a $\sin^2\varphi$ replacing the $\cos^2\varphi$ in Equation (A4.24), i.e.,

$$C_{n_y} \approx -\frac{\eta}{2}\sum_{\nu}\frac{e^{i\eta\left(k_\nu X+\frac{\pi}{4}\right)}}{\sqrt{\frac{\pi}{2}k_\nu X}}p_i^\nu(z_B,\varphi)\;\; p_m^{\nu\,*}(z_A,\varphi). \qquad \text{(A4.26)}$$

Combining (A4.25) and (A4.26) results in Equation (4.16)

$$G_{im}^*(\mathbf{r}_B,\mathbf{r}_A) - G_{im}(\mathbf{r}_B,\mathbf{r}_A) \approx -\eta\sum_{\nu}\frac{e^{i\eta\left(k_\nu X+\frac{\pi}{4}\right)}}{\sqrt{\frac{\pi}{2}k_\nu X}}p_i^\nu(z_B,\varphi)\;\; p_m^{\nu\,*}(z_A,\varphi). \qquad \text{(A4.27)}$$

Appendix 4C: Single source type approximations for surface waves

Wapenaar and Fokkema (2006, eq. 76) show that interferometric integrals, such as Equation (4.1), can be approximated to include the cross-correlation of Green's functions arising from both P- and S-wave type sources. This requires that the integration surface S is a sphere with extremely large radius, and that the region at and around S is homogeneous. In reality we often consider only point-force sources as expressed in Equation (4.7). In this appendix we investigate the effect of using only point-force sources in seismic interferometry for surface waves.

In Chapter 4 we consider the combination of point-force and deformation-rate-tensor sources. In our stationary-phase analysis these appear as

$$p_n^{\nu^*}(z,\varphi)T_n^{\nu}(z,\varphi) - T_n^{\nu^*}(z,\varphi)\,p_n^{\nu}(z,\varphi)\,. \tag{A4.28}$$

In Equation (4.14) we integrate this term over the boundary surface, S, i.e.

$$\int_0^{\infty}\Big[\; p_n^{\nu^*}(z,\varphi)T_n^{\nu}(z,\varphi) - T_n^{\nu^*}(z,\varphi)\,p_n^{\nu}(z,\varphi)\;\Big]\,dS$$

$$= 2ik_{\nu}(\cos\varphi n_x^{sp} + \sin\varphi n_y^{sp})\left[2I_2^{\nu} + \frac{I_3^{\nu}}{k_{\nu}}\right]\,, \tag{A4.29}$$

and following Aki and Richards (2002, eq. 7.76) this becomes

$$\int_0^{\infty}\Big[\; p_n^{\nu^*}(z,\varphi)T_n^{\nu}(z,\varphi) - p_n^{\nu}(z,\varphi)T_n^{\nu^*}(z,\varphi)\;\Big]\,dS = \frac{1}{2}ik_{\nu}(\cos\varphi n_x^{sp} + \sin\varphi n_y^{sp})\,. \tag{A4.30}$$

In Chapter 4 this allows us to solve for the exact inter-receiver surface wave (Equations (4.15) and (4.16)).

We now perform the same analysis but only consider point-force sources (assuming that $\nu = \nu'$) i.e.

$$\int_0^\infty \left[\; p_n^{\nu *}(z,\varphi) p_n^{\nu}(z,\varphi) \right] dS = \int_0^\infty \left[r_1^{\nu}(z) + r_2^{\nu}(z) \right] dS \,. \tag{A4.31}$$

Using Equation (7.74) from Aki and Richards (2002), $I_1^{\nu} = \frac{1}{2} \int_0^\infty \rho(z) \left[\left\{ r_1^{\nu}(z) \right\}^2 + \left\{ r_2^{\nu}(z) \right\}^2 \right] dz$ and from the definition of Equation (4.2) that $8 c^{\nu} U^{\nu} I_1^{\nu} = 1$, then

$$\int_0^\infty \left[\; p_n^{\nu *}(z,\varphi) p_n^{\nu}(z,\varphi) \right] dS = \frac{1}{4 c^{\nu} U^{\nu} \rho}, \tag{A4.32}$$

where we have also assumed that ρ is constant at the boundary, *S* which can be achieved, for example, by assuming that the boundary does not extend to great depth.

By comparison with Equation (A4.30) we can see that this does not introduce the terms necessary to solve for the exact inter-receiver surface wave, as shown in the Chapter 4 (Equation (4.16)). However, we now assume that the boundary of integration is a cylinder with large radius. The direction of the horizontal component of the normal vector to the boundary is then approximately equal to the direction of the pertinent ray at a stationary point for the inter-point Green's function, i.e., $\cos\theta_x^h = \cos\varphi$, and $\sin\theta_y^h = \sin\varphi$. This is similar to the far-field condition used by Wapenaar and Fokkema (2006). In this case Equation (A4.30) becomes

$$\int_0^\infty \left[\; p_n^{\nu *}(z,\varphi) T_n^{\nu}(z,\varphi) - p_n^{\nu}(z,\varphi) T_n^{\nu *}(z,\varphi) \; \right] dS = \frac{1}{2} i k_{\nu} n_j \,. \tag{A4.33}$$

Using the far-field condition this factor $ik_{\nu} n_j / 2$ is required in order to recover the exact inter-receiver surface wave Green's function. By comparing Equations (A4.32) and (A4.33) we can see that in order to recover this factor when using only point-force sources we must multiply the resulting cross-correlations by a modal and frequency dependent scale factor $M^{\nu}(\omega)$,

$$M^{\nu}(\omega) = 2n_j c^{\nu} U^{\nu} \rho \,. \tag{A4.34}$$

Therefore we re-write Equation (4.7) as

$$G^{*}_{im}(\mathbf{r}_B, \mathbf{r}_A) - G_{im}(\mathbf{r}_B, \mathbf{r}_A) \approx ik_{\nu} \int_S \; M^{\nu}(\omega) \; G_{mn}(\mathbf{r}_A, \mathbf{r}) \; G^{*}_{in}(\mathbf{r}_B, \mathbf{r}) \; dS \,. \tag{A4.35}$$

Note that the scale factor is dependent on both frequency (ω) and the density at the boundary, ρ. By using this scale factor it is possible to solve the integral for the inter-receiver surface waves following the approach detailed in the Chapter 4 and in Appendix 4B.

Appendix 4D: Correlation type Rayleigh wave orthogonality relationship

In order to account for cross-terms of two different surface wave modes we require a Rayleigh-wave orthogonality relationship of the correlation type (Equation 4.9).

van Manen *et al.* (2006, eq. 5) derive a reciprocity relation of the correlation type

$$\int_S \left\{ u_i^{(B)} n_j c_{ijkl} \partial_k u_l^{*(A)} - n_j c_{ijkl} \partial_k u_l^{(B)} u_i^{*(A)} \right\} dS = - \int_V \left\{ u_i^{(B)} f^{*(A)} - f^{(B)} u_i^{*(A)} \right\} dV . \quad \text{(A4.36)}$$

If V is source free then

$$\int_S \left\{ u_i^{(B)} n_j c_{ijkl} \partial_k u_l^{*(A)} - n_j c_{ijkl} \partial_k u_l^{(B)} u_i^{*(A)} \right\} dS = 0 . \quad \text{(A4.37)}$$

We define state B to be the particle displacement component associated with the nth Rayleigh wave mode, and state A to be the particle displacement component associated with the mth Rayleigh wave mode

$$u_i^{(A,B)} = p_i^{m,n}(z,\varphi) \frac{e^{i(k_{m,n}X + \frac{\pi}{4})}}{\sqrt{k_{m,n}X}}, \quad \text{(A4.38)}$$

and

$$n_j c_{ijkl} \partial_k u_i^{(A,B)} = T_i^{m,n}(z,\varphi) \frac{e^{i(k_{m,n}X + \frac{\pi}{4})}}{\sqrt{k_{m,n}X}}. \quad \text{(A4.39)}$$

Substituting these into Equation (A4.37) gives the correlation type Rayleigh wave orthogonality relationship (Equation 4.9)

$$0 = \int_S \left(\; p_i^{\,n}(z,\varphi) T_i^{\,m^*}(z,\varphi) - T_i^{\,n}(z,\varphi) p_i^{\,m^*}(z,\varphi) \; \right) dS \,. \qquad \text{(A4.40)}$$

In Appendix 4C we have shown that under certain circumstances we can approximate deformation-rate-tensor sources to be time derivatives of point-force sources modulated by a modal and frequency-dependent scale factor. We therefore assume that it is reasonable to replace the traction terms, $T_i^{\,m}$ by terms $i\omega S_m p_i^{\,m}(z,\varphi)$ (using the same approximations discussed in Appendix 4C)

$$0 \approx -\int_S \left(\; i\omega S_m p_i^{\,n}(z,\varphi) p_i^{\,m^*}(z,\varphi) + i\omega S_n p_i^{\,n}(z,\varphi) p_i^{\,m^*}(z,\varphi) \; \right) dS \,, \qquad \text{(A4.41)}$$

where S_m and S_n are modal and frequency dependent scale factors. Hence, under the approximations in Appendix 4C we can apply the following orthogonality relationship

$$0 \approx \int_S \left(\; p_i^{\,n}(z,\varphi) p_i^{\,m^*}(z,\varphi) \; \right) dS \,. \qquad \text{(A4.42)}$$

Note that Equation (A4.42) is only exact when the required approximations are met and scale factors can be determined (see Appendix 4C).

Appendix 5A: Stationary phase analysis

In this appendix we provide details of our approach. First we state the Green's functions used in Equation (4.1). Then we use a stationary phase analysis to derive the contributing terms to the interferometric relationship, and finally we derive a generalized optical theorem for surface waves.

Following Snieder (2002b), the single (point) scattered surface wave mode σ, $u_i^{\sigma(1)}(\mathbf{r}_B,\omega)$, at a location $\mathbf{r}_B$ due to an incident surface wave mode ν at scattering location $\mathbf{r}_0$, $u_i^{\nu(0)}(\mathbf{r}_0,\omega)$, generated by a point force in the *m* direction at location $\mathbf{r}_A$ is,

$$u_i^{\sigma(1)}(\mathbf{r}_B,\omega)=\sum_{\sigma\nu}\frac{e^{i(k_\sigma X_{0B}+k_\nu X_{A0}+\frac{\pi}{2})}}{\frac{\pi}{2}\sqrt{k_\nu k_\sigma X_{0B}X_{A0}}}\,p_i^{\sigma}(z_B,\varphi_{0B})\,p_m^{\nu *}(z_A,\varphi_{A0})V^{\sigma\nu}(\varphi_{0B},\varphi_{A0}), \qquad \text{(A5.1)}$$

where $\mathbf{r_0}$ is the scattering location, $V^{\sigma\nu}(\varphi_{0B},\varphi_{A0})$ is the scattering matrix for an incident wave with azimuth φ_{A0} and a scattered wave with azimuth φ_{0B} (the depth of the scatterer, z_0 is implicit in $V^{\sigma\nu}$), k_ν is the wavenumber associated with the νth surface wave mode, X_{A0} and X_{0B} are the horizontal offsets between the scatterer at $\mathbf{r}_0$ and locations $\mathbf{r}_A$ and $\mathbf{r}_B$ respectively, φ_{A0} and φ_{0B} are also the azimuth of the horizontal paths between $\mathbf{r}_A$ and $\mathbf{r}_0$, and $\mathbf{r}_0$ and $\mathbf{r}_B$ respectively, and z_A and z_B are the depths of $\mathbf{r}_A$ and $\mathbf{r}_B$, respectively (Figure 5.2). Superscripts (0) and (1) refer to the wavefield in the background medium and the scattered wavefield respectively. Again, to simplify the expression the modal normalization $8c^\nu U^\nu I_1^{\ \nu}=1$ is assumed.

Mode ν of the incident surface wave, due to the same source at location $\mathbf{r}_A$ is given by Equation (4.2). The Green's function is then the sum of the direct and scattered surface wave:

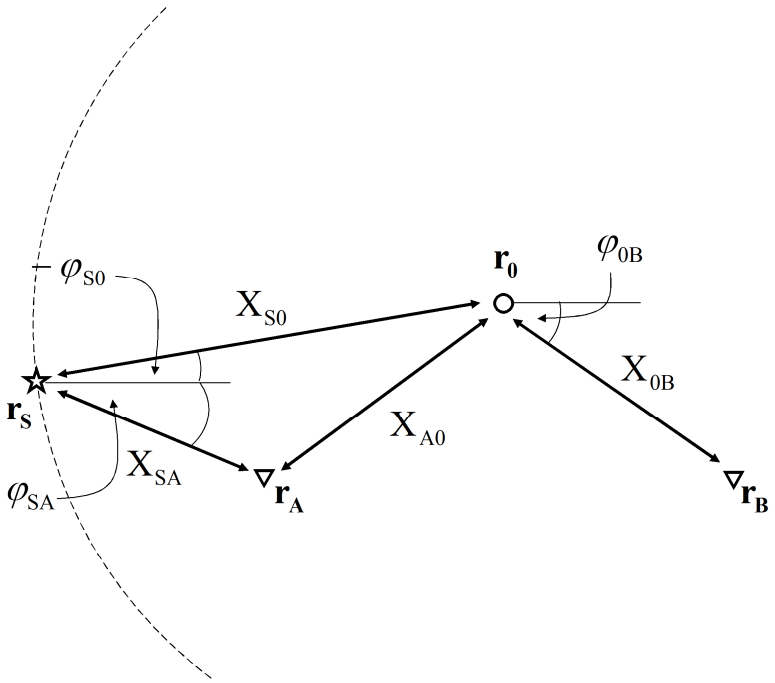

Figure A5.1: Definition of geometric variables required for terms *T2* and *T3* in the horizontal plane.

$$G_{im}^{\sigma\nu}(\mathbf{r}_B,\mathbf{r}_A) = p_i^{\nu}(z_B,\varphi_{AB})\,p_m^{\nu\,*}(z_A,\varphi_{AB})\frac{e^{i\left(k_\nu X_{AB}+\frac{\pi}{4}\right)}}{\sqrt{\frac{\pi}{2}k_\nu X_{AB}}}$$

$$+\frac{e^{i(k_\sigma X_{0B}+k_\nu X_{A0}+\frac{\pi}{2})}}{\frac{\pi}{2}\sqrt{k_\nu k_\sigma X_{0B}X_{A0}}}\,p_i^{\sigma}(z_B,\varphi_{0B})\,p_m^{\nu\,*}(z_A,\varphi_{A0})V^{\sigma\nu}(\varphi_{0B},\varphi_{A0}). \quad \text{(A5.2)}$$

In Equation (5.2) we simplify this expression by writing $G_{im}^{\sigma\nu}(\mathbf{r}_B,\mathbf{r}_A) = G_{im}^{0}(\mathbf{r}_B,\mathbf{r}_A) + G_{im}^{sc}(\mathbf{r}_B,\mathbf{r}_A)$, where $G_{im}^{0}(\mathbf{r}_B,\mathbf{r}_A)$ is the direct wave, and $G_{im}^{sc}(\mathbf{r}_B,\mathbf{r}_A)$ is the scattered wave. The equivalent particle-displacement deformation-rate Green's function is,

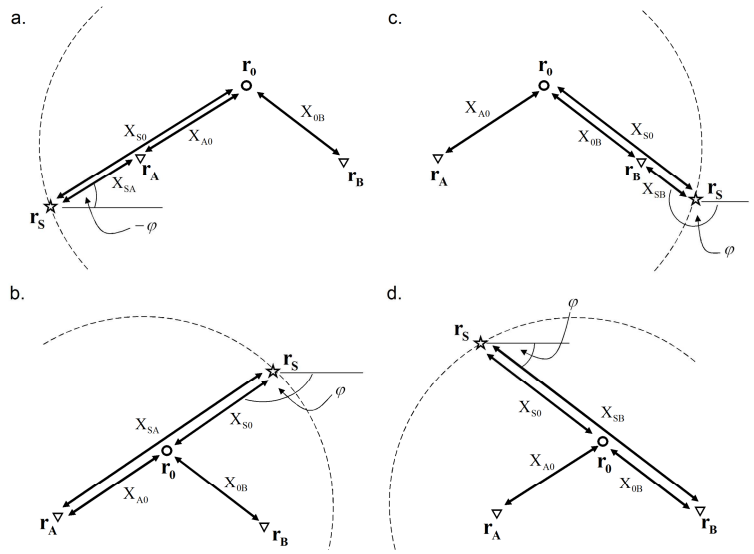

Figure A5.2: There are four types of stationary point, illustrated by boundary locations, $\mathbf{r}_S$, relating to the recovery of a wave propagating from receiver $\mathbf{r}_A$ to receiver $\mathbf{r}_B$, scattered en route by a heterogeneity at $\mathbf{r}_0$. We use a circular boundary of sources for illustration (dashed line). (a) Term *T2* (physical), (b) Term *T2* (non-physical), (c) Term *T3* (physical), (d) Term *T3* (non-physical). To illustrate term *T3* we have defined the additional geometrical term X_{SB} describing the horizontal offset along the path describing the horizontal offset along the path between the source, $\mathbf{r}_S$ and receiver, $\mathbf{r}_B$.

$$n_j c_{njkm} \partial_k G_{im}^{\sigma\nu}(\mathbf{r}_B, \mathbf{r}_A) = p_i^{\nu}(z_B, \varphi_{AB}) T_m^{\nu *}(z_A, \varphi_{AB}) \frac{e^{i\left(k_\nu X_{AB} + \frac{\pi}{4}\right)}}{\sqrt{\frac{\pi}{2} k_\nu X_{AB}}}$$

$$+ \frac{e^{i(k_\sigma X_{0B} + k_\nu X_{A0} + \frac{\pi}{2})}}{\frac{\pi}{2}\sqrt{k_\nu k_\sigma X_{0B} X_{A0}}} p_i^{\sigma}(z_B, \varphi_{0B}) T_m^{\nu *}(z_A, \varphi_{A0}) V^{\sigma\nu}(\varphi_{0B}, \varphi_{A0}), \qquad \text{(A5.3)}$$

where T_n^{ν} is the *n*th component of the traction vector defined in Equations 4.33 to 4.40. Equation (A5.3) is simplified in Equation (5.3) by writing $n_j c_{njkm} \partial_k G_{im}^{\sigma\nu}(\mathbf{r}_B, \mathbf{r}_A) = \partial G_{im}^{0}(\mathbf{r}_B, \mathbf{r}_A) + \partial G_{im}^{sc}(\mathbf{r}_B, \mathbf{r}_A)$.

While Equations (A5.1) to (A5.4) provide semi-analytical representations of Rayleigh-wave Green's functions, similar expressions exist for Love-wave Green's functions, and for scattering conversions between Love-wave modes and Rayleigh-

wave modes (Snieder, 2002b). Hence we expect that our analysis also holds for the Love-wave case.

In the Chapter 5 we discuss the four terms that are introduced when we substitute expressions (A5.2) and (A5.3) into Equation (4.1). Here we analyse each of these terms in turn (excluding *T1* which was the subject of Chapter 4).

Terms *T2 and T3*

After substituting the appropriate Green's functions into Equation (4.1) we find that the second term, T2 is:

$$T2 = \int_S \frac{e^{i\left(-k_\nu X_{SA} + k_\sigma X_{0B} + k_\nu X_{S0} + \frac{\pi}{4}\right)}}{\frac{\pi}{2}\sqrt{\frac{\pi}{2} k_\sigma k_\nu k_\nu X_{SA} X_{0B} X_{S0}}} \; p_i^\sigma(z_B, \varphi_{0B}) \; p_m^{\nu *}(z_A, \varphi_{SA}) V^{\sigma\nu}(\varphi_{0B}, \varphi_{S0})$$
$$\times \left(\; p_n^{\nu *}(z_S, \varphi_{S0}) T_n^\nu(z_S, \varphi_{SA}) - p_n^\nu(z_S, \varphi_{SA}) T_n^{\nu *}(z_S, \varphi_{S0}) \; \right) dS \,, \qquad \text{(A5.4)}$$

where the geometric variables are illustrated in Figure A5.1. In order to analyse this integral we use the cylindrical co-ordinate system introduced in the Chapter 5, and in Appendix 5B we find that the stationary phase conditions are $\varphi_{S0} - \varphi_{A0} = 0$ and $\varphi_{S0} - \varphi_{A0} = \pi$. In cylindrical co-ordinates we have $dS = X_{S0}\, d\varphi_{S0}\, dz$. We use $\varphi_{S0} = \varphi_{SA}$ at the stationary point, and follow Chapter 4 where the isotropic form of the stress tensor is used to solve the depth dependent part of this integral using,

$$\int_0^\infty \; p_n^{\nu *}(z_S, \varphi_{S0}) T_n^\nu(z_S, \varphi_{S0}) - p_n^\nu(z_S, \varphi_{S0}) T_n^{\nu *}(z_S, \varphi_{S0}) \; dz$$
$$= \frac{1}{2} ik_\nu (\cos\varphi_{S0} n_x + \sin\varphi_{S0} n_y) \,. \qquad \text{(A5.5)}$$

Since we are evaluating this integral at the stationary-point the integrand in (A5.6) is only dependent on depth (φ_{S0} is fixed at the stationary point). Note that the integral contains a sum over the index *n*, i.e. we sum over the three components of the normal to the boundary *S*. Expression (A5.6) greatly reduces the complexity of

the problem and allows for the analysis of the integral using the method of stationary phase. If we allow the integration surface to be a cylinder with extremely large radius such that $\cos\varphi_{S0} = -n_x$ and $\sin\varphi_{S0} = -n_y$,

$$\int_0^{\infty} p_n^{\nu\,*}(z_S,\varphi_{S0})T_n^{\nu}(z_S,\varphi_{S0}) - p_n^{\nu}(z_S,\varphi_{S0})T_n^{\nu\,*}(z_S,\varphi_{S0})\; dz = -\frac{1}{2}ik_\nu . \qquad \text{(A5.6)}$$

Using this relationship we find,

$$T2 = -\frac{ik_\nu}{\pi}\int_S \frac{e^{i\left(-k_\nu X_{SA}+k_\sigma X_{0B}+k_\nu X_{S0}+\frac{\pi}{4}\right)}}{k_\nu\sqrt{\frac{\pi}{2}k_\sigma X_{SA}X_{0B}X_{S0}}}\; p_i^{\sigma}(z_B,\varphi_{0B})\;\; p_m^{\nu\,*}(z_A,\varphi_{SA})V^{\sigma\nu}(\varphi_{0B},\varphi_{S0})X_{S0}d\varphi_{S0}. \text{(A5.7)}$$

We now wish to evaluate the integral,

$$I2 = \int_R \frac{e^{i\left(-k_\nu X_{SA}+k_\sigma X_{0B}+k_\nu X_{S0}+\frac{\pi}{4}\right)}}{k_\nu\sqrt{\frac{\pi}{2}k_\sigma X_{SA}X_{0B}X_{S0}}}\; V^{\sigma\nu}(\varphi_{0B},\varphi_{S0})X_{S0}\; d\varphi_{S0}, \qquad \text{(A5.8)}$$

using the method of stationary phase. The integration domain has been changed from the domain S to the domain *R*; this domain *R* represents the horizontal plane of integration described by $X_{S0}d\varphi_{S0}$. This requires the second derivatives of X_{SA} and X_{S0},

$$\frac{\partial^2 X_{SA}}{\partial\varphi_{S0}{}^2} = \frac{X_{S0}X_{A0}\cos(\varphi_{S0}-\varphi_{A0})}{\sqrt{X_{S0}{}^2 - 2X_{S0}X_{A0}\cos(\varphi_{S0}-\varphi_{A0}) + X_{A0}{}^2}}, \qquad \text{(A5.9)}$$

and

$$\frac{\partial^2 X_{S0}}{\partial\varphi_{S0}{}^2} = 0. \qquad \text{(A5.10)}$$

At the first stationary point ($\varphi_{S0} - \varphi_{A0} = 0$) Equation (A5.9) becomes,

$$\frac{\partial^2 X_{SA}}{\partial \varphi_{S0}^{\ 2}} = \frac{X_{S0} X_{A0}}{X_{SA}}, \tag{A5.11}$$

since at this stationary point $X_{SA} = X_{S0} - X_{A0}$ (Figure A5.2a). At the second stationary point $\varphi_{S0} - \varphi_{A0} = \pi$ and $X_{SA} = X_{S0} + X_{A0}$ (Figure A5.2b) so,

$$\frac{\partial^2 X_{SA}}{\partial \varphi_{S0}^{\ 2}} = \frac{-X_{S0} X_{A0}}{X_{SA}}, \tag{A5.12}$$

We first evaluate the stationary point $\varphi_{S0} - \varphi_{A0} = 0$. Following Snieder (2004a) the solution to the integral is,

$$I2 = \frac{e^{i\left(-k_\nu X_{SA} + k_\sigma X_{0B} + k_\nu X_{S0} + \frac{\pi}{4}\right)}}{k_\nu \sqrt{\frac{\pi}{2} k_\sigma X_{SA} X_{0B} X_{S0}}} e^{-i\pi/4} \sqrt{\frac{2\pi}{k_\nu}} \frac{X_{S0}}{\sqrt{\frac{X_{S0} X_{A0}}{X_{SA}}}} V^{\sigma\nu}(\varphi_{0B}, \varphi_{S0}) \tag{A5.13}$$

$$= \frac{2}{k_\nu} \frac{e^{i(-k_\nu X_{SA} + k_\sigma X_{0B} + k_\nu X_{S0})}}{\sqrt{k_\sigma k_\nu X_{0B} X_{A0}}} V^{\sigma\nu}(\varphi_{0B}, \varphi_{S0}). \tag{A5.14}$$

Substituting $I2$ into Equation (A5.7) we obtain

$$T2_p = -\frac{2i}{\pi} \frac{e^{i(-k_\nu X_{SA} + k_\sigma X_{0B} + k_\nu X_{S0})}}{\sqrt{k_\sigma k_\nu (X_{0B} X_{A0})}} p_i^{\sigma}(z_B, \varphi_{0B})\ p_m^{\nu\,*}(z_A, \varphi_{SA}) V^{\sigma\nu}(\varphi_{0B}, \varphi_{S0}), \tag{A5.15}$$

where the subscript *p* indicates that this is a physical term, corresponding to the scattered term of Equation (A5.2). If $\varphi_{S0} - \varphi_{A0} = 0$ then $X_{SA} = X_{S0} - X_{A0}$ and $\varphi_{S0} = \varphi_{SA} = \varphi_{A0}$, so the integral becomes,

$$T2_p = -\frac{e^{i\left(k_\nu X_{A0}+k_\sigma X_{0B}+\frac{\pi}{2}\right)}}{\frac{\pi}{2}\sqrt{k_\sigma k_\nu (X_{0B}X_{A0})}}\, p_i^{\sigma}(z_B,\varphi_{0B})\;\; p_m^{\nu\,*}(z_A,\varphi_{A0})V^{\sigma\nu}(\varphi_{0B},\varphi_{A0}). \qquad \text{(A5.16)}$$

Thus term T2 provides the correct causal scattered surface wave as desired (c.f. the second term of Equation (A5.2)). Following a similar process for the second stationary point (when $\varphi_{S0}-\varphi_{A0}=\pi$, $X_{SA}=X_{S0}+X_{A0}$, and $\varphi_{S0}=\varphi_{SA}=\varphi_{A0}+\pi$) the integral becomes,

$$T2_{np} = -\frac{e^{i(k_\sigma X_{0B}-k_\nu X_{A0})}}{\frac{\pi}{2}\sqrt{k_\sigma k_\nu (X_{A0}X_{0B})}}\, p_i^{\sigma}(z_B,\varphi_{0B})\;\; p_m^{\nu\,*}(z_A,\varphi_{A0}+\pi)V^{\sigma\nu}(\varphi_{0B},\varphi_{A0}+\pi). \qquad \text{(A5.17)}$$

This term does not correspond to any part of the Green's function defined in Equation (A5.2) - subscript *np* indicates that this is non-physical. Note that if we reverse the order of cross-correlation (i.e., use the direct surface wave at $\mathbf{r}_B$ and the scattered surface wave at $\mathbf{r}_A$) and repeat the above process to analyse contribution *T3* we find that the two terms are equal to,

$$T3_p = \frac{e^{-i\left(k_\nu X_{A0}+k_\sigma X_{0B}+\frac{\pi}{2}\right)}}{\frac{\pi}{2}\sqrt{k_\sigma k_\nu (X_{A0}X_{0B})}}\, p_i^{\sigma\,*}(z_B,\varphi_{0B})\;\; p_m^{\nu}(z_A,\varphi_{A0})V^{\sigma\nu\,*}(\varphi_{0B},\varphi_{A0}), \qquad \text{(A5.18)}$$

and for the second term

$$T3_{np} = \frac{e^{i(k_\sigma X_{0B}-k_\nu X_{A0})}}{\frac{\pi}{2}\sqrt{k_\sigma k_\nu (X_{A0}X_{0B})}}\, p_i^{\sigma\,*}(z_B,\varphi_{0B})\;\; p_m^{\nu}(z_A,\varphi_{A0}+\pi)V^{\sigma\nu\,*}(\varphi_{0B},\varphi_{A0}+\pi), \qquad \text{(A5.19)}$$

see Figure c and d. Again by comparing with Equation (A5.2) we see that $T3_p$ contributes the true scattered surface wave event but in the time-reversed part of the interferometric integral due to the complex conjugation of Equation (A5.18) with

respect to the second term in Equation (A5.2). $T3_{np}$ on the other hand contributes a non-physical arrival with the same phase as $T2_{np}$ but with opposite sign and complex conjugation of the scattering matrix.

In the Chapter 5 we combine terms *T1*, $T2_p$ and $T3_p$ which gives the Green's function described by the left hand side of Equation (4.1). However, to satisfy Equation (4.1) we require that the non-physical terms $T2_{np}$ and $T3_{np}$ are cancelled. In the remainder of this appendix, and in Chapter 5, we show that term *T4* allows for the cancellation of the non-physical terms, provided scattering is governed by a generalized optical theorem for surface waves.

T4

Term *T4* is the cross-correlation of the scattered surface waves recorded at both receivers:

$$T4 = \int_S \frac{e^{i\left(-k_\sigma X_{A0} - k_\nu X_{S0} + k_\sigma X_{0B} + k_\nu X_{S0}\right)}}{\frac{\pi^2}{4} k_\sigma k_\nu \sqrt{X_{S0} X_{A0} X_{S0} X_{0B}}}$$
$$\times p_i^{\sigma}(z_B, \varphi_{0B})\ \ p_m^{\sigma^*}(z_A, \varphi_{A0} + \pi) V^{\sigma\nu}(\varphi_{0B}, \varphi_{S0}) V^{\sigma\nu^*}(\varphi_{A0} + \pi, \varphi_{S0})$$
$$\times \Big(\ p_n^{\nu^*}(z_S, \varphi_{S0}) T_n^{\nu}(z_S, \varphi_{S0}) - p_n^{\nu}(z_S, \varphi_{S0}) T_n^{\nu^*}(z_S, \varphi_{S0})\ \Big)\, dS\,. \qquad \text{(A5.20)}$$

Note that the incident wavefield upon the scatterer is the same for both receiver positions. Recalling Equation (A5.6) and by using $dS = dz dr d\varphi_{S0}$ we can solve the depth dependent part of the integral,

$$T4 = -\frac{2i}{\pi^2} \int_R \frac{e^{i\left(-k_\sigma X_{A0} + k_\sigma X_{0B}\right)}}{X_{S0} k_\sigma \sqrt{X_{A0} X_{0B}}}$$
$$\times p_i^{\sigma}(z_B, \varphi_{0B})\ \ p_m^{\sigma^*}(z_A, \varphi_{A0} + \pi) V^{\sigma\nu}(\varphi_{0B}, \varphi_{S0}) V^{\sigma\nu^*}(\varphi_{A0} + \pi, \varphi_{S0}) dr d\varphi_{S0}\,. \qquad \text{(A5.21)}$$

Note again the change of integration domain from *S* to *R*; this domain *R* represents the horizontal plane of integration described by $drd\varphi_{S0}$. Since X_{A0} and X_{0B} are constant this term is always stationary: each source location provides a contribution to the interferometric integral and no such contributions cancel destructively within the integration.

We have already shown that the correct direct and scattered surface waves are recovered from terms *T1, T2*$_p$, and *T3*$_p$. However non-physical arrivals are introduced by terms $T2_{np}$, $T3_{np}$, and *T4*, and since Equation (4.1) is exact these terms must cancel. We group the terms $T2_{np}$ and $T3_{np}$ into a single non-physical term T_{np},

$$T_{np} = -\frac{2}{\pi} A^{\sigma\nu}(X_{0B}, X_{A0}) \times \left[P_{im}^{\sigma\nu}(\varphi_{0B}, \varphi_{A0} + \pi) V^{\sigma\nu}(\varphi_{0B}, \varphi_{A0} + \pi) - P_{im}^{\sigma\nu *}(\varphi_{0B}, \varphi_{A0} + \pi) V^{\sigma\nu *}(\varphi_{0B}, \varphi_{A0} + \pi) \right]. \quad \text{(A5.22)}$$

The propagation characteristics (the phase, wavenumbers and geometrical spreading) of the non-physical term are given by,

$$A^{\sigma\nu} = \frac{e^{i(k_\sigma X_{0B} - k_\nu X_{A0})}}{\sqrt{k_\nu k_\sigma (X_{A0} X_{0B})}}, \quad \text{(A5.23)}$$

and the polarization of the non-physical term is given by,

$$P_{im}^{\sigma\nu}(\varphi_{0B}, \varphi_{A0} + \pi) = p_i^{\sigma}(z_B, \varphi_{0B}) \; p_m^{\nu *}(z_A, \varphi_{A0} + \pi). \quad \text{(A5.24)}$$

We can therefore write term T4 in the following condensed form,

$$T4 = -\frac{2i}{\pi^2} \int_R \left[A^{\sigma\sigma}(X_{0B}, X_{A0}) P_{im}^{\sigma\sigma *}(\varphi_{0B}, \varphi_{A0} + \pi) V^{\sigma\nu}(\varphi_{0B}, \varphi_{S0}) V^{\sigma\nu *}(\varphi_{0A} + \pi, \varphi_{S0}) \right] \times \frac{1}{X_{S0}} drd\varphi_{S0}, \quad \text{(A5.25)}$$

and since X_{S0} is equal to the radius of the cylinder,

$$T4 = -\frac{2i}{\pi^2}\int_0^{2\pi}\Big[A^{\sigma\sigma}(X_{0B}, X_{A0})P_{im}^{\sigma\sigma^*}(\varphi_{0B}, \varphi_{A0}+\pi) \times V^{\sigma\nu}(\varphi_{0B}, \varphi_{S0})V^{\sigma\nu^*}(\varphi_{A0}+\pi, \varphi_{S0})\Big]\, d\varphi_{S0}\,. \tag{A5.26}$$

In the generalized optical theorem the scattering amplitude is often defined in terms of unit vectors in the directions of propagation of the incident and scattered waves. Following this convention, we take the horizontal component of the unit vectors (implicit in the following notation) and recalling our vector definitions (5.1) we redefine the scattering matrix and polarization terms as,

$$V^{\sigma\nu}(\varphi_{0B}+\pi, \varphi_{A0}) = f^{\sigma\nu}(\hat{\mathbf{r}}_B, \hat{\mathbf{r}}_A)\,, \tag{A5.27}$$

and

$$P_{im}^{\sigma\nu}(\varphi_{0B}, \varphi_{A0}+\pi) = P_{im}^{\sigma\nu}(\hat{\mathbf{r}}_B, \hat{\mathbf{r}}_A)\,, \tag{A5.28}$$

where $f^{\sigma\nu}(\hat{\mathbf{r}}_B, \hat{\mathbf{r}}_A)$ is the surface wave scattering matrix for an incident surface wave mode ν travelling in the horizontal direction of unit-vector $\hat{\mathbf{r}}_A$ that is scattered in the horizontal direction of unit-vector $\hat{\mathbf{r}}_B$ as surface wave mode σ. In the Chapter 5 we combine these two terms using $S_{im}^{\sigma\nu}(\hat{\mathbf{r}}_B, \hat{\mathbf{r}}_A) = P_{im}^{\sigma\nu}(\hat{\mathbf{r}}_B, \hat{\mathbf{r}}_A) f^{\sigma\nu}(\hat{\mathbf{r}}_B, \hat{\mathbf{r}}_A)$, where it is understood that $S_{im}^{\sigma\nu}$ includes a combination of the polarization components *i* and *m*. We also replace φ_{S0} with Ω and then Equations (A5.22) and (A5.26) are rewritten to reach Equations (5.6) and (5.8), from which we derive a generalized optical theorem for surface waves.

Finally, in Equation (5.14) we use a term $\mathrm{D}^{\sigma\nu}$ which accounts for the differences in phase and wavenumber of the observed scattered surface wave modes σ and ν

(i.e., the terms that describe the propagation characteristics of each mode). This term is defined as:

$$\mathrm{D}^{\sigma v} = \frac{A^{\sigma\sigma}}{A^{\sigma v}} \tag{A5.29}$$

$$= e^{i(k_v X_{A0} - k_\sigma X_{A0})} \sqrt{\frac{k_v}{k_\sigma}}\,. \tag{A5.30}$$

Appendix 5B: Stationary-phase condition

In this appendix we find the stationary-phase condition for the scattered surface waves. To find the stationary phase condition we need the lengths of each of the propagation paths. In cylindrical co-ordinates the length X_{SA} can be related to the other paths as follows,

$$X_{SA} = \sqrt{X_{S0}{}^2 - 2X_{S0}X_{A0}\cos(\varphi_{S0} - \varphi_{A0}) + X_{A0}{}^2}\,, \tag{A5.31}$$

where geometric variables are illustrated in Figure 5.1. In order to determine the stationary points of the integral we then require the first derivatives of X_{SA}, X_{S0}, X_{A0}, and X_{0B} with respect to the integration direction. Since there is no dependence on z we consider the φ_{S0}-derivatives using the geometry defined in (5.1):

$$\frac{\partial X_{SA}}{\partial \varphi_{S0}} = 2X_{S0}X_{A0}\sin(\varphi_{S0} - \varphi_{A0})\,, \tag{A5.32}$$

$$\frac{\partial X_{A0}}{\partial \varphi_{S0}} = 0\,, \tag{A5.33}$$

$$\frac{\partial X_{0B}}{\partial \varphi_{S0}} = 0\,, \tag{A5.34}$$

$$\frac{\partial X_{S0}}{\partial \varphi_{S0}} = 0\,. \tag{A5.35}$$

In our analysis, we require stationary-phase conditions for integration in the φ_{S0}-direction. The integral *T2* is stationary when,

$$\frac{\partial X_{S0}}{\partial \varphi_{S0}} = \frac{\partial X_{SA}}{\partial \varphi_{S0}}\,, \tag{A5.36}$$

i.e.,

$$0 = 2X_{S0}X_{A0}\sin(\varphi_{S0} - \varphi_{A0}) = 2X_{S0}X_{A0}\sin(\varphi_{S0} - \varphi_{A0}) \qquad \text{(A5.37)}$$

i.e., the stationary-phase conditions are $(\varphi_{S0} - \varphi_{A0}) = 0$ and $(\varphi_{S0} - \varphi_{A0}) = \pi$.

Appendix 6A: Constraints on the scattering amplitude for single-scattered surface waves

In Chapter 5 seismic interferometry, stationary-phase analysis, and scattered surface wave Green's functions were used to derive a generalized optical theorem for surface waves. This theorem correctly describes the amplitude and phase relationship between incident and scattered surface-wave modes from scatterers at any depth in a layered medium. The analysis presented not only has implications for general scattering of surface waves, but there are also insights that can be gained regarding the application of seismic interferometry to scattered surface waves. Rather than simply re-deriving the generalized optical theorem of Chapter 5 we consider the role of each of the terms in the analysis of seismic interferometry for scattered surface waves, before deriving the optical theorem for the specific case of isotropic point scatterers corresponding to density perturbations. This allows us to derive constraints on the real and imaginary parts of the scattering amplitude, which allow us to calculate singly and multiply scattered surface waves efficiently. The results of this analysis are discussed in detail in Section 6.2.

In Chapter 5 we showed that the terms $T2_{np}$ and $T3_{np}$ contribute non-physical arrivals with the same phase but opposite sign and complex conjugation of the scattering matrix (Equations A5.18 and A5.20). Note that if the scattering matrix is real, as is the case in a Born analysis, then $T2_{np}$ and $T3_{np}$ provide mutually-cancelling terms. However, if we wish to consider higher-order terms we must also consider the non-linear feedback of the scatterer on the propagating wavefield. By higher-order we refer to any part of the wavefield that has been influenced by scatterers more than once. We consider term *T4* in Chapter 5 (Equation A5.22) to be a higher order term as even though this is a single-scattering example, term *T4* involves the cross-correlation of two scattered waves; while it would not normally be considered during a Born analysis we now show the importance of this higher-order term in seismic interferometry of single-scattered waves.

To do this we require an optical theorem for surface waves, originally formulated by Snieder (1988) who related the imaginary part of the scattering amplitude to the total scattered power, and further developed by Brandenburg and Snieder (1989) who

investigate the attenuation of surface waves due to scattering. The optical theorem can be used to derive constraints on the real and imaginary parts of scattering amplitudes (e.g., as derived for 2-D acoustic scattering by Groenenboom and Snieder, 1995). We use our interferometric analysis to derive constraints on the real and imaginary parts of the scattering amplitude for surface waves. While similar results have been derived for various types of media, the result for surface waves is new. We show that this allows us to account for terms $T2_{np}$, $T3_{np}$, and *T4*. In Chapter 6 we use this condition to compute realistic scattered surface waves within the optical theorem.

We treat the special case where there are no conversions between different surface wave modes (i.e. $\sigma = \sigma' = \nu$) and define a complex scattering amplitude $V(\varphi_{0B}, \varphi_{A0})$,

$$V(\varphi_{0B}, \varphi_{A0}) = \mathrm{Re}V(\varphi_{0B}, \varphi_{A0}) + i * \mathrm{Im}V(\varphi_{0B}, \varphi_{A0}). \tag{A6.1}$$

If we insert this scattering amplitude into Equations (A5.17) and (A5.19) it is clear that the correct scattered surface wave is recovered. However, inserting this into Equations (A5.18) and (A5.20) results in a non-cancelling term:

$$T2_{np} = i \frac{e^{i\left(k_\nu X_{0B} - k_\nu X_{A0} + \frac{\pi}{2}\right)}}{\frac{\pi}{2}\sqrt{k_\nu k_\nu (X_{A0} X_{0B})}} p_i^\nu(z_B, \varphi_{0B})\ p_m^{\nu *}(z_A, \varphi_{A0} + \pi)$$
$$\times \left[\mathrm{Re}V(\varphi_{0B}, \varphi_{A0} + \pi) + i * \mathrm{Im}V(\varphi_{0B}, \varphi_{A0} + \pi)\right], \tag{A6.2}$$

$$T3_{np} = -i \frac{e^{i\left(k_\nu X_{0B} - k_\nu X_{A0} + \frac{\pi}{2}\right)}}{\frac{\pi}{2}\sqrt{k_\nu k_\nu (X_{0B} X_{A0})}} p_i^{\nu *}(z_B, \varphi_{0B})\ p_m^{\nu}(z_A, \varphi_{A0} + \pi)$$
$$\times \left[\mathrm{Re}V(\varphi_{0B}, \varphi_{A0} + \pi) - i * \mathrm{Im}V(\varphi_{0B}, \varphi_{A0} + \pi)\right]. \tag{A6.3}$$

If we assume that we are interested only in vertical force sources and vertical particle displacement (such that $i = m = 3$) then the non-physical parts of terms *T2* and *T3* can be combined into a single term (T_{np}),

$$T_{np} = -i\frac{e^{i(k_\nu X_{0B} - k_\nu X_{A0})}}{\frac{\pi}{2}\sqrt{k_\nu k_\nu (X_{0B} X_{A0})}} \mathrm{Im} V(\varphi_{0B}, \varphi_{A0} + \pi) \times 2 p_3^\nu (z_B, \varphi_{0B})\ p_3^{\nu *}(z_A, \varphi_{A0} + \pi). \quad \text{(A6.4)}$$

To derive the constraints that the optical theorem places on the real and imaginary parts of the scattering amplitude we consider the forward scattering amplitude (Snieder, 1988; Groenenboom and Snieder, 1995). To do this we assume that geometries are chosen such that $\varphi_{0B} = \varphi_{A0} + \pi$, i.e.

$$T_{np} = -i\frac{e^{i(k_\nu X_{0B} - k_\nu X_{A0})}}{\frac{\pi}{2}\sqrt{k_\nu k_\nu (X_{0B} X_{A0})}} \mathrm{Im} V(\varphi_{0B}, \varphi_{0B}) \times 2 p_3^\nu (z_B, \varphi_{0B})\ p_3^{\nu *}(z_A, \varphi_{0B}), \quad \text{(A6.5)}$$

and

$$T4 = -\frac{2i}{\pi^2}\int_S \frac{e^{i(-k_\nu X_{A0} + k_\nu X_{0B})}}{X_{S0}\sqrt{k_\nu k_\nu X_{A0} X_{0B}}}\ p_3^\nu (z_B, \varphi_{0B})\ p_3^{\nu *}(z_A, \varphi_{0B}) \left|V(\varphi_{0B}, \varphi_{S0})\right|^2 dS \quad \text{(A6.6)}$$

It then follows, that for this scattered wavefield representation to be exact that T_{np} must be equal to *T4*, i.e.

$$-2i\frac{e^{i(k_\nu X_{0B} - k_\nu X_{A0})}}{\frac{\pi}{2}\sqrt{k_\nu k_\nu (X_{0B} X_{A0})}} \mathrm{Im} V(\varphi_{0B}, \varphi_{0B})\ p_3^\nu (z_B, \varphi_{0B})\ p_3^{\nu *}(z_A, \varphi_{0B}) = \frac{2i}{\pi^2}\int_S \frac{e^{i(-k_\nu X_{A0} + k_\nu X_{0B})}}{X_{S0}\sqrt{k_\nu k_\nu X_{A0} X_{0B}}}\ p_3^\nu (z_B, \varphi_{0B})\ p_3^{\nu *}(z_A, \varphi_{0B}) \left|V(\varphi_{0B}, \varphi_{S0})\right|^2 dS. \quad \text{(A6.7)}$$

Finally we remove the resulting common terms from both sides of Equation (A6.7) then the part of this expression dependent on the differing receiver locations is removed, i.e., the right hand side is now equivalent to the power of the scattered wave

$$-\frac{4i}{\pi}\mathrm{Im}V(\varphi_{0B},\varphi_{0B})=\frac{2i}{\pi^2}\int_S\frac{1}{X_{S0}}\left|V(\varphi_{0B},\varphi_{S0})\right|^2 dS\,. \tag{A6.8}$$

and rearranging,

$$-\mathrm{Im}V(\varphi_{0B},\varphi_{0B})=\frac{1}{2\pi}\int_S\frac{1}{X_{S0}}\left|V(\varphi_{0B},\varphi_{S0})\right|^2 dS\,, \tag{A6.9}$$

We can simplify this expression following the approach of Brandenburg and Snieder (1989). First we assume that the surface is a cylinder with extremely large radius. The length X_{S0} is then approximately equal for all points on the boundary, and the horizontal projection of the azimuth from each boundary position is approximately equal to the normal to the boundary. We then use that $dS=drd\phi$, where *r* is the radius of the cylinder and ϕ is the scattering angle ($\varphi_{0B}-\varphi_{S0}$). There is no depth integration as we have already solved the depth dependent part of the integral and the integral then becomes

$$-\mathrm{Im}V(\varphi_{0B},\varphi_{0B})=\frac{1}{2\pi}\int_0^{2\pi}\left|V(\varphi_{0B},\varphi_{S0})\right|^2 d\phi\,. \tag{A6.10}$$

The scattering amplitude for an isotropic density perturbation has two parts, one independent of scattering angle, and one dependent on the scattering angle (Snieder, 2002b, eq. 43). To allow us to calculate synthetic seismograms (in a similar fashion to Groenenboom and Snieder, 1995) we assume that $V(\varphi_{0B},\varphi_{S0})$ has the following form i.e.,

$$V(\varphi_{0B},\varphi_{S0}) = V_1 + V_2\cos\phi\,. \tag{A6.11}$$

We split Equation (A6.10) into two parts, a non-angular dependent part and an angularly dependent part,

$$-\mathrm{Im}V_1 = \frac{1}{2\pi}\int_0^{2\pi} \mathrm{Re}V_1^{\,2} + \mathrm{Im}V_1^{\,2}\,d\phi, \tag{A6.12}$$

and

$$-\mathrm{Im}V_2 = \frac{1}{2\pi}\int_0^{2\pi} \left(\mathrm{Re}V_2^{\,2} + \mathrm{Im}V_2^{\,2}\right)\cos^2\phi\; d\phi\,. \tag{A6.13}$$

Evaluating the integrals we find that the optical theorem places the following constraints on these two parts of the scattering amplitude,

$$\mathrm{Re}V_1 = \sqrt{-\mathrm{Im}V_1(1+\mathrm{Im}V_1)}\,, \tag{A6.14}$$

and

$$\mathrm{Re}V_2 = \sqrt{-\mathrm{Im}V_2(2+\mathrm{Im}V_2)}\,. \tag{A6.15}$$

By equating the non-physical parts of terms *T2* and *T3* with *T4*, we have found the constraints that the optical theorem places on surface waves scattered by an isotropic density perturbation. This is a special case of the generalised optical theorem derived in Chapter 5. Therefore by using Equations (A6.14) and (A6.15) we can be certain that interferometric estimates generated using Equation (4.1) are not affected by non-physical arrivals. Thus, provided scattering is governed by the optical theorem, we have solved the interferometric integral for singly-scattered surface waves. The constraints that we derive are for waves excited by and observed using vertical point-force sources and vertical displacement, respectively. Similar constraints could be

derived for different source and receiver components if required. In Chapter 6 we use relationships (A6.14) and (A6.15) to calculate synthetic seismograms to illustrate our findings.

Appendix 6B: Alterations for convolution interferometry

In the Chapter 6 we discuss the application of convolution-type interferometry to scattered surface waves. In this appendix we adapt our stationary-phase analysis to allow us to consider this convolution-type approach.

It is possible to derive a relationship similar to Equation (4.1) that uses cross-convolution in place of cross-correlation. This is done by using the reciprocity theorem of the convolution-type as the starting point in the interferometric derivation, as opposed to a reciprocity theorem of the correlation-type (Wapenaar, 2007). This derivation is very similar to the derivations of van Manen *et al.* (2006) and Wapenaar and Fokkema (2006), but there is an additional constraint on the location of the two receivers. In this configuration we must have one receiver located inside the source boundary and the second receiver located outside the boundary. In correlation-type interferometry time-reversed wavefields are introduced due to the fact that cross-correlation requires complex conjugation (or time-reversal) of one of the inputs. Since wavefields cannot be time-reversed in the presence of attenuation this places the constraint that the medium of interest must be non-attenuating. In convolution-type interferometry there is no complex-conjugation, hence no time-reversed wavefields are introduced and no constraints are placed on the attenuation of the medium. We can therefore expect this form of interferometry to be useful in the presence of strong attenuation.

Adapting the approach of Slob *et al.* (2007) for the elastic case, the equivalent convolution form of Equation (4.1) is found to be,

$$G_{im}(\mathbf{r}_B,\mathbf{r}_A) = \int_{\mathbf{r}_S\in S}\left\{ G_{in}(\mathbf{r}_B,\mathbf{r}_S)\ n_j c_{njkl}\partial_k G_{ml}(\mathbf{r}_A,\mathbf{r}_S) - n_j c_{njkl}\partial_k G_{il}(\mathbf{r}_B,\mathbf{r}_S)\ G_{mn}(\mathbf{r}_A,\mathbf{r}_S)\right\} dS\,, \tag{A6.16}$$

where one of $\mathbf{r}_A$ and $\mathbf{r}_B$ is inside the volume S, and the other is outside the volume.

With this new configuration in mind, we can make appropriate alterations to the stationary-phase analysis. It can be shown that the combination of the new

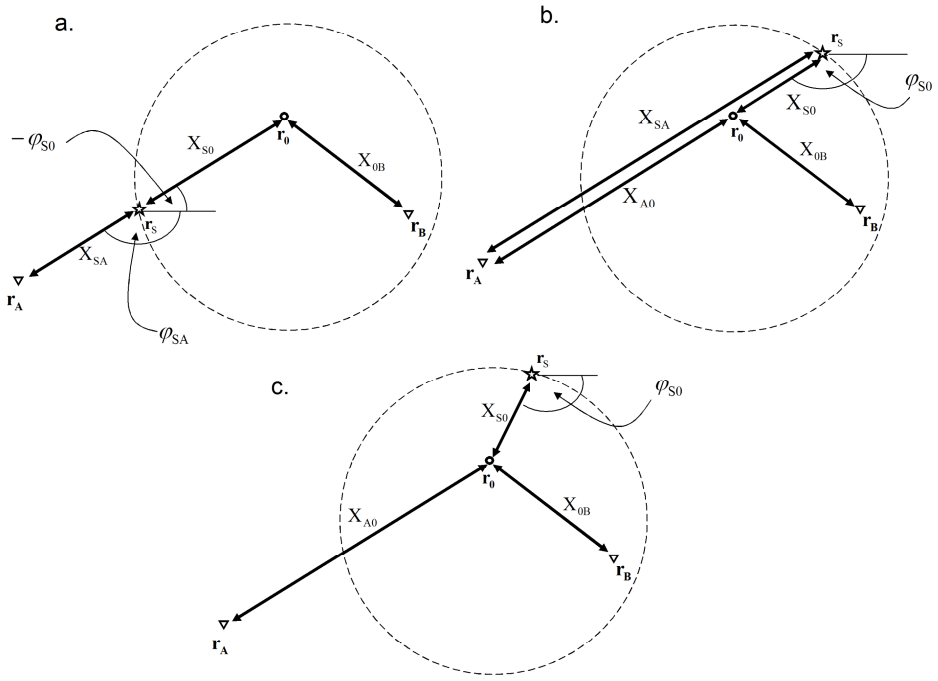

Figure A6.1: (a) Illustration of the stationary point for the scattered surface wave in convolution-type interferometry. (b) and (c) Corresponding geometries for the non-physical part of term T2 (or T3) and Term T4, respectively.

stationary-phase condition and the convolution-type integral has the same result as the combination of the old stationary-phase condition and the correlation type integral. We choose not to present this lengthy derivation, and instead proceed to investigate the differences in stationary-phase conditions and the consequences for estimation of surface waves.

For the stationary points there is a sign change in the phase term. For the direct surface waves the phase term (P) for correlation-type interferometry is,

$$P = ik_v(X_{SA} - X_{SB}), \tag{A6.17}$$

and by taking the first order derivatives we find that the integral is stationary when (Snieder, 2004a; Chapter 4),

$$\varphi_{SA} = \varphi_{SB}. \tag{A6.18}$$

When we consider convolution-type interferometry, there is no complex conjugation, and the phase term in the interferometric integral becomes,

$$P = ik_{\nu}(X_{SA} + X_{SB}), \tag{A6.19}$$

and it is easily shown that the integral becomes stationary when,

$$\varphi_{SA} = \varphi_{SB} + \pi. \tag{A6.20}$$

The same alterations can be made for the integral for scattered surface waves. The stationary-phase conditions change in the same way, i.e. for the physical arrival the condition changes from $\varphi_{S0} = \varphi_{A0}$ in correlation-type interferometry (see Appendix 5A) to,

$$\varphi_{S0} = \varphi_{A0} + \pi, \tag{A6.21}$$

for convolution-type interferometry, and for the non-physical stationary phase the condition changes from $\varphi_{S0} = \varphi_{A0} + \pi$ for correlation-type interferometry to $\varphi_{S0} = \varphi_{A0}$ for convolution-type interferometry. In Figure A6.1a and b we show the geometries for this physical and non-physical stationary point, respectively. In Figure A6.1c we also show the geometry corresponding to term T4.

Using the relationships $p_n^{\nu}(z,-\varphi) = p_n^{\nu *}(z,\varphi)$ and $T_n^{\nu}(z,-\varphi) = T_n^{\nu *}(z,\varphi)$ the stationary-phase analysis is then the same as for the cross-correlation case. If we then consider the source terms for these contributions in the correlation case (e.g. Equation A5.6),

$$p_n^{\nu *}(z_S,\varphi_{S0})T_n^{\nu}(z_S,\varphi_{S0}) - p_n^{\nu}(z_S,\varphi_{S0})T_n^{\nu *}(z_S,\varphi_{S0}), \tag{A6.22}$$

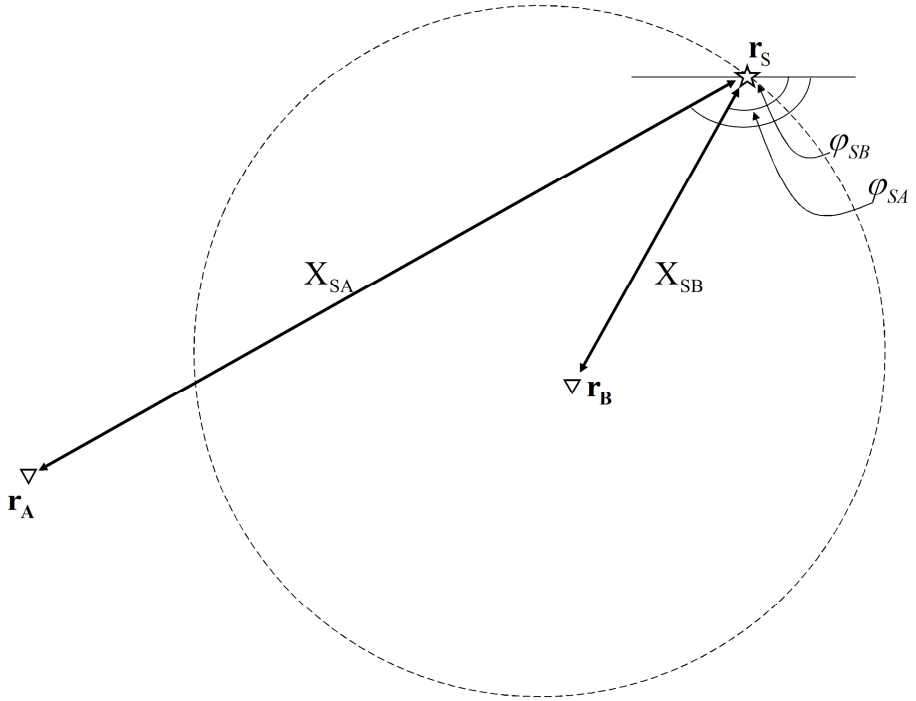

Figure A6.2: Sketch illustrating the geometry of the spurious stationary point arising in convolution-type interferometry.

we find that in the convolution case there is no complex conjugation:

$$p_n^{\nu}\ (z_S,\varphi_{S0})T_n^{\nu}(z_S,\varphi_{S0}) - p_n^{\nu}(z_S,\varphi_{S0})T_n^{\nu}\ (z_S,\varphi_{S0}) = 0\,. \qquad \text{(A6.23)}$$

Hence term *T4* is equal to zero in convolution-type interferometry and there are no non-physical arrivals. That is, despite being stationary these points give a vanishing contribution to the interferometric integral. Hence there is no contribution from term T4 and terms T2 and T3 do not have any non-physical contributions and no mutually-cancelling terms are introduced, the significance of which is discussed in Sections 6.3 and 6.4.

However, there is one further contribution that we must consider. If we only have a boundary of sources at the surface there is one point on the circle which appears to be stationary. At this point the sum of the offsets travelled between the source and receivers one and two is at its maximum, and therefore this looks like a stationary point (Figure A6.2). However, this is not stationary - with a different shape of

boundary this maximum value will occur at a different point because in fact this point is non-stationary across a surface, but it is stationary along a line. We find that this event also cancels given integration with depth, similar to the cancellation of the cross-mode stationary points discussed in Chapter 4. This can be argued as follows: the Rayleigh-wave orthogonality relationship states that the time-domain product of different Rayleigh-wave modal solutions integrates to zero over depth. This holds for any pair of solutions to the Rayleigh-wave eigenvalue problem (and can also be shown to include solutions to the Love-wave eigenvalue problem). Since the convolved waves for this pseudo-stationary source point both travel along different azimuths they can be considered as different solutions. Hence integration of their time-domain product over depth results in a value of zero.

Appendix 7A: On the non-reciprocal nature of non-physical arrivals

In the Chapter 7 we illustrate that non-physical arrivals relating to correlations of direct and scattered waves are non-reciprocal. That is, when the source and receiver position are interchanged the physical arrivals remain the same, but the non-physical arrivals are time-reversed.

We can explain this observation using representation theorems for perturbed acoustic media (Vasconcelos *et al.*, 2009). A representation theorem for loss-less scattering in acoustic media can be written as,

$$G_S(\mathbf{r}_1,\mathbf{r}_2) = \oint_{r\in S} \frac{1}{i\omega\rho}\left[G_S(\mathbf{r}_1,\mathbf{r})\partial_i G_0^*(\mathbf{r}_2,\mathbf{r}) + \partial_i G_S(\mathbf{r}_1,\mathbf{r}) G_0^*(\mathbf{r}_2,\mathbf{r})\right] n_i \; dS$$
$$+ \int_{r\in V} \frac{1}{i\omega\rho} G(\mathbf{r}_1,\mathbf{r})\, V(\mathbf{r})\, G_0^*(\mathbf{r}_2,\mathbf{r})\, dV\,, \qquad \text{(A7.1)}$$

where $V(\mathbf{r})$ is the scattering potential, $G_0(\mathbf{r}_2,\mathbf{r})$ is the wavefield in the background medium, and $G_S(\mathbf{r}_1,\mathbf{r}_2)$ is the scattered wavefield. Rearranging we find,

$$G_S(\mathbf{r}_1,\mathbf{r}_2) - \int_{r\in V} \frac{1}{i\omega\rho} G(\mathbf{r}_1,\mathbf{r})\, V(\mathbf{r})\, G_0^*(\mathbf{r}_2,\mathbf{r})\, dV$$
$$= \oint_{r\in S} \frac{1}{i\omega\rho}\left[G_S(\mathbf{r}_1,\mathbf{r})\partial_i G_0^*(\mathbf{r}_2,\mathbf{r}) + \partial_i G_S(\mathbf{r}_1,\mathbf{r}) G_0^*(\mathbf{r}_2,\mathbf{r})\right] n_i \; dS\,. \qquad \text{(A7.2)}$$

Note the right hand side of expression (A7.2) is very similar to Equation (1.2). However, here we cross-correlate direct waves at one receiver with scattered waves at the other, i.e., this is equivalent to term *T2* in Chapter 7, where the non-physical part is represented by the volume integral on the left hand side of Equation (A7.2).

From Vasconcelos *et al.* (2009) we can also find a representation theorem for $G_S^*(\mathbf{r}_1,\mathbf{r}_2)$,

$$G_S^*(\mathbf{r}_1,\mathbf{r}_2) = \oint_{r\in S} \frac{1}{i\omega\rho}\left[G_S^*(\mathbf{r}_2,\mathbf{r})\partial_i G_0(\mathbf{r}_1,\mathbf{r}) + \partial_i G_S^*(\mathbf{r}_2,\mathbf{r}) G_0(\mathbf{r}_1,\mathbf{r})\right] n_i \; dS$$

$$+ \int_{r\in V} \frac{1}{i\omega\rho} G^*(\mathbf{r}_1,\mathbf{r})\, V(\mathbf{r})\, G_0(\mathbf{r}_2,\mathbf{r})\, dV\,, \qquad \text{(A7.3)}$$

And again we rearrange to find a representation theorem that defines term *T3*,

$$G_S^*(\mathbf{r}_1,\mathbf{r}_2) - \int_{r\in V} \frac{1}{i\omega\rho} G^*(\mathbf{r}_1,\mathbf{r})\, V(\mathbf{r})\, G_0(\mathbf{r}_2,\mathbf{r})\, dV$$

$$= \oint_{r\in S} \frac{1}{i\omega\rho}\left[G_S^*(\mathbf{r}_2,\mathbf{r})\partial_i G_0(\mathbf{r}_1,\mathbf{r}) + \partial_i G_S^*(\mathbf{r}_2,\mathbf{r}) G_0(\mathbf{r}_1,\mathbf{r})\right] n_i \; dS\,. \qquad \text{(A7.4)}$$

The combination of the volume terms on the left hand side of Equations (A7.2) and (A7.4) are the non-physical arrivals such as those we observe in Figure 7.8 and Figure 7.12, i.e.,

$$G_{np1}(\mathbf{r}_1,\mathbf{r}_2) + G_{np2}(\mathbf{r}_1,\mathbf{r}_2)$$

$$= \int_{r\in V} \frac{1}{i\omega\rho}\left[G(\mathbf{r}_1,\mathbf{r})\, V(\mathbf{r})\, G_0^*(\mathbf{r}_2,\mathbf{r}) + G^*(\mathbf{r}_2,\mathbf{r})\, V(\mathbf{r})\, G_0(\mathbf{r}_1,\mathbf{r})\right] dV\,. \qquad \text{(A7.5)}$$

When we exchange source and receiver (as we do in Figure 7.19) we find,

$$G_{np1}(\mathbf{r}_1,\mathbf{r}_2) + G_{np2}(\mathbf{r}_1,\mathbf{r}_2) = G_{np1}^*(\mathbf{r}_1,\mathbf{r}_2) + G_{np2}^*(\mathbf{r}_1,\mathbf{r}_2)$$

$$= \int_{r\in V} \frac{1}{i\omega\rho}\left[G(\mathbf{r}_1,\mathbf{r})\, V(\mathbf{r})\, G_0^*(\mathbf{r}_2,\mathbf{r}) + G^*(\mathbf{r}_2,\mathbf{r})\, V(\mathbf{r})\, G_0(\mathbf{r}_1,\mathbf{r})\right] dV\,. \qquad \text{(A7.6)}$$

Hence the non-physical terms are non-reciprocal: the complex conjugation of the middle of Equation (A7.6) shows that interchanging the source and receiver locations changes the observed wave-field by time-reversing the non-physical waves (while having the physical waves unchanged by source-receiver reciprocity). By using the representation theorems for perturbed media of Vasconcelos *et al.* (2009) we have

explained our observation in Chapter 7 that the non-physical part of the scattered-wave estimate is non-reciprocal.

Appendix 8A: Discussion on stationary phase, source position, and non-physical arrivals

We now consider the distribution of stationary-phase regions for scattered surface wave recovery in relation to the source geometries available in the test data set. For the estimation of a single-scattered surface wave by correlation-type interferometry the stationary regions lie on the extension of the paths between each receiver and the scatterer (Chapter 6). In Figure A8.1a we show a sketch with two receiver positions ($\mathbf{r}_A$ and $\mathbf{r}_B$) and a single scatterer (*sc*), the distribution of sources we consider is illustrated by the grey shaded area. The stationary-phase regions for the single-scattered surface wave propagating from $\mathbf{r}_A$ to $\mathbf{r}_B$ via *sc* are indicated by the yellow shaded areas SR_{P1} and SR_{NP}. Sources in these regions will contribute arrivals to the interferometric estimate that stack constructively in the application of Equation (8.5). For a source in the stationary region SR_{P1} the cross-correlation removes the common path from the waves observed at each receiver. In this case the common path is the path between the source in SR_{P1} and the virtual source $\mathbf{r}_A$. Removing this path results in the observation of the scattered wave at $\mathbf{r}_B$ as if it had been excited by a source at $\mathbf{r}_A$, i.e., this contributes a physical arrival. However, for a source located within the stationary region SR_{NP} the common path is the path between the source and the scatterer. The resulting arrival observed at $\mathbf{r}_B$ has a phase which is the same as the phase difference of a wave propagating between the scatterer (*sc*) and each receiver ($\mathbf{r}_A$ and $\mathbf{r}_B$). This arrival does not correspond to the physical scattered wave and results in a non-physical term. For the off-line scatterer considered here, we observe that this non-physical stationary region does not coincide with the source distribution. Therefore, if we choose sources for interferometry that lie to the left of receiver $\mathbf{r}_A$ (the virtual source), and coincide with the region SR_{P1}, we can be confident that we can estimate offline scattered waves while mitigating for some of the non-physical arrivals that may be introduced.

In Figure A8.1b we show a similar sketch for an in-line scatterer. The physical stationary-phase region again is located to the left of receiver $\mathbf{r}_A$, but the non-physical stationary-phase region also coincides with the source distribution in this

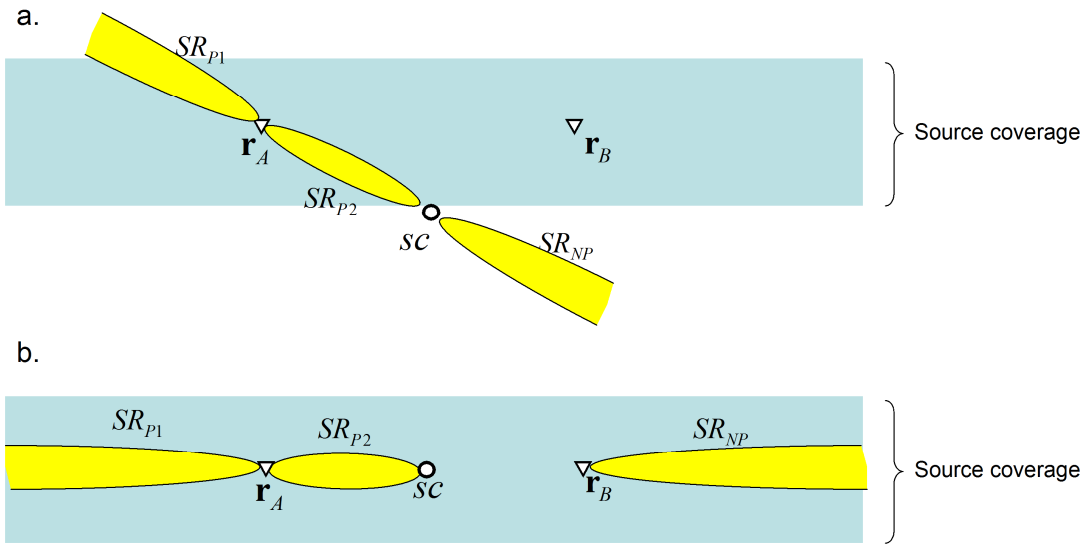

Figure A8.1: Sketch geometry showing the source distribution (grey shaded area), two receivers (triangles), a single scatter (circle) and various stationary phase regions discussed in the appendix for (a) an offline scatterer and (b) an inline scatterer.

case. Hence, by following the observations of our previous work, we can attempt to mitigate for non-physical scattered arrivals but we can also select sources from which we can expect to construct scattered surface waves.

A similar analysis for the convolution case is simpler, since in this case (and in the specific configurations shown) the stationary phase region, SR_{P2}, is located between the scatterer and the receiver and there is *only* a physical contribution. In both of our sketches, the source coverage coincides with the stationary-phase region for the scattered wave when applying convolution-type interferometry.

By applying intuition from our previous stationary-phase analysis, using the limited source geometries available we have identified that we can expect to reconstruct the physical scattered surface waves, but we can also choose sources such that we limit the introduction of non-physical arrivals. Vasconcelos *et al.* (2009) identify similar non-physical arrivals for acoustic waves. They propose to limit the choice of boundary sources such that non-physical arrivals do not appear in their interferometric estimates in a similar fashion to the case shown in our sketches.

References

Aki, K., 1957. Space and time spectra of stationary stochastic waves with special reference to microtremors, *Bulletin of the Earthquake Research Institute,* 35**,** pp 415-456.

Aki, K. & P.G. Richards, 2002. Quantitative Seismology, *University Science Books, California*.

Al-Husseini, M.I., J.B. Glover & B.J. Barley, 1981. Dispersion patterns of the ground roll in eastern Saudi Arabia, *Geophysics,* 46**,** 121-137.

Bakulin, A. & R. Calvert, 2004. Virtual Source: new method for imaging and 4D below complex overburden, *74th Annual International Meeting, SEG, Expanded Abstracts***,** 2477-2480.

Bakulin, A. & R. Calvert, 2006. The virtual source method: Theory and case study, *Geophysics,* 71**,** SI139-SI150.

Barbier, M.G., P. Bondon, R. Mellinger & J.R. Viallix, 1976. Mini-SOSIE for land seismology, *Geophys. Prosp.,* 24**,** 518-527.

Beaty, K.S., D.R. Schmitt & M. Sacchi, 2002. Simulated annealing inversion of multimode Rayeligh wave dispersion curves for geological structure, *Geophys. J. Int.,* 151**,** 622-631.

Blonk, B., G.C. Herman & G.G. Drijkoningen, 1995. An elastodynamic inverse scattering method for removing scattered surface waves from field data, *Geophysics,* 60**,** 1897-1905.

Blonk, B. & G.C. Herman, 1996. Removal of scattered surface waves using multicomponent seismic data, *Geophysics,* 61**,** 1483-1488.

Born, M. & E. Wolf, 1999. Principles of Optics, *Cambridge University Press, Cambridge, UK*.

Bostock, M.G., 1990. On the orthogonality of surface wave eigenfunctions in cylindrical coordinates, *Geophys. J. Int.,* 103 763 - 767.

Brandenburg, A. & R. Snieder, 1989. The attenuation of surface waves due to scattering, *Geophys. J.,* 8**,** 183-194.

Budreck, D.E. & J.H. Rose, 1992. A Newton-Marchenko equation and generalized optical theorem for elastodynamics, *J. Maths. Phys.,* Vol. 33**,** 2903-2915

Burnett, D. & R.L. Holford, 1998. Prolate and oblate spheroidal acoustic infinite elements *Comput. Methods Appl. Mech. Eng.,* 158**,** 117-141.

Campillo, M. & A. Paul, 2003. Long-Range Correlations in the Diffuse Seismic Coda, *Science* 299**,** 547 - 549.

Campman, X.H., K. van Wijk, J.A. Scales & G.C. Herman, 2005. Imaging and suppressing near-receiver scattered surface waves, *Geophysics,* 70**,** V21-V29.

Campman, X.H., G.C. Herman & E. Muyzert, 2006. Suppressing near-receiver scattered waves from seismic land data, *Geophysics,* 71**,** S121-S128.

Campman, X.H. & C.D. Riyanti, 2007. Non-linear inversion of scattered seismic surface waves, *Geophys. J. Int.,* 171**,** 1118-1125.

Cara, M., 1978. Regional variations of higher Rayleigh-mode phase velocities: a spatial-filtering method, *Geophys. J. R. astr. Soc.,* 54**,** 439-460.

Carney, P.S. & E. Wolf, 1997. Statistical generalizations of the optical cross-section theorem with application to inverse scattering, *J. Opt. Soc. Am. A,* 14**,** 3366-3371.

Cassereau, D. & M. Fink, 1992. Time-Reversal of Ultrasonic Fields - Part III: Theory of the Closed Time-Reversal Cavity, *IEEE Trans. Ultrason. Ferroellectr. Freq. Control,* 39**,** 579-592.

Cassereau, D. & M. Fink, 1993. Focusing with Plane Time-Reversal Mirrors: an Efficient Alternative to Closed Cavities, *J. Acoust. Soc. Am.,* 94**,** 2373.

Chadan, K. & P.C. Sabatier, 1989. Scattering amplitudes from elastic cross sections, *Inverse problems in Quantum Scattering Theory,* 2nd ed. Springer, New York.

Chávez-García, F.J. & F. Luzón, 2005. On the correlation of seismic microtremors, *J. Geophys. Res.,* 110**,** B11313.

Chinnery, P.A., J. Zhang & V.F. Humphrey, 1997. Acoustic scattering by nonmetallic and metallic cubes in the elastic resonance regime: Experimental

measurements and combined finite element/boundary element modeling, *J. Acoust. Soc. Am.,* 84**,** 2280-2284.

Claerbout, J., 1976. Fundamentals of Geophysical Data Processing, *Blackwell Scientific Publications.*

Claerbout, J.F., 1968. Synthesis of a layered medium from its acoustic transmission response, *Geophysics,* 33**,** 264-269.

Claerbout, J.F., 1998. Multidimensional recursive filters via a helix, *Geophysics,* 63**,** 1-13.

Claerbout, J.F., 2004. Earth Soundings Analysis: Processing versus Inversion, *available at http://sepwww.stanford.edu/sep/prof/.*

Clayton, R.W. & R.A. Wiggins, 1976. Source shape estimation and deconvolution of teleseismic body waves, *Geophys. J. Royal Ast. Soc.,* 47**,** 151-177.

Crampin, S. & M. Bath, 1965. Higher Modes of Seismic Surface Waves: Mode Separation, *Geophys. J.,* 10**,** 81-92.

Curtis, A. & J. Robertsson, 2002. Volumetric wavefield recording and near-receiver group velocity estimation for land seismics, *Geophysics,* 67**,** 1602-1611.

Curtis, A., P. Gerstoft, H. Sato, R. Snieder & K. Wapenaar, 2006. Seismic Interferometry - Turning Noise into Signal, *The Leading Edge,* 25**,** 1082-1092.

Dahlen, F.A. & G. Nolet, 2005. Comment on 'On sensitivity kernels for 'wave-equation' transmission tomography' by de Hoop and van der Hilst, *Geophys. J. Int.,* 163**,** 949-951.

de Hoop, A.T., 1985. A time-domain energy theorem for scattering of plane waves in fluids, *J. Acoust. Soc. Am.,* 77**,** 11-14.

de Hoop, A.T., 1995. Handbook of Radiation and Scattering of Waves, *Academic Press, San Diego.*

de Hoop, M.V. & R.D. van der Hilst, 2005a. On sensitivity kernels for 'wave-equation' tomography, *Geophys. J. Int.,* 160**,** 621-633.

de Hoop, M.V. & R.D. van der Hilst, 2005b. Reply to comment by F.A. Dahlen and G. Nolet on 'On sensitivity kernels for 'wave-equation' transmission tomography', *Geophys. J. Int.,* 163**,** 952-955.

de Rosny, J. & M. Fink, 2002. Overcoming the Diffraction Limit in Wave Physics Using a Time-Reversal Mirror and a Novel Acoustic Sink, *Physical Review Letters,* 89**,** 124301.

Derode, A., P. Roux & M. Fink, 1995. Robust Acoustic Time Reversal with High-Order Multiple Scattering, *Phys. Rev. Lett.,* 75**,** 4206-4209.

Derode, A., E. Larose, M. Campillo & M. Fink, 2003a. How to estimate the Green's function of a heterogeneous medium between two passive sensors? Application to acoustic waves, *Applied Physics Letters,* 83**,** 3054-3056.

Derode, A., E. Larose, M. Tanter, J. de Rosny, A. Tourin, M. Campillo & M. Fink, 2003b. Recovering the Green's function from field-field correlations in an open scattering medium, *J. Acoust. Soc. Am.,* 113**,** 2973-2976.

Dong, S., R. He & G. Schuster, 2006. Interferometric prediction and least squares subtraction of surface waves, *76th Annual International Meeting, SEG, Expanded Abstracts***,** 2783-2786.

Dost, B., 1990. Upper Mantle Structure Under Western Europe From Fundamental and Higher Mode Surface Waves Using the Nars Array, *Geophys. J. Int.,* 100**,** 131-151.

Douma, H. & R. Snieder, 2006. Correcting for bias due to noise in coda wave interferometry, *Geophys. J. Int.,* 164**,** 99-108.

Draganov, D., K. Wapenaar & J. Thorbecke, 2004. Passive seismic imaging in the presence of white noise sources, *The Leading Edge,* 23**,** 889-892.

Draganov, D. & R. Ghose, 2006. Seismic Interferometry in Near-Surface Seismics - An Experiment, *EAGE, Near Surface 2006, Helsinki***,** A045.

Draganov, D., K. Wapenaar, W. Mulder, J. Singer & A. Verdel, 2007. Retrieval of reflections from seismic background-noise measurements, *Geophysical Research Letters,* 34**,** L04305.

Draganov, D., R. Ghose, E. Ruigrok, J. Thorbecke & K. Wapenaar, 2008. Effect of Intrinsic Losses on Seismic Interferometry, *Rome 2008, 70th EAGE Conference and Exhibtion.*

Ernst, F., G.C. Herman & B. Blonk, 2002a. Reduction of near-surface scattering effects in seismic data, *The Leading Edge,* 17**,** 759.

Ernst, F., G.C. Herman & A. Ditzel, 2002b. Removal of scattered guided waves from seismic data, *Geophysics,* 67**,** 1240-1248.

Fink, M., D. Cassereau, A. Derode, C. Prada, P. Roux, M. Tanter, J.-L. Thomas & F. Wu, 2000. Time-reversed acoustics, *Rep. Prog. Phys. ,* 63**,** 1933-1995.

Foldy, L.L., 1945. The Multiple Scattering of Waves. I. General Theory of Isotropic Scattering by Randomly Distributed Scatterers, *Phys. Rev.*, 67**,** 107-119.

Gabriels, P., R. Snieder & G. Nolet, 1987. In situ measurements of shear-wave velocity in sediments with higher-mode Rayleigh waves, *Geophysical Prospecting,* 35**,** 187-196.

Gertstoft, P., K.G. Sabra, P. Roux, W.A. Kuperman & M.C. Fehler, 2006. Green's functions extraction and surface-wave tomography from microseisms in southern California, *Geophysics,* 71**,** SI23-SI31.

Glauber, R. & V. Schomaker, 1953. The Theory of Electron Diffraction, *The Physical Review,* 89**,** 667-671.

Gosselet, A. & S.C. Singh, 2007. Using symmetry breaking in time-reversal mirror for attenuation determination, *SEG Expanded Abstracts,* 26**,** 1639-1643.

Groenenboom, J. & R. Snieder, 1995. Attenuation, dispersion and anisotropy by multiple scattering of transmitted waves through distributions of scatterers, *J. Acoust. Soc. Am.,* 98**,** 3482-3492.

Guitton, A., B. Kaelin & B. Biondi, 2007. Least-squares attenuation of reverse-time-migration artifacts, *Geophysics,* 72**,** S19-S23.

Haddon, R.A.W., 1986. Exact evaluation of the response of a layered elastic medium to an explosive point source using leaking modes, *Bull. Seis. Soc. Am,* Vol. 76**,** 1755-1775.

Hargreaves, N.D. & A.J. Calvert, 1991. Inverse-Q filtering by Fourier transform, *Geophysics,* 56**,** 519-527.

Herman, G.C., P.A. Milligan, R.J. Huggins & J.W. Rector, 2000. Imaging shallow objects and heterogeneities with scattered guided waves, *Geophysics,* 65**,** 247-252.

Herman, G.C. & C. Perkins, 2006. Predictive removal of scattered noise, *Geophysics,* 71**,** V41-V49.

Hermann, F.J., D. Wang & D.J. Verschuur, 2008. Adaptive curvelet-domain primary-multiple separation, *Geophysics,* 73**,** A17-A21.

Hong, T.-K. & W. Menke, 2006. Tomographic investigation of the wear along the San Jacinto fault, southern California, *Phys. Earths Planet. Inter.,* 155**,** 236-248.

Hwang, H.J. & B.J. Mitchell, 1986. Interstation surface wave analysis by frequency-domain wiener deconvolution and modal isolation, *Bulletin of the Seismological Society of America,* 76**,** 847-864.

Kaslilar, A., 2007. Inverse scattering of surface waves: imaging of near-surface heterogeneities, *Geophys. J. Int.,* 171**,** 352-367.

Korneev, V.A. & A. Bakulin, 2006. On the fundamentals of the Virtual Source Method, *Geophysics,* 71**,** A13-A17.

Laake, A., C. Strobbia & A. Cutts, 2008. Integrated approach to 3D near surface characterization in desert regions, *First Break,* 26**,** 109-112.

Lai, C.G. & G.J. Rix, 1998. Simultaneous Inversion of Rayleigh Phase Velocity and Attenuation for Near-Surface Site Characterization, *Report No. GIT-CEE/GEO-98-2, School of Civil and Environmental Engineering, Georgia Institute of Technology.*

Larose, E., A. Derode, D. Clorennec, L. Margerin & M. Campillo, 2005. Passive retrieval of Rayleigh waves in disordered elastic media, *Phys. Rev. E,* 72**,** 046607.

Levander, A., 1990. Seismic scattering near the earth's surface, *Pure Appl. Geophys.,* 132**,** 21-47.

Lin, F.-C., M.P. Moschetti & M. Ritzwoller, 2008. Surface wave tomography of the western United States from ambient seismic noise: Rayleigh and Love wave phase velocity maps, *Geophys. J. Int.,* 173**,** 281-298.

Lobkis, O.I. & R.L. Weaver, 2001. Ultrasonics without a Source: Thermal Fluctuation Correlations at MHz Frequencies, *Phys. Rev. Lett.,* 87**,** 134301.

Louie, J.N., 2001. Faster, Better: Shear-Wave Velocity to 100 Meters Depth from Refraction Microtremor Arrays, *Bulletin of the Seismological Society of America,* 91**,** p. 347-364.

MacBeth, C.D. & P.W. Burton, 1985. Upper crustal shear velocity models from higher mode Rayleigh wave dispersion in Scotland, *Geophys. J. R. astr. Soc.*, 83**,** 519-539.

Malcolm, A.E., J.A. Scales & B.A. van Tiggelen, 2004. Extracting the Green function from diffuse, equipartitioned waves, *Phys. Rev. E*, 70**,** 015601

Marquering, H. & R. Snieder, 1995. Surface-wave mode coupling for efficient forward modelling and inversion of body-wave phases, *Geophys. J. Int.*, 120**,** 186-208.

Marquering, H., F.A. Dahlen & G. Nolet, 1999. Three-dimensional sensitivity kernels for finite-frequency traveltimes: the banana-doughnut paradox *Geophys. J. Int.*, 137**,** 805-815.

Marston, P.L., 2001. Generalized optical theorem for scatterers having inversion symmetry: Applications to acoustic backscattering, *J. Acoust. Soc. Am.*, 109**,** 1291-1295.

Mehta, K., A. Bakulin, J. Sheiman, R. Calvert & R. Snieder, 2007. Improving the virtual source method by wavefield separation, *Geophysics,* 72**,** pp. V79–V86.

Mehta, K., J. Sheiman, R. Snieder & R. Calvert, 2008. Strenghtening the virtual-source method for time-lapse monitoring, *Geophysics*, Vol. 73**,** S73-S80.

Meier, T., G. Lebedev, G. Nolet & F.A. Dahlen, 1997. Diffraction tomography using multimode surface waves, *J. Geophys. Res.*, 102**,** 8255–8267.

Mitchel, R.G., 1980. Array measurements of higher mode Rayleigh wave dispersion: an approach utilizing source parameters, *Geophys. J. R. astr. Soc.*, 63**,** 311-331.

Montelli, R., G. Nolet, F.A. Dahlen, G. Masters, G. Engdahl & S.-H. Hung, 2004a. Finite-frequency tomography reveals a variety of plumes in the mantle, *Science*, 303**,** 338-343.

Montelli, R., G. Nolet, F.A. Dahlen, G. Masters, G. Engdahl & S.-H. Hung, 2004b. Global P and PP travel time tomography: rays vs. waves, *Geophys. J. Int.*, 158**,** 637-654.

Morse, P.F. & G.F. Hildebrandt, 1989. Ground-roll suppression by the stack array, *Geophysics*, 54**,** 290-301.

Moschetti, M.P., M. Ritzwoller & N. Shapiro, 2007. Surface wave tomography of the Western United States from ambient seismic noise: Rayleigh wave group velocity maps, *Geochem., Geophys., Geosys,* 8**,** Q08010.

Newton, R.G., 1968. Determination of the amplitude from the differential cross section by unitarity, *J. Math. Phys.,* 9**,** 2050-2055.

Newton, R.G., 1976. Optical theorem and beyond, *American Journal of Physics,* 44**,** 639-642.

Nolet, G., 1975. Higher Rayleigh modes in Western Europe, *Geophysical Research Letters,* 2**,** 60-62.

Nolet, G. & G.F. Panza, 1976. Array analysis of seismic surface waves: limits and possibilities, *Pure Appl. Geophys,* 114**,** 776-790.

Nolet, G., R. Sleeman, V. Nijhof & B.L.N. Kennet, 1989. Synthetic reflection seismograms in three dimensions by a locked-mode approximation *Geophysics,* Vol. 54**,** 350-358.

Özbek, A., 2000a. Adaptive beamforming with generalized linear constraints, *SEG Expanded Abstracts,* 19**,** 2001-2084.

Özbek, A., 2000b. Multichannel adaptive interference cancelling, *SEG Expanded Abstracts,* 19**,** 2088-2091.

Park, C.B., R.D. Miller, J. Xia & J. Ivanov, 2007. Multichannel analysis of surface waves (MASW) - active and passive methods, *The Leading Edge,* 26**,** 60-64.

Pedersen, H.A., F. Krüger & the SVEKALAPKO Seismic Tomography Working Group, 2007. Influence of the seismic noise characteristics on noise correlations in the Baltic shield, *Geophys. J. Int.,* 168**,** 197-210.

Picozzi, M., S. Parolai, D. Bindi & A. Strollo, 2009. Characterization of shallow geology by high-frequency seismic noise tomography, *Geophys. J. Int.,* 176**,** 164-174.

Regone, C.J., 1998. Suppression of coherent noise in 3-D seismology, *The Leading Edge,* 17**,** 1584-1589.

Rhie, J. & B. Romanowicz, 2004. Excitation of Earth's continuous free oscillations by atmosphere-ocean-seafloor coupling, *Nature,* 431**,** 552-556.

Rhie, J. & B. Romanowicz, 2006. A study of the relation between ocean storms and the Earth's hum, *Geochem., Geophys., Geosys,* 7**,** Q10004.

Ritzwoller, M., N. Shapiro, M.P. Barmin & A.L. Levshin, 2002. Global surface wave diffraction tomography, *J. Geophys. Res.,* 107**,** ESE4.1-ESE4.13.

Robertsson, J.O.A., J.O. Blanch & W.W. Symes, 1994. Viscoelastic finite-difference modeling, *Geophysics,* 59**,** 1444-1456.

Robertsson, J.O.A. & A. Curtis, 2002. Wavefield separation using densely deployed, three component, single sensor groups in land surface seismic recordings, *Geophysics,* 67**,** 1624-1633.

Roth, M. & K. Holliger, 1999. Inversion of source-generated noise in high-resolution seismic data, *The Leading Edge,* 18**,** 1402-1406.

Ruigrok, E., D. Draganov & K. Wapenaar, 2008. Global-scale seismic interferometry: theory and numerical examples, *Geophysical Prospecting,* 56**,** 395-417.

Sabra, K.G., P. Roux & W.A. Kuperman, 2005. Arrival-time structure of the time-averaged ambient noise cross-correlation function in an oceanic waveguide, *J. Acoust. Soc. Am.,* 117**,** 164-174117.

Shapiro, N. & M. Campillo, 2004. Emergence of broadband Rayleigh waves from correlations of the ambient seismic noise, *Geophysical Research Letters,* 31**,** L07614.

Shapiro, N., M. Campillo, L. Stehly & M. Ritzwoller, 2005. High-Resolution Surface-Wave Tomography from Ambient Seismic Noise, *Science,* 307**,** 1615-1617.

Shearer, P., 1999. Introduction to Seismology, *Cambridge University Press.*

Slob, E. & K. Wapenaar, 2007. Electromagnetic Green's functions retrieval by cross-correlation and cross-convolution in media with losses, *Geophysical Research Letters,* 34**,** L05307.

Slob, E., D. Draganov & K. Wapenaar, 2007. Interferometric electromagnetic Green's functions representations using propagation invariants, *Geophys. J. Int.,* 169**,** 60-80.

Snieder, R., 1986. 3D Linearized scattering of surface waves and a formalism for surface wave holography, *Geophys. J. R. astr. Soc.,* 84**,** 581-605.

Snieder, R. & G. Nolet, 1987. Linearized scattering of surface waves on a spherical Earth, *J. Geophys.,* 61**,** 55-63.

Snieder, R., 1988. The optical theorem for surface waves and the relation with surface wave attenuation, *Geophys. J.,* 95**,** 293-302.

Snieder, R., 2002a. General theory of elastic wave scattering *in Scattering and Inverse Scattering in Pure and Applied Science , Eds. Pike, R. and P. Sabatier, Academic Press, San Diego***,** 528-542,.

Snieder, R., 2002b. Scattering of surface waves, *in Scattering and Inverse Scattering in Pure and Applied Science, Eds. Pike, R. and P. Sabatier, Academic Press, San Diego***,** 562-577.

Snieder, R., 2004a. Extracting the Green's function from the correlation of coda waves: A derivation based on stationary phase, *Phys. Rev. E,* 69**,** 046610.

Snieder, R., 2004b. A Guided Tour of Mathematical Methods for the Physical Sciences, 2nd Edition, *Cambridge University Press, Cambridge, UK*.

Snieder, R., K. Wapenaar & K. Larner, 2006. Spurious multiples in seismic interferometry of primaries, *Geophysics,* 71**,** SI111-SI124.

Snieder, R., 2007. Extracting the Green's function of attenuating heterogeneous media from uncorrelated waves, *J. Acoust. Soc. Am.,* 121**,** 2637-2643.

Snieder, R., K. Wapenaar & U. Wegler, 2007. Unified Green's function retrieval by cross-correlation; connection with energy principles, *Phys. Rev. E,* 75**,** 036103.

Snieder, R., K. van Wijk, M. Haney & R. Calvert, 2008. The cancellation of spurious arrivals in Green's function extraction and the generalized optical theorem, *Phys. Rev. E,* 78**,** 036606.

Spetzler, J. & R. Snieder, 2001. The effect of small-scale heterogeneity on the arrival time of waves, *Geophys. J. Int.,* 145**,** 786-796.

Spetzler, J., J. Trampert & R. Snieder, 2002. The effect of scattering in surface wave tomography, *Geophys. J. Int.,* 149**,** 755-767.

Steg, R.G. & P.G. Klemens, 1974. Scattering of Rayleigh waves by surface defects, *J. Appl. Phys.,* 45**,** 23-29.

Stehly, L., M. Campillo & N. Shapiro, 2006. A study of the seismic noise from its long-range correlation properties, *J. Geophys. Res.,* 111**,** B10306.

Steiner, B., E.H. Saenger & S.M. Schmalholz, 2008. Time reverse modeling of low-frequency mircotremors: Application to hydrocarbon reservoir localization, *Geophysical Research Letters,* 35**,** L03307.

Stenflo, L. & M.Y. Yu, 2002. An exact solution for externally driven surface plasma waves, *Physics of Plasmas,* 9**,** 5129-5130.

Stolt, R.H., 2002. Seismic data mapping and reconstruction, *Geophysics,* 67**,** 890-908.

Stork, C., 2007. Fixing the Non-Uniform Directionality Problem of Seismic Interferometry May Be Crucial to its Success, *69th EAGE Conference & Exhibition, London. Also, SEG Technical Program Expanded Abstracts***,** pp. 2713-2717.

Tan, T.H., 1977. Reciprocity relations for scattering of plane, elastic waves, *J. Acoust. Soc. Am.,* 61**,** 928-931.

Trampert, J. & J.H. Woodhouse, 1995. Global phase velocity maps of love and rayleigh waves between 40 and 150 seconds, *Geophysical Journal International* 122**,** 675-690.

van der Hilst, R.D. & M.V. de Hoop, 2005. Banana-doughnut kernels and mantle tomography, *Geophys. J. Int.,* 163**,** 956-961.

van der Neut, J. & A. Bakulin, 2009. Estimating and correcting the amplitude radiation pattern of a virtual source, *Geophysics,* 74**,** SI27-SI36.

van Heijst, H.J. & J. Woodhouse, 1997. Measuring surface-wave overtone phase velocities using a mode-branch stripping technique, *Geophysical Journal International,* 131 209–230.

van Manen, D.-J., J.O.A. Robertsson & A. Curtis, 2005. Modeling of wave propagation in inhomogeneous media, *Phys. Rev. Lett.,* 94**,** pp. 164301-164301 - 164301-164304.

van Manen, D.-J., A. Curtis & J.O.A. Robertsson, 2006. Interferometric modeling of wave propagation in inhomogeneous elastic media using time reversal and reciprocity, *Geophysics,* 71**,** SI47-SI60.

van Manen, D.-J., J.O.A. Robertsson & A. Curtis, 2007. Exact wavefield simulation for finite-volume scattering problems, *J. Acoustic. Soc. Am. Express Letters,* 122**,** pp. EL115-EL121.

van Vossen, R., A. Curtis & J. Trampert, 2005. Subsonic near-surface P velocity and low S velocity observations using propagator inversion, *Geophysics,* 70**,** R15-R23.

Vasconcelos, I.R., 2007. Interferometry in perturbed media, *Ph.D. dissertation, Colorado School of Mines.*

Vasconcelos, I.R., R. Snieder & B. Hornby, 2007. Target-oriented interferometry - Imaging with internal multiples from subsalt VSP data, *77th Annual International Meeting, SEG, Expanded Abstracts***,** 3069-3073.

Vasconcelos, I.R. & R. Snieder, 2008a. Interferometry by deconvolution: Part 1 - Theory for acoustic waves and numerical examples, *Geophysics,* Vol. 73**,** S115-S128.

Vasconcelos, I.R. & R. Snieder, 2008b. Interferometry by deconvolution: Part 2 - Theory for elastic waves and application to drill-bit seismic imaging *Geophysics,* Vol. 73**,** S129-S141.

Vasconcelos, I.R., J. Gaiser, A. Calvert & C. Calderón-Macías, 2008. Retrieval and suppression of surface waves using interferometry by correlation and by deconvolution, *SEG Expanded Abstracts,* 27**,** pp. 2566-2570.

Vasconcelos, I.R., R. Snieder & H. Douma, 2009. Representation theorems and Green's function retrieval for scattering in acoustic media *Physical Review E,* 80**,** 036605.

Vermeer, G., 2002. 3D Seismic Survey Design, *Society of Exploration Geophysics.*

Wang, Y., 2002. A stable and efficient approach of inverse-Q filtering, *Geophysics,* 67**,** 657-663

Wapenaar, K., 2003. Synthesis of an inhomogeneous medium from its acoustic transmission response, *Geophysics,* 68**,** 1756-1759.

Wapenaar, K. & J. Fokkema, 2004. Reciprocity Theorems for Diffusion, Flow, and Waves, *J. Appl. Mech.,* 71**,** 145-150.

Wapenaar, K., J. Thorbecke & D. Draganov, 2004. Relations between reflection and transmission responses of three-dimensional inhomogeneous media, *Geophys. J. Int.,* 156**,** 179-194.

Wapenaar, K., 2004. Retrieving the elastodynamic Green's function of an arbitrary inhomogeneous medium by cross correlation, *Phys. Rev. Lett.,* 93**,** 254301.

Wapenaar, K. & J. Fokkema, 2006. Green's function representations for seismic interferometry, *Geophysics,* 71**,** SI33-SI44.

Wapenaar, K., 2006. Green's function retrieval by cross-correlation in case of one-sided illumination, *Geophysical Research Letters,* 33**,** L19304.

Wapenaar, K., E. Slob & R. Snieder, 2006. Unified Green's function retrieval by cross-correlation, *Phys. Rev. Lett.,* 97**,** 234301.

Wapenaar, K., 2007. General representations for wavefield modeling and inversion in geophysics, *Geophysics,* Vol. 72**,** SM5-SM17.

Wapenaar, K., J. van der Neut & E. Ruigrok, 2008a. Passive seismic interferometry by multidimensional deconvolution, *Geophysics,* Vol. 73**,** A51-A56.

Wapenaar, K., E. Slob & R. Snieder, 2008b. Seismic and electromagnetic controlled-source interferometry in dissipative media, *Geophysical Prospecting,* 56**,** 419-434.

Weaver, R.L. & O.I. Lobkis, 2001. On the emergence of the Green's function in the correlations of a diffuse field, *J. Acoust. Soc. Am.,* 110**,** pp. 3011-3017.

Wixforth, A., J.P. Kotthaus & G. Weimann, 1986. Quantum Oscillations in the Surface-Acoustic Wave Attenuation Caused by a Two-Dimensional Electron System, *Physical Review Letters,* 56**,** 2104-2106.

Xia, J., R.D. Miller & C.B. Park, 2000. Advantages of calculating shear-wave velocity from surface waves with higher modes, *70th Annual International Meeting, SEG, Expanded Abstracts***,** 1295-1298.

Yang, Y., M. Ritzwoller, A.L. Levshin & N. Shapiro, 2007. Ambient noise Rayleigh wave tomography across Europe, *Geophys. J. Int.,* 168**,** 259-274.

Yao, H., C. Beghein & R.D. van der Hilst, 2008. Surface wave array tomography in SE Tibet from ambient seismic noise and two-station analysis - II. Crustal and upper-mantle structure, *Geophys. J. Int.,* 173**,** 205-219.

Yilmaz, Ö., 2001. Seismic data analysis: Processing, Inversion, and Interpretation of Seismic Data *Society of Exploration Geophysicists*.

Yoshizawa, K. & B.L.N. Kennet, 2004. Multi-mode surface wave tomography for the Australian region using a three-stage approach incorporating finite frequency effects, *J. Geophys. Res.,* 109**,** B02310.